Antigen-antibody interactions measurements using surface plasmon fluorescence spectroscopy

De Mello Lebre Marques Vareiro, Margarida

Award date:
2006

Awarding institution:
University of Bath

Antigen-Antibody Interactions Measurements Using Surface Plasmon Fluorescence Spectroscopy

Margarida de Mello Lebre Marques Vareiro

A thesis submitted for the degree of Doctor of Philosophy

University of Bath
Department of Chemistry
Bath
June 2006

ProQuest LLC
789 East Eisenhower Parkway
P.O. Box 1346
Ann Arbor, MI 48106-1346

TABLE OF CONTENTS

LIST OF FIGURES

LIST OF TABLES

Acknowledgements

I would like to thank Dr. Toby Jenkins for making this research project possible and for giving me the opportunity to come to England to work on it.

I would like to acknowledge Unipath for funding the project especially to my industrial supervisors Dr. Kris Zak and Prof. David Williams for the valuable exchange of ideas and constructive and helpful comments.

I am grateful to Prof. Wolfgang Knoll for accepting me on a visit to his lab for 2 months, and specially for giving me the opportunity to work with Dr. Jing Liu to whom I am grateful for all valuable advices and research interaction in the course of this work.

At the Department of Chemistry and more specifically in the Physical Chemistry Research group I have benefited from valuable exchange of ideas, constructive critics and supportive comments from Killian Lobato, who worked with me as if my project was his project. (Obrigada Ki).

To the other members of the Physical Chemistry Group I would like to give a special thanks to Hayley Dash, Tom Williams, Jonathan Olds, Dr, Russel Keay, Dr. Steve Flower, Dr. Stephen Hill for all their support through periods of good and bad times in the lab. Thank you for generating such pleasant working environment and for all the encouragement.

I would like to thank to all my new friends in England, specially to Cristina, Carla, Amilcar, Ramon, Killian, Phil, Kam, Ana, for their unlimited support, encouragement and for all the good times spent together that made these years so enjoyable.

At last, I would like to thank my family for all their understanding and for their encouragement in this project of life, far away form the ones that care and love me. To my newborn nephews and nice that have understood why their aunt was away for such long periods during this research period, I have never forgotten them.

Abbreviations

[Q]	Quencher concentration
A	Absorbance
A	Surface Protein Concentration
a	Particle radius
A'	Constant related with molecular properties
A,G,T,C	Adenine, guanine, thymine, cytosine
Abs I^{FL}	Absolute fluorescence intensity
ADIFAB	Acrylodan-derivatised I-FABP
AF-anti-α-hCG	Alexa Fluor 647 labelled anti-α-hCG
AF-anti-β-hCG	Alexa Fluor 647 labelled anti-β-hCG
AFM	Atomic Force Microscopy
A_H	Hamaker constant
Anti-α-hCG	Monoclonal antibody against the α region of hCG
Anti-β-hCG	Monoclonal antibody against the α region of hCG
ATR	Attenuated Total Reflection
$\vec{B}$	Magnetic flux density
b-anti-α-hCG	Biotin labelled anti-α-hCG
b-anti-β-hCG	Biotin labelled anti-β-hCG
b-anti-HSA	Biotion labelled HSA antibody
b-Fab	Biotin labelled Fab
biotin-Thiol	1*H*-thieno[3,4-*d*]imidazole-4-pentanamide,hexahydro-*N*-[2-[2-[2-[(11-mercapto-1-oxoundecyl)amino]ethoxy]-ethoxy]ethyl]-2-oxo-,[3aS(3aa,4b,6aa)]
b-Protein A	Biotin labelled Protein A
BSA	Bovine Serum Albumin
c	Concentration
χ	Mole fraction
c	Velocity of light
CF	Correction Factor
CM5	BIACORE dextran with carboxymethyl groups sensor chip
CPS	Counts Per Second
Cy5, Cy3	Cyanine dyes
$\vec{D}$	Electric Displacement Field
δ,d	Layer thickness
DADOO	2,2'-(ethylenediooxyl)bis-(ethylamine)
ΔG	Gibb's free energy
DMF	Dimethylformamide
DMP	Dimethyl Pimelimidate Dihydrochloride
DMSO	Dimethyl sulfoxide
DNA	Deoxyribonucleic Acid
DoL	Degree of Labelling
dsDNA	Double strand DNA
ΔW	Work
ε	Dielectric permittivity
$\vec{E}$	Electric field
ε	Molar absorptivity
E3G	estrone-3-glucuronide
EDAC	1-ethyl-3-(3-dimethylaminopropyl)-carbodiimide
EIA	Enzyme immunoassay

ELISA	Enzyme-linked immunosorbent assay
$\varepsilon_{\min}$	Potential well
EPA	5,8,11,14,17-Eicosapentanoic acid
f	Focus point
F	Fluorescence
FA	Fatty Acid
Fab	Antigen binding fragment
FABP	Fatty Acid Binding Protein
Fc	Antibody Fragment C-Terminal
FCFD	Fluorescent capillary fill device
FFA	Free Fatty Acids
FRET	Fluorescence Resonance Energy Transfer
FSH/hFSH	human Follicle-Stimulating Hormone
FTIR	Fluorescence Total Internal Reflection
FTIR	Fourier Transform Infrared Spectroscopy
GN	Gold Nanoparticles
H	Distance between particles
h	Planks constant
$\hbar$	reduced Planck's constant
$\vec{H}$	Magnetic field intensity
hCG	Human Chorionic Gonadotrophin
He-Ne	Heon-Neon laser
HEPES	N-(2-hydroxyethyl)piperazine-N'-(2-ethanesulfonic acid)
HEPES-PF 68	HEPES buffer with Pluoronic F-68
HF	Hydrofluoric Acid
HIV	Human Immunodeficiency Virus
HPDP	N-6-(biotinamido)-hexyl-3'-2'-pyridyldithio)propionamide
HSA	Human Serum Albumin
H_Z	Hertz
I, L, H-FABP	Intestinal, Liver and Heart-FABP
I_0	Intensity of exciting light
IC	Internal conversion
I^{FL}	Fluorescence Intensity
IgG, A, M, E, D	Immunoglobulin G, A, M, E, D
IR	Infrared
IRE	Internal Reflection Element
IRMA	Immunoradiometric assay
ISC	Intersystem Conversion
IUPAC	International Unit of Pure and Applied Chemistry
IU	International Units
κ_B	Boltzmann constant
κ	Inverse Debye length
$\vec{k}_i$	Wave vector
k_i	Momentum
k	Kinetic rate constants
K_D, K_S	Stern-Volmer Dynamic Quenching and Association Constants
K_D, K_A	Dissociation and Association Constant
kDa	Kilo Dalton.
K_{SV}	Stern-Volmer constant
l, L,l	Length

$LaSFN_9$	High refractive index glass
LH/hLH	human Luteinising Hormone
LoD	Limit of Detection
MHA	16-mercapto-1-hexadecanoic acid
MSKA	Metre, Second, Kilo, Ampere units
MTX	Methotrexate
MUOH	11-mercapto-1-undecanol
MW	Molecular weight
n	Refractive index
Norm I^{FL}	Normalised Fluorescence Intensity
NSB	Non Specific Binding
OH-Thiol	11-mercapto-1-undecanol
$\vec{P}$	Electric polarisation
P	Phosphorescence
PBS	Phosphate Saline Buffer
PBSTA	Phosphate Saline Buffer with Tween 20 and Sodium Azide
PMT	Photomultiplier Tube
PNA	Peptide Nucleic Acid
PRB	Plasmon Resonance Band
Py-CH2-NH2	Pyrene chromophore
θ_C	Critical angle
θ, ϕ	Angles
R	Reflectance, reflectivity
r	Radius
R	System response (reflectivity, fluorescence, etc)
RIA	Radioimmunoassay
RNA	riboxynucleic acid
R_0	Forster distance
r	Distance
S	Scattering coeficient
S_0, S_1, S_2	Singlet electronic states
SA	Streptavidin
SAM	Self Assembled Monolayer
SCB	Sodium Carbonate Buffer
SEM	Scanning Electron Microscopy
SP	Surface Plasmon
SPB	Surface Plasmon Band
SPFS	Surface Plasmon Fluorescence Spectroscopy
SPR	Surface Plasmon Resonance
SPRS	Surface Plasmon Resonance Spectroscopy
ssDNA	Single strand DNA
T	Temperature
τ, τ_0	Fluorescence lifetime and unquenched lifetime
τ_D	Decay rate
T_1	Triplet electronic state
TEM	Transmission Electron Microscopy
TIRF	Total Internal Reflection Fluorescence
TSH/hTSH	Thyroid Stimulating Hormone
UPDGA	Uridine diphosphoglucurionic acid
UV	Ultra-violet
VR	Vibrational Relaxation
VPC	Ventricular Premature Complexes

ν	Frequency
ω	Angular Frequency
XANES	X-Ray Absorption Near-Edge Structure
XPS	X-Ray Photoelectron Spectroscopy
XRD	Powder X-Ray Diffractometry
ζ	Zeta potential
z	Counter ions valence

Abstract

The ability to measure interaction properties of biological macromolecules quantitatively and qualitatively for a wide range of affinity, size, and purity is important. Interactions between an antigen, hCG, and antibodies, anti-α -hCG and anti-β-hCG, were measured by SPR and SPFS, on developed and optimised sensor surfaces. The influence of the concentration of biotinylated thiol on the binding of biotinylated antibody and its functionality, in terms of its ability to bind to hCG, was studied. This allowed determination of the optimum biotin-thiol mole fraction in the mixed SAM allowing maximisation of the binding of hCG on streptavidin-bound antibody. SPFS studies of the binding of a fluorescently labelled antibody to hCG showed that detection of 2 mIU mL^{-1} hCG (4 x 10^{-12} mol L^{-1}) could be realised. The system was further optimised by using a more oriented and organised surface through adsorption of monobiotinylated Fab-hCG in place of the whole antibody. A limit of detection of 0.3 mIU mL^{-1} (6 x 10^{-13} mol L^{-1}) was achieved for this system. This work illustrated the importance of antibody orientation, both on the planar surface and in terms of position of binding site, in maximising sensor sensitivity.

In this work a sensor surface was developed for detection of low molecular weight, non-tightly packed molecules with relatively low binding constants such as fatty acids. SPR is ineffective to detect these molecules, as the response is proportional to the mass density of the bound analyte. In order to overcome this problem a competitive assay for detection of FFA using SPFS was employed. A new fluorescent probe consisting of a small chain fatty acid attached to Cy5 fluorophore at the terminal end of the alkyl chain and a new developed fatty acid antibody were employed for sensing and surface structure, respectively. The equilibrium dissociation constants of the fluorescently labelled FA and unlabelled FA binding to FA-antibody of 40 μg mL^{-1} ± 5.6 μg mL^{-1} and 50 μg mL^{-1} ± 30 μg mL^{-1} were determined, respectively. Experiments were run to determine the equilibrium desorption constant of a more clinically relevant molecule, bilirubin. The decrease of the fluorescent signal with the increase of bilirubin concentration was followed. The overall results suggested that the newly developed FA-antibody had different binding sites and some more studies should follow to understand the locations and specificity of the binding sites.

Modified gold nanoparticles surface plasmon band were employed to explore the possibility of enhancing the excitation of chromophores present in vicinity of the field. Nanoparticles present a characteristic oscillation frequency of the plasmon resonance

band, which reflects the deep red colour of gold nanoparticles solutions in water reflects. The preliminary measurements produced in this work have shown that when Alexa Fluor 555-ssDNA hybridises with biotinylated DNA bound to gold nanoparticles there is an increase in fluorescence emission intensity.

1 Introduction

In this chapter, the molecules used in this work and their biological function are described. Then, follows a description of the methodology employed in this work, the different types of biosensors and their applications, more specifically of the optical methods Surface Plasmon Resonance and Fluorescence Spectroscopy. A brief introduction to immobilisation strategies is also presented.

1.1 Proteins

Proteins are linear polymers of amino acids that participate in almost every single biological process. Biochemists have been studying protein function and activity for more than a century and this understanding is critical for advances in health care.

Protein function depends on structure (primary, secondary, tertiary) and location in a biological system. Proteins can act as enzymes, transporters and binders of other molecules for storage; structural proteins providing support and shape to cells; assemblies of proteins can produce mechanical work, such as the movement of flagella or contraction of muscles. Some proteins are gene expression regulators participating in decoding cell information; some proteins can act as hormones, which regulate biochemical activities in target cells or tissues; and some proteins have a defence function, for example, antibodies, also called immunoglobulins, against, amongst other things, bacterial or viral infections [1].

In the work presented in this thesis, some well studied proteins were employed and will be described in detail in section 1.1.2. These proteins, a hormone and different immunoglobulins, were used to optimise the analytical methods used, SPR and SPFS (Surface Plasmon Resonance and Fluorescence Spectroscopy), for optimisation of the sensor surface modification and protein binding properties.

1.1.1 Human Chorionic Gonadotrophin (hCG)

Hormones (from Greek *horman* "to set in motion") are biochemical messengers. Most hormones are chemical substances produced by specialised tissue formations. The substances are secreted directly into the bloodstream, other body fluids, or into adjacent tissues. The purpose of hormones is to regulate metabolic activity of organs or tissues in the body.

There are a number of different hormones and they can be classified according to their function, structure, biochemical composition and way of action and transmission. In part of this work a reproductive hormone, hCG (Human Chorionic Gonadotrophin), has been studied.

These hormones are produced in four major endocrinal systems:

1. Diverse areas of the hypothalamus
2. Interior and exterior hypophysis lobus
3. Testicles and ovary, including interstitials tissues and corpus luteum
4. Uterus and placenta

One of the main functions of the human chorionic gonadotrophin (hCG), the placental hormone, is to stimulate the production of progesterone by the corpus luteum. The corpus luteum is an endocrine structure in the ovary that develops after fertilisation. This process of hCG-stimulated progesterone production is crucial in sustaining the early weeks of pregnancy. After the second month, the placenta starts to take over the vital task of producing progesterone and estrogens by itself and at this point it is possible to remove the ovaries and the pregnancy will continue.

hCG is secreted by placental trophoblast cells to control the levels of progesterone in the mother. This maintains the uterine lining and sustains the growing foetus. Hence, with the synthesis of this hormone beginning even before implantation, the presence of hCG in the urine can be used as an early marker for pregnancy [2]. Ever since the discovery of hCG by Hirose and Ascheim and Zondek [2-4] almost a century ago, its measurements have been the basis of pregnancy diagnosis, and coincidentally, for many trophoblastic and nontrophoblastic tumours, including some testicles tumours, as well [2].

hCG belongs to the glycoprotein family of hormones whose members share a common α-subunit and vary in their β-subunits on their molecular structure. hCG has a very high content of carbohydrates, particularly in the terminal sialic acid, which gives structure and prevents from proteolytic attack. The β-subunits determine the specificity of each individual hormone for its target receptor. The three other glycoprotein hormones are human Luteinising Hormone (hLH), human Follicle-Stimulating Hormone (hFSH) and human Thyroid Stimulating Hormone (hTSH). These three proteins are produced in the pituitary gland in contrast with hCG which is secreted by the trophoblast

Lapthorn et al. and Wu et al. [5, 6] determined the structure of anhydrous hydrofluoric acid (HF)-modified hCG, one at 3.0 Å and the other at 2.6 Å resolution, respectively. The subunits were found to have an elongated shape with dimensions 60 Å _ 25 Å _ 15 Å and 65 Å_ 25 Å _ 20 Å for the α and β-subunits, respectively. These subunits associate in a dimer which also has an elongated shape (75 Å _ 35 Å _ 30 Å). Unexpectedly, as there are no sequence similarities, the folding of the two subunits was found to be similar, with three pairs of extended strands characteristically bridged by disulphide bonds.

The subunits are intimately associated in the heterodimer like embraced hands [7]. The α-subunit has a molecular mass of 14.5 kDa contains 5 disulphide bridges and 2-N linked glycosylation sites, while β-subunit has a molecular mass of 23 kDa and contains 6 disulphide bridges, 2-N linked and 4-O linked glycosylation sites. The dissociation of hCG into α and β-subunit results in a large decrease in the biological activity, i.e., the two subunits have no activity when dissociated from each other.

From a practical point of view, the HF-treated hormone was a good candidate for structural studies, since the heterogeneity and the large amount of the surface carbohydrates, which would normally have prevented crystallisation, were eliminated. The treated hormone continued to have the ability to bind to receptors and the structures of the deglycosylated and native hormones were shown to be identical.

Studies in the 1960's allowed the quantification of hCG and also differentiation between the whole molecule, free subunits and fragments. Since it was characterised, a number of different hCG structures that depended on the sialic acid content, carbohydrate structure and composition, free subunits, and bond cleavages and fragmentation of the β-subunits were determined. Some of these diverse hCG-associated molecular variants have potential clinical relevance. For example, the hCG β-core fragment in urine and hCG β-subunit in serum are both associated with malignancies and have been proved to be useful tumour markers [8].

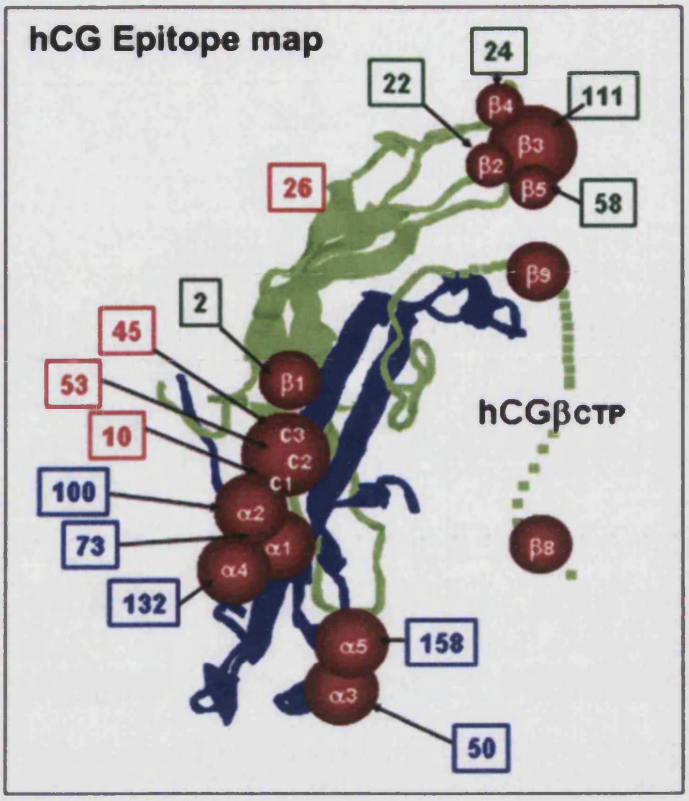

Figure 1.1 Structure of hCG with its epitopes location for different antibodies [8].

hCG concentration is measured in International Units (IU). The IU is measures of the specific biological activity of a unit weight of a substance. IUs are used as a means of standardising protein activity measurements. All international units are officially defined by the International Conference for Unification of Formulae. For hCG, the activity relates to the stimulation of steroid secretion from the ovary. The activity of the hCG used in this work is 11243 IU/mg.

hCG production starts at an early stage of development, just a few days after conception, before implantation of the fertilised egg in the uterus. hCG enters the maternal circulation almost immediately after implantation of the embryo (blastocyst) on about day 21 of the menstrual cycle. hCG is approximately eighty times more potent than its sister hormone produced by the pituitary gland LH. The small amount of hCG that enters the maternal circulation on day 21 (<5 mIU ml^{-1} in serum or plasma), while too small to be detected by pregnancy tests, is sufficient to stimulate the corpus luteum of the ovary to produce progesterone.

The concentration of hCG in the circulation then rises in an geometric manner, doubling approximately every two days. By day 28 (first day of missed menses) the median hCG level in serum, plasma or urine is about 100 mIU ml^{-1}. There is a very large variation in individual hCG concentrations. At this time, the extremes of normal levels are approximately 5 to 450 mIU ml^{-1}in serum or plasma samples. hCG can also be produced by early pregnancy loss (EPL) or pregnancies that fail to start or properly implant. hCG from these pregnancies can also be detected at this time.

Circulating hCG continues to increase (doubling about every 2 days) until it reaches a peak at about 10th week of gestation (since last menstrual period), at which time the median hCG concentration in serum or plasma samples is around 60,000 mIU ml^{-1}.

In the next the 10 weeks (10th to the 20th week of gestation), circulating hCG levels decrease, reaching a median concentration of about 12,000 mIU ml^{-1}. The hCG concentrations remains at around this level until the term (20 to 40 weeks of gestation).

Early clinically useful, bioassays that measured the biological protein activity, were introduced by Ascheim in 1927, Zondek in 1931, the Friedman test in 1931, and the Xenopus laevis test in Shapiro 1934. These first tests could confirm pregnancy approximately two months after a missed period. Due to poor sensitivity, these assays were replaced by immunoassays, with the first being reported in 1960 [9]. Sensitive radioimmunoassay (RIA), immunoradiometric (IRMA) and enzyme immunoassay (EIA) techniques, now available, allow an accurate quantification of hCG through the use of highly specific antibodies. The hCG test or pregnancy test is one of the most common immunoassays run in clinical laboratories and at home nowadays.

At present, all of the home pregnancy tests available use monoclonal or polyclonal antibodies in an enzyme-linked immunoassay format. Monoclonal antibodies are highly sensitive to one specific site on the hCG molecule. If hCG is present in urine, it will be trapped by the anti-hCG antibody that is bound to a solid surface. A second antibody labelled with a polymer bead or a gold nanoparticles marks the presence of the hCG. When the anti-hCG is formed complex, it causes a colour change, producing a positive result.

These tests can detect pregnancy by the first day of the missed menstrual period. The development of monoclonal antibodies to hCG has supplied homogeneous antibodies and improved the specificity of the assay [10, 11]. Consequently, commercially

available pregnancy tests are much less susceptible to interference from other substances than were the earlier immunoassays.

As a well-known and reproducible test, the hCG assay was chosen for this project as a model system to enable the understanding, optimisation and determination of kinetic constants for hCG/anti-hCG and the sensitivity of Surface Plasmon Resonance Spectroscopy (SPRS) and Surface Plasmon Fluorescence Spectroscopy (SPFS). HCG assay allowed characterising the effect of the surface sensor architecture on the sensitivity, as well.

The hCG model system has been used in many different analytical techniques to help determine their sensitivity and efficiency. Homola *et al* described a sensor based on surface plasmon resonance in an integrated optical waveguide-coupled SPR sensing device, using hCG as a model [12]. For the development of surface plasmon resonance biosensors Jiang *et al* have developed a novel SPR sensor on-chip self-referencing where the hCG model system was employed. In 1993, Knoll *et al* reported the first attempt to measure hCG concentrations using SPR. It was used a multi-layer system of proteins and organic thiols self-assembled on a gold surface – biotinylated thiols; streptavidin; biotinylated Fab (antibody fragment); human chorionic gonadotrophin; monoclonal antibody. It was concluded that the system was not sensitive enough for practical applications [13]. In this report optimisation of this strategy and association with SPFS are presented. A more detailed description of the system can be found in chapter 4.

1.1.2 Immunoglobulins

In 1890 von Behring and Kitasato prepared bacterial antitoxins and demonstrated their neutralising properties. This discovery instigated a new era of serological studies, remarkable for its achievements in revealing both properties of antibodies and complement in bacterial infections and the diagnostic value of antisera in, for example, typhoid (Widal Test, 1986) and syphilis (Wasserman Test, 1906) [14].

Immunoglobulins (or antibodies) are proteins, as mentioned previously, of the immune system, i.e., they have a defensive function. Immunoglobulins react against specific foreign molecules and thereby render these inactive. These large proteins have a strict relationship between their quaternary structures and their biological function.

Antibodies are symmetrical molecular structures with two identical glycosylated heavy chains (M_r= 50000 – 75000) and two identical nonglycolisylated light chains (M_r= 25000). The heavy chains are joined to each other by disulfide bonds, and each light chain is joined by a disulfide to one heavy chain, constituting the basic subunit of two heavy chains and two light chains.

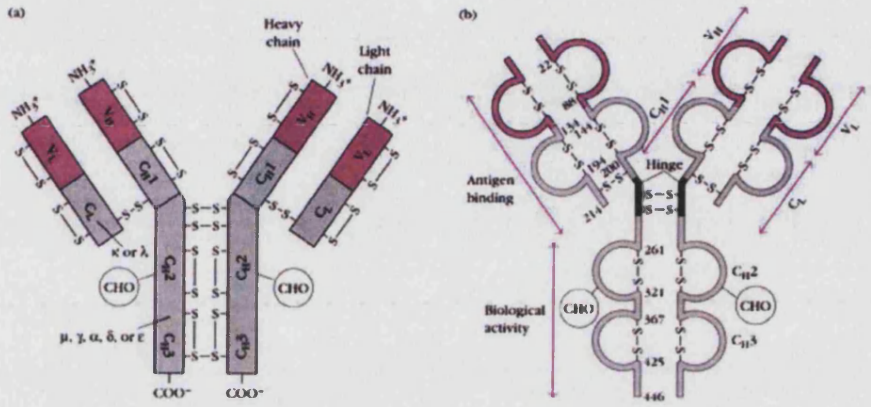

Figure 1.2 General structure of an IgG molecule. Each chain is made up of a series of homologous units of approximately 110 amino acids. The different regions present in these proteins are detailed. The region highlighted in pink is called the Fab portion of the immunoglobulin. The 'F' stands for fragment and the 'ab' stands for antigen binding, which is the region where antigen binding takes place. The Fab portion of an antibody is made up of the N-terminal domains of both the heavy and light chains. This domain of the antibody is called the variable (V) domain (VH on the heavy chain, VL on the light chain) because there is such high variability between antibodies in this area. This allows antibodies to recognise thousands of different antigens [15].

Immunoglobulins may be grouped into five main classes: IgM, IgD, IgG, IgE and IgA. The class of each different immunoglobulin is determined by its heavy chain. Thus, IgM, IgD, IgG, IgE and IgA possess μ, δ, γ, ε and α heavy chains. IgM immunoglobulin forms polymers where multiple immunoglobulins are covalently linked together with disulfide bonds, usually as a pentamer or a hexamer. This immunoglobulin has a constant presence in serum and is called the natural antibody, as it is found in the serum without any evidence of prior contact with antigen. IgD immunoglobulin, the policeman of blood, is rarely secreted and its main function appears to be as a receptor for antigen. IgE immunoglobulin is responsible for hypersensitivity and allergic reactions. IgA is the main immunoglobulin of body fluids, such as saliva, tears, colostrums and intestinal secretions, and is also present at low concentrations in serum.

IgG is by far the most abundant immunoglobulin in serum. This is the only immunoglobulin that can pass through the placenta, thereby providing protection to the

foetus in its first weeks of life before its own immune system is developed. It can bind to many kinds of pathogen, for example viruses, bacteria, and fungi and protects the body against them by complement activation (classical pathway), opsonisation for phagocytosis and neutralisation (immunology) of their toxins [16].

In a typical immune reaction the antibody response will be directed against many different regions of each antigen, and some regions may produce a more vigorous response than others. In most immune responses, the antibodies produced are polyclonal as they are able to detect different regions of the antigen producing a more effective response. While this is a desirable effect in the immune response, the non-specific nature of the polyclonal IgGs is a disadvantage in the design of a sensor system, where a high degree of analyte specificity is required.

This limitation has been partly solved by the development of single analyte specific antibodies known as monoclonal antibodies. The ability to produce monoclonal antibodies overcame all these problems, allowing extreme specificity, not just for the immunising protein but for a particular region on it, without the need of using extremely pure antigens [17-20]. Figure 1.3 illustrates how monoclonal antibodies are produced:

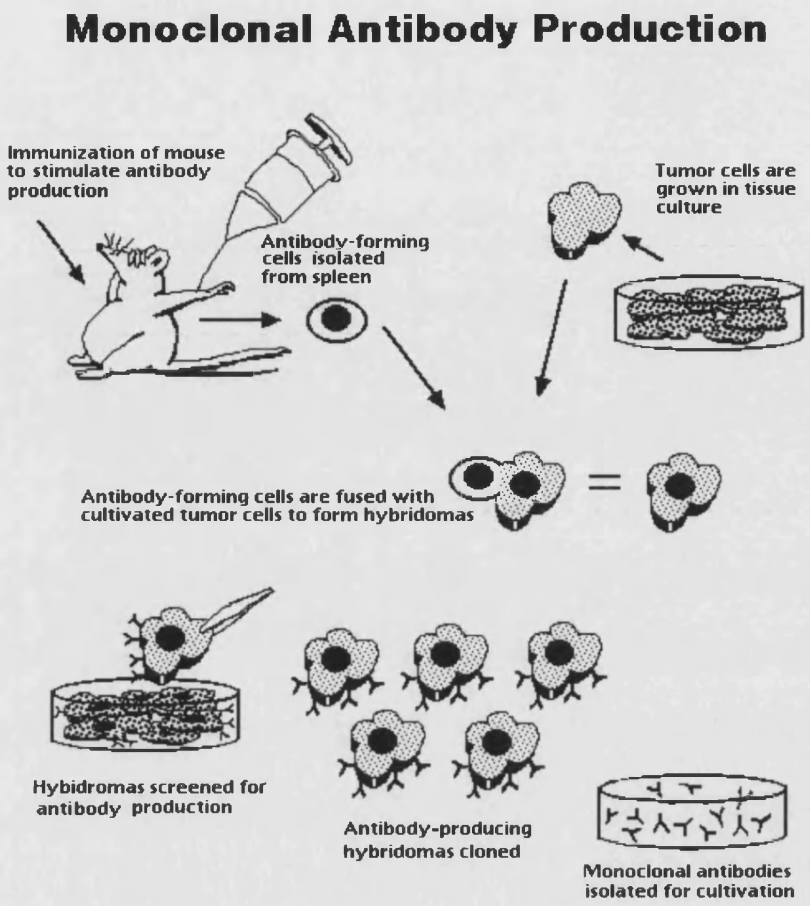

Figure 1.3 Schematic representation for production of monoclonal antibodies derived from hybridomas [21]

To produce monoclonal antibodies, tumour cells that can replicate endlessly are fused with mammalian cells that produce antibodies. The result of this cell fusion is a "hybridoma", which will continually produce antibodies. Usually the tumour cells come from a myeloma, which is a tumour in the bone marrow, and the antibody-producing cells come from the spleen. The spleen is an organ that has the function to screen the blood for foreign molecules or organisms, where the density of memory B-cells is very high. The hybridomas are capable of producing large amounts of monoclonal antibodies and have the ability to grow continually, making it highly efficient, and reducing the need for large numbers of animals in the lab.

In this work different types of monoclonal antibodies were used, e.g., monoclonal antibodies specific to the α region of hCG and to the β region of hCG that will be referenced in chapter 4.

1.2 Methodology

1.2.1 Biosensors

The determination of the basic forces that act during molecular recognition processes is critical for both the understanding mechanisms of biological interactions and to facilitate the discovery of innovative biotechnological methods and materials for therapeutics, diagnostics and separation science. The ability to measure interaction properties of biological macromolecules quantitatively and qualitatively for a wide range of affinity, size, and purity is important. Biosensors have been used widely in the past years to provide these forms of study [22-33].

A biosensor is an analytical device incorporating an element sensor connected or integrated into a transducer (e.g. an electrode or an optical detector) that provides either qualitative or quantitative information [34]. Biosensors make use of the highly biological specificity of biomolecules, such as enzymes, antibodies, nucleic acids and other molecules that may be immobilised on to a physical-chemical transducer surface. The specific bio-element recognises a specific analyte and the sensor-element transduces the change in the biomolecule into an electrical signal.

The history of biosensors started in 1962 when Leland C. Clark developed enzyme electrodes [35]. Clark trapped an enzyme that reacts with oxygen (glucose oxidase) on the surface of a platinum electrode and reasoned that it was possible to follow the enzyme activity by measuring oxygen concentration changes due the reduction of oxygen in the presence of the enzyme. In other words, the electrochemical reaction at the surface of the platinum electrode produced a measurable change in current – thus a chemosensor became a biosensor.

Depending on the transducer device used, different types of measurements and thus different biosensors can be obtained. Guilbault and Montalvo in 1969 described the first potentiometric enzyme electrode. In this experiment, urease was immobilised on an ammonium-selective liquid membrane electrode and was able to detect urea [36]. In 1974 Cooney *et al* and Mosbach proposed the use of thermal transducers for biosensors. Normally an enzymatic reaction is exothermic, and by placing a thermistor strategically in solution, a relation in the change in temperature where the substrate concentration was obtained [37].

In 1975, Davis et al suggested that bacteria could be harnessed as the biological element in microbial electrodes enabling the measurement of alcohol [38]. This paper is the start of all the effort made in research for biotechnological and environmental applications of biosensors [39].

Many biosensors with different transducers have been developed in the past three decades: Conductiometric – where Pt or Au electrodes have been used to detect changes in the electrode double layer capacitance as the ionic strength is increased by generation of ions [40]. Acoustic – where piezoelectric devices have been used to monitor the changes in the adsorbed mass on the sensor surface. These piezoelectronic crystal or acoustic wave devices have been used for environmental monitoring, food microbial testing and for clinical analysis [24, 41]; Optical – where different optical signals (absorbance, fluorescence/phosphorescence, bio/chemiluminescence, reflectance, light scattering and refractive index) have been used to monitor binding and dissociation events by transducing the mass changes on the sensor surface [24].

Biosensing technology offers a powerful tool for fast and reliable detection of specific compounds and continuous monitoring of analytes on-line or in real time. Nowadays biosensors are widely used in scientific, bio-medical, pharmaceutical, veterinary and environmental research as well as in industry on processes that need monitoring in situ [34].

Biosensors present different advantages over other analytical techniques: high sensitivity and selectivity, fast and reliable responses, low detection limits, reproducibly, reusability, possible miniaturisation and ease and low fabrication costs. Biosensors are reusable due to immobilisation of the sensing bio-molecule on the surface made possible by a simple washing step to separate bound an unbound species. In some cases, such as evanescent wave techniques, the washing step becomes unnecessary because they are insensitive to the presence of the analyte in the bulk solution.

1.2.2 Optical Biosensors

One of the most common type of biosensors is optical biosensors because whatever the biorecognition chemistry, the response is followed in a non-destructive matter and a large number of wavelengths can be used, broadening the spectrum of the systems available for studying [24].

The use of optical biosensors in research and development has been described in more than 3,000 scientific publications [25] using different optical methods: absorption and reflection spectroscopy, chemi- and bio-luminescence, fluorescence and phosphorescence spectroscopy and evanescent waves techniques.

Absorption of light (energy) produces transitions in the electronic, vibrational and/or rotational of atoms and molecules. These transitions only occur when the difference between the energy levels are equal to the energy of the exciting photons. Visible and ultraviolet radiations induce electronic excitation, infrared radiation promotes vibrational excitation, and microwave radiation produces rotational transitions. Absorption of the excitation energy leads to a decrease of the power of the emitted radiation after passing through the sample. The decrease in light intensity is determined by the Beer-Lambert equation:

$$A = \log I_0 / I = \varepsilon l c \tag{1.1}$$

Where A is the absorbance, l is the path length and ε is the molar absorptivity, which is characteristic of the analyte substance at a given wavelength and I_0 is the intensity of the incident light.

Reflection of radiation happens when light runs into a boundary surface. The light reflection can occur via specular reflection when the interface does not let any light pass through or via diffuse reflection where the light penetrates and subsequently reappears at the surface followed by partial absorption and multiple scattering within the system. Diffuse reflectance is dependent on the composition of the system, similar to light absorption. Reflectance is most commonly determined by Kubelka-Munk theory:

$$F(R) = (1 - R)^2 / 2R = \varepsilon c / S \tag{1.2}$$

Where a thick semi-infinite scattering layer is assumed and reflectance, R, is a function of the concentration, c, of the absorbing species on the scattering layer through the molar absorptivity, ε, and the scattering coefficient, S [42].

Absorption of the energy associated with a photon excites atoms or molecules to transition to higher energy levels. The excited species can relax via different pathways. One of the relaxation modes is luminescence, when a radiation of a lower frequency is emitted. When relaxation occurs from a singlet state then the emission is called

fluorescence and when it occurs from a triplet state is called phosphorescence. In both cases, the emitted radiation has a different wavelength when compared with the exciting radiation, and its intensity, I_L, is dependent on the intensity of the exciting light, I^0, and on the concentration of the luminescent species, c. In the presence of quenching species, e.g. oxygen, the mean lifetime of the activated species is decrease and luminescence intensity, I_L, is related to the concentration of the quenching species, c_q, by the Stern-Volmer equation:

$$I^0/I_L = 1 + K_{SV} c_q \tag{1.3}$$

Where I^0 is the luminescence intensity in the absence of the quencher and K_{VS} is the Stern-Volmer constant. If an excited species is generated through a chemical reaction, the measured light is known as chemiluminescence. Fluorescence will be described in more detail in the following chapter

There is an extensive number of publications where luminescence (either, fluorescence or phosphorescence) has been reported [43-48]. An example of a luminescence biosensor is a luminescence optical biosensor for measuring free cholesterol in serum [49] where the luminescence of the complex tris(4,7-diphenyl-1,10-phenanthroline) ruthenium (II) is sensitive to changes in the oxygen concentrations allowing the oxidation of cholesterol by cholesterol oxidase to be followed.

The change of the refractive index at the sensor surface is related to the total internal reflection of the light at the sensor surface phenomenon. When the light travels through a medium of higher refractive index and hits a medium of lower refractive index the light is totally internally reflected at a certain critical angle θ_C, and follows Snell's Law:

$$\sin\theta_C = \frac{n_{smaller}}{n_{higher}} \tag{1.4}$$

Where n is the refractive index of the respective medium. When total internal reflection happens, an evanescent wave is formed at the interface and penetrates in both media. A number of reports have been published and reviewed elsewhere [22, 25, 27]. One interesting refractometric sensor is the immunosensor for thyroid stimulating hormone (TSH), where anti-TSH is immobilised on the surface and TSH binding was detected

[24] by measuring the change in the refractive index as the analyte comes in contact with the evanescent wave associated with the total internal reflection at the surface interface.

1.2.3 Evanescent Wave Techniques

Optical techniques that use the evanescent wave phenomenon as a sensor are used for monitoring sensing events on the sensor surface and can be distinguished between direct and indirect optical sensing techniques. Direct optical sensing techniques include internal reflection spectroscopy, attenuated total reflection and surface plasmon resonance spectroscopy. Indirect sensors often employ fluorescent labels to detect protein interactions. An evanescent wave is an event that happens at the interface of two different refractive index media. When light is totally internally reflected within the denser medium an electromagnetic wave is formed in the more optically thinner medium [34]. The optical interaction can be followed as a change in the intensity of light that exists on the optically denser medium or internal reflection element (IRE). The IRE can be designed as a single or multiple reflection elements. The latter are called waveguides. Biosensing with waveguides has been extensively applied in two techniques e.g. attenuated total reflection (ATR) and total internal reflection fluorescence (TIRF).

In ATR, the light energy absorbed from the evanescent wave produced on the sensor surface can be monitored as an attenuation of the internally reflected light beam. The light energy is absorbed from the evanescent wave into an optically absorbing film present on the waveguide interface, thus attenuating the internally reflected light beam. TIRF is based on the same concept but the surface bound molecules absorb evanescent photons and re-emit the energy at a longer wavelength as fluorescence. [11, 29, 34, 39, 50]

ATR was first use by Baier and Dutton in 1969 to monitor interactions of blood with a foreign surface [51] and Harrick and Loeb (1973) applied TIRF to monitor bovine serum albumin-dansyl chloride bound to a quartz waveguide surface [52]. Around the same time Kronick and Little realised that TIRF could be applied in fluorescent immunoassays, eliminating the washing or separation step[53, 54]. As a result, since then the combination of evanescent detector and antibody for biosensors has become common routine [55].

ATR has been applied to follow protein and immunological interactions at surfaces in both the infrared (IR) and ultra-violet–visible (UV-Vis) regions of the spectrum. Ockman in 1978 applied ATR to the IR region [56] to monitor different serum albumins interacting with their corresponding antisera in a germanium-liquid interface. In the visible spectrum, Sutherland 1984 monitored attenuation in transmittance at 410 nm with binding of haemoglobulin to hydrophobic quartz surfaces. In the UV region (310 nm) [57], Sutherland followed the immunoreaction of the chemotherapeutic agent methotrexate (MTX) and MTX at an aqueous quartz surface through transmission attenuation. However, these sensors were limited by the need to match the maximum wavelength of absorbance for the dye to the available light-emitting diode and photodiode detectors. [55]

Evanescent wave TIRF immunosensors have been employed with both planar waveguides and optical fibres. The planar fluorescent capillary fill device (FCFD) developed by Badley et al 1987 for detection of different biomolecules has been proven to be successful [58], and it has been used to measure for example hCG [59], rubella antibody in serum [60], and estrone-3-glucuronide (E3G) in urine [61]. Choquette et al 1992 [62] described a competitive assay with liposome-enhancement for theophylline. Many other single-mode fibres based on TIRF for measuring other biomolecules, for example penicillin and glucose, have been described [63, 64].

If the surface of the IRE is covered with a thin metal layer, the evanescent field wave can excite the quasi-free electron gas of the metal. Illumination by a laser light can be used to excite the plasmons in the metal surface and excitation of the resulting surface wave is enhanced by fifty-fold amplification (depending on the metal and thickness surface used) when compared to ATR [34]. The enhancement field effect increases the sensitivity of the IRE since the angular position of the resonance minimum becomes more sensitive to changes in the refractive index of the metal/dielectric interface. Since the electric field extends to only a few hundred nanometres from the metal surface, the resonance energy is susceptible to the thickness of the films adsorbed on the surface. This is the characteristic used for sensing applications. The use of this optical phenomenon for measuring changes on the surface was developed into the technique: Surface Plasmon Resonance Spectroscopy (SPRS).

Liedberg et al described the first optical biosensor SPRS in 1982 [65, 66], where the change of the refractive index due to the adsorption of human gamma globulin IgG on a silver surface was monitored. Afterwards, in the same work, a solution of antihuman

gamma globulin IgG was injected resulting in specific binding to the IgG; producing in another shift of the minimum of resonance. Various concentrations of anti-gamma globulin were used for binding with gamma globulin IgG and it was observed that the initial rate was proportional to the anti-gamma globulin concentration in the concentration range 200-0.02 mg mL^{-1}. Thus, Liedberg produced the first immunoassay monitored by SPRS and so prompted an intensive research in this field.

SPRS has been used to determine physical quantities including humidity using humidity-induced refractive index changes of porous thin layers [27, 67] and polymers; and temperature based on the thermooptic effect in hydrogenated amorphous silicon [68]. Another application of SPR is chemical sensing. The technique has been used to measure variations due to adsorption or chemical reaction of an analyte with a transducing medium, which results in changes in its optical properties. Applications based on changes in the refractive index of molecules include monitoring of the concentrations of hydrocarbons, aldehydes and alcohols by adsorption on to a polyethylene glycol films [69]; monitoring of vapours of chlorinated hydrocarbons by adsorption on polyfluoroalkylsiloxane [70]; detection of vapours of tetrachlorethene adsorbing in polydimethylsiloxanse film [71]; and detection of vapours of aromatic hydrocarbons in Teflon films [72]. Palladium has been used as well to sense hydrogen because palladium adsorbs hydrogen molecules. Silver and gold are the most common resonance metal surfaces employed but, in this example, palladium was used as the actual surface plasmon resonance metal surface[73, 74].

Recently a sensitive sensor for NO_2 using chemisorption of NO_2 molecules in a gold SPR active layer has been reported [75]. Other compounds have been detected based on the interaction between the analyte molecules with the transducing layer, e.g., toluene interacting with copper and nickel phthalocyanine [76], NO_2 interacting with copper and cobalt phtalocyanine films [77, 78], and NO_2 and H_2S interacting with a polyaniline film [79]. NH_3 vapours have been detected via reaction of ammonia with a bromo-cresol purple film [80]. SPR has been applied in combination with anodic stripping voltametry to detect copper and lead ions[81].

In the early 90's a large interest in the construction of organised organic monolayers on metal surfaces by processes of self-assembly was growing. Self-Assembled Monolayers (SAM) are good model systems for studies of physical chemistry and statistical physics in 2D and the crossover to 3D. Self-assembling is an elegant and simple method that allows the production of a variety of structure controlled surfaces

employed in a wide range of surface effects studies. Spinke et al. [82] used this system to study with SPR molecular interactions at the interface of different controlled and engineered surface structures.

Various reports appeared in the mid-80s for immunosensors on metalised surfaces including interactions between HSA (Human Serum Albumin) and anti-HSA [83, 84], BSA (Bovine Serum Albumin) and anti BSA [85], a-feto protein and anti-a-feto protein [86], ferritin and anti ferritin [87]and IgG and anti-IgG [66, 88-91]. In 1994 SPR was used in a different way. An immunoreaction was followed by monitoring the changes in reflectivity at a fixed angle adjacent to that of the plasmon minimum in time. Ferritin to anti-ferritin were both adsorbed onto the metal surface and the kinetics of the binding events were studied. The theoretical effective thickness of the protein layer was determined by comparing full plasmon resonance curves with theory, assuming the value for the refractive index of the protein layer [92].

The use of surface plasmon resonance spectroscopy allows the analysis of biomolecular interactions in real time without labelling requirements. Several assay formats for SPR sensors have been tested. In direct SPR biosensors, the analyte quantification is carried out by direct detection of the binding reaction however, the adsorption may not be sufficient to be detected directly. In order to overcome this problem the use of particles, such as latex particles, colloidal gold, polystyrene, titanium dioxide polymethyl methacrylate and silica that are bound to the analyte before introducing it to the sensor surface has been reported in [93, 94]. Hence, when binding occurs, a larger signal will be induced by the presence of the particles in the sensing layer. An example of this method was described by Leung et al where an enhancement of the sensitivity in the detection of sheep antibody linked to polystyrene beads was obtained [93].

Another approach to enhance sensitivity is the use of indirect methods e.g. like sandwich or competitive [95, 96]. Typical biological systems examined by this technology are antibody-antigen interactions and nowadays SPR biosensors commercially available compete directly with the typical immunoassays. SPR sensors have to compete with the existing technologies on the basis of factors such as low cost, ease of use, robustness, sensitivity and stability. Another method to enhance the immunosensor signal is fluorescence labelling and it is extensively used in ELISA assays. SPR can be coupled with fluorescence and the phenomenon will be described in the following section.

1.2.4 Enhancement of SPRS Response by Fluorescence

Clinicians, food technologists and environmentalists have an interest in generally increasing sensitivity and limits of detection for a range of analytes. Sensitivity and detection limit problems arise if very dilute lateral packing of the analyte or capture proteins is achieved on a sensor surface, or if a very small analyte of low molecular mass is to be detected. In these cases, only a very low density molecular films are formed, resulting in angular shifts too low to be detected [13]. This generates severe sensitivity limitations and, as a consequence, the concept of using indirect detections via fluorescence labelling techniques in combination with surface plasmon spectroscopy as means to enhance the signal of the interfacial binding events is to be considered.

The excitation of fluorophores via evanescent wave techniques has been demonstrated for waveguides and fibre-optic devices [43, 97, 98] and fully revised [50]. The evanescent electrical field can excite fluorescent molecules close to the sensor surface. However, when a metal is evaporated onto the surface of a higher refractive index medium, a greater enhancement of the intensity of the evanescent field is produced. Coupling SPR with fluorescence via an indirect procedure was first reported by Attridge et al in 1991 [99] where the surface field intensity enhancement produced by SPR was first used to heighten the emission from fluorescently labelled immunoassay complexes at a metal surface. To demonstrate this method, human Chorionic Gonadotrophin immunoassay was used directly on the metal surface. After applying surface plasmon fluorescence spectroscopy (SPFS) with an immunoassay Schmidt et al [100] reported the use of this technique to monitor the binding of monoclonal and polyclonal antibodies labelled fluorescently on to a surface of a peptide supported lipid membrane with acetylcholine receptor dimer incorporated.

Neumann et al investigated some of the characteristics of surface plasmon field-enhanced fluorescence spectroscopy [101]. The excitation of fluorescence in the evanescent field of the plasmons is stronger close to the metal surface, although the presence of the metal can reduce the observed fluorescence intensity by inducing quenching processes that are metal distance dependent. Excitation and quenching processes exhibit different distance dependencies. An optimal distance to the metal exists at which maximal fluorescence excitation is observed. Therefore, the experimental design of the sensor surface architecture has to be optimised in order to obtain an efficient and sensitive sensor concept.

In 2000 Liebermann et al [102, 103] proposed a new technique for a biosensor where specific interfacial architectures were used in order to ensure that the bound fluorescent analytes were still within the exponential decaying of the evanescent field although sufficiently distanced from the acceptor states of the metal surface to avoid Förster quenching of the emitted fluorescence. In their work a biotinylated self assembled monolayer on the metal surface was used, for binding of streptavidin.

The first application for use of this supramolecular structure was reported by Liebermann et al for detection of hybridization reactions of fluorophore-labelled 15mer target oligonucleotides in solution to a surface-attached probe DNA using surface plasmon fluorescence spectroscopy [103] and microscopy [104]. It was proven that this technique was highly sensitive and rate of association and dissociation constants were determined for the full complementary strand, single mismatch and second mismatch oligonucleotides strands. It was shown that the hybridization followed the simple Langmuir model with a single mismatch reducing the equilibrium constant by two orders of magnitude and a second mismatch another three orders of magnitude. A comparison between DNA and PNA (peptide nucleic acid) binding constants determined by SPFS were also reported. It was found that PNA had a strong deviation from that predicted by the single exponential kinetics Langmuir model [105].

Other features of surface plasmon field-enhanced fluorescence spectroscopy have been discussed in order to best understand and optimise the technique for biosensing [106]. Specific interactions between antibody-antigen were used in order to study for comparison between the fluorescence of Cy5 and Alexa Fluor 647 in SPFS-immunoassay. It was shown that Cy5 exhibited stronger self-quenching effects, which makes it unsuitable for use in quantitative measurements. Another feature of SPFS was also studied regarding the angular detuning effect. It was demonstrated that when large SPR signals are detected (meaning large shifts of the resonance minimum) the linear relationship for the fluorescence signal is also maintained.

SPFS is dependent on the strength of the surface plasmon resonance generated evanescent field at the metal dielectric interface [107-113]. The greatest evanescent field amplitude is obtained when a non-adsorbing dielectric is used. The SPR curve is affected by an adsorbing dielectric and is characterised by a higher value of the reflectance minimum and a broader curve. However, Ekgasit et al [110] studied this effect for a thin (nanometre thickness) layer of confined fluorophores (a weakly

adsorbing dielectric) and determined that the adsorption was too small to induce a significant change in the SPR curve, therefore small quantities of fluorophores adsorbed on the surface do not influence the SPR curve and the intensity of the evanescent field. Moreover, Ekgasit et el [109] has shown that an in-depth analysis of the SPR curve of an absorbing medium and its relationship with the material characteristics can be performed, as the adsorption contribution of the adsorbing dielectric can be separated from that of the metal film via knowledge of evanescent field distribution.

This technique has been optimised in order to measure very low concentrations of analyte. In order to obtain very low limits of detections Yu et al used a three dimensional extended matrix. A CM5 sensor chip, developed by Biacore was used allowing for a larger amount of sensing antibody to be loaded on the surface, with this matrix a concentration of limit of detection of approximately 500 10^{-18} mol L^{-1} was determined [114].

Surface Plasmon Fluorescence Spectroscopy allows detection of fluorescent analytes with high sensitivity using a biofunctional supramolecular interfacial architecture and the power of this tool for biosensing has been shown for not only DNA detection but also commercially available proteins.

With the ability to measure, simultaneously the change in refractive index and the fluorescent signal, this technique was used in this work to optimise the maximum binding capacity of captured antibodies surface, minimising steric hindrance effects of the analyte (hCG) by varying the molar ratio of biotinylated thiols on the SAM used as the foundation of the supramolecular architecture. The limit of detection (LoD) was determined for the optimised surface using sandwich immunoassay strategy by detecting the increase in fluorescence signal due to adsorption of fluorescently labelled antibody.

SPFS was also employed for the development of a fatty acid immunosensor where a fluorescently labelled fatty acid competed with a non-labelled fatty acid for the same binding pockets of a fatty acid antibody. The binding constant of the fluorescently labelled fatty acid interacting with fatty acid antibody was also determined.

1.3 Supramolecular Structures

1.3.1 Self Assembled Monolayers (SAM)

Biosensors use the high selectivity provided by biomolecules or, more complex, biological system, e.g., receptors, whole cells, for molecular recognition. The capture molecule, i.e., the biological components, is immobilised on the surface. Therefore, it is important to retain the biological activity of these molecules. In order to maintain their activity it can be important to mimic the biological environment of the molecule when adsorbed on the surface.

Different strategies have been used to immobilise biomolecules on the surface e.g. direct immobilisation involving physisorption, although with this technique, there is no control of the orientation of the active centre and a decrease in the biological activity of the molecule is observed. More sophisticated strategies using Protein A or G, and biotin-avidin chemistry can improve the control over the immobilisation process. Other strategies exploit hydrogels or poly-L-lysine with specific linkage reagents such as carbodiimide or priodate that crosslink with the biomolecule in specific regions. Functionalised SAMs have proven to offer alternatives to binding and organisation of the captured biomolecule [115].

There are two methods to deposit molecular layers on solid substrates Langmuir-Blodgett technology and self-assembly, although self-assembly is the method used in this work

Langmuir-Blodgett films are made by dipping a solid substrate up and down through a monolayer, produced in the air/liquid interface, and simultaneously keeping the surface pressure constant via a Langmuir balance system. The floating monolayer is adsorbed on the solid substrate and multilayer structures can be produced in this way. The cohesion of the monolayer is ensured by keeping the surface pressure constant although the attraction between the monolayer molecules is sufficiently high to guarantee assembly during transference to the solid surface [116]. Langmuir-Blodgett films and its applications in biosensing are extensively reviewed in [117]

SAMs are ordered molecular assemblies formed by the adsorption of an active surfactant on a solid surface. It is a simple method that has attracted research studies an its implementation in the industry [118]. The order in these 2 D formed systems is produced by the spontaneous bond formation at the interface and by intermolecular

forces between adsorbed molecules, as the system approaches equilibrium. SAMs are highly structured and oriented and can incorporate a number of different groups either in the alkyl chain or in the terminal group providing a variety of surfaces with specific interactions [119].

There are a number of different surfactants that can be used to form SAMs. Fatty acid SAMs are important systems that make a link between Langmuir-Blodgett and self-assembly techniques that continue to be studied. Silanes on hydroxylated surfaces are important technological systems, however the reproducibility of the monolayer is still producing some problems but research is carrying on [119].

SAM of alkanethiolates on Au (111) surfaces are the most studied SAMs and the most well understood system and a number of studies has been reported [119]. Gold is a transition metal that forms clusters that have the possibility to form multiple bonds with sulphur. The adsorption of alkanethiolates on Au (111) is characterised by two distinct adsorption kinetics for diluted solutions: one very fast step due to diffusion-controlled Langmuir adsorption kinetics that by the end has contact angles close to their final value; and one slow step which last for several hours can be described by surface crystallisation processes to achieve the final organisation with the final contact angles and the final thickness values [120].

It has been observed that kinetics of the second step is faster for longer alkyl chains, probably due to the increase of Van der Waals interactions that decrease with the diminution of the alkyl length. However, if the chain contains large groups, the two step kinetics are coupled, and the chemisorption kinetics is greatly impeded by the chain disorder [121].

The reaction of alkanethiol with gold is considered an oxidative addition of the S – H bond to the gold surface, followed by a reductive elimination of the hydrogen following the reaction:

$$R - S - H + Au^0_n \leftrightarrows R - S\ Au^+ \bullet Au^0_n + \tfrac{1}{2} H_2 \qquad (1.5)$$

Electron diffraction studies of monolayers of alkanethiolates on Au (111) surfaces have shown that the symmetry of sulphur atoms is hexagonal with an S---S distance of 4.97 Å and calculated area per molecule of 21.4 $Å^2$ [118].

FTIR studies have shown that the alkyl chains in SAMs of thiolates adsorbed on Au (111) are tilted ~26–28° from the surface normal and display ~52–55° rotation about the molecular axis. This tilt is a result of the chains optimising their spacing through Van der Waals contact forces. However, on a silver surface, where th inter-atomic spacing between silver atoms, and hence thiol groups is lower than on gold, measurements have shown that alkyl thiol SAMs such as octadecanethiol are orientated with a tilt angle of 0° to the normal, since the inter thiol spacing is also the optimum Van-der Waals distance for the alkyl chains [122].

It has been shown that ω-substituted alkanethiols are densely packed and highly oriented and ordered as long as the end group (NH_2, OH) is relatively small (< 5 Å) and do not perturb the orientation of the SAM. Moreover the alkyl chain must contain a minimum of 9 carbons. Van der Waals interactions between adjacent alkyl thiols increase with chain length (for up to ca. 20 carbons) and hence longer alkyl thiol SAMs (C18) are more stabilised and better packed than short ones (C2) However, the presence of more bulky groups in the tail of the alkanethiol decreases the density packing and the ordering [115].

The incorporation of a number of different groups, either in the alkyl chain or in the terminal group provided a variety of surfaces with specific properties. In this work, different SAMs were prepared and are described in more detail in chapter 3. The possibility to dilute alkanethiols substituted with functional groups with shorter non-substituted thiols in the SAM makes available the possibility to immobilise larger biomolecules with a decrease of steric hindrance effects.

1.3.2 Supramolecular Architectures Using Biotin/Streptavidin Model System

Biotin (Vitamin H) has an extremely high binding constant (K_A= 10^{15} M^{-1}) to streptavidin. Streptavidin is a tetrameric protein with approximately 54 x 58 x 48 Å [123], and with molecular weight of 60 000 Da. Streptavidin has four binding pockets for biotin, two binding sites on each side of two opposing faces.

SAMs with a biotinyl functional group present in the alkanethiol tail adsorb strongly streptavidin producing an almost indestructible surface i.e. it is hard to remove streptavidin from the surface without damaging the protein activity.

The physical and chemical properties of biotin functionalised and patterned surfaces bound to streptavidin have been studied. It was found that the mole fraction of the

biotin-functionalised thiol influenced the streptavidin surface density. For higher mole fractions of the biotin label present in the SAM, the ability to bind streptavidin was less effective. It was shown through SPR that low surface coverage and therefore good accessibility of the labels by the protein lead to very fast, diffusion controlled adsorption of streptavidin [124]. Another aspect was also observed for the binding of biotin to streptavidin, the biotinyl functional group in the mixed SAM has to be displaced sufficiently from the assembling thiol chains by a flexible and hydrophilic spacer as the biotin binding site is buried in the streptavidin [125, 126].

In this work, it will be discussed to a further extent, the influence of high surface coverage of streptavidin in the adsorption of larger biomolecules as for example, immunoglobulins.

2 Theoretical Introduction

An introduction to the theory of Surface Plasmon Resonance Spectroscopy with a detailed description of the excitation of plasmon on the dielectric/metal interface is presented. An introduction to the different decaying channels of an excited stated, with focus on fluorescent processes is described, followed by a description of the Surface Plasmon Fluorescence Spectroscopy process. Finally description of the process of molecular adsorption onto the sensing surface using the Langmuir isotherm model is described.

2.1 Surface Plasmon Resonance Spectroscopy

In the work presented in this thesis, Surface Plasmon Resonance Spectroscopy (SPRS) and Surface Plasmon Fluorescence Spectroscopy (SPFS) techniques were employed. In order to use these techniques an instrument was built and optimised. These techniques allow one to perform measurements of a different processes taking place at the interface solid/liquid or solid/air. In order to understand these techniques this chapter will detail the essential theoretical background to describe plasmon resonance as well as other theories necessary to understand the project.

2.1.1 Surface Plasmons [127, 128]

Plasmons are quasiparticles, which are density waves of the charge carriers in a conducting medium such as a metal, semiconductor, or plasma. Surface plasmons are longitudinal waves with both longitudinal and transverse wave components

Plasmons play a large role in the optical properties of metals. Light of frequency below the plasma frequency is reflected, because the electrons in the metal screen the electric field of the light. Light of frequency above the plasma frequency is transmitted, because the electrons cannot respond fast enough to screen it. In most metals, the plasma frequency is in the ultraviolet range, making them shiny in the visible range, though some like gold and copper have plasma frequencies in the visual range, giving them their distinct colour. In doped semiconductors, the plasma frequency is usually in the infrared.

These surface plasmon waves are described by the electromagnetic waves equations, considering an interface (1/2) in an isotropic, homogenous medium of a semi-infinite solid with a two-layer system where a p-polarised wave propagates in the x direction.

There is no y dependence. The magnetic and electric fields are described as followed (please see Appendix I for more information):

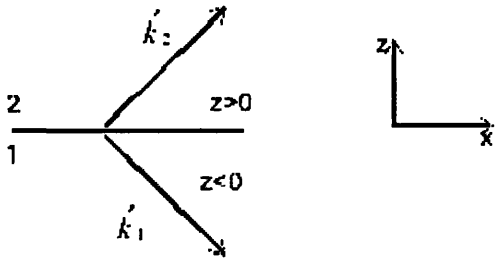

$$z>0 \quad \vec{H}_2 = (0, H_{y2}, 0)\exp i(k_{x2}x + k_{z2}z - \omega t) \tag{2.1}$$

$$\vec{E}_2 = (E_{x2}, 0, E_{z2})\exp i(k_{x2}x + k_{z2}z - \omega t) \tag{2.2}$$

$$z<0 \quad \vec{H}_1 = (0, H_{y1}, 0)\exp i(k_{x1}x - k_{z1}z - \omega t) \tag{2.3}$$

$$\vec{E}_1 = (E_{x1}, 0, E_{z1})\exp i(k_{x1}x - k_{z1}z - \omega t) \tag{2.4}$$

Surface plasmons propagate in the interface between media 1 and 2. The wave vector $\vec{k}_1$ has the components $\vec{k}_x$ and $\vec{k}_{z1}$. Considering the material equations and the Maxwell's equations in MKSA units, the described fields are solutions of these equations:

Maxwell's Equations (MKSA units)		Continuity relations	
$\nabla \times \vec{H} = \frac{\partial}{\partial t}\vec{D} + \vec{J}$	(2.5)	$\vec{E}_{x1} = \vec{E}_{x2}$	(2.6)
$\nabla \times \vec{E} = -\frac{\partial}{\partial t}\vec{B}$	(2.7)	$\mu_1 \vec{H}_{y1} = \mu_2 \vec{H}_{y2}$	(2.8)
$\nabla \cdot \vec{D} = \rho$	(2.9)	$\varepsilon_1 \vec{E}_{z1} = \varepsilon_2 \vec{E}_{z2}$	(2.10)
$\nabla \cdot \vec{B} = 0$	(2.11)	$k_{x1} = k_{x2} = k_x$	(2.12)
$\vec{D} = \varepsilon_0 \vec{E} + \vec{P}$	(2.13)	$\vec{H} = \mu_0^{-1}\vec{B} - \vec{M}$	(2.14)
$\vec{D} = \varepsilon_r \varepsilon_0 \vec{E}$	(2.15)	$\vec{B} = \mu_r \mu_0 \vec{H}$	(2.16)

When solving these equations (Appendix I) an expression that gives a relation for the dispersion of surface plasmons on a surface of a semi-infinite solid with the dielectric function ($\varepsilon_1 = \varepsilon_1' + i\varepsilon_1''$) adjacent to a medium ε_2 as air or vacuum, it is obtained from equation (2.5)

$$k_{z1}\vec{H}_1 = \omega \varepsilon_0 \varepsilon_r \vec{E}_{x1} \tag{2.17}$$

$$k_{z2}\vec{H}_1 = -\omega \varepsilon_0 \varepsilon_r \vec{E}_{x2} \tag{2.18}$$

From the continuity equations (2.9) and (2.10) together with (2.17) and (2.18)

$$\overrightarrow{H_1} - \overrightarrow{H_2} = 0 \tag{2.19}$$

$$\frac{k_{z1}}{\varepsilon_1}\overrightarrow{H_1} + \frac{k_{z2}}{\varepsilon_2}\overrightarrow{H_2} = 0 \tag{2.20}$$

In order to solve these equations it is necessary to consider the determinant of this matrix:

$$\begin{vmatrix} 1 & -1 \\ \frac{k_{z1}}{\varepsilon_1} & \frac{k_{z2}}{\varepsilon_2} \end{vmatrix} = 0$$

$$\frac{k_{z1}}{\varepsilon_1} + \frac{k_{z2}}{\varepsilon_2} = 0 \tag{2.21}$$

or

$$\frac{k_{z1}}{k_{z2}} = -\frac{\varepsilon_1}{\varepsilon_2} \tag{2.22}$$

If a closer look is taken into equation (2.22) , it can be concluded that the dispersion of surface plasmons only happens in an interface between two materials with two dielectric constants of opposite signs. Therefore, plasmons can be excited at the interface between metal layers (metals are an example of a negative dielectric constant) and dielectrics. Considering the interface to be between a metal with a complex dielectric function $\varepsilon_1 = \varepsilon_1' + i\varepsilon_1''$, where $\varepsilon_1' < 0$ and $|\varepsilon_1'| > 1$, and a dielectric material $\varepsilon_2 = \varepsilon_2' + i\varepsilon_2''$, than the coupling of light is between the collective plasma oscillations of the nearly free electron gas in a metal with the electromagnetic field. These excitations are called plasmon surface polaritrons or surface plasmons.

When applying the curl operator onto equation (2.5) and following the treatment in Appendix I, it is obtained the dispersion relation of the surface plasmons at the interface:

$$k_x^2 + k_{zi}^2 = \frac{\varepsilon_r \omega^2}{c^2} \qquad i = 1,2 \tag{2.23}$$

or

$$k_{zi} = \sqrt{\varepsilon_r \frac{\omega}{c^2}^2 - k_x^2} \tag{2.24}$$

The wave vector k_x is continuous through the interface (for the derivations see Appendix I). Therefore, the dispersion relation (2.23) can be written as:

$$k_x = \frac{\omega}{c}\sqrt{\frac{\varepsilon_1 \varepsilon_2}{\varepsilon_1 + \varepsilon_2}} \tag{2.25}$$

In the usual treatment, ω is considered to be a real number and the dielectric function for the metal is a complex number $\varepsilon_1 = \varepsilon_1^{'} + i\varepsilon_1^{''}$, if it is also assumed that $\varepsilon_1^{''} < \left|\varepsilon_1^{'}\right|$ then $\vec{k}_x$ is also complex, i.e. $k_x = k_x^{'} + ik_x^{''}$. As a consequence, the surface plasmon modes propagates along the metal/dielectric interface decreases as $e^{-2k_x^{''}x}$ and has a finite length L_x after which the intensity decreases $1/e$ given by $L_x = \frac{1}{2k_x^{''}}$ that has an important impact on the lateral resolution of SPR which is essential for SPR imaging to characterise laterally structured samples. On the other hand the penetration length of the light into the dielectric $(i = 2)$, l_c, decays exponentially as well on to the surface $e^{-|k_{zi}||z|}$ and for $1/e$ is given by $l_c = \frac{1}{|k_{zi}|}$. The penetration depth depends on the surface specificity, yielding an evanescent probe field, as it is sensitive to changes in the dielectric.

2.1.2 Excitation of Surface Plasmons with Light

Excitation of surface plasmons is usually produced by applying incident transversal magnetic (TM) radiation as these have electric field components perpendicular to the magnetic field. Several conditions have to be fulfilled, in order to excite surface plasmons.

In the working frequency :

$$\sqrt{\varepsilon_2} \leq \sqrt{\frac{\varepsilon_1 \varepsilon_2}{\varepsilon_1 + \varepsilon_2}} \tag{2.26}$$

This means that the momentum of a free photon k_{ph} propagating in the dielectric medium, is always smaller than the momentum of a surface plasmon mode k_{sp} propagating along an interface between that same dielectric medium and the metal, $\left|\vec{k}_{ph}\right| < \left|\vec{k}_{sp}\right|$.

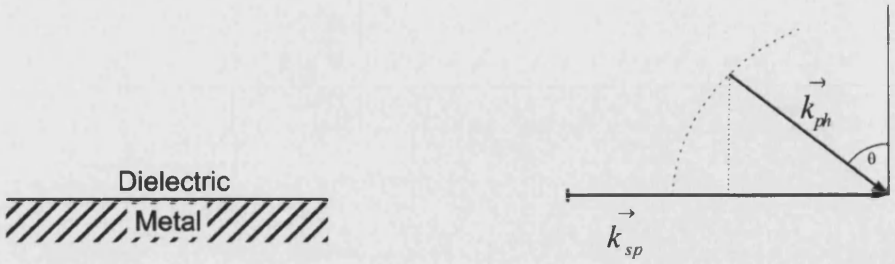

Figure 2.1 Momentum relation between a surface plasmon, k_{sp}, propagating along the x and a photon, k_{ph}, incident at the dielectric/metal interface at an angle θ.

For the surface plasmons excitation only the incident photon wave vector projection to the x-direction is the relevant parameter, i.e., $k_{ph}^{x} = k_{ph} \cdot \sin\theta$. If, for example, a laser light is simply being reflected with energy $\hbar\omega$ at a smooth dielectric/metal interface it is possible to change the angle of incidence from zero until the full wave vector k_{ph} (point 1 in Figure 2.2). Although, it can be observed from Figure 2.2, that changing the angle of incidence of the laser light is not sufficient to fulfil the momentum matching condition for production of resonant surface plasmons excitation. Because for low energies, the surface plasmon dispersion curve tends to the light line but never touches it, while for higher energies it approaches the maximum frequency, ω_{max}, determined by the plasma frequency of the metal in use.

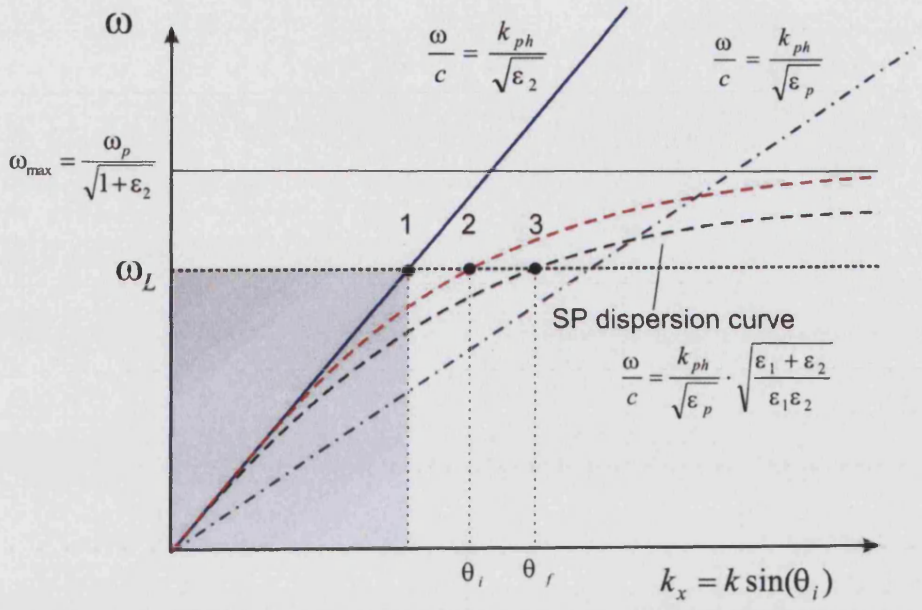

Figure 2.2 Dispersion relation of (black line) free photons, (dash-point-dash line) free photons passing through a system using a coupled prism. It can be observed that momentum of the free photons never matches with the momentum of the surface plasmons. Red-dashed and blacked-dashed lines are a comparison of the dispersion relation of surface plasmons at the interface between the metal and the dielectric, before (red) and after (black) adsorption of an additional dielectric layer. When using the prism coupled system the momentum and the energy of the photons for a certain wavelength (ω_L) matches the dispersion relation of surface plasmons in points (2,3).

It is important to realise that with these conditions it is not possible to excite surface plasmons using simply a laser light travelling in vacuum and incident directly onto the surface. In Figure 2.2 the grey area represents the frequency/wave vector combinations that are accessible in vacuum. Thus, to excite surface plasmons it is necessary that the two wave vectors are equal. This can be achieved by increasing the x-direction component of the photon wave vector.

One way in which is possible to increase the amplitude of the x-projection of the photon wave vector is by passing the light through a medium of higher refractive index than the dielectric. An example of high refractive index medium is a prism. When the incident light passes through the high refractive index prism the surface plasmons are excited by the evanescent field of the reflected light produced under total internal reflection conditions (for more information see Appendix II). A detailed description of the prism coupling can be found in [128, 129].

The first set-up was developed by Otto. In the Otto-configuration the photons pass, through the high refractive index medium (prism) and at a certain angle greater than

the critical angle, total internal reflection is reached and the evanescent wave is formed. In this configuration, after the prism is a thin layer of air (dielectric) with 200nm thickness to facilitate the excitation of the plasmons on the metal layer located immediately after the dielectric by the evanescent wave.

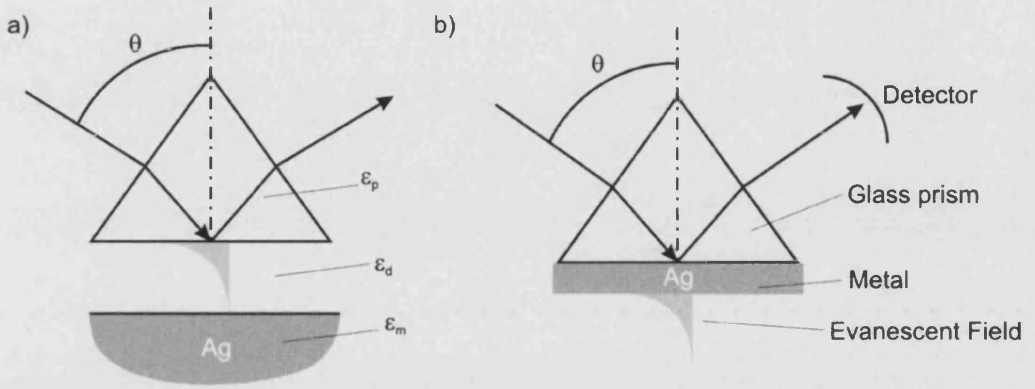

Figure 2.3 a) The Otto configuration is based on the total internal reflection of a plane wave incident at an angle θ at the base of a prism. The evanescent tail of this inhomogeneous wave can excite surface plasmon states at a metal-dielectric interface, provided the coupling gap is sufficiently narrow. b) Attenuated total internal reflection (ATR) construct for surface plasmons excitation in the Kretschmann configuration. A thin metal layer (d~50 nm) is evaporated immediately at the base of the prism and acts as a resonator driven by the photon field incident at an angle θ.

This conformation has brought a number of problems, for example, even a few dust particles can behave as a spacer preventing efficient coupling. Thus, in this work a prism coupling with Kretschmann configuration is used. In the Kretschmann configuration (see Figure 2.3), a thin metal film is evaporated directly onto the base plate of the prism or onto a glass slide which is then index-matched to the base of the prism, and plasmon excitations are found on both sides of the metal film.

The excitation of the surface plasmons is only possible when the system enters in resonance, this means when by changing the angle θ of incidence until the projection of $k_{ph}^{x} = k_{ph} \cdot \sin\theta$ matches the surface plasmon wave vector. This situation occurs in the intersection 2 in Figure 2.2 where the resonance coupling happens at a given combination of frequency and incident angle.

However, this new configuration produces other radiative-loss channels for surface plasmons, besides the intrinsic dissipation in the metal. In particular, the presence of a metal layer with a finite thickness evaporated directly on to prism lets some surface plasmon light to couple out through the thin metal layer and the prism.

If the reflectivity is monitored, it is observed that there is a decrease in reflected intensity while the system is in resonance, as the system is being excited by the energy from the incident light. Therefore, a resonance minimum is observed when plotting the intensity of the reflected light versus the applied incident angle.

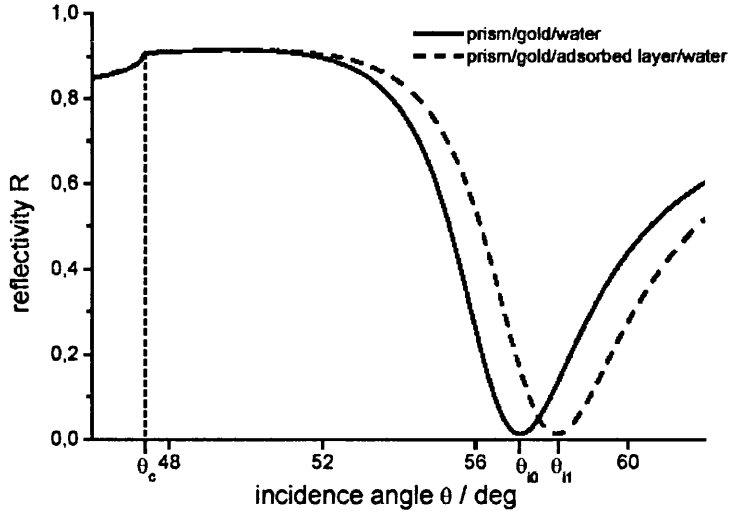

Figure 2.4 Resonance curve obtained when using a system with Kretschmann configuration. Note that resonance angle of the system is shifted if an additional layer at the gold is taken in consideration.

The resonance angle at which the maximum energy is transferred can be determined using the dispersion equalities at interception point 2:

$$k_{ph}^{x} = k_{ph} \cdot \sin\theta_i = \frac{\omega}{c}\sqrt{\varepsilon_p}\,\sin\theta_i = k_{sp} = k_x = \frac{\omega}{c}\sqrt{\frac{\varepsilon_1\varepsilon_2}{\varepsilon_1+\varepsilon_2}}$$

$$\theta_i = \arcsin\sqrt{\frac{\varepsilon_1\varepsilon_2}{\varepsilon_p(\varepsilon_1+\varepsilon_2)}} \qquad (2.27)$$

2.2 Sensitivity of Surface Plasmons to Optical Changes

Biomolecular interactions occurring at the surface change the optical properties of the evanescent wave will modify the conditions at which the dispersion of surface plasmons is excited. Adsorption of a new dielectric layer at the interface can be sensed by the excited plasmons field and monitored via the changes observed in the angle of resonance for maximum energy transfer.

If a layer with higher dielectric constant is adsorbed onto the metal layer then the mean refractive index of the area that is being sensed by the evanescent plasmons field is increased. As result, the dispersion relation of the new surface plasmons is shifted towards larger wave vectors as illustrated in Figure 2.2 in intercept 3.

$$k_{p2} = k_{p1} + \Delta k \tag{2.28}$$

Where k_{p1} and k_{p2} are the wave vectors before and after the adsorption of the new dielectric layer. Δk is the increment acquired which depends on the refractive index and the thickness of the new layer adsorbed. Consequently, a new resonance angle with maximum energy transfer is obtained and equation (2.28) has to be adjusted. The shift of the resonance minimum is fundamental for the experimental application in methods like surface plasmons resonance spectroscopy or microscopy. In the case of non-adsorbing layers ($\varepsilon'' \geq 0$) the measured angle shift $\Delta\theta$ is proportional to the change of the optical layer thickness (d) and refractive index:

$$\Delta\theta \approx \Delta n \times \Delta d \tag{2.29}$$

One of the parameters has to be known in order to calculate the other one, as there are many combinations of optical layers thickness and refractive index for the same resonance shift.

2.3 Surface Plasmon Field Distribution

The electromagnetic field decays exponentially on both sides of the metal, but only the enhanced plasmons at the metal/dielectric interface are considered here, since these can be used to sense changes in the adjacent dielectric. At this point it is important to mention that for any oscillator the maximum amplitude and the width of the resonance curve depends on the degree of damping that exists in the system, which is governed by the imaginary part of the dielectric function. In order to understand the influence of the damping on the intensity of the field a representation of the field intensities at the surface for different metallic surfaces and a pure dielectric interface are considered [102].

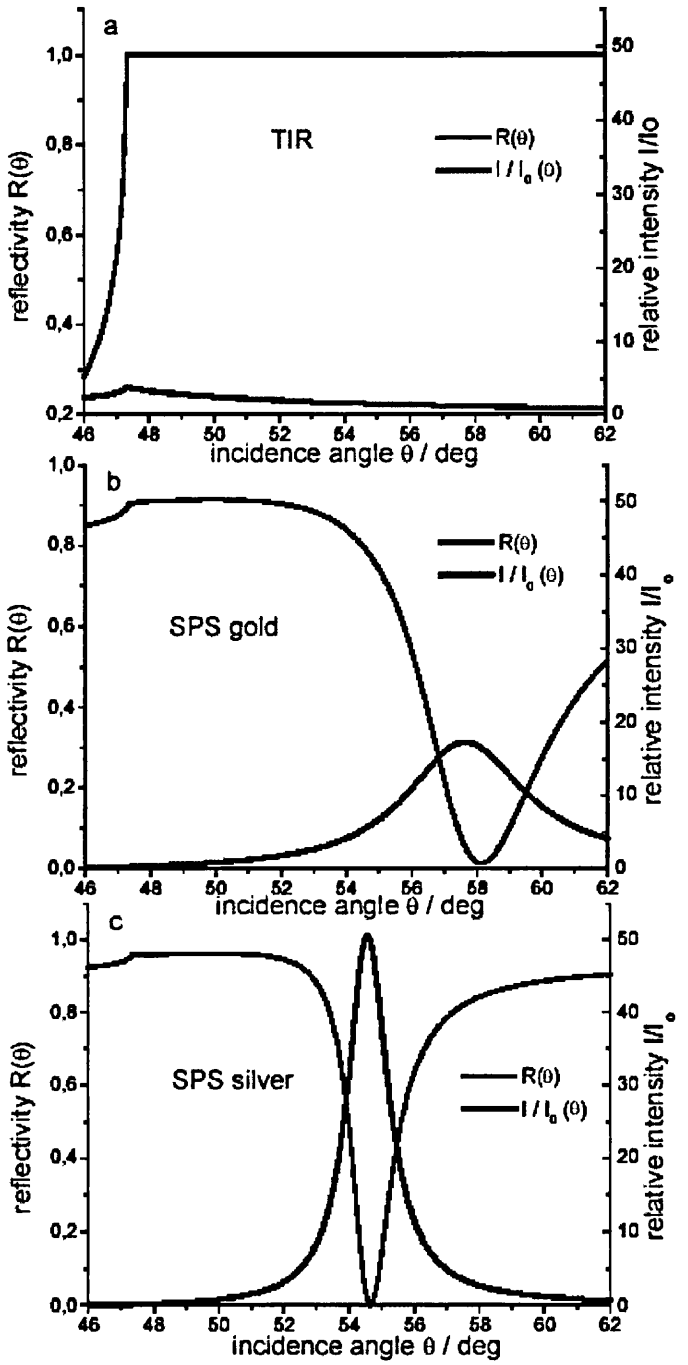

Figure 2.5 Comparison between TIR and surface plasmon excitation by considering calculated reflectivity R and relative intensity at the surface in the case of a) glass/water interface b) gold and c) silver [102].

When considering the description given by Maxwell's equations the dissipation of energy in the metal damping mechanism given by the imaginary (loss) part of the dielectric function ε'' is relevant. In the example above, silver (Ag) and gold (Au) are the two metals used. For frequencies around 630 nm, Ag is the metal with the smallest imaginary dielectric function $(\varepsilon''_{Ag} = 0.5, d = 50nm)$, followed by Au $(\varepsilon''_{Au} = 1.3, d = 50nm)$ As a result, the surface plasmon reflectivity curve for an Ag/air interface has the

smallest width, for a given laser wavelength λ, and consequently shows the highest enhancement factor for the field intensity. The resonance at an Au/air interface is a only some degrees wider depending on the homogeneity of the evaporated Au layer, whose granular structure with the several grain boundaries, gives rise to new additional radiative-loss mechanisms via scattering.

In the case of the glass/water interface in Figure 2.5 a) total internal reflection is observed: below the critical angle, θ_C, the reflectivity is low because most of the light is transmitted. However, when the θ_C is approached, the intensity increases steeply and reaches unity above the θ_C. A small enhancement of the field intensity (factor of 4) at the θ_C is observed due to the constructive interference of the two amplitudes of the incoming and reflected electromagnetic field at θ_C. This enhancement together with the evanescent character of this light surface is used successfully in surface selective fluorescence [52]

For the case of the glass surface covered with a thin metal layer Figure 2.5 b) and c) the total reflection edge is still observed. However, the intensity of the reflected light at the metal/dielectric interface decreases strongly as one approaches the resonance condition for the excitation of a surface plasmon. However, the peak field intensity is found at these conditions.

The field peak intensity is at slightly lower angle of incidence than the minimum of the reflected intensity light. In surface plasmon resonance there is a coherent superposition of the reflected light at the metal/prism interface and the surface plasmon mode reradiated into the prism. When in the presence of a radiative-loss free metal surface the resonance phase difference between the surface plasmon modes relative to the field photon momentum, in these conditions (radiative-loss free metal), is 180°. Therefore, the observed the minimum of resonance is explained by a destructive interference of these two waves.

In a real metallic system, any damping smears out the phase change at the plasmon resonance angle and consequently, the field peak intensity and the resonance minimum are shifted by a small amount. The damping is described by the imaginary part of the dielectric constant of the metal and therefore the angular position is larger for Au then Ag. Although Ag presents a higher enhancement factor [102], in this work gold is used due to its known resistance against oxidation and buffer solutions.

2.4 Fluorescence

2.4.1 Principles of Fluorescence

Fluorescence is a well-characterised phenomenon that describes the emission of photons from molecules that undergo a transition from an electronically excited state to the ground state [130]. Fluorophores often exhibit strongly delocalised electrons in conjugated double bonds or aromatic systems. The schematic Jablonsky energy level diagram shown in Figure 2.6 illustrates the molecular process during absorption and emission of photons.

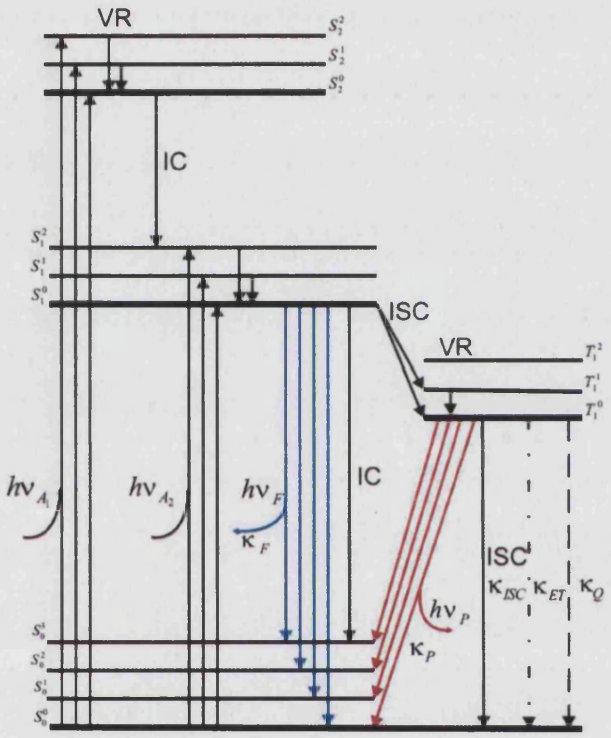

Figure 2.6 Excitation and relaxation of molecules due to absorption and emission of light. $h\nu_{A_1}$ and $h\nu_{A_2}$ are the electronic absorption resulting in the excitation from the ground state S_0 to the excited singlet states S_1 and S_2. Adsorption of light is followed by vibrational relaxation (VR) or radiationless internal conversion (IC) between electronic states. The superscripts of the electronic states represent the vibrational quantum numbers of the various vibrational sublevels. Return to the ground state from S_1^0 can be proceed by internal conversion, fluorescence (F) or intersystem crossing to the lowest triplet state (T_1). The triplet state is deactivated by phosphorescence (P) or radiationless intersystem crossing.

The singlet ground and first electronic states are depicted by S_0 and S_1, respectively. At each of these electronic energy levels, the fluorophores can exist in a number of vibrational energy levels denoted by 0, 1, 2, etc.

Fluorescence is induced by absorption of electromagnetic wave energy. Following light absorption, several processes usually occur. A fluorophore can be excited to higher vibrational levels of S_1 or S_2 and rapidly relaxes to the lowest vibrational level of S_1. This process is called internal conversion and generally occurs in 10^{-12} s or less. Since fluorescence lifetimes are typically 10^{-8} s, internal conversion is complete before emission occurs. Therefore, fluorescence emission results from the lowest-energy vibrational state of S_1 (Kasha's law). From this excited state, the molecule can decay to different vibrational levels of the state S_0 by emitting light with a constant rate κ_F. This leads to the fine structure of the emission spectrum by which one can obtain information about the electronic ground state S_0.

The transition between two states of the same spin multiplicity is a quantum mechanically allowed process and the rate of emission is high, typically near 10^8 s^{-1}. By comparing absorption and emission spectra it is possible to observe the Stokes´ shift of the fluorescence emission to a lower wavelength (red shift) relative to the absorption. This shift can be explained by energy losses between the two processes due to the rapid internal conversion in the excited states (S_1, S_2) and the subsequent decay of the fluorophore to higher vibrational levels of S_0. This shift is fundamental to the sensitivity of fluorescence techniques because it allows the emitted photons to be isolated from excitation photons detected against a low background.

In contrast, absorption spectroscopy requires the measurement of transmitted light relative to high incident light levels of the same wavelength. Generally the fluorescence emission spectrum appears to be a mirror picture of the absorption spectra, because of the same transitions that are involved in both processes and the similarities among the vibrational levels of S_0 and S_1. Often deviations to this mirror rule can occur due to excited state reactions and geometric differences between electronic ground and excited states.

A fluorescence emission spectrum is recorded by holding the excitation wavelength constant and detecting the fluorescence intensity over a range of emission

wavelengths. In contrast to this an excitation spectrum is recorded by holding the emission wavelength constant and scanning over a range of excitation wavelengths.

With a few exceptions, the excitation spectrum of a fluorescent species in dilute solutions is identical to the absorption spectrum. Under the same conditions, the fluorescence emission spectrum is independent of the excitation wavelength. Starting from the excited state S_1 the fluorophore can not only dissipate its energy by fluorescence emission with the rate κ_F, but several other radiationless decay channels can be found that lead to a depopulation of S_1. Electronic transition to triplet states by intersystem crossing (ISC) as well as quenching processes (κ_Q) and resonant energy transfer (κ_{ET}) can result in a decrease of the fluorescence quantum yield, which is defined as:

$$\phi = \frac{\kappa_F}{k_F + k_0} \tag{2.30}$$

This is equivalent to the ratio of the number of emitted photons over the absorbed ones. The rate constant κ_0 combines all possible radiationless decay channels including internal conversion losses (k_{IC}).

$$\kappa_0 = \kappa_{ISC} + \kappa_{IC} + \kappa_Q + \kappa_{ET} \tag{2.31}$$

The fluorescence lifetime τ is defined as the average of the time that a molecule excited spends in the excited state prior to return to the ground state. It is a sensitive measure of parameters influencing the fluorophore in the excited state.

$$\tau = \frac{1}{\kappa_F + \kappa_0} \tag{2.32}$$

Additionally, the environment of the fluorescent species like the polarity of the solvent or the pH can influence the intensity and the wavelength of emitted fluorescence. The interaction with the fluorophore's dipole moment and chemical reactions between the dye and solvent molecules (hydrogen bonding, acid-base chemistry or charge transfer interactions) can alter the fluorescence intensity. These solvent effects are often used to sense the environment in which the fluorophore exists and have some biochemical impact for protein folding studies. In the following sections quenching and resonant transfer effects will be discussed.

2.4.2 Fluorescence Quenching

The intensity of fluorescence can be decreased by a number of processes, for example complex formation, energy transfer, excited state reactions or collision of molecules.

Such decreases in intensity are called quenching. Quenching occurs via various mechanisms. Collisional quenching occurs when the excited-state fluorophore is deactivated upon contact with some other molecule in solution, which is called the quencher. This process is known as dynamic quenching. Static quenching happens when the fluorophore and the quencher form a nonfluorescent complex. For collisional quenching, the decrease in intensity is described by Stern-Volmer equation.

$$\frac{I_0}{I} = 1 + \kappa_Q \tau_0 [Q] = 1 + K_D [Q] \tag{2.33}$$

In this expression I_0 and I are the fluorescence intensities in the absence and presence of the quencher, respectively. K_D is the Stern-Volmer dynamic quenching constant, κ_Q is the bimolecular quenching constant, τ_0 is the unquenched lifetime, and $[Q]$ is the quencher concentration. Quenching data are usually plotted as I_0/I versus $[Q]$.This is expected to give a linear dependence. Deviations from linearity often indicate that two different populations of fluorophores may be present, one of which is not accessible by the quencher. A similar expression can be derived for quenching by complex formation or static quenching.

$$\frac{I_0}{I} = 1 + K_S [Q] \tag{2.34}$$

where K_S is the association constant for the complex formation.

Combining static and collisional quenching of the same fluorophore can be described by the modified Stern-Volmer equation:

$$\frac{I_0}{I} = (1 + K_S [Q])(1 + K_D [Q]) \tag{2.35}$$

By multiplying the terms in brackets and simplifying the expression it is obtained:

$$\frac{I_0}{I} - 1 = K_{app} \text{ where } K_{app} = (K_D + K_S) + K_D K_S [Q] \tag{2.36}$$

Therefore, a plot of K_{app} versus $[Q]$ is linear with a slope equal to $K_D K_S$ and an intercept of $K_D + K_S$. By solving the quadratic equation one can obtain the different individual values and, with further considerations, determine which values of K_D and K_S better reflect reality.

2.4.3 Resonant Energy Transfer

Fluorescence resonance energy transfer from a donor to an acceptor is an important mechanism for the depopulation of the excited electronic states of a fluorophore [130]. This interaction is distance dependent between the electronic excited states of two fluorophores, the donor molecule (D*) and the acceptor (A), where excitation energy is transferred from D* to A without the emission of a photon. Once excited, the acceptor can return to the ground state via the same pathways as described previously in Figure 2.6.

$$D^* + A \rightarrow D + A^* \tag{2.37}$$

If the acceptor molecule is also fluorescent, then it is possible to detect the fluorescence emission of the molecule given that the acceptor will emit always at a longer wavelength than the donor will. This transfer of energy is radiationless and it can be attributed to resonant interaction of the transition dipole moments of donor and acceptor molecules. At the so-called Föster distance, the resonant energy transfer is 50% efficient, typically the range of 20 to 60 Å. The rate κ_{ET} of energy transfer from D* to A is given by:

$$\kappa_{ET} = \frac{1}{\tau_D}\left(\frac{R_0}{r}\right)^6 \tag{2.38}$$

Where R_0 is the Föster distance, at which one-half of the donor molecules decay by energy transfer and one-half decay by the usual radiative and nonradiative rates, τ_D is the decay time of the donor in the absence of acceptor and r is the donor to acceptor (D–A) distance. One can easily determine whether the rate of transfer will compete with the decay rate, τ_D^{-1}, of the donor. If the transfer rate is much faster than the decay rate, then energy transfer will be efficient. If it is the other way around, then little transfer will occur during the excited state lifetime, and energy transfer will be inefficient.

The efficiency of energy transfer (E) is the fraction of photons absorbed by the donor that are transferred to the acceptor and it is given by:

$$E = \frac{k_T}{\tau_D^{-1} + k_T} = \frac{R_0^6}{R_0^6 + r^6} \tag{2.39}$$

An example of the FRET efficiency versus donor-acceptor distance if the Föster distance is 5nm is shown in Figure 2.7.

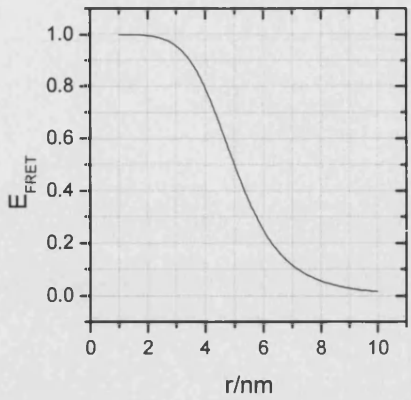

Figure 2.7 Simulation of the energy transfer efficiency versus the distance between two dyes calculated with equation (2.39).

Fluorescence resonance energy transfer (FRET) is a powerful technique for studying conformational distribution and dynamics of biological molecules, thus it has been widely used [131] for example in real time PCR DNA detection.

2.5 Surface Plasmon Field Enhanced Fluorescence

In the past it has been shown that fluorophores close to the metal surface experience the plasmon field enhancement and are excited resonantly by this field, but only few studies are known to use surface sensitive enhancement for sensing purposes [99, 101, 103]. Surface plasmon resonance spectroscopy as a direct detection method is known to be deficient in sensitivity for detection of low molecular mass analytes as well as for dielectric layers with small lateral packing [132], as SPR is sensitive to mass density change on the surface. In order to enhance sensitivity and to improve the detection limit the technique was combined with fluorescence methods in surface plasmon field enhancement fluorescence spectroscopy (SPFS) as described in [102]

The presence of a metal surface is essential for SPFS technique, since it is the evanescent surface plasmon field produced by the coupling of light with the surface plasmons at the metal interface that excite the fluorophores present in the dielectric. Although it is important to keep in mind that since a metal surface is in contact with the dielectric the fluorescence emitted by the excited fluorophores is dependent on the distance between the dye and the surface, as different decay channels are possible. The metal surface is an extremely good quencher. The study of the behaviour of dyes close to the metal is now well understood and detailed in reference [133].

Fluorescence intensity emitted from fluorophores is also dependant, for a given wavelength, on the intensity of the optical excitation field and the probability for radiative decay from the excited state to the ground state.

Thus, for SPFS the intensity of fluorescence dependence is controlled by the behaviour of fluorophores in the front of a metal surface due to quenching processes. Figure 2.8 summarises some of the observed distance dependent energy transfer mechanism.

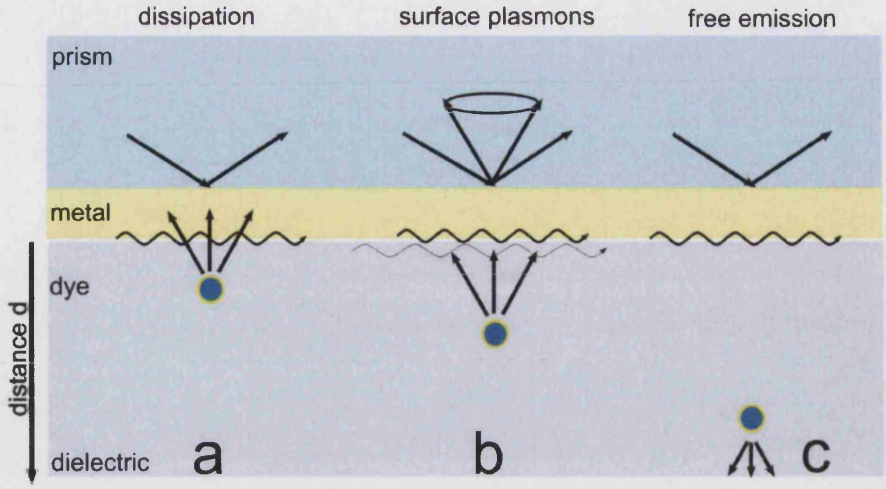

Figure 2.8 Major decays channels for fluorescence near metallic surfaces [102]. While at close distances quenching due to the metal layer is found (a), the excitation of plasmons by the red-shifted fluorescence light is dominating fluorescence intensity up to distance of about 20 nm (b). Finally, at large distances to the metal the free emission of photons can be found (c).

As fluorophores come closer and closer to the metal surface they are able to couple electronically their localised molecular orbitals with the extended band structure of the metallic electrons in the solid substrate. This generates new decay channels for the excitation energy of the dye leading to a large modification of radiative lifetimes and fluorescence intensities.

For a very short separation distance between the fluorophores dipoles and the metal surface, a substantial radiationless de-excitation with a corresponding reduction of the radiative lifetime and of the fluorescence intensity is found: the fluorescence is quenched, dissipating the excitation energy in the metal as heat.

For intermediate separation distances, the optically excited fluorophores can excite surface plasmon modes at the Stoke's red shifted wavelength. This can couple the light if momentum matching via prism occurs. This type of excitation typically becomes dominant at dye-metal distances of about 20 nm. The back radiation through the prism will lead to an emission cone, since the wavevector of the excited plasmons is fixed, but no plane of incidence can be defined anymore because fluorophores emit in random directions.

For larger separation distances, no immediate modification of the radiative emission of the excited state of the fluorophores exists and fluorescence signal can be monitored.

Fluorophores further away from the metal surface cannot be excited due to insignificance evanescent field.

As discussed before, the evanescent field decreases exponentially into the dielectric layer adjacent to the metal film. The penetration depth into the dielectric, at which the surface field intensity drops down to 1/e of the interface value, is in the order of the wavelength of the incident light. Thus, by carefully designing the supramolecular interfacial architectures that provides binding sites for a bio-recognition process of a fluorescently labeled analyte, one can measure surface sensitive fluorescence since only dyes in the proximity to the metal film contribute significantly to a measurable signal [134].

2.6 Langmuir Adsorption

2.6.1 Langmuir Adsorption

One of the simplest models that describes the interaction between two molecules on surfaces is the Langmuir adsorption isotherm [135, 136]. This model has been widely used and it is based on three basic assumptions: i) Adsorption of molecules produces only a homogenous monolayer; ii) all binding sites are equivalent; iii) all occupied sites do not influence the binding reaction in adjacent places.

In order to understand the processes of molecular interactions on a surface it is assumed that a limited number of binding sites are available, which can be occupied by binding molecules until the complete surface is saturated and all sites are blocked.

Consider a reversible interaction between two molecules, A the ligate and B the immobilised ligand:

$$A+B \underset{k_{off}}{\overset{k_{on}}{\rightleftharpoons}} AB \tag{2.40}$$

The process at the surface is described by the rate constants of adsorption k_{on} and desorption k_{off} from the surface, respectively, which are related with the association rate of A and B $k_{on}[A][B]$ and with the dissociation rate of AB complex $k_{off}[AB]$.

When the two species are present in solution association and dissociation will occur and with time the rates will become equal. When this occurs, it is defined as equilibrium. In equilibrium conditions the concentration of $[A], [B]$ and $[AB]$ are constants and so it can be written:

$$k_{on}[A][B] = k_{off}[AB] \tag{2.41}$$

Rearranging the equation

$$\frac{[A][B]}{[AB]} = \frac{k_{off}}{k_{on}} = K_D \tag{2.42}$$

Where K_D is the dissociation equilibrium constant and is the reciprocal of the association equilibrium constant K_A:

$$K_A = \frac{1}{K_D} \tag{2.43}$$

The association rate constant has units k_{on} of $mol^{-1}Ls^{-1}$ and the dissociation rate constant has units of k_{off} s^{-1}, it follows that the association constant K_A has $mol^{-1}dm^3$ units and the dissociation constant K_D has mol L^{-1} units.

The case described above is the simplest bimolecular interaction where other factors will not influence the interaction between the two species however, as one of the species does not move freely in solution, there are important factors that should considered. The most important factor is the transport of the species A from the bulk into the interface where species B is present in very high concentration (see Figure 2.9).

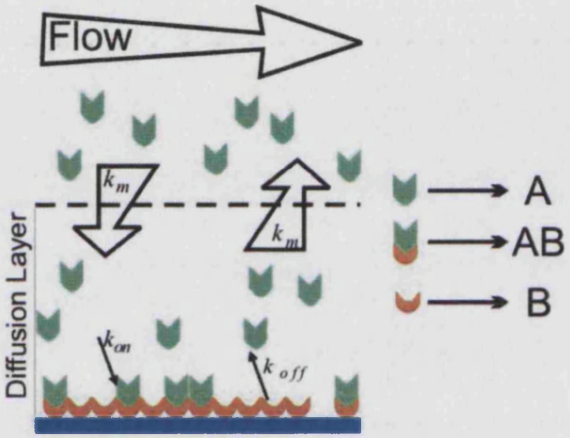

Figure 2.9 Scheme showing the different factors influencing the interactions between two different species, one present in the bulk solution only and the other immobilised on the surface. The ligate (A) is flowed through the surface where the ligand (B) is present. k_m is the mass transport coefficient that describes the diffusion of the ligate from the bulk solution onto the surface. This distance is defined as diffusion layer [137].

Therefore, the rate of formation of the complex specie (AB) is also influenced by the mass transport rate constant from the bulk to the interface

$$A_b \underset{k_m}{\overset{k_m}{\rightleftharpoons}} A_i + B \underset{k_{off}}{\overset{k_{on}}{\rightleftharpoons}} AB \qquad (2.44)$$

Where A_b is the concentration of ligate in the bulk solution and A_i is the concentration at the interface. The rate of consumption of the ligate at the interface A_i is given then by:

$$\frac{d[A]_i}{dt} = k_m([A]_b - [A]_i) - k_{on}[A]_i[B] + k_{off}[AB] \qquad (2.45)$$

Considering the steady state approximation where it is assumed that after an initial induction period the rates of change of concentration of all reaction intermediates are

negligibly small, $d[A]_i/dt \approx 0$ [136], then the concentration of ligate at the interface A_i is equal to:

$$[A]_i = \frac{k_m[A]_b + k_{off}[AB]}{k_{on}[B] + k_m} \tag{2.46}$$

So the rate formation of the complex AB at the surface

$$\frac{d[AB]}{dt} = k_{on}[A]_{interface}[B] - k_{off}[AB] \tag{2.47}$$

And substituting the concentration of ligate at the interface A_i with equation (2.46) then

$$\frac{d[AB]}{dt} = \frac{k_{on}k_m}{k_m + k_{on}[B]}[A]_b[B] - \frac{k_{off}k_m}{k_m + k_{on}[B]}[AB] \tag{2.48}$$

or

$$\frac{d[AB]}{dt} = k_f[A]_b[B] - k_r[AB] \tag{2.49}$$

Where k_f if the forward rate constant and k_r is the reverse rate constant, which are equal to:

$$k_f = \frac{k_{on}k_m}{k_m + k_{on}[B]} = \frac{k_{on}}{1 + \frac{k_{on}}{k_m}[B]} \tag{2.50}$$

$$k_r = \frac{k_{off}k_m}{k_m + k_{on}[B]} = \frac{k_{off}}{1 + \frac{k_{on}}{k_m}[B]} \tag{2.51}$$

If the mass transport coefficient k_m is very small, e.g., at low flow rates or very high molecular weight molecules, or the concentration of ligand is very high, i.e., $k_m <<< k_{on}[B]$, then equation (2.48) for the mass transport dependence of the formation of complex AB becomes:

$$\frac{d[AB]}{dt} = k_m[A]_b - \frac{k_m k_{off}}{k_{on}[B]}[AB] \tag{2.52}$$

And the diffusion layer is very thick.

In the beginning of the process of AB complex formation, the concentration of this species is very small so the second fraction of the rate formation of the complex species (AB) is negligible and the equation is simplified to:

$$\frac{d[AB]}{dt} = k_m[A]_b \tag{2.53}$$

Analysing this equation it can be observed that the formation of the complex AB is totally dependent on the concentration of the ligate A in solution, and the binding curve is linear. This is situation is defined as binding of the ligate with mass transported control.

However, if the mass transport coefficient is larger than the rate formation k_{on} or the concentration of the immobilised ligand is very low than the forward rate constant k_f and the reverse rate constant k_r become close to the association rate constant and the dissociation rate constant and the rate formation equation (2.48) becomes:

$$\frac{d[AB]}{dt} = k_{on}[A][B] - k_{off}[AB] \tag{2.54}$$

Over time the concentration of free ligand sites decreases with the ligate binding so, the concentration of free ligand sites at time t is equal to maximum number of binding sites or to the concentration of ligand at the starting time ($[B]_0$) minus the sites bound at time t, i.e, ($[B]_t$) = $[B]_0 - [AB]_t$. Therefore, equation (2.52) becomes:

$$\frac{d[AB]}{dt} = k_{on}[A]([B]_0 - [AB]_t) - k_{off}[AB]_t \tag{2.55}$$

The formation of complex AB is the signal response that in this case is reflectivity or fluorescent in photons counts per second. This it will be define as R_t in this theoretical part. The maximum signal obtained when all binding sites are occupied and is equal to $[B]_0$ which is defined as R_{max}. So equation (2.55) becomes:

$$\frac{dR_t}{dt} = k_{on}[A](R_{max} - R_t) - k_{off}R_t \tag{2.56}$$

Integrating this equation it becomes from $t = 0$ till t it becomes:

$$R_t = \frac{k_{on}[A]R_{max}}{k_{on}[A] + k_{off}}\left(1 - e^{-(k_{on}[A] + k_{off})t}\right) \tag{2.57}$$

Where

$$R_{eq} = \frac{k_{on}[A]R_{max}}{k_{on}[A] + k_{off}} = \frac{[A]R_{max}}{[A] + K_D} = \frac{[A]R_{max}K_A}{K_A[A] + 1} \tag{2.58}$$

R_{eq} is the equilibrium response for each different ligate concentration $[A]$ used, then equation (2.57) can be written:

$$R_t = R_{eq}\left(1 - e^{-(k_{on}[A] + k_{off})t}\right) \tag{2.59}$$

With the equation (2.55) it is possible to fit mathematically the model to the different binding data obtained for the different concentrations. Figure 2.10 is the simulation of the different binding data.

Consider the dissociation process the concentration of the ligate A is zero so the response is independent of their concentration and is expressed by:

$$\frac{dR_t}{dt} = -k_{off}R_t \tag{2.60}$$

Integrating the equation the solution is given by

$$R_t = R_0 e^{-k_{off} t} \tag{2.61}$$

Where R_0 is the response at the starting point of the dissociation process.

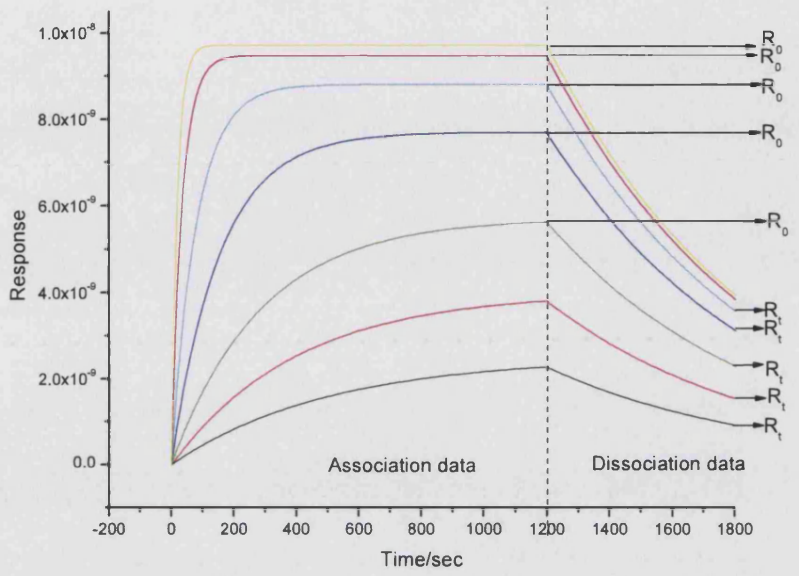

Figure 2.10 Kinetic measurements for different concentrations of ligate used. Fitting this data allows to determine the kinetic constants.

Fitting the data obtained via nonlinear least squares fit using equations (2.55) and (2.57) yields the values of the association and dissociation rate constants, k_{on} and k_{off} respectively.

Alternatively, it is possible to determine the different equilibrium constants using the equilibrium response for each concentration of ligate used, i.e., at each concentration of ligate a value of the response at equilibrium (R_{eq}) is obtained equivalent to the amount of complex AB formed at equilibrium.

$$R_{eq} = \frac{k_{on}[A]R_{\max}}{k_{on}[A] + k_{off}} \tag{2.62}$$

$$R_{eq} = \frac{[A]R_{\max}}{[A] + k_{off}/k_{on}} \tag{2.63}$$

$$R_{eq} = \frac{[A]R_{\max}}{[A] + K_D} \tag{2.64}$$

By plotting R_{eq} against the free ligate concentration the Langmuir adsorption curve is obtained. The concentration required to saturate the 50% of the available ligands sites is $R_{\max}/2$.

$$R_{\max}/2 = \frac{[A]R_{\max}}{[A]+K_D} \tag{2.65}$$

$$[A] = K_D \tag{2.66}$$

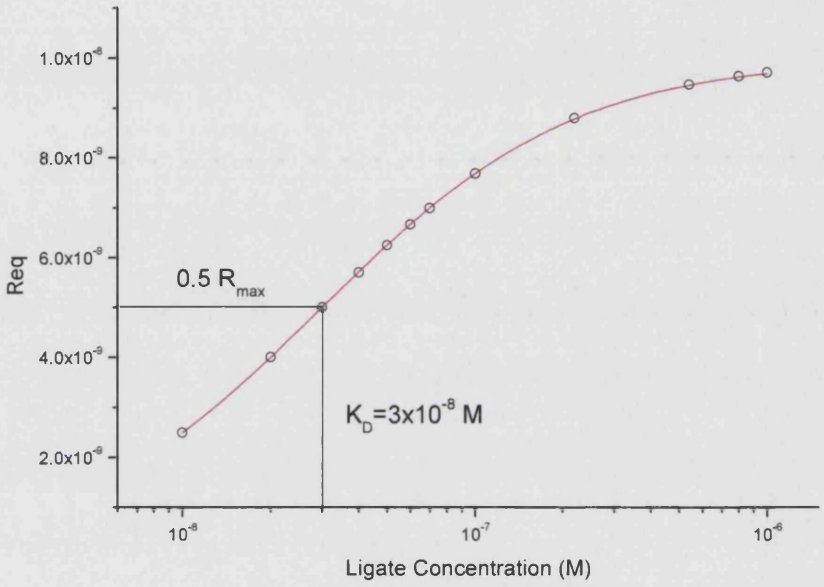

Figure 2.11 Langmuir Isotherm. Direct determination of the different equilibrium constants.

In conclusion, the dissociation equilibrium constant K_D can be obtained directly form the Langmuir adsorption curve when the response is equal to $R_{\max}/2$.

Experimentally these measurements are achieved by a stepwise saturation of the ligand on the surface by a consecutive addition of ligate concentrations and wait for equilibrium to be achieve, as it will be shown further in this research.

3 Experimental Methods

In this chapter, a detailed description of the establishment, optimisation and development of the experimental set-up is presented. The different experimental procedures for the production of the supramolecular sensing surface are described, followed by a description of the experimental methods employed.

3.1 Optical Methods

Surface Plasmon Resonance Spectroscopy (SPRS or SPR for shorter) is the main technique used in this work. SPR measures the kinetic rates and equilibrium constants of analytes adsorbing and desorbing from a sensor surface. Furthermore, the experimental contribution of simultaneous fluorescence detection with adaptation of the SPR set-up to a Surface Plasmon Fluorescence Spectroscopy (SPFS) set-up enables the measurement of smaller quantities of analyte..

3.1.1 Experimental Set-up – Overview

First period

The experimental set-up picture presented in Figure 3.1 illustrates a conventional home made surface plasmon resonance spectrometer that was built in this lab previously to the start of this work. This system consisted of a He-Ne laser (Melles Griot Ltd, 5mW, λ=632.8 nm), that excites surface plasmons present at the metal/dielectric interface. Two polarizers, positioned in the same alignment as the laser beam, adjust the intensity of the laser beam, as well as, cut off the transversal electric field polarisation. As mention in the previous chapter, only the transversal magnetic field has the adequate polarisation to excite the surface plasmons. The system combines a goniometer (Huber) where the sample holder and photodiode are mounted.

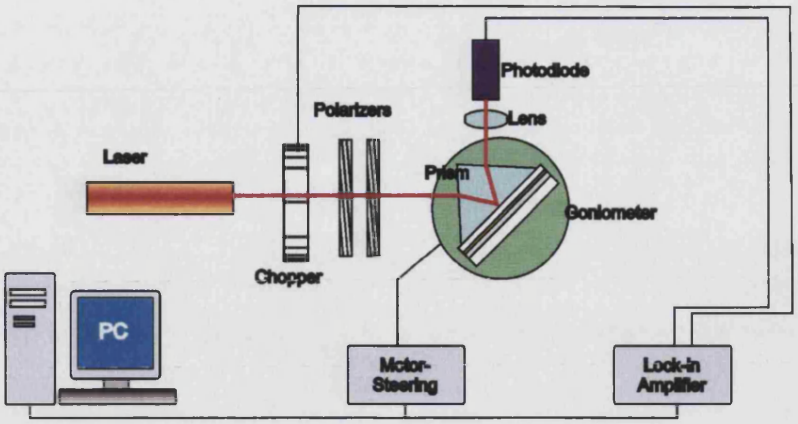

Figure 3.1 SPR experimental set-up. At the time the set-up was not adapted to an SPFS set-up.

When the incident light reaches the base plane of the prism (Schott, 90°, $LaSFN_9$) the light is reflected, focused by a lens (f=25mm, Ovis) and the intensity is monitored by the photodiode located at 45° of the prism.

The photodiode is connected to a lock-in amplifier to reduce the noise and the influence of daylight in the measurements. The lock-in amplifier filters out all frequency not modulated by the attached chopper (Amatek, U.K.) . When working in a lab environment (this was the case) multiple frequencies of 50 Hz should be avoided, since this is the frequency of electric ceiling lamps, for example. Upon my arrival to the project, the set-up was completely unprotected from working light, thus the lock-in amplifier was not producing its effect as it can be observed in Figure 3.2.

The sample holder is mounted onto a two-phase goniometer enabling angle dependent measurements. The goniometer is able to move 0.005° steps controlled by personal computer with a program developed by Scheller [138]. The sample holder is mounted onto two xy-tables and two tilting tables, which allow for the optimal adjustment of the set-up. This adjustment is described in detail in the alignment section.

The optical system is built on an optical table (Melles Griot) isolated from the bench with squash balls[1]. The laser light was allowed to move freely around the whole lab as the system was completely unshielded. A picture of the set-up is shown in Figure 3.2. The first set of experiments, until the experiments of biotinylated anti-antigoat/anti-goat

[1] When I arrived the system was isolated from the bench by four (4) completely smashed squash balls.

inclusive, was produced with the set-up in these conditions. At this point, the instrument was not able to produce measurements using florescence, as the necessary equipment was not set-up.

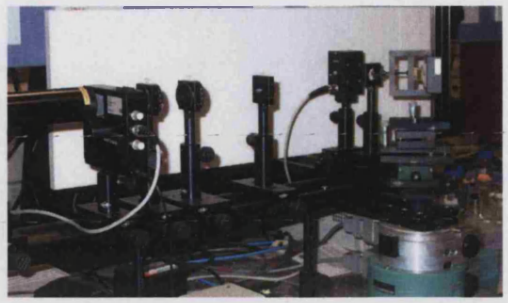

Figure 3.2 Picture showing the set-up immediately before starting the work at with it. The laser light was unshielded and allowed to be reflected freely in the lab.

Second period

After producing the first set of measurements with the set-up in these conditions, it was observed that the noise of the signal was very high. Results will be presented in section 4.1. It was necessary to optimise the system as well to understand where the noise was coming from.

The first measure taken, to optimise the system noise, was to isolate the system from any source of light. This decision was taken not only on the basis that the noise was coming from the light in the lab, but from the fact that it was necessary to protect the sample from the light, as fluorescence measurements were to be produced.

In order to isolate the set-up cardboard sheets, steel edges and black paint were bought. A hand made box was built in the lab and it was inserted on the top of the set-up. Holes were made on the top side of the box in order to facilitate the passage of the cables from the lock-in amplifier.

This box presented some problems, since it had no door and it did not block the light to pass through the edges. The sheets of cardboard were not able to seal the light from coming inside the box. In order to avoid these problems first, a door with hinges was screwed on the bottom of the box and duck tape was passed along the edges. This can be observed in Figure 3.3.

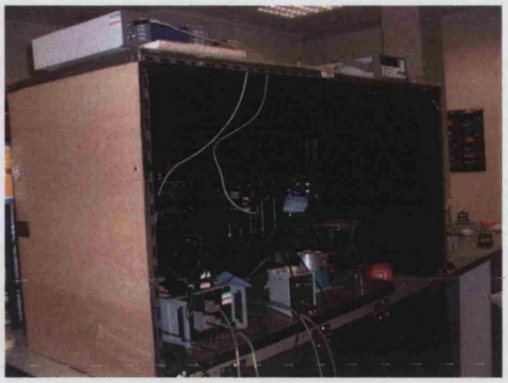

Figure 3.3 A picture of the experimental set-up protecting the laser light from travelling in the lab. With this protection, the set-up was ready to receive the PMT.

With this experimental set-up, the fluorescence unit was added the SPR system. A schematic representation of the final version is presented in Figure 3.4.

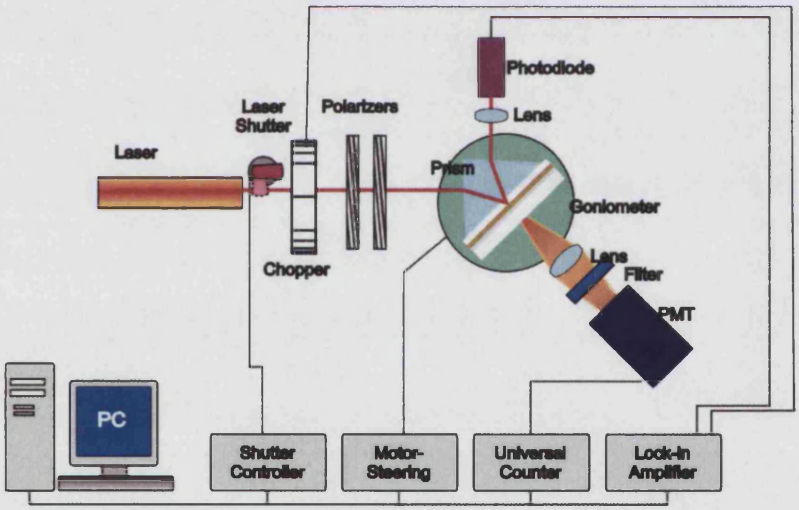

Figure 3.4 Surface plasmon fluorescence spectroscopy set-up. This set-up measures reflectivity and fluorescence intensity at the same time.

In order to measure fluorescence a photomultiplier tube (PMT) (Hamamatsu) was attached behind the sample holder and on an arm support. The PMT moved at the same rotation speed as the sample holder. The fluorescence was focused to the PMT by a collecting lens (f=50 mm, Ovis) position between the sample holder and the PMT. The first lens used had 25 mm diameter, but a 50 mm diameter lens substituted it in order to collect a larger quantity of fluorescence.

Max-Planck Institute engineers built a protection unit and a programmable switch box, around the PMT to avoid from light interference. The PMT was connected to a counter

(HP) to detect photons. A controlled shutter was also implemented on the set-up, just after the laser, in order to prevent fluorophores from photobleaching.

When the fluorescence unit was built, it was necessary to optimise the isolation of the set-up from light. At this time, the exiting door presented problems, for example, the lack of practicality and not being able to stop all the light to come through. These were the most critical problems. Therefore, a thick black curtain for photographic purposes was bought and substituted the door. All the light holes were covered with aluminium foil (from the outside and the inside of the box) and with black non-conductive tape from the inside.

The noise was still very high and a new He-Ne laser was bought from Uniphase. A considerable decrease in the signal to noise was observed when the laser was left over night.

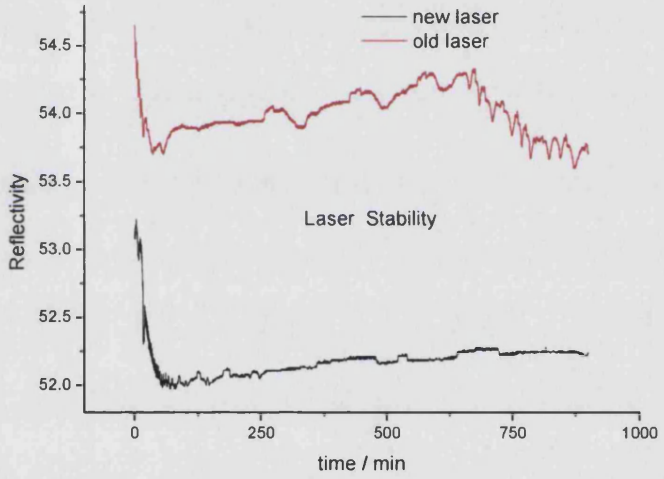

Figure 3.5 Comparison study of the stability of the two lasers used during this work.

However, the intensity of the reflected light signal was still showing some instability and it was observed that changes in temperature due to drafts in lab made by people passing through close to the instrument would influence the measurements. Therefore, the solution introduced by the curtain was considered not sufficient.

Faraday box – Final Achievement

The last project to produce the optimised box consisted, finally, on the construction of a Faraday box. A Faraday box isolates the set-up from all the external interferences, especially from light infiltration and temperature change, which of special relevance when a change in the refractive index is considered.

The aluminium box was built in the Mechanical Engineering workshop. A hole was made on the side for the cables, and the optical table was removed from the bench and set inside the box. While transferring the optical table it was observed that the table was seat on four squash balls in order to isolate the vibrations from the bench. However, the squash balls were completely burst and so the final isolation effect was not efficient. For better isolation conditions, the optical table was then sat on the top of twenty eight equally distributed squash balls. It was observed that the reflectivity signal showed a reduction on the noise level.

The final version of Faraday box is shown in Figure 3.6. The SPFS set-up is inside the box with all the control boxes, as for example, the lock-in amplifier, the motor steering controller, the PMT switch on/off controller and the photon counter located outside.

Figure 3.6 Faraday box with SPFS set-up inside. All the cables came out through a hole produced on the side and all the controlled boxes and instrumentation were located outside the set-up.

With this experimental set-up, fluorescence measurements were optimised. All the best results were produced using this experimental set-up.

3.1.2 Preparation and Optimization of the Flow Cell

In the beginning of this project, an earlier flow cell of quartz glass (Herasil, Schott) was used. This cell had two holes on the top. The schematic representation is presented on Figure 3.7.

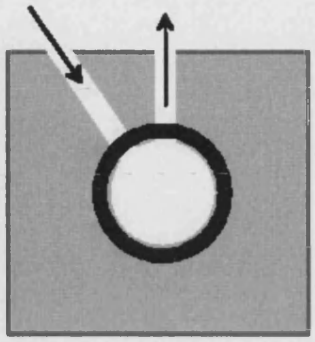

Figure 3.7 Earlier flow cell used for experiments. The inlet and the outlet are positioned on the same side and solutions were injected using an excess in volume with a syringe.

The solutions were injected through with a syringe and there were no connections for inlet and outlet, thus the solutions just went over the flow cell when filled. A larger volume than the necessary to fill the flow cell was used in order to assume that all previous solution was totally removed.

With the intention of avoiding the spillages of buffer solution that were corroding the goniometer mechanical system, a new flow cell was used based on the work produced by the Knoll group. A quartz flow cell supplied by the Max-Planck Institute (Germany) with a volume of 85 μL was employed. This flow cell has the inlet and the outlet located in opposite sides. A schematic representation of the flow cell used is presented in Figure 3.8. The flow cell was connected to a peristaltic pump (Rego Analog, Ismatec) by gluing two needles sections onto the two opposite holes and joining them with Tigon tubes with an inner diameter equal to 0.76 mm. At the end of the two bound tubes, two needles sections were inserted. For every experiment, the flow cell was washed thoroughly and then connected with two new Tigon tubes and two end needles, in order to avoid contamination.

The sample was contained in an eppendorf tube and two needle ends were inserted in the eppendorf for injection. A representation of the flowing system is presented in Figure 3.8. The circulating volume was approximately 400 μL of sample volume, with a circulation rate of 4 mL min^{-1} for optimised analyte delivery, minimising mass transport effects. The flow cell was placed onto a low fluorescent quartz slide (Herasil, Schott)

and sealed with two Viton O-rings. Introduction of analyte and buffer solutions was performed via the pump/flow system.

The gold-LaSFN$_9$ glass slide is placed onto the flow cell and finally a high refractive index prism (LaSFN$_9$, n=1.845) is mounted on the top of the glass sample. To allow optimal coupling of the incident light with the surface plasmons modes of the metal a thin film of refractive index matching oil was added between the two glass units. This fluid should have a similar refractive index as the prism and the glass sample with the purpose of optimising the coupling of the two wave vectors. On the other hand, the higher the refractive index of matching fluid the higher the vapour pressure thus the easier the fluid evaporates at room temperature. Therefore, for practical reasons, a less volatile index match liquid is frequently used with the drawback of a lower refractive index and non-optimal match.

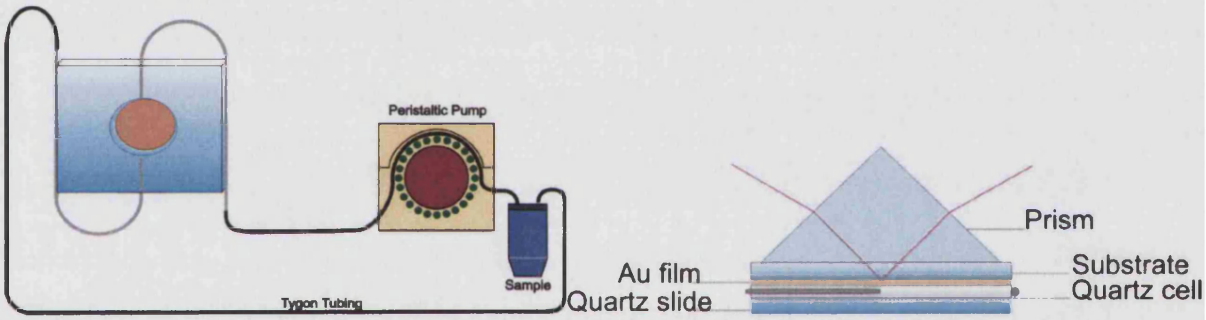

Figure 3.8 Schematic representation of the flow system associated with the flow cell. A peristaltic pump is used to deliver solutions and prevent mass transport binding effects.

3.1.3 Practical Alignment Instructions

Alignment of the set-up is one of the most important steps preceding any measurement. It is necessary to align the laser light with the centre of the flow cell. The spotlight during scanning measurements should not move from its position. The laser beam has to be aligned with the photodiode for SPR measurements and the colleted emitted fluorescence is necessary to be aligned with the PMT.

SPR Alignment

In order to align the system is necessary to setup two iris diaphragms (25 mm diameter, Ovis) one just immediately after the polarizer and another one set after the laser beam has been reflected from the sensor surface. These two apertures have to be regulated for the height at which the laser beam is being incident when the sample is not present.

Prior to insertion of the assembled flow cell in the sample holder, the detector motor is rotated to 180° and the height and orientation of the photodiode is adjusted based on the two iris diaphragms. Subsequently, the detector motor is moved back to 90° and the sample holder is inserted. According to the law of reflection, the sample motor moves to 45°. At this stage, a part of the incident light is back reflected into the iris setup after the polarizer and another part is passed through the other iris directly onto the photodiode.

During this alignment period, both diaphragms are closed, and just a very small intensity of laser passes through. If the laser light was not passing through the middle of the closed diaphragms, than the height of the sample holder was adjusted using the titling stages. The tilt stage that controls the height of the reflected light was adjusted prior to the tilt stage that controlled the height of the back reflected light. This back reflected tilt stage influences the height of both split beams, thus the back reflected light was adjusted later using the other tilting stage.

The beam spot of the incident light on the gold sample and the reflected light on the iris diaphragm located before the photodiode were maintained fixed when moving the sample motor and the detector motor by θ and 2θ, respectively. If movement of the beam spot was observed than xy stages mounted below the sample holder were adjusted in order to adjust the z direction and x direction represented in Figure 3.9. The z direction should be adjusted first, and when the beam spot is fixed the x direction should be adjusted in order to set the spot light in the middle of the flow cell.

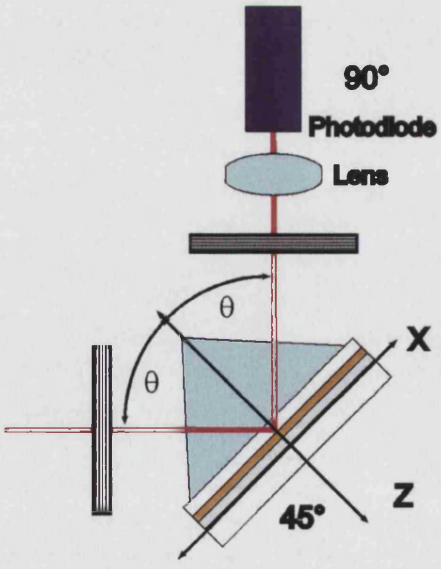

Figure 3.9 Schematic representation of the SPR alignment.

SPFS Alignment Considerations

Fluorescence measurements were produced simultaneously with reflectivity, therefore before any fluorescence measurement the set up was also align for SPR measurements followed by the alignment of the fluorescence experimental set-up.

In order to properly align the fluorescence set-up, the PMT was built on the top of a xy stages (relate coordinates with Figure 3.11), and it was also adapted a ring on the pin holder, in other to adjust the PMT as a function of the orientation angle.

The PMT (H6240-01, Hamamatsu) has low noise and a spectral response range of 185 up to 850 nm, and it has a specific linearity up to 2.5 Mcps (10^6 Counts Per Second). The PMT was built on a counting head that has leads connected with the outside photon counter controller. The PMT has an area where is highly sensitive, therefore, it is essential to align the focus point of the lens directly onto this area. The counting head and the PMT are depicted on Figure 3.10.

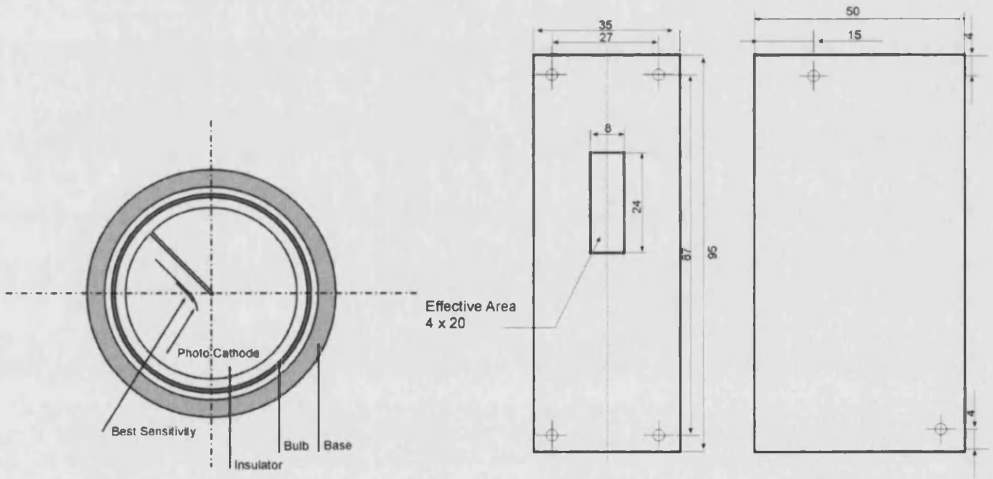

Figure 3.10 The PMT is located inside a counting head and only a very small area is actually effective for the fluorescence measurements, therefore is it crucial to align meticulously the PMT with focus point of the fluorescent collecting lens.

The fluorescence-collecting lens was positioned the closest to the flow cell as possible in order to gather the largest quantity of fluorescently emitted light. The height of the incident laser light was determined and the centre of the collecting lens was positioned at the same height. The distance of the sample holder to the lens was measured and PMT stage was positioned at the same distance after the lens.

The alignment of the fluorescence set-up was produced in iterative form, starting with the distance between the PMT tube and the collecting lens, followed by the height adjustment by the y translation stage and followed by the lateral adjustment using the x translation stage. Every time a new position was acquired, a measurement of fluorescence was taken. When a first optimum was obtained, the same procedure was repeated until it was not observed a large change in position.

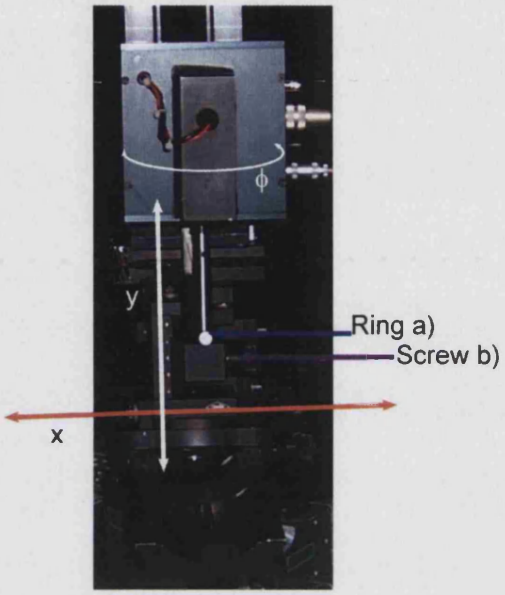

Figure 3.11 Picture of the PMT attached to the experimental set-up depicting the different degrees of freedom for alignment optimization.

Following the xyz position optimisation, a new iterative procedure was followed. A ring a) was adapted onto the pin holder and, when the screw b) was unscrewed, it would hold the PMT at the same height thus optimisation of the orientation angle ϕ was possible. The x and y translation stages were once more optimised after the optimised anlge ϕ was obtained. The procedure was repeated until no change in position or the maximum of fluorescence detection was not changed.

Alignment of the PMT was carried out every time a new set of experiments was produced.

3.1.4 Measurement Procedures

In this section, a detailed description of the measurement procedures used in this work is presented. The measurements are divided into: Scan curves and resonance kinetic measurements, fluorescence scan curves and kinetic fluorescence measurements.

Resonance Scan Curve

After alignment of the set-up with the flow-cell was inserted in the sample holder, a resonance spectrum was obtained by reflecting the polarised laser beam off the base plane of a prism and plotting the normalised reflected intensity versus the incident angle. The range of the angles measured is related with Snell's law and is important, since the resulting scan should cover both the total internal reflection edge and the resonant minimum.

The measurements produced in this work were carried out in water solution, so the resonant minimum is approximately at 57°. An example of the resonance scan obtained for the different measurements is represented in Figure 3.12. The adsorption of an additional layer, e.g., adsorption of streptavidin onto the biotinylated self-assembled monolayer on the gold surface, changes the optical properties of the dielectric next to the metal and results in a shift in the minimum of resonance and is depicted in Figure 3.12, as well.

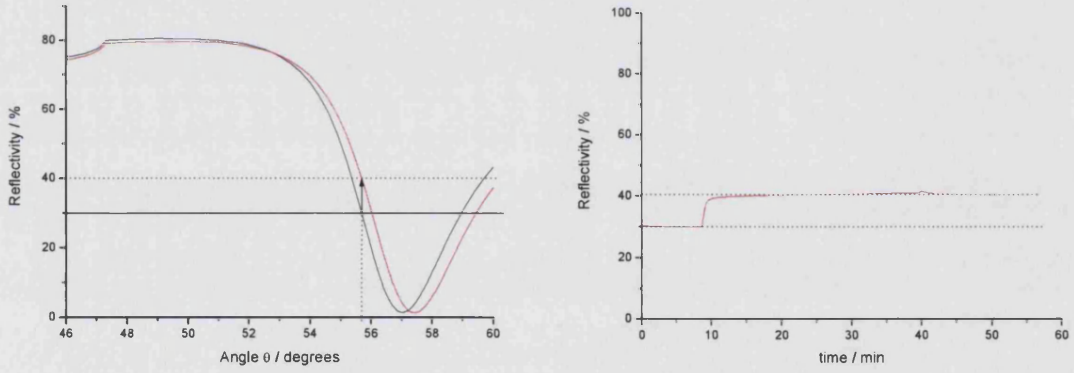

Figure 3.12 Scan curves and associated kinetics. Note that the reflectivity is increased if the incidence angle is fixed and the resonance curve is shifted due to adsorption of a new layer close to the metal surface.

Resonance Kinetic Measurements

Kinetic measurements were obtained by recording the change in the intensity of the reflected light during adsorption of a new layer. In order to obtain this measurement, a fixed angle position, normally around 30 % of reflectivity, was chosen.

The reflectivity at this fixed incidence angle increases if the resonance is shifted to higher angles and the detected shift represents a linear time dependence of the optical properties of the investigated system. It is assumed, as well, that the dependence of

the resonance minimum shift on optical changes is linear too. In addition, it is assumed that the shape of the scan curve in this region is not changed during adsorption of the new layer; otherwise, the linearity of the kinetic response curve would be lost.

After adsorption of a new layer, in all the systems studied in this work, a resonance curve was measured, except when stated otherwise. Figure 3.12 shows an example of the effect that a new layer added onto the surface produces on the intensity of the reflected light.

Scan Fluorescence Measurements

Fluorescence measurements were carried out when the sensor surface was built. Due to the low molecular weight, low concentrations and low surface mass layer density of the different analytes employed in this work, no change in the resonance minimum was observed therefore, fluorescence coupled with SPR technique was used in order to enhance the response signal and optimise the limit of detection.

Prior to adding the fluorescently labelled molecule, a scan was run to determine the background noise measured by the photomultiplier. Simultaneous measurement of the intensity of the reflected was carried out, as the software is able to move both goniometers in predefined steps and can collect data detected by the universal photon counter and by the lock-in amplifier.

At this point, the laser light is striking continuously on the sample, as there are no fluorescently labelled molecules present in solution. An example of the curves obtained is presented in Figure 3.13.

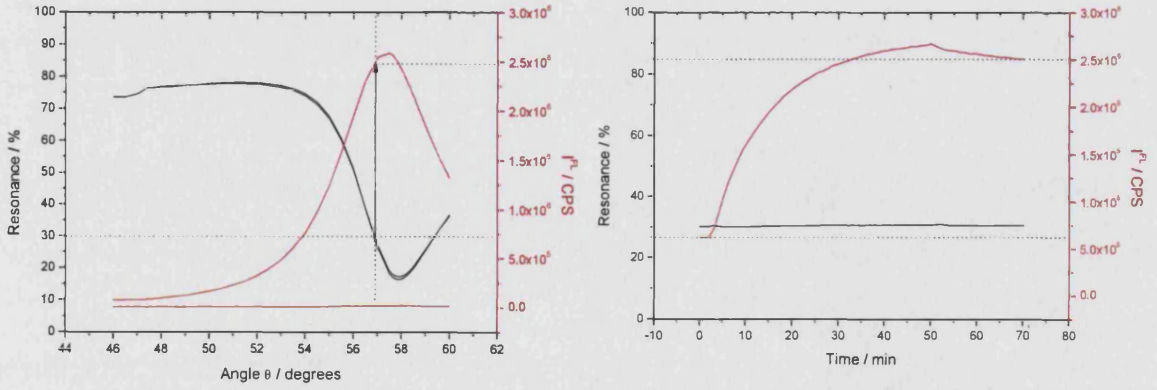

Figure 3.13 Scan curves and associated kinetics. Note that the reflectivity is increased if the incidence angle is fixed and the resonance curve is shifted due to adsorption of a new layer close to the metal surface.

Fluorescence Kinetics Measurements

In order to produce a fluorescence kinetic measurement, the angle at which the kinetics was followed was chosen, around 56°. At this angle the linearity of the reflectivity is found and no significant change in the reflectivity scan curve is observed. Therefore, the time dependence fluorescence measurement reflects changes in the signal under constant excitation conditions. It is important to guarantee these conditions since when large shifts are observed a deviation has to be considerer, the signal has to be compensated, because fluorescence signal is changed due to changes in the fluorescent peak [102].

When producing the fluorescence kinetic measurements it is assumed that filter effects and photobleaching do not influence the observed fluorescence signal. However, the measured intensity is not directly converted to the number of adsorbed fluorophores. A practical approach is rather complicated, since SPR is not sensitive enough to detect small molecular weight fluorescent dyes and a theoretical approach is rather difficult, as the problem should be described as statistics problem. Although, Ekgasit et al has proven that is possible to describe the fluorescence intensity in an SPFS curve in terms of the evanescent filed amplitude [110]. This approach is beyond our spectrum of study.

However, the difference between the observed fluorescence increase during adsorption of the fluorescently labelled molecule and the virtually unchanged reflectivity demonstrates the sensitivity enhancement of surface plasmon spectroscopy by the additional detection of SPFS. The enhancement of sensitivity may be observed in the example represented in Figure 3.13.

Measurement Sequence

The measurement sequence depends on the strategy adopted to sense the analyte, i.e. it also depends on what is being measured. However, the usual and most common procedure is described below:

1. Building sensing surface: The flow cell assembled with evaporated gold sample is filled with running buffer and the different layers necessary to produce the sensing surface are adsorbed. The adsorption of each layer is followed with SPR and after rinsing a scan curve is ran.
2. Fluorescence Measurements: Following the adsorption of the last layer (the sensing layer) the flow is washed with running buffer and a scan using SPFS is

measured. The background noise is determined and PMT alignment is evaluated. The fluorescently labelled molecule is adsorbed on the surface and simultaneous resonance and fluorescence kinetics measure the phenomenon.

3. After rinsing the excess of the fluorescently labelled molecule a simultaneous fluorescence and resonance scan curve is obtained.

For every sensing experiment this sequence is followed, if not otherwise it is referenced in the specific chapters.

3.2 Surface Modification Techniques

3.2.1 Substrate Preparation

The substrate used in this work was a high refractive index glass $LaSFN_9$ (Berliner glass). Previous to its used, the glass was thoroughly clean with a standard procedure. First the glass was sonicated for 15 minutes in a detergent (2 % Deconex) solution, and then rinsed extensively for 10 times with MiliQ water. This step was repeated twice. Subsequently, the substrates were sonicated for 10 minutes just in MiliQ water, in order to remove completely the detergent solution from the surface of the glass and from the container, and to avoid any contaminations. The final washing procedure was sonication for 15 minutes in Ethanol (Absolute Ethanol, Fisher Scientific) of the glass substrates. After cleaning, the glass substrates were dried in a nitrogen stream and placed immediately on the metal evaporation system (Edwards, Emitech K975X).

3.2.2 Metal evaporation

Gold 99.99% (Advent) was thermally evaporated directly onto the cleaned substrates using the evaporation equipment. The pressure of the system was brought down to $3x10^{-6}$ mbar. A current of 3 to 4 amps to heat and evaporate the gold was passed through a tungsten basket containing, approximately, 117 – 119 mg of gold. The optimised quantity of gold necessary to produce the most adequate metal thickness was obtained via experimental error.

While using this equipment, it was also observed that evaporation onto the gold slides was not homogenous, and extra careful should be given to the localisation of the glass substrates inside the evaporation unit, as the evaporation basket was not centred with the glass substrates holder.

Immediately after evaporation, the glass slides, now covered with a thin layer of gold, were carried to a furnace with a temperature of 450°C for 1 and 1/2 minutes, to smooth the surface. AFM images, presented in section 4.2.2 reveal high surface roughness. After removing the glass substrates from the furnace, they were cooled down to room temperature and inserted in a container with Argon atmosphere to avoid oxidation of the gold surface. The samples were then used within a week.

3.2.3 Self Assembled Monolayer

In order to produce the sensor surface for a biosensor, the proteins should be adsorbed maintaining their function and conformational organisation, as a protein is

only active if the quaternary and the tertiary structures are preserved. The environment where the protein is present should the most similar to its natural environment. The use of self assembled monolayers has the purpose to convert the rather hydrophobic metal layer into a more hydrophilic surfaces [82, 123, 125, 139].

Biotin-HPDP self assembled monolayer

The first procedure adopted to form a SAM, was followed as described in [140]. 1 mg of biotin-HPDP **1** (N-6-(biotinamido)-hexyl-3'-2'-pyridyldithio)propionamide) form Pierce was dissolved in 100 µl of N,N-dimethylformamide (DMF, Acros Organics). 5 µl of tri-n-butylphosphine (Sigma) was added and let to react for 5 min. It was observed that the reduced solution was yellow. This mixture was then added to 4 ml of water/methanol (1:1) solution. The solution obtained, was then directly injected in the primarily adopted flow cell (Figure 3.7) and the assembling on the surface was follow over night using surface plasmon resonance spectroscopy.

1

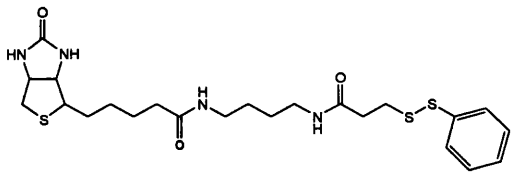

After reduction, the disulphide bond is broken and a mixture of 1:1 thiols is presumably obtained. Therefore, self-assembled monolayer is also established with a ratio of 1:1 of the different thiols. This strategy was immediately not continued as it was shown in [125, 126] that streptavidin has the binding pockets for biotin located in the interior of the molecule.

Synthesis of biotinylated-thiol directly on the surface

The second procedure adopted is described in [141]. The samples were immersed in 11-mercapto-1-undecanol (MUOH) **2** (Aldrich) 0.1mM and 16-mercapto-1-hexadecanoic acid (MHA) **3** (Aldrich) 0.9mM mixture solution overnight at room temperature. After formation of alkanethiols self-assembled monolayers, the samples were rinsed with ethanol and dried under a stream of nitrogen.

The mixed MUOH/MHA SAMs were immersed in a DMF solution of 0.1 M 1-ethyl-3-(3-dimethylaminopropyl)-carbodiimide (EDAC) (Sigma) and 0.2 M PFP (Aldrich) for 20 mins, rinsed with ethanol and dried under a stream of nitrogen. Afterwards, the slides were immersed in a solution of 10 mM 2,2'-(ethylenediooxyl)bis-(ethylamine) (DADOO) (Sigma) for 20 mins, rinsed with ethanol and dried under a stream of nitrogen.

And finally, the samples were immersed in a solution of D-biotin succinimidyl ester (5mg/ml in DMF) for 2h at room temperature. The samples were rinsed with ethanol, dried under a stream of nitrogen and stored in Argon at 4°C. The schematics of the synthesis procedure are shown in Figure 3.14.

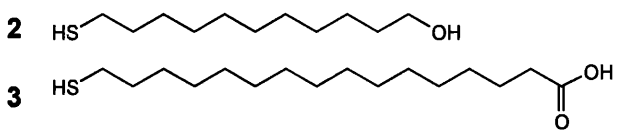

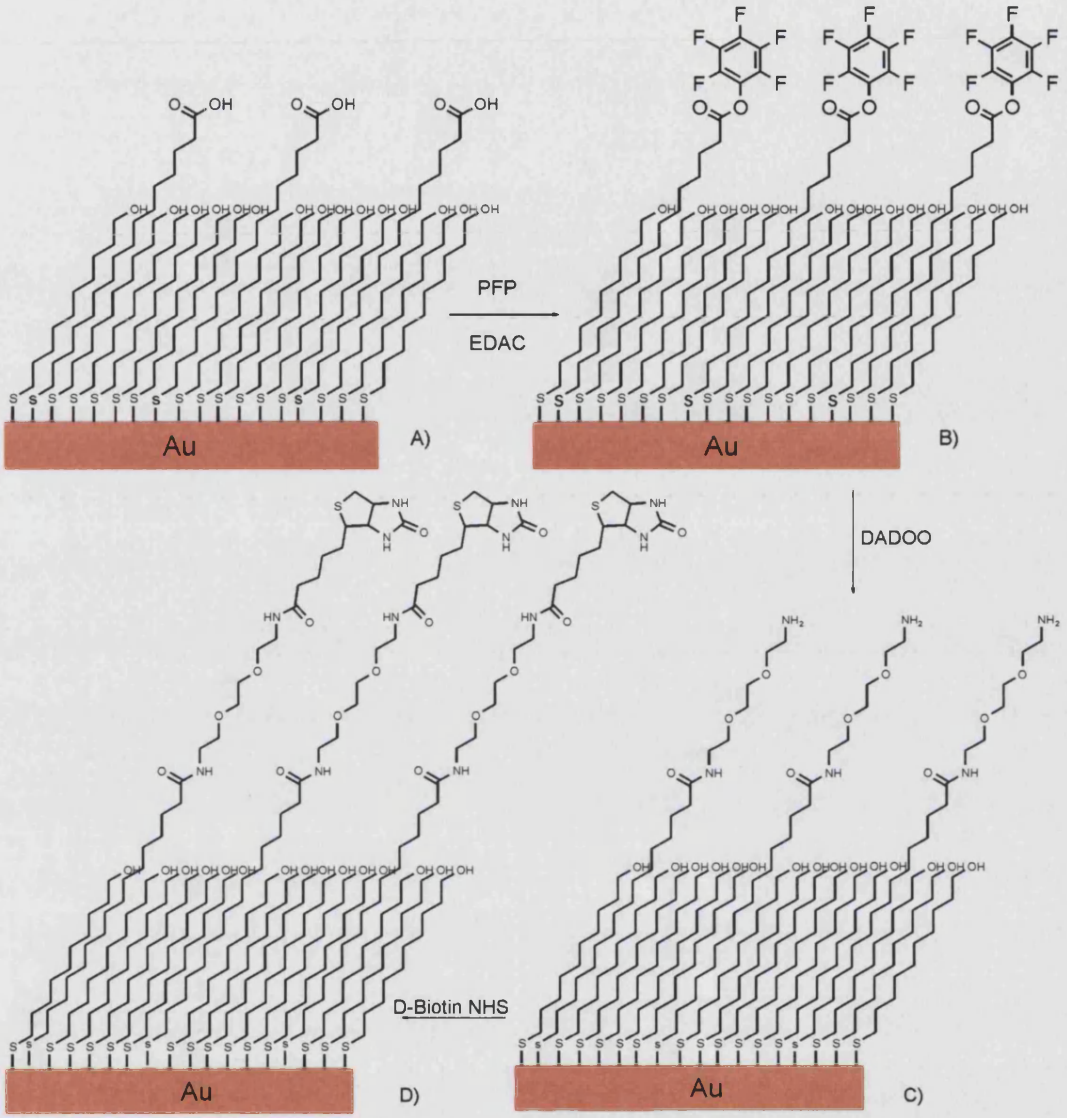

Figure 3.14 Schematic of the preparation of a biotinylated self-assembled monolayer. A) Mixed self-assembled monolayer of MUOH/MHA on gold; B) PFP-activated self-assembled monolayer prepared by coupling PFP to the carboxylic acid group of the mixed SAM in the presence of EDAC. C) DADOO-derived self-assembled monolayer by coupling DADOO to the PFP-activated self-assembled monolayer. D) d-Biotin-NHS ester – self-assembled monolayer prepared by coupling d-Biotin-NHS ester with the terminal group in the DADOO-derived self-assembled monolayer.

Information about the organic mechanism for the synthesis of the biotinylated thiol can be found in the Appendix IV.

Optimised Self-Assembled Monolayer

The third procedure adopted to produce the biotinylated self-assembled monolayer is based on the work developed by Häussling et al.[124, 139] **4** (1*H*-thieno[3,4-*d*]imidazole-4-pentanamide,hexahydro-*N*-[2-[2-[2-[(11-mercapto-1-oxoundecyl)amino]ethoxy]-ethoxy]ethyl]-2-oxo-,[3aS(3aa,4b,6aa)]) was custom synthesised at the Max-Planck-Institut für Polymerforschung (Germany).

4 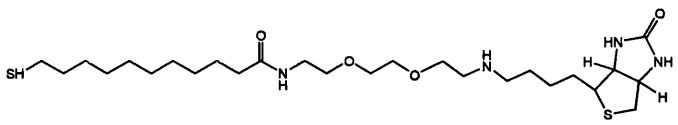

The gold evaporated slides were immersed in ethanolic solution containing the two thiol mixture, 11-mercapto-1-unadecanol spacer molecule **2** and a biotin-thiol **4**. The total thiol concentration was 0.5 10^{-3} mol L^{-1}. The mole fraction of the two thiols was varied systematically for one of the studies produced in the section 4.2. The thiol mixture was allowed to self-assemble on the gold film for >16 h, before rinsing with ethanol and drying under nitrogen. It is assumed that the mole fractions present in the SAM are roughly the same as in the prepared solutions [115, 135, 142, 143].

3.3 Preparation of Protein Solutions for hCG Experiments

All protein solutions were prepared with phosphate buffer saline (PBS) (Tablets, Sigma) with 0.005%(v/v) Tween 20 (polyoxyethylene(20)sorbitan monolaurate, polysorbate 20) (Sigma) and 0.01% (w/v) NaN_3 (Sigma) pH 7.4. This buffer will be referred to as PBSTA in the text.

3.3.1 Streptavidin

Solutions of 500 10^{-9} mol L^{-1} of streptavidin (Sigma) were prepared and injected on the biotinylated sensor surface to prepare the sensor for adsorption for other proteins.

3.3.2 Biotinylation and Fluorescently Labelling of Antibodies

Anti-α-hCG and anti-β-hCG antibodies were supplied by Unipath Ltd. Antibodies starting solutions were passed through pre-equilibrated Sephadex 10 columns (Fisher Scientific) with sodium carbonate buffer (SCB) solution pH 9.3 (Na_2CO_3 and $NaHCO_3$, Fisher Scientific). Absorbance of antibody recovered solutions was measured using UV-Vis (Thermal) and starting concentration was determined (E^{280nm}=1.4).

In order to biotinylate antibodies, biotinamidocaproate N-Hydroxysuccinimide Ester (Sigma) was dissolved in 30 μL of DMSO (Fisher Scientific) and 470 μL of SCB solution to obtain 10 mg mL^{-1} solution. On the other hand, Alexa Fluor® 647 (Invitrogen) was dissolved in 100 μL of DMSO to obtain a final concentration of 10 mg mL^{-1} in other to label the different antibodies. For each antibody a solution, a ratio of 1 antibody to 10 biotin molecules, was prepared and stirred for 30 minutes. The excess of biotin and the excess of Alexa Fluor® 647 were removed using Microcon® Centrifugal Filter Units (Millipore).

After each centrifugation, 500 μL of PBSTA buffer was added and solution was spun down again. This procedure was repeated three times for each solution of antibody. Once finished, 500 μL of PBSTA were added and the filter device was shaken gently for labelled-antibody total recovery. The final labelled-antibody solution, now in PBSTA, was diluted 1:10 for absorbance measurements and determination of antibody solutions concentration.

3.3.3 Determination of the Degree of Labelling (DoL)

The relative efficiency of a labelling reaction was determined by measuring the absorbance of the protein at 280 nm and the absorbance of the dye at its absorbance

maximum (λmax=647 nm). The Beer-Lambert law was used to calculate the approximate number of dye molecules per protein molecule though a correction needs to be made for the absorbance of the dye at 280 nm. For Alexa Fluor® 647 the correction factor(CF) is 0.3 [144].

To determine the concentration of the protein in mg mL-1 the following equation was used

$$A_{protein} = A_{280nm} - A_{647nm} \times CF \tag{3.1}$$

$$CF = \frac{A_{280nm} AlexaFluor647}{A_{647nm} AlexaFluor647} \tag{3.2}$$

Where $A_{protein}$ is the corrected value of absorbance, A_{280nm} and A_{647nm} are the absorbance of the measured protein-labelled solution at 280 nm and 647 nm, respectively, and CF is the correction factor that relates the absorbance of free Alexa Fluor® 647 at 280nm and 647 nm.

After determining the correct concentration of protein at 280 nm, the DoL was calculated using the following equation

$$DoL = \frac{A_{\max} \times MW}{[protein] \times \varepsilon_{AlexaFlor647}} \tag{3.3}$$

Where MW is the molecular weight of Alexa Fluor® 647 and $\varepsilon_{AlexaFluor647}$ is the extinction coefficient of Alexa Fluor® 647 at its absorbance maximum and $[protein]$ the protein concentration in mg mL-1.

3.3.4 Human Chorionic Gonadotrophin Solutions

Human chorionic gonadotrophin (hGC) was supplied by Unipath Ltd. The protein was extracted from pregnant women's urine. The protein was tested and found negative for HIV I & II types antigens, hepatitis B surface antigen and hepatitis C antibodies.

The supplied protein was tested to determine its activity using the radial immunodiffusion assay vs the 1st international reference preparation for hCG quantisation. The hCG used in this work was determined to have 11243 IU mg^{-1}. The protein concentration was determined by dried weight. An International Unit is an internationally accepted amount of a certain substance.

The supplied hCG was diluted to 10 000 IU mL^{-1} with PBSTA buffer and aliquot in 1 mL vials for storage in the freezer. Every time a new aliquot was used it was allowed to defrost slowly and once stirred vigorously previous to use.

In order to determine the kinetic rate constants and equilibrium constants for hCG interacting with its antibody, hCG was fluorescently labelled using the procedure described in the previous section.

4 Surface Plasmon Fluorescence Measurements of hCG

In this chapter, a detailed description of the characterisation and optimisation of the sensing surface is presented, supported by SPR measurements. Results on the determination of the limit of detection of the optimised surfaces using SPFS are presented. The binding constants with the corresponding rate constants have been determined for the different sensing surfaces and are presented.

4.1 Preliminary Measurements Using Surface Plasmon Resonance Spectroscopy

In order to produce a highly active active and reproducible sensor surface for subsequent SPFS studies, SPR measurements of commercially available proteins – antibody systems were performed. The system chosen was the goat IgG (Sigma-Aldrich, UK) analyte binding to a biontinylated anti-goat IgG (Sigma-Aldrich, UK) sensing surface. Biotinylated protein was dissolved in PBS to produce a 6.7 μM solution and was adsorbed onto a non-optimised SAM-streptavidin supramolecular architecture surface. Figure 4.1 shows a schematic of the non-optimised streptavidin – antibody layer used in this preliminary investigation. The ability to follow binding of this pre-biotinylated protein confirmed that the streptavidin adsorbed on the SAM was active and that it was possible to measure the binding of a biotinylated antibody. Moreover, measurement of the binding of the antigen in this case goat IgG, allowed us to conclude that it was possible to measure protein – antibody interactions, with the home made SPR. Results of the scanning curve and of the binding kinetics are presented in Figure 4.1.

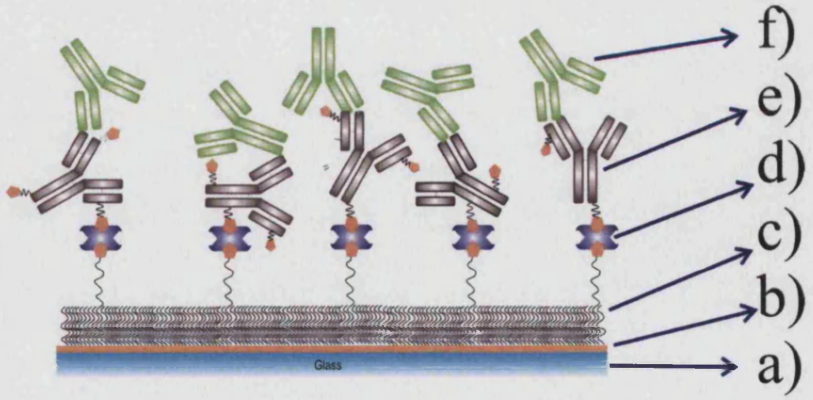

Figure 4.1 Schematic representation of the anti-goat IgG surface sensor for detection goat IgG. . a) LaFSN9 glass; b) 50 nm gold; c) non-optimised SAM using EDAC and PFP surface chemistry for biotinylated thiol synthesis; d) Streptavidin; e) biotinylated anti-goat IgG; f) goat IgG.

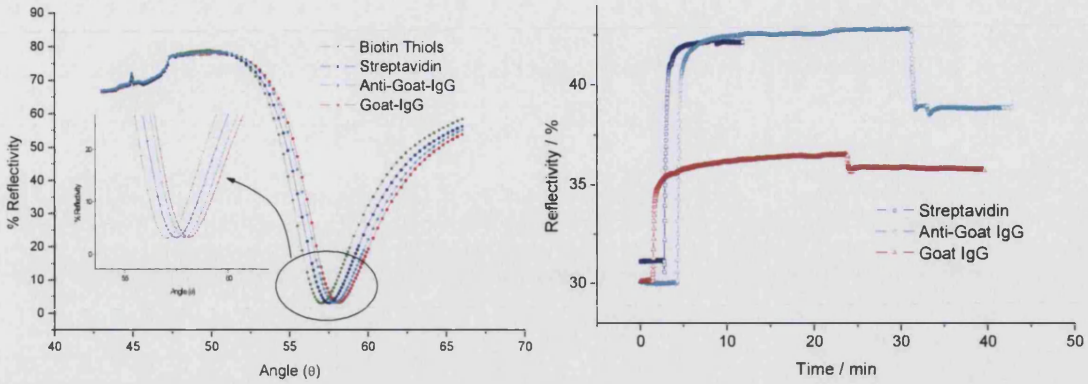

Figure 4.2 Scan and binding kinetics of a standard protein system using streptavidin binding to biotinylated anti-goat IgG that binds specifically to goat IgG.

In surface plasmon resonance spectroscopy the shift of the resonance minimum is proportional to the layer optical thickness, as mentioned in section 2.2, and presented in equation (2.29).

$$\Delta\theta \approx \Delta n \times \Delta d \tag{2.29}$$

Providing the refractive index of a homogenous adsorbed layer is known, the geometrical thickness can be determined, and vice versa. By using the computer program Winspall developed by Scheller [138], the scan curve can be fitted using an iterative procedure based on the Fresnel equations and thus the refractive index and the geometrical thickness can be estimated.

However, the Fresnel model was principally developed to study thin, close packed optically homogenous films. Adsorbed protein layers are generally less homogenous and as a consequence the Fresnel model is not always appropriate for quantifying protein adsorption, hence an empirical relationship between the shift of the resonance minimum shift $\Delta\theta$ and the adsorbed mass density has been estabilished. This is based on the work of Yu et al [145]:

$$A = \frac{\Delta\theta}{0.1868^{o}} (ng\ mm^{-2}) \tag{4.1}$$

The the results obtained for the binding of Goat IgG onto a capture Anti-goat IgG surface are presented in Table 4-1.

Table 4-1 Preliminary results of a standard system for SPR spectroscopy.

Protein layer	$\Delta\theta$ (°)	Stoichiometric mole ratio / adsorbed streptavidin	A ng mm^{-2}
Streptavidin	0.475°	1	2.54
Anti-goat IgG	0.45 °	0.38	2.41
Goat IgG	0.2 °	0.16	1.07

It is important to mention that these results were produced using a non-optimised SPR system, i.e., the flow system was not implemented and the set-up was still in the as detailed in section 3.1.1 – First period. The set-up was not protected from light and external factors and the solutions were injected and left to stabilise without recirculation and no surfactant was used in the buffer solution. In these conditions, non-specific adsorption proteins are more likely to occur.

From these preliminary results, it was found that the streptavidin that adsorbed onto the mixed SAM was active, although the SAM employed was not optimised. The adsorption of a biotinylated antibody and antigen could be observed using SPR spectroscopy.

4.2 Supramolecular Sensor Surface Optimisation

4.2.1 Optimisation of surface

In order to measure binding interactions between protein and antibodies using SPR/SPFS the well characterised hCG immunoassay was chosen as a model system. This immunoassay is characterised by the interaction of two immunoglobulins (antibodies) to the same antigen, in this case hCG.

As mentioned in chapter 1, hCG is a protein that consists of two different molecular sub-units, an α-subunit and a β-subunit, and monoclonal antibodies specific to these two different regions of the protein are commercially available and therefore were used in this project.

A sensor surface was developed using the well characterised supramolecular structure of biotin-Self Assembled Monolayer (SAM)-streptavidin system [146], with the optimised thiols (Figure 4.3), and an adsorbed randomly biotinylated hCG monoclonal antibodies layer in order to detect hCG. Depicted on Figure 4.4 is the strategy used.

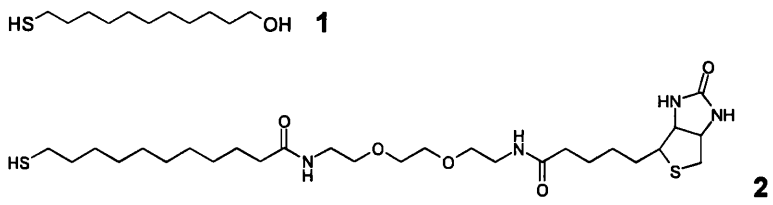

Figure 4.3 Molecular structures of the OH-terminated thiol 1 and biotin-EG-C11 thiol 2 used to prepare the mixed SAM on the gold film capable of binding streptavidin monolayer and prevent from non-specific binding due to hydrophilic surface.

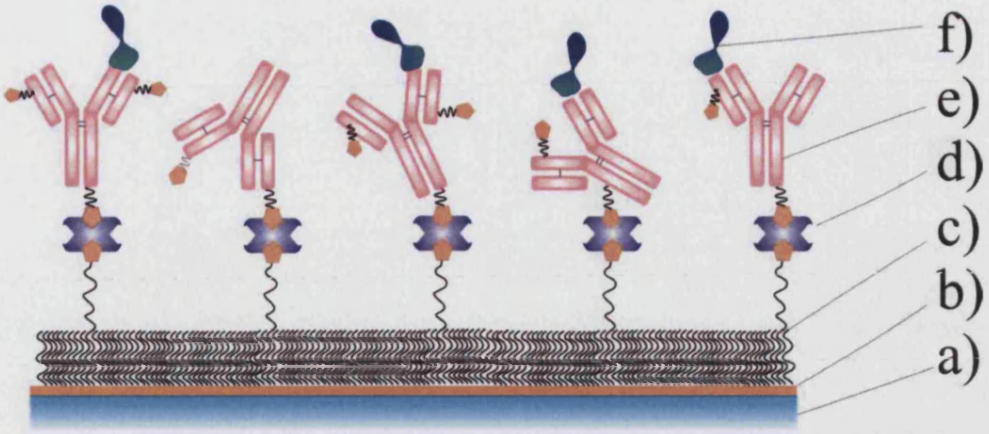

Figure 4.4 Sensor surface architecture with randomly biotinylated antibodies for detection of hCG using SPR. a) LaFSN9 glass; b) 50 nm gold; c) binary mixed thiol SAM; d) Streptavidin; e) randomly biotinylated antibodies; f) hCG.

Optimisation of biotinylated capture antibody

The hCG antibodies used in this work were randomly biontinylated using the methodology described in section 3.3.2. However, it is important to mention that the first adopted purification method to purify the biotinylated antibodies solutions was using PD 10 size exclusion columns. When the collected purified solution from these columns was injected onto the streptavidin surface a very small change in the resonance shift was observed.

Therefore, a new post biotinylation purification strategy, using ultrafiltration with Microcon® spin filters (Millipore) was implemented enabling the complete separation of the excess of biotin label and was used in the following experiments. In Figure 4.5 is presented the comparison between the purified biotinylated antibody solutions, using PD10 columns and using ultrafiltration.

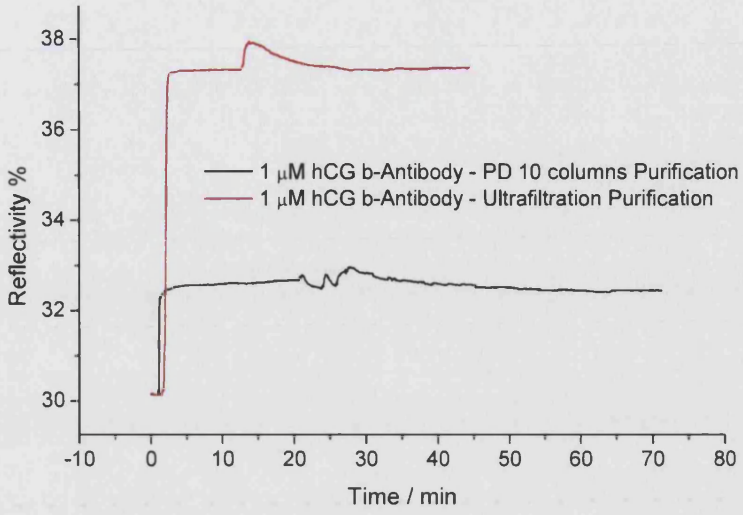

Figure 4.5 Adsorption of randomly biotinylated antibodies onto the streptavidin layer. The antibodies were purified using different processes. Black line purified using PD 10 columns and red line purified using ultrafiltration.

From the scan curves measured after rinsing of both surfaces, it was observed a resonance shift of 0.125° for the PD-10 purified solution of biotinylated antibody and 0.375° which corresponds to 2 ng mm^{-2} for the spin filtered proteins, corresponding to a three times higher binding efficiency. These values are in the same order of magnitude as the work reported by Scheneider et al [147] of 3.52 ng mm^{-2}, where biotinylated randomly orientated 3H-Mab-A94 antibodies bound to avidin-coated SiO_2 were used.

These results suggested that PD 10 columns were not efficient for separating biotin reagent from antibodies, and therefore we can assume that the remaining biotin label was still present in the collected solution. The low molecular weight, free biotin label (with a high diffusion coefficient) competed for the streptavidin binding pockets thus impeding the binding of biotinylated antibody.

The streptavidin layer was tested for non-specific binding of the hCG antibodies onto the surface. Solutions of non-biotinylated antibody in PBS and in PBS containing 0.005% of non-ionic surfactant, Tween 20 were prepared. Tween 20 has been used previously in protein buffer solutions in order to prevent from non-specific binding [148].

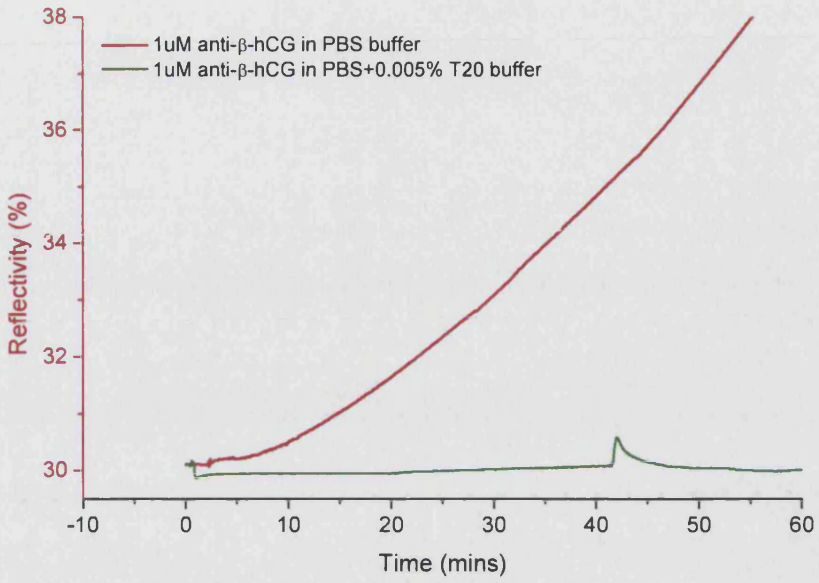

Figure 4.6 Binding of anti-β-hCG onto the streptavidin layer. Comparison between buffers solutions with and without the presence of Tween 20 in solution.

In Figure 4.6 are presented the results of the adsorption of non-biotinylated antibody solutions with and without the presence of a surfactant that prevents from non-specific binding. It can be observed that the buffer solution containing 0.005% of Tween 20 prevented the non-specific adsorption of non-biotinylated antibody. Hence, all the subsequent experiments were performed using buffer solutions prepared with 0.005% of Tween 20.

Optimisation of SAM for hCG binding

In order to maximise the sensitivity of the sensor surface, the first experiment performed was to study how changes in the composition of the binary SAM would affect binding of hCG onto the layer of capture antibodies immobilised on the streptavidin-SAM matrix.

This experiment was carried out using SPR only, with a relatively high concentration of 286 IU $ml^{-1}$of hCG, in order to observe binding. From the former work of Knoll it was assumed that one biotinylated antibody will bind to one streptavidin molecule on the mixed biotin-thiol/OH-thiol SAM [146]. Therefore, variations in the biotin-thiol concentration on the surface allow for control of surface streptavidin density and consequently control of surface capture antibody density.

Antibodies are large proteins and are affected by inter-protein steric hindrance. Therefore, the optimum sensor surface in terms of antigen mass density may not necessarily correspond to the maximum surface density of the immobilised capture antibody. Moreover, since biotin labeling can take place on different lysine residues, not all antibodies will be optimised in terms of having their antigen binding site orientation away from the surface. Figure 4.4 illustrates how steric hindrance might affect the efficiency of antigen binding.

A systematic study was carried out, varying the concentration of the biotin thiol moiety **2** and the lateral OH thiol spacer **1** in a binary mixed SAM. Structures are presented in Figure 4.3. The following mole fractions of biotin-thiol **2** were used: χ = 0.002, 0.005, 0.01, 0.05, 0.1. The mole fraction in the thiol solution will correlate with surface mole fraction, as both molecules have a C11 alkyl chain tether [120, 135]. In this work b-anti-β-hCG was chosen to form the capture antibody layer because it has higher affinity towards hCG than anti-α-hCG, this detail will be discussed later in the chapter.

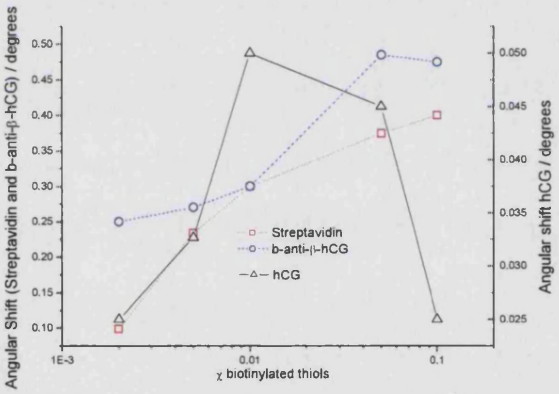

Figure 4.7 Correlation between mole fraction of biotin thiol in SAM forming solution to SPR angular shift for streptavidin and b-anti-β-hCG (left hand axis) and hCG (right hand axis). 63% of the available antibodies bound to hCG with χ=0.01.

The left hand axis of Figure 4.7 is represented the angular shift of streptavidin and b-anti-β-hCG as the concentration of biotin-thiol on the mixed SAM increases from χ = 0.002 up to χ = 0.1. It can be observed that both streptavidin and b-anti-β-hCG increased with mole fraction of biotin-thiol, although b-anti-β-hCG attachment levels off at 0.1 biotin-thiol mole fraction. This is in agreement with previous work [149, 150] which showed that the maximum streptavidin mass density is obtained for a χ=0.1.

In Figure 4.7 the right hand axis shows the angular shift for hCG binding to the surface bound b-anti-β-hCG for the various mole fractions of biotin-thiol. The binding of hCG to the surface bound b-anti-β-hCG does not show the same pattern of streptavidin and b-anti-β-hCG. It can be observed that maximum angular shift, which corresponds to maximum hCG binding, is achieved for a mole fraction of biotin-thiol at χ = 0.01 (1 mol %). At mole fractions of 0.05 or greater, even though there is more surface bound antibody, hCG binding is lower. A possible explanation is that binding of antigen is affected by steric hindrance effects of the surface bound antibodies.

In the results presented here, for a χ=0.01, a mass density of b-anti-β-hCG of approximately 1.58 x10^{-9} g mm^{-2} was calculated from the SPR angular minimum shift, however a higher degree of hCG / antibody binding was achieved, with a calculated 63 % of antibodies binding to an hCG antigen.

These results can be considered in the context of the work by Schneider[147]. It was found that a maximum level of antigen binding was obtained for a surface concentration of antibodies calculated to be 3.52 ng mm^{-2}, which equated to 28 % of the available antibodies binding to a hCG antigen.

It can be noted that when capture antibody concentration was increased, with a biotin-thiol mole fraction of χ = 0.05, a higher mass density (2.63 x10^{-9} g mm^{-2}) of antibody was obtained but a lower total hCG surface density was achieved. Thus, a significantly lower hCG / capture antibody ratio binding was determined, with only ca. 34% of the antibodies bound to hCG. This illustrates the importance of steric effects on reducing the effectiveness of antigen binding on to the antibody capture layer due to overcrowding of the sensor surface.

4.2.2 AFM Images

AFM measurements were made to image the lateral spacing of proteins on the surface. Measurements were made on a Nanoscope III Atomic Force Microscope by Dr. Holger Schönherr, Twente University, Netherlands.

Glass slides for AFM with a pre-evaporated gold layer were annealed with a hydrogen flame and immersed onto a solution containing a mixture of 1:99 biotin/OH-thiol. The thiols were left to self assemble for 16 hours. Figure 4.8 shows the effect of annealing

on decreasing the gold roughness. In figure 1.7b the triangular terraces characteristic of an annealed gold can be observed.

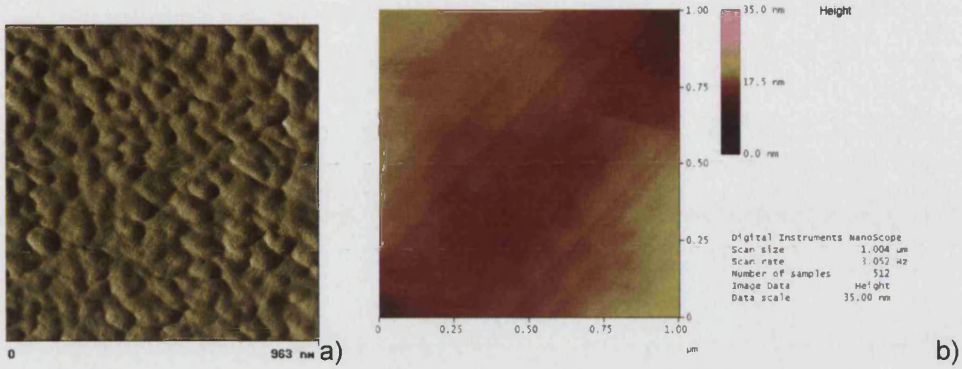

Figure 4.8 Comparison between evaporated gold surface a) after 1.5 min in 450°C b) after anneling with an hydrogen flame. Measurements made in air and in contact mode.

Therefore, the image in Figure 4.8 (a) is representative of the gold used in standard SPR / SPFS measurements detailed in this thesis. However, in order to observe adsorbed protein by AFM, it was necessary to use the annealed gold.

To produce AFM measurements on the different protein layers and to follow their formation, different slides with the different steps, were produced. One slide with the SAM only was made, and two others were immersed on a streptavidin solution. After 30 minutes one of the streptavidin coated slides was immersed in a biotinylated antibody solution for 30 minutes, for adsorption of the antibodies onto the streptavidin layer. All the slides were kept under MilliQ water during AFM measurements. Measurements of the adsorbed protein were made in Tapping mode. The images obtained are presented in Figure 4.9.

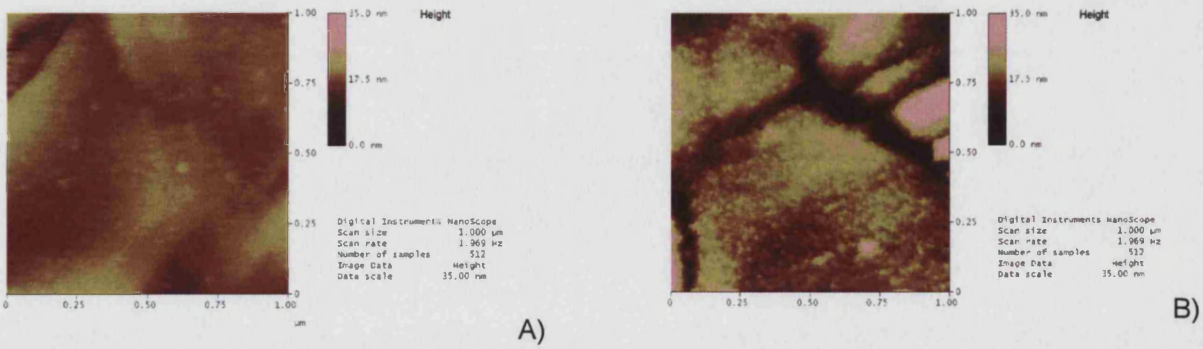

Figure 4.9 AFM pictures of the three steps to produce the sensor surface. A) Streptavidin layer in tapping mode; C) b-anti-β -hCG in tapping mode.

It can be observed from Figure 4.9 that the different layers are distinguished between each other. It can be observed in Figure 4.9 that there is a visible difference between the layer of streptavidin and the layer of antibody. In order to detect with more evidence a zoomed scan was performed in both layers and is presented in Figure 4.10.

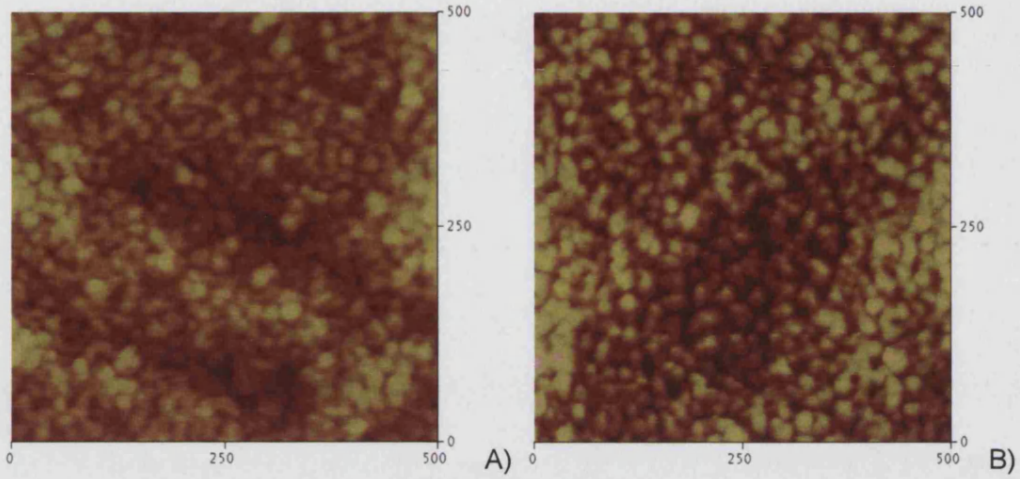

Figure 4.10 A) Streptavidin layer in tapping mode; B) b-anti-β-hCG in tapping mode. Scale in micrographs are in nm.

The roughness of each surface was calculated. For the annealed gold surface a rougness (the parameter determined was the image root mean square) obtained was 0.544 nm, for streptavidin 0.75 nm and for antibody layer 1.073 nm. Unfortunately, it was not possible to obtain an image of a single streptavidin or of an antibody. But the increase of roughness from one layer to the other indirectly indicates the process of streptavidin and antibody immobilisation on the surface.

4.3 Measurement of Dose Response of hCG on a Randomly Organised Capture Antibody Layer

4.3.1 SPFS: Sensor Surface Considerations

SPR uses an evanescent wave phenomenon to detect changes in the refractive index of the surface medium. SPR has been used in a variety of applications, especially in biosensing, and has been shown to be applicable to a wide range of molecules [151, 152]. The details of this technique have been described in chapter 2.

The label-free nature of SPR, considered to be an advantage, limits its ultimate sensitivity. This is particularly the case when detecting the binding of small molecules, e.g. DNA, or looking at very low binding density of larger molecules, since SPR effectively measures changes in mass density at the surface.

This problem is illustrated by attempts to measure the direct binding interactions of low molecular weight molecules, where alternative methods such as equilibrium analysis and competitive assays have had to be adopted [153-155]. Competitive binding assays are discussed in more detail in Chapter 5. Indirect optical immunosensors using the field enhancement phenomenon, like SPFS, provide a method to overcome many of the limitations of the direct sensors and offer attractive routes to improving sensitivity [103, 130, 156, 157].

As has been described in chapter 2, SPFS uses the strong evanescent optical field, produced by optical resonance of surface plasmons, to excite fluorophores located at or near to the metal-dielectric liquid interface, resulting in a strong fluorescence signal. The evanescence field increases in intensity as the maximum resonance condition of the surface plasmons is reached at θ_{res}. The field intensity is enhanced by as much as 16x on gold and 50x on silver when excited by laser light (λ=633 nm) [102].

The evanescent field decays exponentially in the dielectric medium with a penetrating depth of approximately L_z = 150 nm, depending on the wavelength of the excitation light (Appendix II). If a fluorescent dye is present at the interface it can be excited by the electromagnetic field and an intense fluorescence signal can be measured. Hence both fluorescence and the reflected light intensity signal could be measured simultaneously. Recently, Liebermann and Knoll [103] described a set-up for SPFS

capable of measuring both changes in the refractive index and fluorescence emission simultaneously. It was shown to be able to detect DNA hybridization and antibody-antibody interactions [103, 104, 150].

A reproducible and methodical application of SPFS has been implemented to measure binding interactions between hCG and its antibodies, using the well-studied biotin-SAM-streptavidin supramolecular structured surface to minimise steric hindrance effects and to optimise limit of detection. hCG was adsorbed onto one specific antibody sensing surface and detected with a fluorescently labelled complementary antibody. The strategy is depicted on Figure 4.11 and the typical response of both scan and kinetic measurement using SPFS is presented in Figure 3.12 in chapter 3.

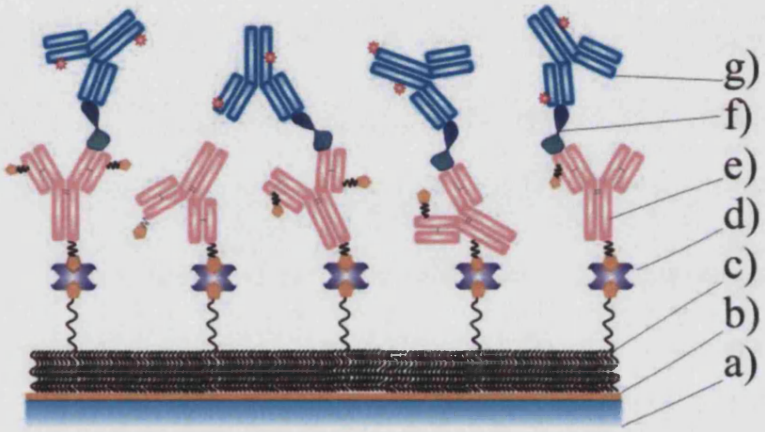

Figure 4.11 Schematic representation of immunoassays used in this work. Formation of different layers was followed by SPR and binding of fluorescently labelled antibody was followed by SPFS. Sensor surface using randomly biotinylated antibody. An attempt to illustrate steric hindrance effects on the sensor surface;. a) LaFSN9 glass; b) 50 nm gold; c) binary mixed thiol SAM; d) Streptavidin; e) randomly biotinylated hCG antibody; f) hCG; g) fluorescently labelled antibody.

An earlier attempt to sense hCG in serum using the phenomenon of fluorescence emission due to presence of an evanescent wave formed on a silver substrate was previously described by Attridge [158]. A sensitivity lower than 80 mIU ml^{-1} hCG was determined (protein with different activity of ca. 8400 IU mg^{-1}), which is above the range of clinical interest. However, neither surface structure studies of capture antibody surface orientation, nor distance control of fluorophore to metal surface was performed.

One difficulty with performing fluorescence measurements close to a gold surface is that gold is an efficient fluorescence quencher, via Fluorescence Resonance Energy Transfer (FRET). Since FRET is a distance related phenomenon, it is critical to design a sensor surface that provides sufficient spatial separation between the quencher, the

gold film, and the fluorophore. Experimentally, it has been determined that this distance requires to be at least 20 nm [101]. Such a distance can be achieved by a number of surface modification strategies.

In this work, the well characterised biotin-SAM-streptavidin system was employed [146]. This strategy allows the control, not only of fluorophore distance from the surface in the Z direction but also control of capture antibody density on the surface, in the X-Y plane. The employment of the biotin-SAM-streptavidin matrix, and further separation by bound hCG and capture antibody represents a total distance of the fluorescently tagged antibody from the gold surface of approximately ~ 20 nm (thiols and streptavidin thickness ca. 1 nm and ca. 4 nm respectively [146]; antibody vertical height is ca. 12 nm [159]; X-ray crystallographic measurements of hCG molecular diameter was estimated at 4 nm [6], (Protein Data Bank code 1HCN)). Approximate calculations and assumptions about protein orientation on the surface were made.

4.3.2 Detection of Non-Specific Binding

In this section of work, two sensing surfaces were studied, one with randomly b-anti-α-hCG and another one with randomly b-anti-β-hCG. Both surfaces were tested for non-specific binding of the fluorescently labelled antibodies onto the biotinylated antibody sensing surface in the absence of protein antigen hCG. AF-anti-α-hCG was tested on the sensing surface assembled with b-anti-β -hCG and AF-anti-β-hCG was tested on the surface structured with b-anti-α -hCG.

In Figure 4.12 shows an example for the test of non-specific binding of AF-anti-α-hCG onto the a sensing surface structured with b-anti-β -hCG.

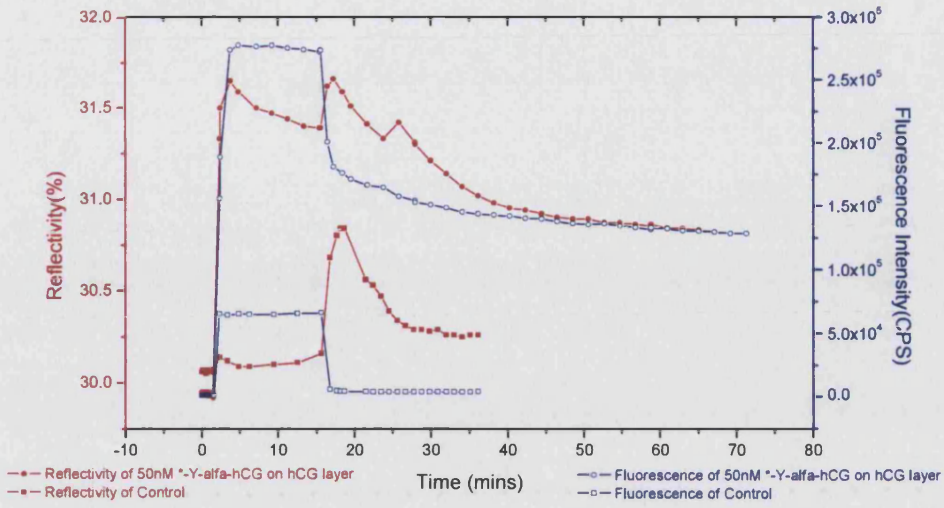

Figure 4.12 Testing for non-specific binding of AF-anti-α-hCG onto the sensing surface without the presence of hCG. The surface was rinsed at 15 minutes.

It can be observed in Figure 4.12 that when hCG has been pre-adsorbed the fluorescence signal increases considerably when the solution of AF-anti-α-hCG is injected over the surface (as expected). During the washing of the surface with buffer (at 15 min.) the signal decreases gradually, as there is desorption of AF-anti-α-hCG from hCG. When hCG is not present on the surface, the fluorescence intensity increase is considerably smaller. The small increase in fluorescence is due to the fluorophores that come close to the surface and are excited by the evanescent wave tail of the excited electromagnetic field. When the surface is washed with fresh buffer there is an abrupt decrease of the fluorescence signal, as fluorophores are no longer present in solution.

The non-specific binding of AF-anti-α-hCG on the sensor surface was initially tested by measuring the fluorescence signal after injection of fluorescently labelled antibody prior to addition of hCG. The signal obtained of approximately 8 $x10^4$ Counts per Second (CPS) was considered to be the background signal at 0 IU ml^{-1} hCG. No non-specific binding was found since fluorescence intensity dropped back to its original value after rinsing with running buffer. Hence, this fluorescence background was used as a base line relative to which all other changes in the fluorescence signal were determined; this was termed the absolute intensity of fluorescence I^{FL}.

4.3.3 Determination of the Best Regeneration Buffer

Prior to production of the immunosensor to detect hCG using SPFS, another aspect of the sensor design was studied: the regeneration of the sensing surface. Regeneration is the process of removing all the bound analyte, in this case hCG from the sensing surface, while maintaining the activity of the ligand, in this case the biotinylated antibody. An efficient regeneration buffer implies that the sensor surface may be reused for many analysis cycles.

Two regeneration buffers were tested on the surface. It is important to observe what type of response is given by the SPR reflectivity signal. If after each regeneration the reflectivity signal becomes lower than the starting point then the regeneration conditions are too harsh for the system. On the other hand, if the reflectivity signal starts to increase then regeneration conditions are too mild and the analyte accumulates on the surface.

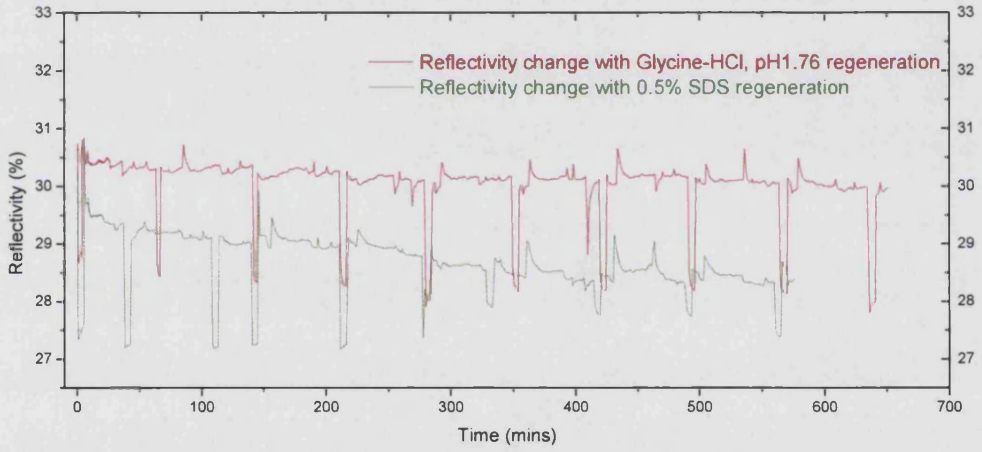

Figure 4.13 Reflectivity intensity change through consecutive regeneration cycles using Glycine-HCl and 0.5% SDS regeneration buffer.

In Figure 4.13 it can be observe that 0.5% SDS regeneration buffer is too harsh for the surface as the reflectivity signal decreases as consecutive regeneration cycles are carried out. Therefore, Glycine-HCl pH 1.76 was chosen as the regeneration buffer. With this buffer the reflectivity signal was stable for a longer period of time, allowing constant activity of the antibodies bound on the surface and complete removal of hCG.

4.3.4 Comparison of Biotinylated Capture Antibodies: anti-α -hCG vs.anti-β -hCG

With the sensor surface now optimised, the dose response for hCG in the b-anti-α-hCG / hCG / AF-anti-β-hCG and b-anti-β-hCG / hCG / AF-anti-α-hCG sandwich assays were studied using SPFS. In order to determine the dose response of the

optimised sensor surface, the χ=0.01 biotin-thiol SAM was prepared in two glass slides, as described previously. Streptavidin was adsorbed on the surfaces and, in one slide b-anti-α-hCG was immobilised and on the other slide b-anti-β-hCG was immobilised. Both capture antibodies surfaces have low density but maximum binding capacity of the antigen as explained in section 4.2.1. Experiments were repeated two times.

The effects of mass transport on the rate and degree of hCG binding on this system were minimised by using high flow rates of ~ 4 mL min^{-1} and working on a planar surface. On dextran chips, such as the system described by Yu et al [114] where AF-RaM (Alexa Fluor Rabbit anti-Mouse IgG) binding to mouse IgG was studied, a very high capture antibody density was achieved on the 3 dimensional surface. However antibody orientation could not be controlled and diffusion of antigen to antibodies buried in the dextran capture matrix affected the response, since the capture surface became effectively non-uniform.

Various known standard concentrations of hCG in a range of 0-10 IU mL^{-1} were injected cyclically and allowed to bind for 30 minutes, followed by rinsing. A sensor surface with b-anti-α-hCG adsorbed onto the streptavidin was used to adsorb different concentrations hCG. Different concentrations of hCG were detected using a solution of AF-anti-β-hCG of 50 x 10^{-9} mol L^{-1}. The increase in fluorescence signal as the labelled antibody bindind to hCG was followed for 10 minutes. Subsequently, the surface was rinsed with running buffer and then regenerated with 10 mM glycine pH 1.76.

Regeneration of the surface removed both hCG and AF-anti-β-hCG, but retained the b-anti-α-hCG capture surface, which was used for further measurements. All measurements for a specific hCG concentration were repeated twice and found to be reproducible. A typical fluorescence – hCG concentration response is shown in Figure 4.14.

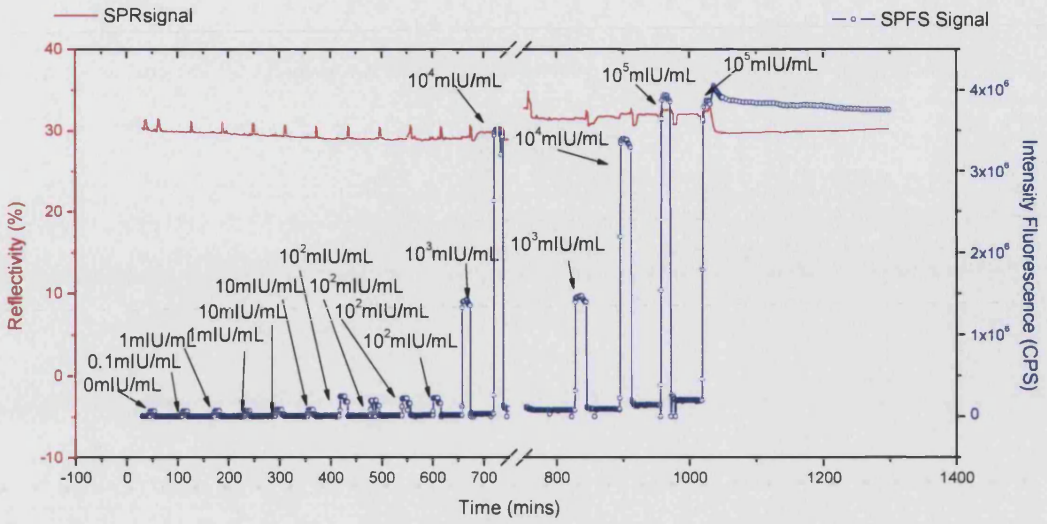

Figure 4.14 Determination of hCG dose response by cyclical injection of hCG followed by addition of 50 $x10^{-9}$ mol L^{-1} AF-anti-β-hCG. Left hand y-axis is the reflectivity change and the right hand y-axis the fluorescence signal change. Numbers in graph refer to concentration of titrated hCG in mIU mL^{-1}.

The SPR response, read on the left hand y-axis, shows small changes in signal in all range of concentrations due to changes in temperature, flow or refractive index of the solution. On the other hand, large changes in fluorescence signal, read on the right hand y-axis, due to changes in the hCG concentration were observed as the concentration of hCG increased following binding of the fluorescently labelled secondary antibody.

The background noise, considered to be the fluorescence intensity value obtained for an hCG concentration of 0 mIU mL^{-1}, was removed from all fluorescence data points, and designated the absolute fluorescence intensity (Abs I^{FL}). After removing the background, the last value of fluorescence counts obtained for each concentration was considered and statistical analysis performed. The statistics analysis results obtained were plotted versus the hCG concentration and the dose response for a the immnoassay of b-anti-α-hCG / hCG / AF-anti-β-hCG was obtained and is presented in Figure 4.15.

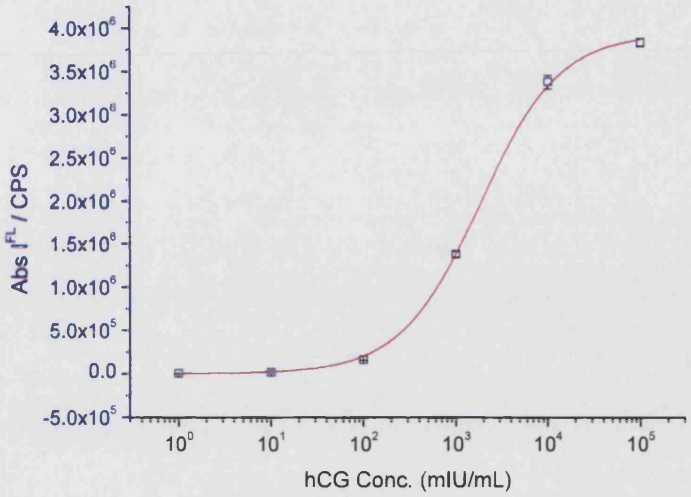

Figure 4.15 Dose response obtained for the sandwich assay of b-anti-α-hCG / hCG / AF-anti-β-hCG.

The data points were fitted with the Levenberg-Marquardt nonlinear least squares algorithm to the Langmuir adsorption curve. As a result an estimation of the desorption constant K_D was obtained. More considerations will be carried out in section 4.5.

The same procedure was followed for the other glass slide prepared with a sensor surface with randomly b-anti-β-hCG. Solutions with various known standard concentrations of hCG in the same range of concentrations used previously were injected cyclically and allowed to bind for 30 minutes, followed by rinsing. Following each hCG concentration adsorption, this time, a solution of AF-anti-α-hCG of 50 x 10^{-9} mol L^{-1} was injected. The increase in fluorescence signal was follow for 10 minutes and the surface was regenerated using the same regeneration buffer. The sensorgram obtained for b-anti-β-hCG/hCG/ AF-anti-α-hCG is presented in Figure 4.16.

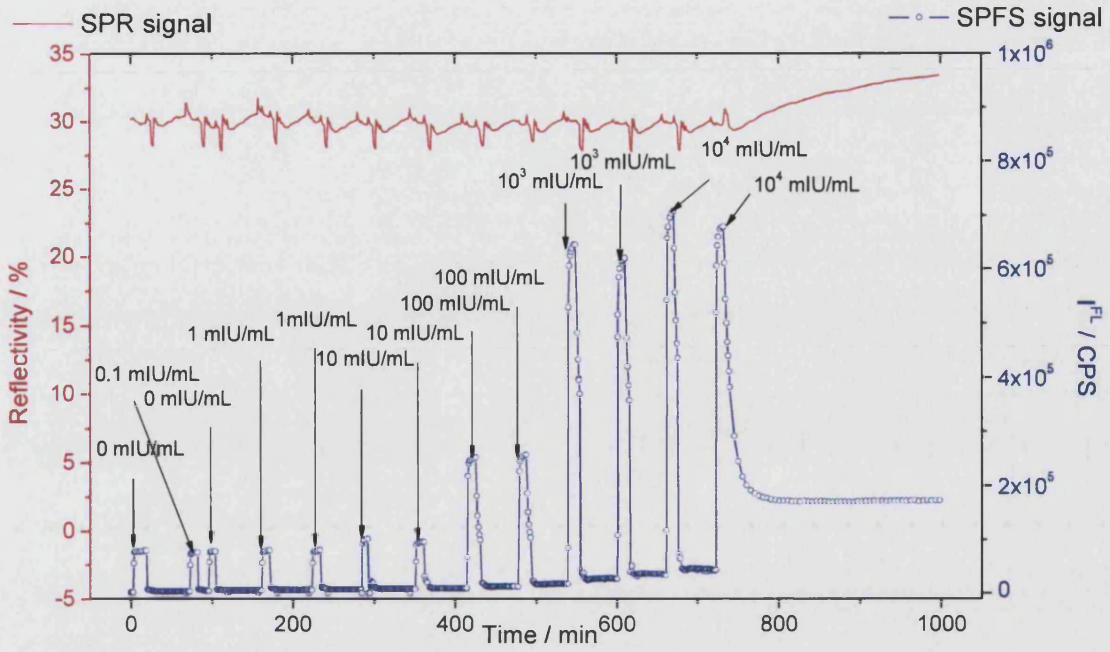

Figure 4.16 Sensorgram obtained for b-anti-β-hCG/hCG/ AF-anti-α-hCG. In the last concentration desorption was let to carry out for longer period of time in order to determine the desorption rate constant.

The same data treatment employed in the previous sensorgram for the sensing surface using b-anti-α-hCG / hCG / AF-anti-β-hCG was carried out. In Figure 4.17 is presented the calibration curve in which the absolute fluorescence intensity changes as a function of hCG concentration.

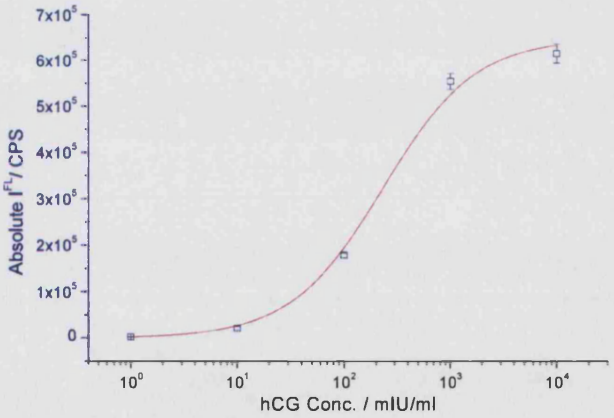

Figure 4.17 Dose-response curve for determination of hCG using the system with b-anti-β-hCG and detection with AF-anti-α-hCG. The red line in main graph is a Langmuir isotherm fit.

The data points were fitted Langmuir adsorption curve following the procedure described above and an estimation of the desorption constant K_D was also obtained.

In order to determine which capture antibody was the best, a comparison between the two systems was carried out by considering the desorption curves of the two different sensing surfaces. The fluorescence signal obtained in each case was normalised for the maximum intensity in order to compare the two systems.

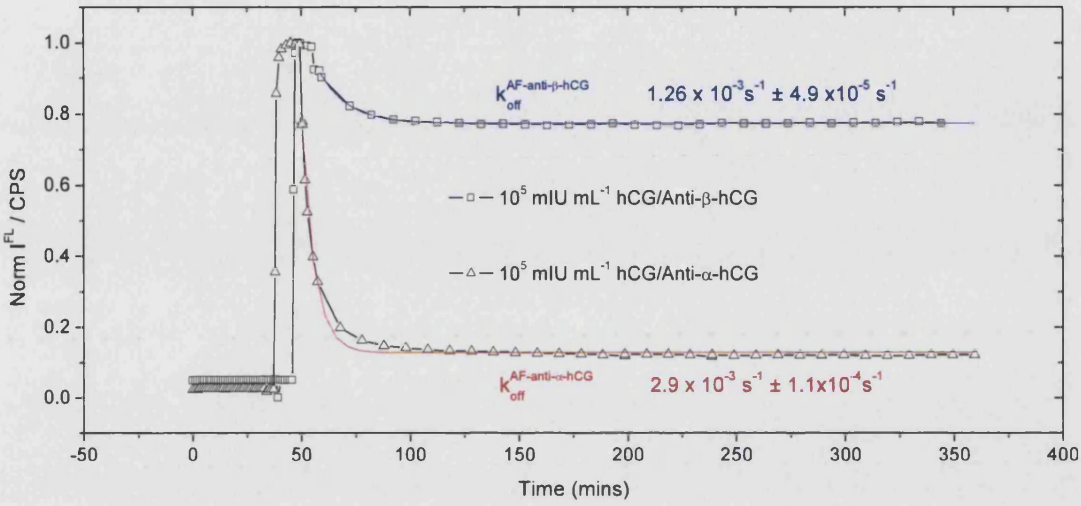

Figure 4.18 Normalised fluorescence intensity measurements of the fluorescently labelled antibodies desorption for the two sandwich immunoassays.

From Figure 4.18 it can be observe that AF-anti-α-hCG desorbs faster than AF-anti-β-hCG. One explanation to this could be related to the differences in size of the desorbing antibody or the antibody-antigen conjugate. The antibody-antigen conjugate will have a larger size than the single antibody and therefore a smaller diffusion coefficient (from the Stokes-Einstein equation [136]). When the system is rinsed either just the single antibody desorbs or the antibody-antigen conjugate will desorb. This effect depends on the relative magnitude of the dissociation constant. Since the dissociation constant for anti-α-hCG is larger than the anti-β-hCG (*vida infra*) it can be concluded that when the capture antibody is anti-α-hCG the anti-β-hCG-antigen conjugate is more likely to desorb as a single unit with a lower diffusion coefficient than the single antibody.

The desorption curves were fitted to the equation (2.61) and the desorption rate constants k_{off} were determined. Although of the same order of magnitude AF-anti-β-hCG k_{off} is three times smaller than AF-anti-α-hCG k_{off} (1.26×10^{-3} s^{-1} < 2.9×10^{-3} s^{-1}). Therefore, it was concluded that b-anti-β-hCG / hCG / AF-anti-α-hCG was a better system as b-anti-β-hCG would form a more stable hCG layer.

The dose response curve obtained for the b-anti-β-hCG / hCG / AF-anti-α-hCG was used to determine the sensitivity and the limit of detection of this system. A signal from a concentration of hCG as low as 1 mIU mL^{-1} (2.2 $x10^{-12}$ mol L^{-1}) was resolved, thus illustrating the measurement sensitivity of the SPFS technique on this sensor surface [160].

4.3.5 Sensitivity and Limit of Detection

This sensitivity is approximately two orders of magnitude greater (80 mIU mL-1) than that found by the pioneering work of Attridge in 1991 [158]. This sensitivity is 1 order of magnitude greater than the work produced by Chetcuti et al. (10 mIU mL^{-1}) where an indirect electrochemical immunosensor measured horseradish peroxidase conjugated to a second hCG antibody activity [161]. The sensitivity determined in the work developed by Dostálek et al for detection of hCG using a SPR biosensor based on an integrated optical waveguide [12] was the same as in the work by Chetcuti et al.. Schneider et al was obtained a sensitivity of 10 mIU mL^{-1} using an optical chip based on the Hartman interferometer [162], but using human whole blood samples. However, Schneider et al obtained for the same technique but using human serum samples a sensitivity of 1.6 mIU mL^{-1} [147]. And Zhang et al using a piezoelectric quartz immunosensor were able to resolve a concentration of 2.5 mIU mL^{-1} [163].

In order to determine the LoD, the IUPAC methodology was employed where is defined as being: the concentration of analyte corresponding to the average fluorescence value of the baseline measurement added to three times the standard deviation. Hence, the linearity of the dose response presented in figure was taken into account.

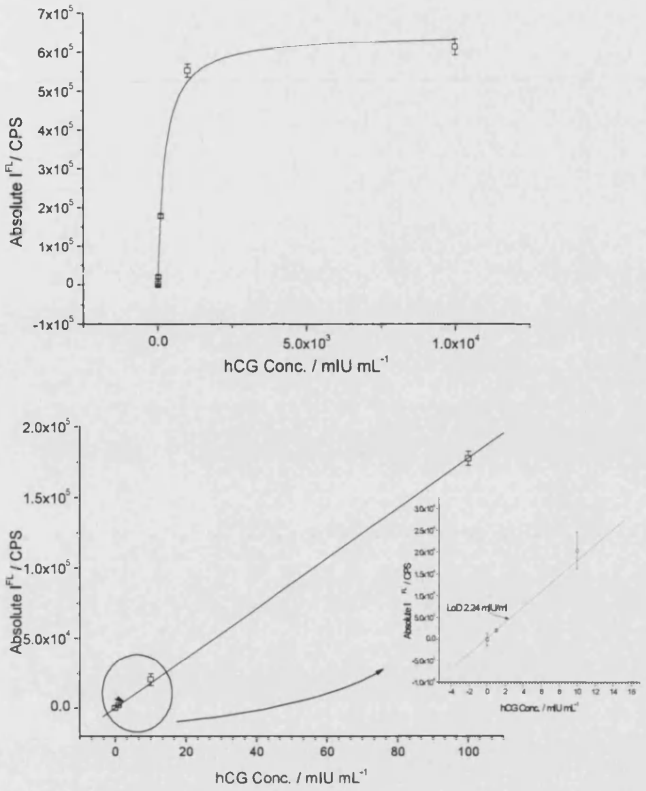

Figure 4.19 Langmuir adsorption curve for b-anti-β-hCG /hCG/AF-anti-α-hCG system. Linearity is obtained in hCG concentration range of 0 to 100 mIU mL^{-1}.

Linearity was assumed between 0 and 100 mIU mL^{-1} hCG. The standard deviation obtained for the mean of the two measurements for 0 mIU mL^{-1} hCG gave the limit of detection which was found to be 2 mIU mL^{-1} (4.5×10^{-12} mol L^{-1}) and is demonstrated in the inset graphic of the linear relationship at low hCG concentrations. This value is lower than the clinical relevant range of hCG detection which is 5 – 25 mIU mL^{-1} as described in section 1.1.1 [147]. This level of detection is already well below the threshold of 25 mIU mL^{-1} of hCG in serum considered necessary for a reliable pregnancy diagnosis [161].

4.4 Further optimisation of sensor surface: Utilisation of biotinylated Fab fragments for hCG sensing

Studies by Spinke et al [82] have shown that steric hindrance, among other factors, limits the sensitivity of antibody sensor surfaces. From the initial study described above, it can also be observed that by reducing the number of binding sites on a planar surface it is possible to minimise access effects. As a consequence, in the immunoassay configuration with low binding capcity, a protein bound to the capture antibody will not influence the binding of neighbouring capturing antibodies binding sites.

In order to improve ultimate sensor sensitivity Fab fragments (fragment with the antigen binding site) mono-biotinylated in the hinge region were immobilised on the SAM-streptavidin matrix. The biotinylated Fab-hCG fragment ensured that the hCG antigen binding site was optimally oriented away from the surface minimising problems of structuring of the hCG layer and reduced the steric hindrance effects on binding of the labelled antibody. Figure 4.20 illustrates the new sensor system where the Fab fragments replace the randomly organised antibody layer.

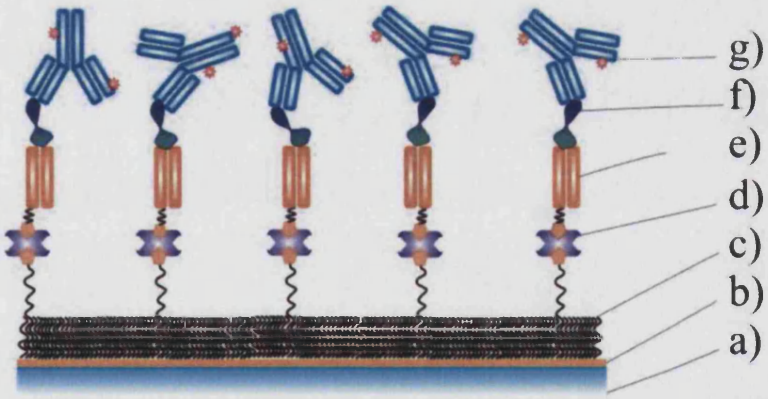

Figure 4.20 Sensor surface using Fab-hCG mono-biotinylated fragment. A more oriented and organised surface is obtained. A) LaFSN9 glass; b) 50 nm gold; c) binary mixed thiol SAM; d) Streptavidin; e) Fab-hCG mono-biotinylated in the hinge region to allow orientation of binding site on the surface; f) hCG; g) fluorescently labelled antibody.

However, it is important to know which hCG epitope Fab fragment binds to, in order to determine which fluorescently labelled antibody has the antigen available for binding. The genetically modified Fab with biotin on the hinge region binds specifically to the C-terminal region of hCG. The structure of hCG was reported by Berger et al. [8] and is shown in Figure 4.20. In order to optimise hCG detection the fluorescently labelled antibody AF-anti-β-hCG was used.

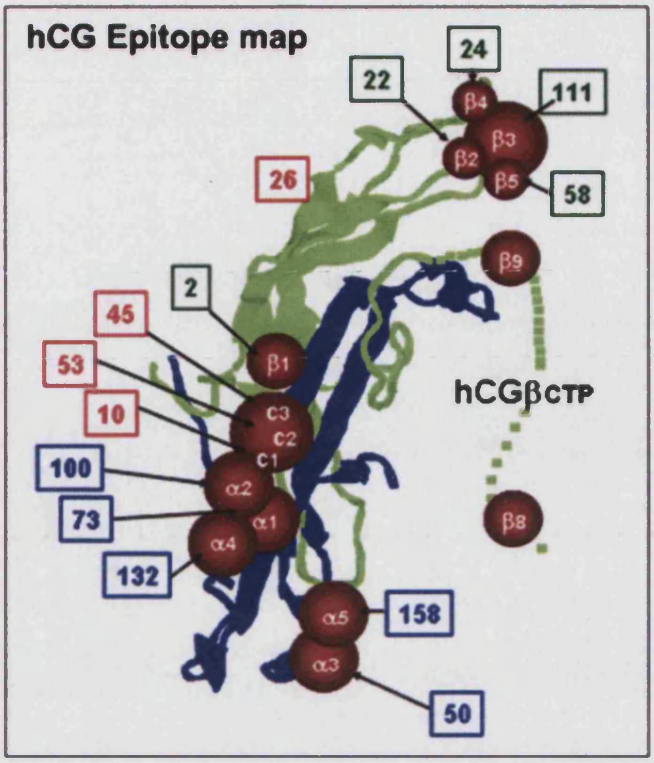

Figure 4.21 HCG epitope map with the α region in blue and the β region in green. The C-terminal region of the hCG is located where the epitopes C1-C3 are depicted.

Figure 4.21 shows that the β region is located further away from the C-terminal region than the α region for AF-anti-α-hCG. Therefore, when the Fab-hCG is immobilised on the surface binding to the C-terminal region of hCG, the β region of hCG will more accessible to the antibody detection than the α region. Therefore, in order to optimise the level of detection, AF-anti-β-hCG detecting antibody was employed, instead of the AF-anti-α-hCG as used previously (*vida supra*).

The first attempt to produce the immunoassay was using the 1:9 mixed SAM-streptavidin layer as it was employed in the work developed by Spinke et al. [82] using SPR detection only. However the same sensitivity of 1 mIU mL^{-1} was obtained as in the previously studied sandwich immunoassay as depicted in Figure 4.22.

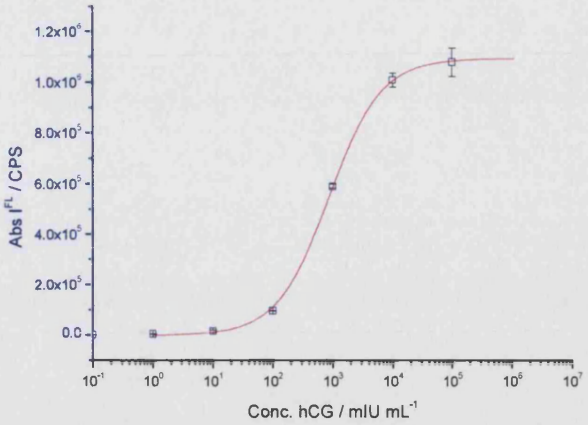

Figure 4.22 Dose response obtained for the system using 1:9 mixed SAM-streptavidin matrix with biotinylated Fab-hCG capture surface.

It is assumed, therefore, that high density of capture biotinylated Fab-hCG fragments on the surface also affects the binding capacity of the surface as well as generating steric hindrance problems for antibody-antigen interaction.

Therefore, a new sensor surface with a χ=0.01 biotin-thiol as used previously was assembled. The same hCG titration procedure employing the cyclic binding for hCG concentration in the range of 0.01 – 10^5 mIU mL^{-1} and surface regeneration of the surface with the same buffer was used as before. No non-specific binding were detected and a background fluorescence signal of 8 x 10^4 CPS was measured seven times for 0 mIU mL^{-1} hCG, and taken as the baseline. No increase in the fluorescence background was found after consecutive surface regenerations. A concentration of 50 x10^{-9} mol L^{-1} AF-anti-β-hCG detection antibody was used.

The dose – response curve is shown in Figure 4.23, where the absolute fluorescence intensity versus hCG concentration is plotted for this system. hCG at a concentration of 0.1 mIU mL^{-1} (2.24 x 10^{-13} mol L^{-1}) was titrated onto the surface and an increase in the fluorescence signal was found, however no fluorescence increase was resolved for a 0.01 mIU mL^{-1} (2.24 x 10-14 mol L^{-1}) hCG concentration. The system sensitivity was determined and found to be 0.1 mIU mL^{-1} hCG. This is one order of magnitude lower than in the work described by Schneider et al [147] with human serum samples. For the low hCG concentrations, the measurements were three times repeated. The limit of detection was determined following the procedure described above and was found to be 0.3 mIU mL^{-1} hCG (6.7 x 10^{-13} mol L^{-1}) for this system.

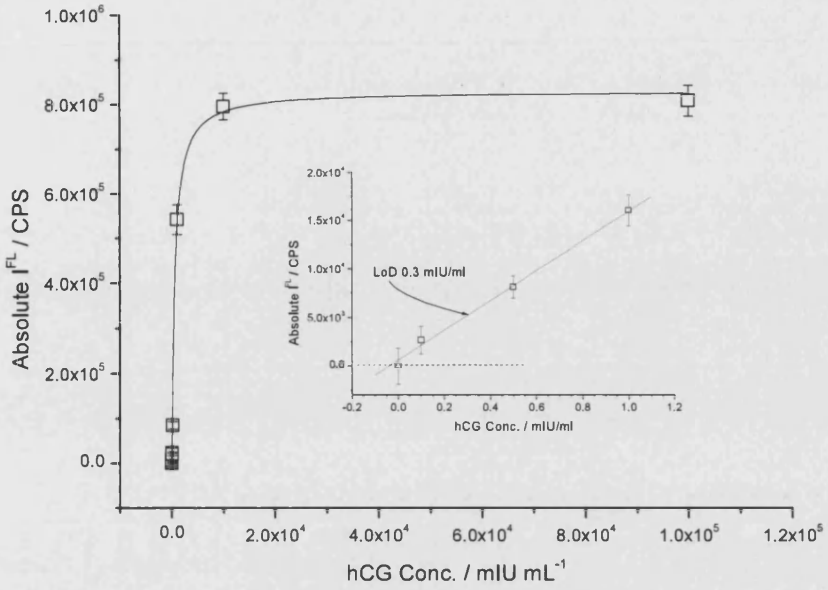

Figure 4.23 Dose response curve for determination of hCG using an Fab-hCG fragment to optimise orientation of antigen binding site on the sensor surface. Linearity is obtained for hCG concentrations between 0.1 and 1 mIU mL^{-1}. Black line in main graph is Langmuir isotherm fit. Line in inset graph is linear relationship at low hCG concentrations to determine the limit of detection (LoD).

4.5 Determination of Binding Affinities

The affinity of the antigen towards its antibodies is the main analytical measurement for the development a biosensor. However, the affinity of hCG towards the antibodies used in this thesis has already been extensively studied. Nevertheless, affinity measurements of hCG to its antibodies have not been reported using SPFS.

A standard measurement was performed for b-anti-β-hCG, b-anti-α-hCG and biotinylated Fab-hCG fragments. Three gold coated glass slides were incubated with the 1:99 mixed SAM-streptavidin, following the procedures described previously. Then, 500 x 10^{-9} mol L^{-1} solutions of the different biotinylated antibodies in PBSTA were circulated for 30 minutes on the streptavidin surface followed by rinsing with the running buffer (PBSTA).

In order to obtain the kinetic measurements hCG was fluorescently labelled using the protocol described previously in section 3.3.2 and from is designated AF-hCG. A degree of labelling of 2:1 (label:hCG) was determined from absorbance measurements using UV-Vis. hCG was labelled because the SPR angular shift is too small and below the noise level to allow detection of small changes in the mass density of the sensor surface.

A titration method using equilibrium analysis was chosen instead of the interaction controlled kinetics study, because it was hard to fit a single exponential Langmuir fitting curve for all the different hCG concentrations adsorbed onto the sensing surface. Therefore, AF-hCG solutions ranging from 10 x10^{-12} mol L^{-1} – 10 x10^{-9} mol L^{-1} were prepared. After injecting each solution, the system was let to reach equilibrium and only then a new concentration was injected.

All equilibrium values for each system were normalised and plotted versus AF-hCG concentrations. A Langmuir isotherm was fitted to the data points and the values of K_D were determined. The obtained graphics are depicted in Figure 4.24

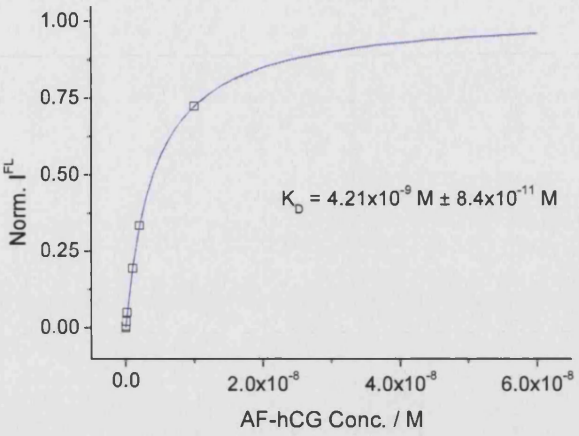

A)

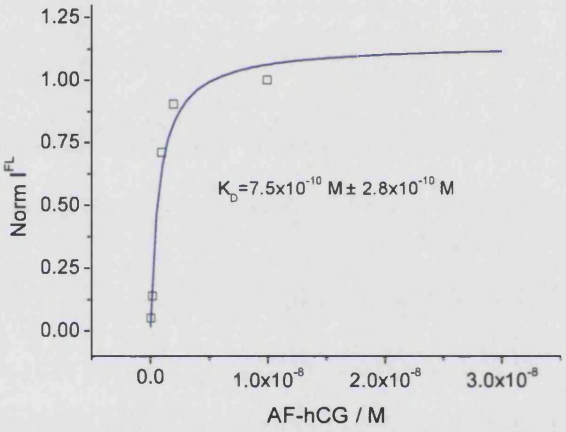

B)

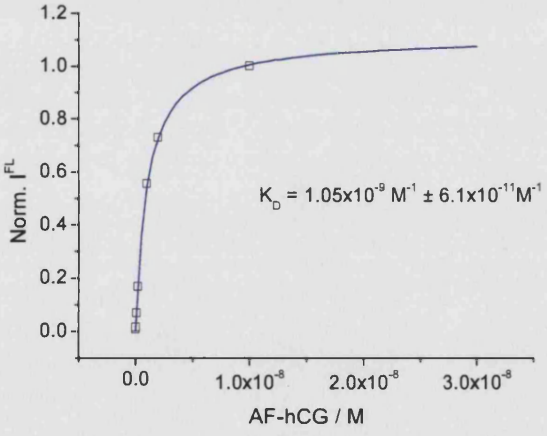

C)

Figure 4.24 Determination of the desorption binding constants using titration method for A) b-anti-α -hCG; B) b-anti-β -hCG; C)b-Fab-hCG systems.

The values obtained for the affinity binding constants compared with the systems used for sensitivity and limit of detection determination shown earlier are presented in Table 4-2.

Table 4-2 Comparison between the estimation of affinity binding constants determined using SPFS and the literature

K_A	AF-hCG (M^{-1})	sandwich hCG sensing (M^{-1})	Literature (M^{-1})
anti-α -hCG	$2.38x10^8 \pm 4.7x10^6$	$1.9x10^9 \pm 2.7x10^8$	$9.1\ x10^9$ [161]
anti-β -hCG	$1.3x10^9 \pm 4.9x10^8$	$2.43x10^8 \pm 9.5x10^6$	$1.3\ x10^{10}$ [161]
b-Fab-hCG	$9{,}5x10^8 \pm 5.5x10^7$		$2.1x10^9$ [8]

From Table 4-2 it can be observed that the experimentally determined association constant values are lower than the values presented in the literature. In order to understand the factors that might influence these values, it is necessary to consider each case separately.

First, for the system of indirect detection of hCG with fluorescently labelled antibodies (column 3) it can be observed that the values are lower compared to literature, this is due to the measurement strategy employed. In every cycle hCG was allowed to adsorb only for 30 minutes and detection with the labelled antibody was followed for only 10 minutes. In this time, equilibrium was not completely reached for low concentrations of hCG hence, the association values are under estimated.

Second, the anti-α-hCG and anti-β-hCG surfaces for direct detection of AF-hCG have values of the affinity lower than in the literature. In this system, this might be due to hCG being labelled and thus, the labels might occur in the specific binding epitope if lysine amino acids are present. Another reason for under estimated values is due to the activity of the antibodies. These were the last experiments produced after three years of the biotinylated antibody being in the fridge, thus some loss of activity might be expected.

Finally, the affinity constant value determined for b-Fab-hCG is only two times smaller than the one described in the literature. Therefore, it can be considered that SPFS is a valid technique for analytical purposes and can be applied in clinical assays.

4.6 Conclusions

Surface Plasmon Resonance and Fluorescence Spectroscopy were used to detect Human Chorionic Gonadotrophin. An immunoassay detecting strategy was employed and studies of the factors that influence the sensitivity of the immunosensors were performed.

Studies of non-specific binding and of the best regeneration buffer were carried out. Tween 20 was used in the protein buffer solutions in order to prevent non-specific binding and Glycine-HCl pH 1.76 buffer was found to be the best regeneration buffer.

The study of the influence of steric effects on analyte binding to the capture surface was carried out using SPR. It was shown that maximum binding of hCG to surface immobilised b-anti-β-hCG occurred for surfaces with χ = 0.01 density of a biotin-thiol **2** molecule in a binary SAM with a 11-mercapto-1-unadecanol **1** lateral spacer. From this result it was concluded that a lower density of capture antibodies on the surface increases the degree of sensitivity (within certain limits). This was probably due to reduction in steric interaction between hCGs on the capture surface. In order to increase the detection sensitivity of the system SPFS was employed.

SPFS allowed measurement of fluorescently labelled detection antibodies on the bound hCG layer, thus allowing a higher analyte detection sensitivity. Two studies to determine the LoD using SPFS were carried out. First, a randomly organised biotinylated capture antibody layer was immobilised on the optimised SAM – streptavidin layer used previously. On this system, an LoD of 2 mIU mL^{-1} was determined. Second, in order to orientate the antigen binding site, a mono-biotinylated Fab-hCG was used. The same optimised SAM – streptavidin layer used previously was employed. An LoD of 0.3 mIU mL-1 was calculated. From this work, it can be concluded that spatial control of the capture antibody surface, both on the x-y plane, and in terms of the orientation of binding sites, is critical for optimising biosensor sensitivity.

Finaly a study of the affinity binding constant of hCG to the several sensing surfaces was preformed. In order to detect hCG the protein was fluorescently labelled as extremely low concentration solutions were used. The equilibrium tritation method was employed for affinity constant determination. The affinity binding constants determined

were lower than those presented in literature. These results are associated with the lower activity of the antibodies that were employed and other experimental factors.

5 Detection of Fatty Acids using SPFS

An introduction to fatty acid molecules and their biological functions is presented followed by a detailed description of previous methods employed to determine fatty acid concentration in solution, plasma and blood samples. The development of the sensing surface and the strategy employed for detection of fatty acids, with a theoretical description of the competition model, are described.

5.1 Structural and Functional Diversity of Lipids [1]

Lipids are one of the four major classes of biomolecules (the others being: proteins; carbohydrates; and nucleotides) essential for the composition of all living organisms. Lipids, however, have widely varied structures. They are often defined as water-insoluble organic compounds, hydrophobic or amphiphilic.

Figure 5.1 shows a diagram of the different types of lipids and their structural relationship to one another.

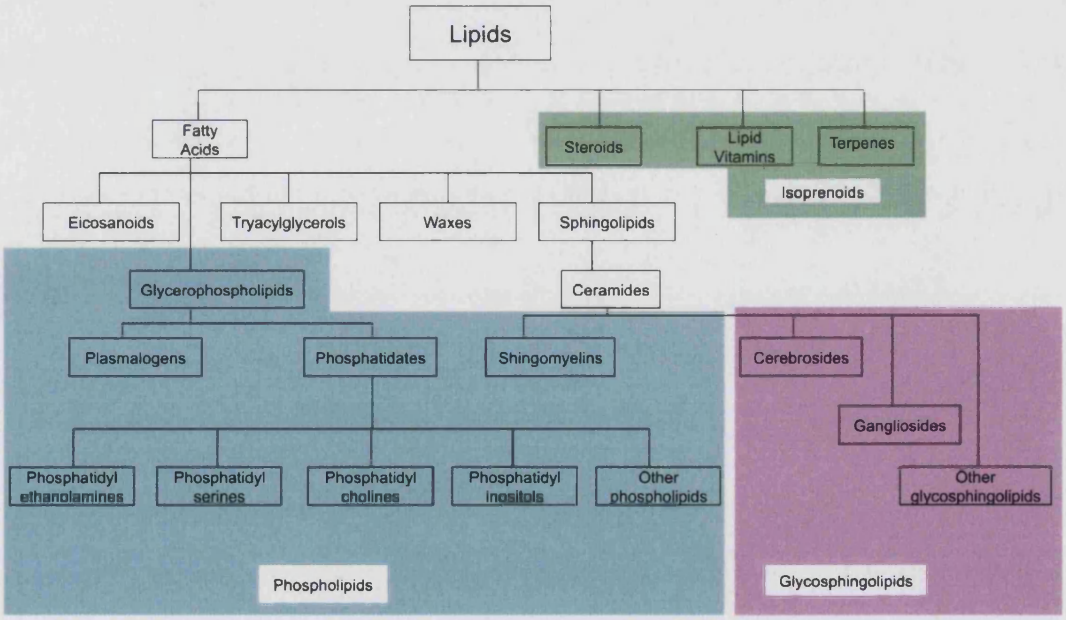

Figure 5.1 Major classes of lipids. Fatty acids are the simplest lipids. A number of other lipids either contain or are derived from fatty acids [1].

The simplest and largest class of lipids are the fatty acids. They are the precursors for all other lipid classes. The glycerophospholipids and the sphingomyelins contain a phosphate group and are classified as phospholipids. Cerebrosides and gangliosides contain shingosine and carbohydrate and are therefore classified as

glycosphingolipids. Steroids, lipid vitamins and terpenes are called isoprenoids because they are related to the five-carbon molecule isoprene.

Each class of lipid shows a range of biological functions. Even so, the most important role is to give structure to cells and to protect them against external aggressions. Biological membranes constitute a variety of amphiphilic lipids, such as glycerophospholipids and sphingolipids. The presence of waxes in cell walls, exoskeletons, and skins functions to provide structural and surface protection. Triacylglycerols are, in most organisms, intracellular molecules for storing metabolic energy. Lipids also have the function to provide animals with thermal insulation and padding.

Some lipids have highly specialised functions. For example, the steroid hormones regulate metabolic activities in animals. Eicosanoids are used to regulate blood pressure, body temperature, and smooth-muscle contraction. Ganglosides and other glycosphingolipids are located at the cell wall and participate in cell recognition.

5.1.1 Fatty Acids [1]

There are a large variety of fatty acids in microorganisms, plants and animals. The difference between one another is the length of the hydrocarbon chain, the degree of unsaturation (the number of double bonds) and the positions of the double bonds in the chain. The most common fatty acids found in mammals are presented in Table 5-1.

Table 5-1 Some of the common fatty acids that can be found in most mammals

Symbol	Common Name	Systematic Name	Structure	mp (°C)
Saturated Fatty Acids				
12:0	Lauric acid	Dodecanoic acid	$CH_3(CH_2)_{10}COOH$	44.2
14:0	Myristic acid	Tetradecanoic acid	$CH_3(CH_2)_{12}COOH$	52
16:0	Palmitic acid	Hexadecanoic acid	$CH_3(CH_2)_{14}COOH$	63.1
18:0	Stearic acid	Octadecanoic acid	$CH_3(CH_2)_{16}COOH$	69.6
20:0	Arachidic acid	Eicosanoic acid	$CH_3(CH_2)_{18}COOH$	75.4
22:0	Behenic acid	Docosanoic acid	$CH_3(CH_2)_{20}COOH$	81
24:0	Lignoceric acid	Tetracosanoic acid	$CH_3(CH_2)_{22}COOH$	84.2
Unsaturated Fatty Acid (all double bonds are cis-bonds)				
16:1	Palmitoleic acid	9-Hexadecanoic acid	$CH_3(CH_2)_5CH=CH\ (CH_2)_7COOH$	-0.5
18:1	Oleic acid	9-Octadecanoic acid	$CH_3(CH_2)_7CH=CH\ (CH_2)_7COOH$	13.4
18:2	Linoleic acid	9,12-Octadecadienoic acid	$CH_3(CH_2)_4(CH=CHCH_2)_2\ (CH_2)_6COOH$	-9
18:3	α-Linolenic acid	9,12,15-Octadecatrienoic acid	$CH_3CH_2(CH=CHCH_2)_3\ (CH_2)_6COOH$	-17
18:3	γ-Linolenic acid	6,9,12-Octadecatrienoic acid	$CH_3(CH_2)_4(CH=CHCH_2)_3\ (CH_2)_3COOH$	
20:4	Arachidonic acid	5,8,11,14-Eicosatetraenoic acid	$CH_3(CH_2)_4(CH=CHCH_2)_4\ (CH_2)_2COOH$	-49.5
20:5	EPA	5,8,11,14,17-Eicosapentanoic acid	$CH_3CH_2(CH=CHCH_2)_5\ (CH_2)_2COOH$	-54
24:1	Nervonic acid	15-Tetracosenoic acid	$CH_3(CH_2)_7CH=CH(CH_2)_{13}COOH$	39

Fatty acids are named according to the IUPAC Rules for Nomenclature of Organic Chemistry. Fatty acids are numbered with the carbon atom of the carboxylic group as C-1. The short nomenclature using numbers, e.g. 18:2, indicates the number of carbons in the main chain and the number of double bonds. Most fatty acids have a pK_a of about 4.5 to 5 and are therefore ionised at physiological pH. Fatty acids with no double bond present in their structure are called saturated fatty acids, whereas those with at least one double bond are called unsaturated fatty acids. Unsaturated fatty acids with only one carbon-carbon double bond are called monounsaturated, and those with two or more are called polyunsaturated.

The physical properties of saturated and unsaturated fatty acids are considerably different and depend on the number of double bonds and chain length. At room temperature, saturated fatty acids are solid and unsaturated fatty acids are liquid, as shown in Table 5-1.

The length of the hydrocarbon chain of a fatty acid and its degree of unsaturation influence the melting point. As the length of the hydrocarbon tail increases, the melting point of the saturated fatty acids also increases, since the number of Van der Waals interactions among neighbouring hydrocarbon chains increases as the chains become longer. Therefore, more energy is required to disrupt these interactions.

When comparing saturated fatty acids with unsaturated fatty acid of the same chain length it can be observed that the melting point of the latter is lower. This is due to the presence of the double bond that produces a pronounced bend in the hydrocarbon chain, hindering the rotation and decreasing the Van der Waals interactions among hydrocarbon chains.

Free fatty acids occur only in trace amounts in living cells. Most fatty acids are esterified to form more complex lipid molecules. The abundance of particular fatty acids varies with the type of organism, type of organ and food source. Oleate (18:1), palmitate (16:0) and stereate (18:0) are the most abundant fatty acids in animals. Some polyunsaturated fatty acids, such as linoleate (18:2), which is abundant in plant oils, and linolenate (18:3), which is found in plants and fish, are called essential fatty acids since animals are unable to synthesise them. Essential unsaturated fatty acids have *cis* double bonds.

5.1.2 The Importance and Biological Role of Fatty Acids

Fatty acids (FA), as previously mentioned, are extremely important for organisms as they are the main constituent of the cellular membrane. Therefore, FA are needed in the diet of most living creatures. FA are transported in mammalian systems via albumin, otherwise they form micelles and other supramolecular structures in solution, in order to stabilise their hydrophobic interactions.

Furthermore, free fatty acids (FFA) present in blood plasma are the main metabolic and energetic source for the heart muscle at rest. Therefore, elevated plasma FFA concentrations may have beneficial effect of improving heart function. Clinical studies have suggested that a diet rich in fish oil and other unsaturated FFA can prevent cardiac and arrhythmias nevertheless not all published data support the importance of this relationship [164-168]. However, in the 1950's it was recognised that a high intake of saturated FFA was a major risk factor for myocardial infarction and stroke [169].

The possibility of dietary lipids causing cardiac arrhythmias became apparent in the late 60s when the severity of ventricular arrhythmias in patients after myocardial infarction was found to correlate with very high levels of circulating FFA. The development of irreversible myocardial ischemic injury is associated with progressive degradation of membrane phospholipids, producing an increase in FFA plasma concentration, more specifically of arachidonate, which then may accumulate in the blood vessels. This process is also associated with electrolyte changes including calcium accumulation [170].

Evidence that the concentration of FFA in plasma may be related to ventricular premature complexes has been demonstrated by Paolisso et al [171] in 1997. Ventricular premature complexes (VPC) are the most common ventricular arrhythmias in patients with heart conditions that can instigate in sudden cardiac death. The group reported that in nonischemic patients with non-insulin-dependent diabetes mellitus (a variable disorder of carbohydrate metabolism) had elevated plasma FFA concentrations, which predicted the development of a larger number of VPC's.

However, when Jouven et al in 2001 attempted to demonstrate the relationship between the increased concentrations of nonesterified FA after an ischemic condition, which has a proarrythmic effect responsible for ventricular tachyarrhythmias, the group concluded that elevated circulation of nonesterified FA was an independent risk factor for sudden death in middle-aged men free of known cardiovascular disease. It was also concluded that further studies should take place in order to assess the potential contribution of nonesterified FA measurement for prediction of sudden death in clinical practice. It was noted that the decrease in nonesterified FA levels in blood plasma may help prevent sudden death due to cardiovascular disease [172].

The mechanisms that may produce either pro- or antiarrhythmic effects of FFA are explained by their interactions with the biological membranes. It is apparent that hydrophobic portions of membrane proteins interact specifically with lipids within the core bilayer. This specificity is one reason why changes in membrane composition alter membrane protein functions due to incorporation of FA into the bilayer.

Lemaitre et al produced a study to observe the relationship between the concentration of trans-FA and primary cardiac arrest [173]. It was found that the concentration of trans-FA in erythrocytes cell membranes from survivors of a cardiac arrest was greater than that in membranes from age and sex-matched controls. When a *cis*-FA or a *trans*-

FA is inserted in the lipid bilayer, both interact with hydrophobic regions of a membrane protein changing the conformation around the membrane-spanning α-helices, but because these FA differ structurally, the conformational change in the cytoplasmic region and extracellular peptide chains are different [169]. Further epidemiological evidence that a *trans*-FA rich diet is associated with the increase of coronary heart disease risk are presented in a case study of the Dutch population over a 10 year period [174].

Other perturbations caused by the increase of the plasma FFA concentration have been presented by the Kleinfeld group [175-178]. This group has shown that when plasma FFA concentration are elevated to very high levels by stress or disease conditions may modulate the immune response, since transmembrane signalling in cytotoxic T lymphocytes was found to be extremely sensitive to short term exposure to long chain FFA.

It is important to note, that for all the clinical case studies presented above, a good system to determine the concentrations of FFA in plasma is necessary. A direct way to measure the influence of the plasma FFA concentration is an alternative way to establish the relationship between plasma FFA concentration and cardiac conditions.

5.2 Determination of Free Fatty Acids

5.2.1 Fatty Acid Binding Protein (FABP)

Fatty acids are extremely important molecules in most organisms and especially in mammals. A human heart uses FA as its main source of energy when at rest and, as mentioned previously, the levels of plasma FFA concentration may signal the state of health of the heart itself.

Considerable amounts of FA are transported in mammalian plasma to meet energy, structural, and signalling requirements. Because of the low aqueous solubility of long chain FA, most FA are carried in a complex with albumin. Only a small fraction of the total FA is dissolved or is free in aqueous phase.

Fatty acid-binding proteins (FABP) are cytoplasmatic proteins that play a role in cytosolic FA transport, similar to the FA transport function of albumin in the blood [148]. FABP constitute a family of small (~15 kDa) proteins with considerable amino acid sequence variation among different tissues, but with similar three-dimensional structures. There are three major cytosolic FABP that are generally named according to their tissues of greatest abundance. These proteins are present in the intestine, liver and heart muscle and are therefore denominated as I-FABP, L-FABP and H-FABP, respectively [148].

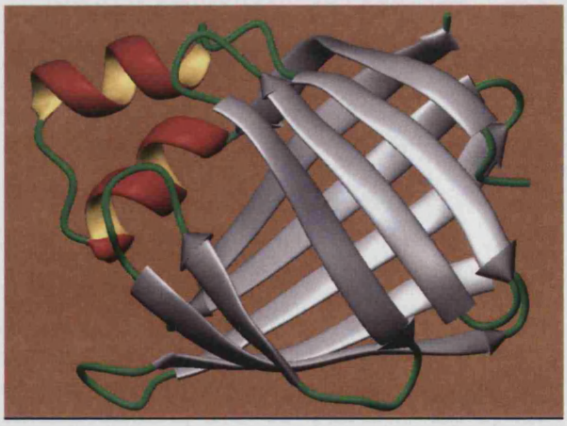

Figure 5.2 Ribbon diagram of I-FABP. It can be observed that the ten anti-parallel β-strands are organised into two nearly orthogonal, β-sheets. Two short α-helices are connected to the first two β-strands. The structure resembles a clam shell and has been called β-clam. The cavity enclosed by the β-sheets serves as a binding site for the FA ligand [179, 180].

Kleinfeld et al developed a new fluorescent probe derived from a fatty acid-binding protein in order to study the equilibrium binding between long chain FA and the

fluorescently modified I-FABP. The FABP was covalently modified with the fluorescent compound Acrylodan and designated ADIFAB. The binding of a FA to the ADIFAB was observed to induce a large shift in the florescence emission wavelength from 432 nm to 505 nm. Therefore, the direct measurements of FA were accomplished by determining the ratio of the emission intensities. In addition, the fluorescent response of this new probe allowed the measurement of FFA concentration directly, as they were continuously released from IgE receptors activated rat basophilic leukaemia cells [181].

In order to understand the functional role of FABP, it was natural to characterise the equilibrium binding reaction between FA and the FABP. In the past, the majority of the binding measurements were determined using methods that physically separated FFA and FABP-bound to FA [148]. However, the separation of the two main subjects of an equilibrium reaction perturb significantly the equilibrium, making it difficult to obtain accurate value for the equilibrium constants [181]. Equilibrium binding constants have also been determined without physical separation of the FA and FABP by measuring the binding of fluorescently labelled FA or by the displacement of the fluorescent FA from the binding pocket of the FABP [182-184].

The work of Kleinfeld et al. [181], the binding of FA in a single binding site at concentrations below the critical micelle concentrations for oleate, palmitate, linoleate, arachidonate, and linolenate acids was described. The fluorescently labelled FABP dissociation constants were determined at 37°C.

With this new probe, Kleinfeld and co-workers studied different equilibrium reactions for FFA with its different transporting proteins. The affinities of long chain FA to the different FABP were measured by monitoring the concentrations of FFA in equilibrium with the FABP using the fluorescent probe ADIFAB without the need to physically separate any of the reactants.

It was found that the equilibrium constants were extremely dependent on the tissue of origin of the FABP but independent of species. It was found as well, that for all FABP the dissociation constants values for FA with the same chain length were lower for saturated FA than polyunsaturated FA, which reflects the lower aqueous solubility of saturated FA [185].

When studying the thermodynamics of FA binding to the different FABP it was found that the free energies of binding were determined to have large negative enthalpies

that tended to decrease with the increase of FA unsaturation, as the FA becomes more soluble in water [186]. Measurements of the partition of FA between unilamellar lipid vesicles and water were also determined, in order to assess the role of FA aqueous solubility in FABP binding. It was observed that the lipid/water partition coefficients were independent of the temperature. Therefore, it was concluded that the binding of FA to the different FABP in aqueous solution was governed by the sum of all contributions of the various interactions between FA, water and FABP [186].

5.2.2 Fatty Acids and Their Interaction with Albumin

The physiological role of albumin started to be clarified in the late 50's when a number of studies of FFA binding to albumin were carried out. At this time, plasma albumin came into use clinically and fatty acids were noted to stabilise the protein against denaturation [187], so it was important to understand how FFA interacted with albumin.

The first indication that FFA binding to albumin would be important metabolically came from studies on the interactions between FFA and plasma. It was observed that albumin was the acceptor of FFA released from certain activated lipases, and an extremely high turnover rate of plasma FFA was measured. It was observed that the turnover rate was responsive to metabolic and nutritional changes as well. Finally, the central role of albumin was established when it was shown that albumin was the transport vehicle for FFA in blood [188].

Albumin is a single polypeptide chain molecule with a molecular weight of approximately 67kDa. Albumin is a spherical molecule with a negative charge at physiological pH. Human plasma albumin contains only one tryptophan that is responsible alone for its ultraviolet fluorescence spectrum. Conformational changes of albumin are accompanied by changes in the emission fluorescence spectrum, and therefore studies of the localisation of FFA binding sites in relation to tryptophan location are possible, especially in human serum albumin where there is only one tryptophan residue.

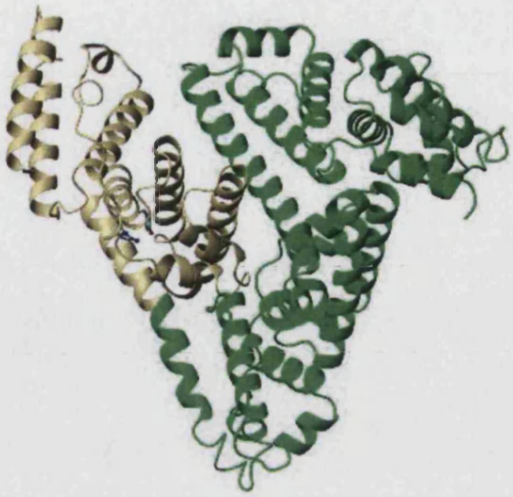

Figure 5.3 Ribbon diagram of human serum albumin, it has 67% α-helix with no β-sheet structure. The surface of HSA is very hydrophilic. This makes the protein very soluble in water. Thus HSA forms a hydrophilic cover for the very hydrophobic fatty acid molecules and dissolves them in the plasma [189].

The hydrophobic interactions between the hydrocarbon groups and the albumin binding site extend along the entire length of the fatty acid chain. The caboxylate group also contributes to the fatty acid binding, although on a smaller scale, shown when methyl esters of fatty acids analogues were found to bind to albumin less strongly. This indicated that electrostatic or hydrogen bonding interactions were involved [188]. As a result, hydrophobic interactions are much more important than the contributions from the carboxylic group, which plays a minor role, in FA binding to the strongest albumin binding site.

It was shown that albumin demonstrates configuration adaptability, i.e., a subtle conformational change when present in a physiological medium. It is known that albumin binding sites are adaptable and can be reorganised in different configurations that have nearly the same energies. An organic anion stabilises the new configuration which permits maximum interaction between itself and the binding site [190-192].

The interactions of FA and albumin in the blood stream serves to buffer the level of FFA and therefore to regulate the rate at which FFA are transported to the appropriate tissues. The capacity of albumin to buffer the level of FFA in serum is important because, as mentioned previously, elevation of the FFA levels are associated with a number of diseases such as ischemic injury [170, 193, 194], diabetes [195] and cancer (elevated FFA levels may modulate the immune response in cancer patients[196, 197]).

Kleinfeld et al during the 90's studied the interactions of FAs with albumin in serum and *in vivo* [198-200]. Previously, FFA levels of long chain FA had not been measured directly in serum, in equilibrium with albumin, or in cellular studies. However, values of FFA levels have been estimated from studies that determined the FA-albumin association constants in a series of measurements of the distribution of FA between the water-albumin and the heptane phase [201, 202].

However, two potential problems arise from this procedure: i) The direct measurements of FFA in equilibrium with albumin-cell system have not yet been determined (at time of writing); ii) the FFA concentration is an exponential function of the ratio of the total FA to albumin for ratio values exceeding ~3 [201, 202]. For these large ratios, small errors in the observed ratio result in large errors in the estimated FFA concentrations values, which therefore make estimating critical FFA concentrations levels extremely difficult.

In order to overcome these problems, Kleinfeld et al used their designed fluorescently labelled I-FABP probe (ADIFAB). The fluorescence of this probe, under the physiological conditions, is not affected and neither are the binding constants for FA by the presence of other macromolecules, and therefore is suited to the monitoring FFA concentrations in equilibrium with albumin, serum, or cells [198].

As a result, the group studied the equilibrium binding of long-chain fatty acids for a number of albumins, e.g., human serum, bovine serum and murine serum albumin. It was concluded in most cases that the association constant for the first site was greater than or equal to that of succeeding sites. However, arachidonate binding to human albumin suggests that positive cooperativity might be involved [198], and measurements of the unbound serum FFA were also performed. It was observed that levels of the unbound serum FFA correlated well with the total serum FFA concentration, therefore providing a sensitive method for assessing the physiological state.

Moreover, Kleinfeld et al applied this technique to measure the serum unbound free fatty acid concentration of patients undergoing percutaneous transluminal coronary angioplasty (PTCA). These measurements suggested that the increase in serum unbound FFA levels reflected the angioplasty-induced ischemia and that they were more sensitive than electrocardiographic measurements. It was also concluded that elevated serum unbound FFA levels are harmful and may warrant treatment strategies designed to reduce these levels to block their deleterious effects [200].

In this work, a new FA sensor was developed. The strategy adopted was based on the work developed in chapter 4, a sensing surface was developed for detection using SPFS. In order to detect FA an newly synthesised FA antibody was immobilised on the surface using the biotin-SAM-streptavidin-b-Protein A strategy. A competition assay using a new synthesised fluorescent probe was tested in order to determine FA concentrations.

5.3 Competition Assay: Kinetics Theory

Consider a situation where two ligates (FA^* and FA) compete for the same binding site of a ligand immobilised on the surface R, then the reactions that occur on the surface are:

$$FA^* + R \underset{k_2}{\overset{k_1}{\rightleftharpoons}} FA^*R \tag{5.1}$$

$$FA + R \underset{k_4}{\overset{k_3}{\rightleftharpoons}} FAR \tag{5.2}$$

Where FA^* is the fluorescently labelled ligate and FA is the competitor for the ligand (R). k_1 and k_3 are the association rate constants for the respective binding of ligate and competitor to the receptors and are presented in units of $s^{-1}M^{-1}$. And k_2 and k_4 are the respective dissociation rate constants in units of s^{-1}.

For the model that will be described, it is assumed that all binding sites are homogeneous, the displacement of either ligate is purely competitive and non-specific binding is neglected. The signal of the binding is given in this descriptive model by the fluorescently labelled ligate FA^*. The binding reactions and the conservation of mass laws lead to the following equations:

$$\frac{d[FA^*R]}{dt} = k_1[FA^*][R] - k_2[FA^*R] \tag{5.3}$$

$$\frac{d[FAR]}{dt} = k_3[FA][R] - k_4[FAR] \tag{5.4}$$

$$R = I_{\max}^{FL} - [FA^*R] - [FAR] \tag{5.5}$$

Where R are the free binding sites that decrease in time as adsorption of both ligates occurs, and $I_{\max}^{FL}$ is the maximum binding capacity for the mixed concentrations of FA^* and FA.

The analytical solution to these differential equations has been well described in refs [203, 204]. By transforming this solution in terms of SPFS fluorescence signal:

$$I_{FA^*}^{Fl} = \frac{I_{\max}^{FL} k_1 [FA^*]}{K_F - K_S}\left[\frac{k_4(K_F - K_S)}{K_F K_S} + \frac{(k_4 - K_F)}{K_F}\exp(-K_F t) - \frac{(k_4 - K_S)}{K_S}\exp(-K_S t)\right] \tag{5.6}$$

Where the follow new variables are used:

$$K_F = 0.5\left[\left(K_A + K_B + \sqrt{(K_A - K_B)^2 + 4k_1k_3[FA^*][FA]}\right)\right] \tag{5.7}$$

$$K_S = 0.5\left[\left(K_A + K_B - \sqrt{(K_A - K_B)^2 + 4k_1k_3[FA^*][FA]}\right)\right] \tag{5.8}$$

$$K_A = k_1[FA^*] + k_2 \tag{5.9}$$

$$K_B = k_3[FA] + k_4 \tag{5.10}$$

The general properties of equation (5.6) are expected: i) At time $t = 0$ the equation reduces to zero as there is no binding of ligates; ii) As equilibrium is approached as time $t \to \infty$ the exponential terms approaches zero and may be ignored and therefore, the equation for equilibrium is reduced to:

$$I^{Fl}_{FA^*\,eq} = \frac{I^{FL}_{\max} k_1 k_4 [FA^*]}{K_F K_S} = \frac{I^{FL}_{\max}[FA^*]}{K_{D(FA^*)}\left(1 + \frac{[FA]}{K_{D(FA)}} + \frac{[FA^*]}{K_{D(FA^*)}}\right)} \tag{5.11}$$

Where $K_{D(FA^*)}$ and $K_{D(FA)}$ are respectively the dissociation constants for the fluorescently labelled ligate and the non-labelled competitor.

In order to compare the binding of the fluorescently labelled ligate in the presence of the competitor with the binding of the fluorescently labelled ligate alone, both signals and a plot of the response ratio vs the concentration of competitor were considered.

$$\frac{I^{Fl}_{FA^*}(FA)}{I^{Fl}_{FA^*\,eq}(notpresent)} = \frac{K_{D(FA^*)} + [FA^*]}{K_{D(FA^*)}\left(1 + \frac{[FA]}{K_{D(FA)}} + \frac{[FA^*]}{K_{D(FA^*)}}\right)} \tag{5.12}$$

Fitting mathematically the ratio response curve, it was possible to determine the dissociation constant of the non-labelled competitor ligate $K_{D(FA)}$.

It is also important to understand difference of the kinetics of the fluorescently labelled ligate when the non-labelled competitor is absent and present. Figure 5.4 presents simulated binding curves displayed as the ratio of $I^{Fl}_{FA^*}(FA) / I^{Fl}_{FA^*\,eq}(competitor\ not\ present)$.

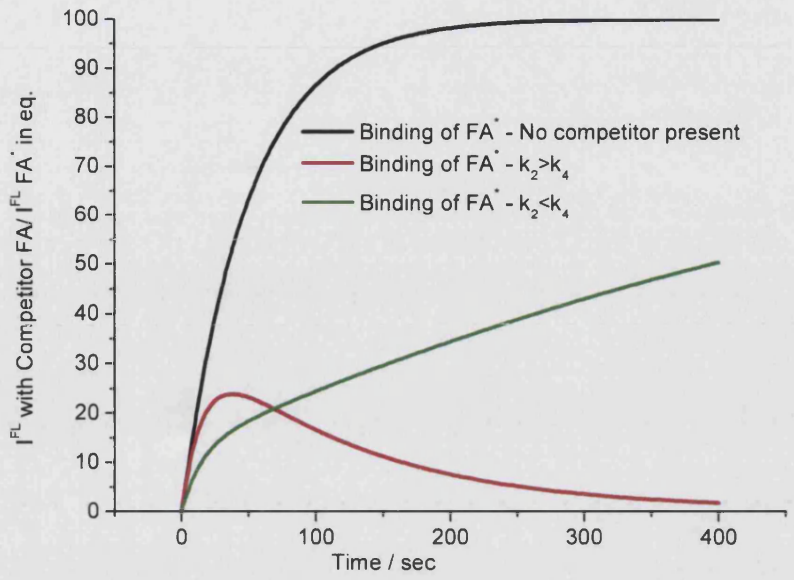

Figure 5.4 Binding of the fluorescently labelled ligate in the absence and presence of the non-labelled competitor. Binding parameters for each curve are: $[FA^*]$ 1x10^{-7} M; $[FA]$ 1x10^{-7} M; k_1 1x10^5 M^{-1}s^{-1} k_3 5x10^5 M^{-1}s^{-1}. k_2 1x10^{-2} s^{-1} and k_4 1x10^{-2} s^{-1} for $k_2 > k_4$ and for $k_2 < k_4$ k_4 1x10^{-2} s^{-1} and k_2 1x10^{-2} s^{-1}.

It can be observed in Figure 5.4 that the fluorescently labelled ligate dissociates from the receptors faster than the competitor when $k_2 > k_4$. The binding of the fluorescent labelled ligate in the presence of the competitor overshoots its equilibrium value, which suggests that at some intermediate interval of time there will be more fluorescently labelled ligate bound to the receptors than there will be at equilibrium.

Moreover, when the fluorescently labelled ligate dissociates form the receptors surface slower than the competitor ($k_2 < k_4$) the specific binding does not overshoot its equilibrium value but rather approaches monotonically the equilibrium.

5.4 Development of a Fatty Acids Sensor Using Fatty Acid Antibody and Human Serum Albumin

5.4.1 Sensor Surface Consideration

The strategy used to prepare a sensor surface for determination of FA using SPFS was the same as employed in the previous chapter 4. A thin gold layer was evaporated onto high refractive index glass. A solution of mixed biotin/OH-thiols was assembled on the gold surface followed by adsorption of a streptavidin layer.

It is important to mention that from the previous chapter 4 that it was concluded that the best loading of an antigen was obtained when the antigen binding site of the antibody was turned away from the surface. Therefore, the optimised sensing surface employed a genetically modified protein, corresponding to the fragment of the antibody where the antigen binding site is found where a biotin labelled was located exactly on the other extreme side of the antibody molecule, allowing orientation of the antigen binding site towards the solution.

However, for this project, the only antigen binding site available was present on the whole antibody, and therefore the whole FA antibody was used. In the previous chapter, randomly biotinylation of the antibody was used to build an antibody sensing surface. In this project, a new strategy was employed to orientate the antigen binding sites on the surface.

The new strategy consisted of using biotinylated Protein A (b-protein A) to adsorb specifically to the Fc region of the antibody. This protein binds specifically to the Fc (referred in chapter 1) region of the antibody orientating the antigen binding region away from the surface [205]. Therefore, a new protein layer was added to build a more organised structure Figure 5.5.

Moreover, the ratio of biotin/OH-thiols was changed to 1:9. b-Protein A has a considerably lower molecular weight compared with antibodies. Additionally, the antigen is a low molecular weight molecule and, therefore, the steric hindrance problem is less critical than in the situation considered in chapter 4.

Immediately following streptavidin adsorption, a solution of 50 μg mL^{-1} of b-Protein A in 10 mM HEPES-PF68 (150 mM NaCl, 5 mM KCl, 1 mM $NaHPO_4$, Pluoronic F-68 0.005%[2]) buffer solution was injected onto the surface.

In order to adsorb the antibodies on the b-Protein A layer, the running buffer was changed to Sodium Borate (commonly known as Borax) 100 mM pH 9.2 buffer as Protein A binds to the Fc region of antibodies optimally at basic pH. A solution of 50 μg mL^{-1} of FA-antibody in 100 mM Borax pH 9.2 was injected and left to adsorb overnight.

This FA-antibody was developed by Unipath Ltd. where it was produced via techniques of immunology. The new FA-antibody was raised against FA using stearic acid (C18-FA) conjugated to CD40, a glycoprotein that mediates the immune response. Mice were immunised with 100 mg of the conjugated C18-FA-CD40 in Freund's complete adjuvant, followed by a 2 weekly injections of C18-FA-CD40 50 mg in incomplete Freund's adjuvant.

Protein A binds very strongly to antibodies produced in rabbits but only binds to12% of antibodies produced in mice (solid-phase assay of immunoglobulin reactivity normalised to rabbit IgG) [206]. Therefore, an extra step of cross-linking protein A to the FA-antibody was employed. A solution of Dimethyl Pimelimidate Dihydrochloride (DMP) 50 mM in Borax 100 mM pH 9.2 was prepared and injected for 30 minutes. The surface was then thoroughly rinsed with HEPES-PF68 buffer. A schematic of the surface is presented in Figure 5.5.

[2] Pluoronic F-68 was used in order to prevent from non-specific binding.

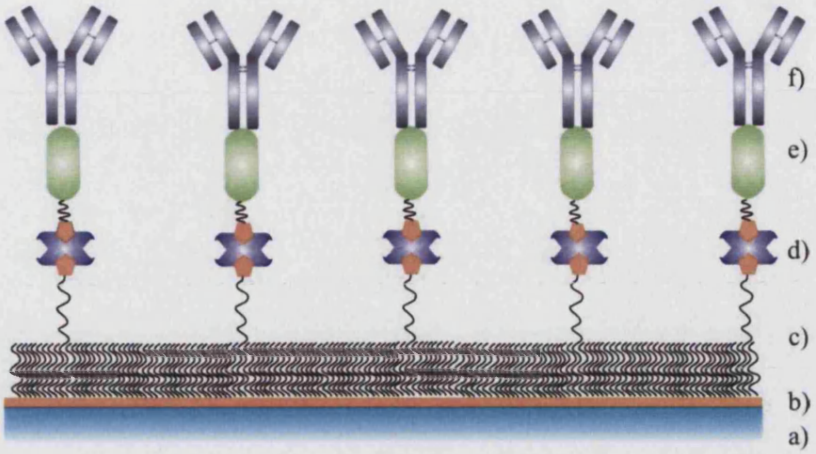

Figure 5.5 Schematic representation of the optimised sensor surface produced to enable the detection of FA in solution. a) LaFSN9 glass; b) 50 nm gold; c) binary mixed thiol SAM 1:9; d) Streptavidin; e) b-Protein A; f) FA-antibody cross linked to b-Protein A via DMP with the antigen binding sites turned away from the surface.

The binding of all different layers were followed with SPR and results presented in Figure 5.6. It can be observed that, although using the highest flow rate of ~ 4 mL min^{-1}, the binding equilibrium of FA-antibody to b-Protein A is very slow.

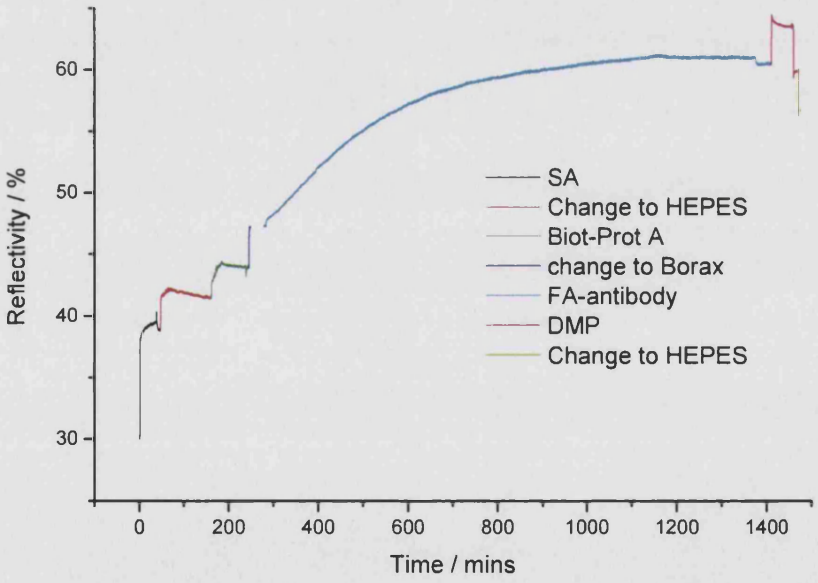

Figure 5.6 Adsorption of the different layers in order to produce an optimise sensor surface to detect FA in solution. At the end the circulating buffer is HEPES-PF68 10 mM pH 7.4.

5.4.2 Equilibrium Dissociation Constant Determination for Fluorescently Labelled FA

The classical method of detecting FFA is to use the fluorescent probe Acrylodan Intestinal Fatty Acid Binding Protein (ADIFAB) and binding constants of long chain fatty acid with ADIFAB have been determined as mentioned in section 5.2.1 [181, 185, 186].

In this work a new fluorescent probe has been synthesised consisting of a small chain FA attached covalently to a Cy5 fluorescent molecule at the terminal end of the alkyl chain. The molecular structure is presented in Figure 5.7. This molecule was synthesised by the Department of Chemistry, University College London.

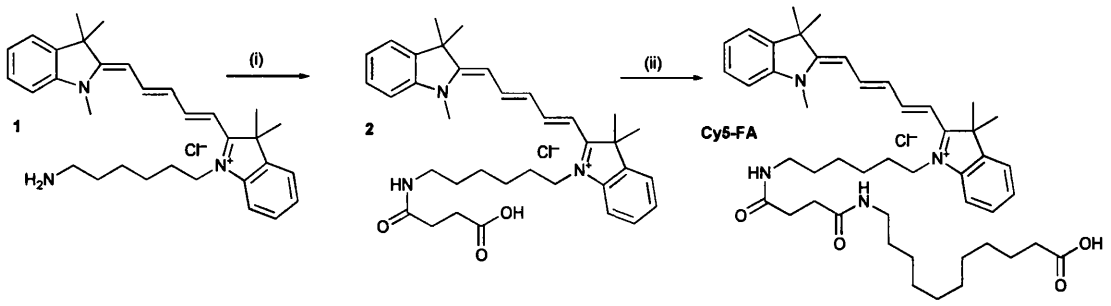

Figure 5.7 Synthesis of cyanine dye Cy5-FA developed by Tranchant , I., Tabor, A. B.,. Hailes, H. C. [3]

[3] Reagents and conditions: (i) DMAP, succinic anhydride, 18 h, rt, 60%; (ii) HOBT, DCC, 11-aminoundecanoic acid, 18 h, rt, 20%.

1. General Methods: All moisture-sensitive reactions were performed under a nitrogen atmosphere using oven-dried glassware. Unless otherwise indicated, reagents were obtained from commercial suppliers and were used without further purification. Reactions were monitored by TLC on Kieselgel 60 F_{254} plates with detection by UV, or permanganate and phosphomolybdic acid stains. Flash column chromatography was carried out using silica gel (particle size 40-63 μm). Cy5 was synthesised in-house using a modified version of the original published protocol (207. Unlu, M., M.E. Morgan, and J.S. Minden, *Difference gel electrophoresis: A single gel method for detecting changes in protein extracts.* Electrophoresis, 1997. **18**(11): p. 2071-2077.)as recently reported (208. Chan, H.L., et al., *Proteomic analysis of redox- and ErbB2-dependent changes in mammary luminal epithelial cells using cysteine- and lysine-labelling two-dimensional difference gel electrophoresis.* Proteomics, 2005. **5**(11): p. 2908-2926.)

2. Cy5-FA. The reaction was carried out under anhydrous conditions. To 2 (8 mg, 0.012 mmol) in CH_2Cl_2 (5 mL) was added 1-hydroxybenzotriazole (4 mg, 0.03 mmol) and dicyclohexylcarbodiimide (6 mg, 0.03 mmol). After stirring the reaction for 2 h, 11-aminoundecanoic acid (2 mg, 0.006 mmol) was added and the reaction was stirred for 18 h at rt. The solvents were removed in vacuo and the residue purified by flash silica chromatography (CH_2Cl_2 then CH_2Cl_2/MeOH/CH_3CO_2H, 90:9:1) to afford Cy-FA (2 mg, 20%) as a blue oil. ^{1}H NMR (300 MHz; $CDCl_3$) δ 1.10–1.38 (14H, m), 1.45 (6H, m), 1.60 (2H, m), 1.68 (12H, m), 1.78 (2H, m), 2.35 (2H, m), 2.53 (2H, m, CH_2CO), 2.65 (2H, m, CH_2CO), 3.19 (2H, m), 3.70 (3H, br s), 4.07 (4H, m), 6.41 (2H, m), 6.76 (1H, m), 7.12, (2H, m), 7.21 (2H, m), 7.36 (4H, m), 7.94 (2H, m); m/z (ES+) 753 (MH^+, 10%).

This work group kindly supplied a small quantity, 2 mg, of fluorescently labelled FA. The solid was dissolve in 10 μL of DMSO and 190 μL of HEPES buffer (without PF-68). The solution was aliquot into 100 μL and frozen for further use.

The non-specific binding of fluorescently labelled FA was tested at the sensor surface. and tested in three different slides with different layers. The first slide consisted only of SAM and streptavidin layers, the second was prepared with SAM, streptavidin and b-Protein A and the third one was prepared with a cross-linked anti-goat IgG, instead of FA-antibody. In order to test for non-specific binding a solution of 1 μg mL^{-1} fluorescently labelled FA was injected in each different slide and fluorescence was measured. The results are presented in Figure 5.8.

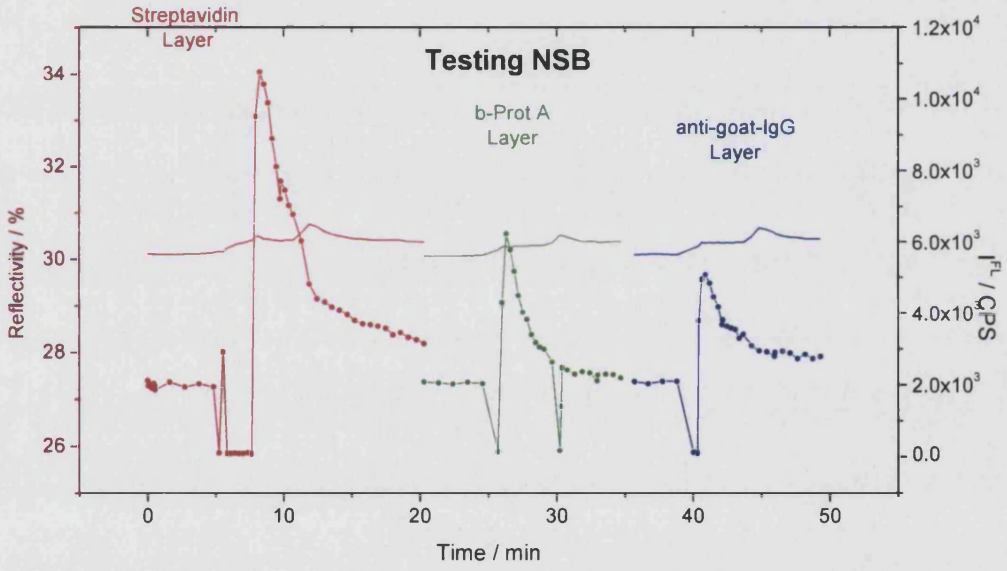

Figure 5.8 Non-specific binding tested in three different layers: Streptavidin; b-Protein A and anti-goat IgG.

In Figure 5.8 it can be observed that the fluorescence signal increases immediately after the injection the solution with the fluorescent probe, but decreases immediately after, finishing close to the initial value. The sudden increase in fluorescence may be due to the passage of fluorescence probes close to the enhanced evanescent field on the surface but little or no binding is detected. Therefore, it can be assumed that the fluorescently labelled FA does not bind non-specifically to the layers supporting the FA-antibody sensing surface.

In order to determine the dissociation binding constant of the fluorescently labelled FA to the FA-antibody, solutions of the fluorescently labelled FA with concentrations ranging from 500 ng mL^{-1} to 50 μg mL^{-1} were injected on the flow cell at a flow rate of ~ 4000 μL min^{-1}. Immediately after the whole solution is injected, the flow rate was changed to 42 μL min^{-1} to reduce hydrodynamic sheer forces on the bound FA. The increase of the fluorescence signal was followed during the introductions of the different solutions. The results are presented in Figure 5.9.

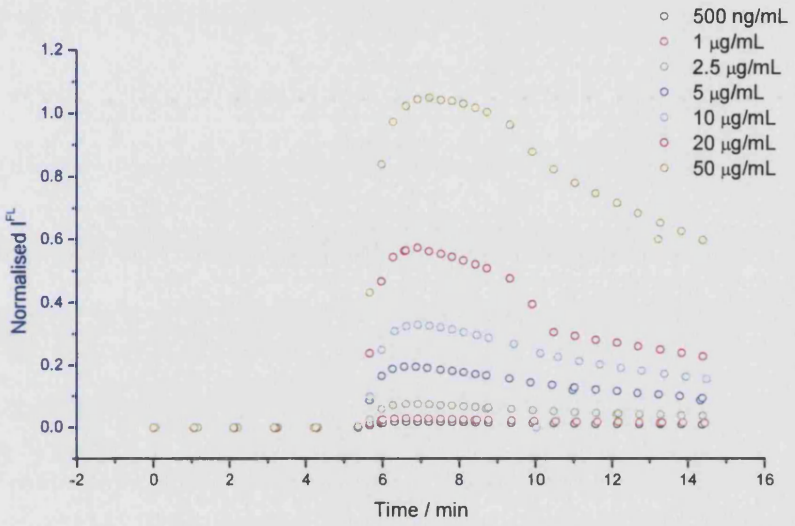

Figure 5.9 Normalised fluorescence kinetics measurements obtained for the range 500 ng mL^{-1} to 50 μg mL^{-1} Cy5-FA solutions.

Previous to the execution of the experiments, a test for the best regeneration buffer was carried out. Different buffers with different characteristics, such as Glycine HCl pH 1.7 used extensively in the previous chapter and NaOH 0.1 N pH 11 were tested for the complete desorption of the fluorescently labelled FA. However, only the Ethylene-Glycol (50% (v/v) buffer gave nearly complete regeneration of the surface, and was therefore chosen for the following experiments. The regeneration of the surface was carried out using a flow rate of ~ 4000 μL min^{-1}.

The experiments were reproduced three times for the same concentrations range in different prepared sensor surfaces. All experiments were reproducible and the fluorescence signal reached a maximum value after approximately 70 seconds. The maximum fluorescence signal was used, because for each concentration the maximum

value of the fluorescence signal corresponds to maximum number of occupied binding sites.

Figure 5.10 illustrates the plot of the normalised fluorescence signal against the concentration of the fluorescently labelled FA. The data was fitted with the Langmuir equation using the nonlinear least square fitting.

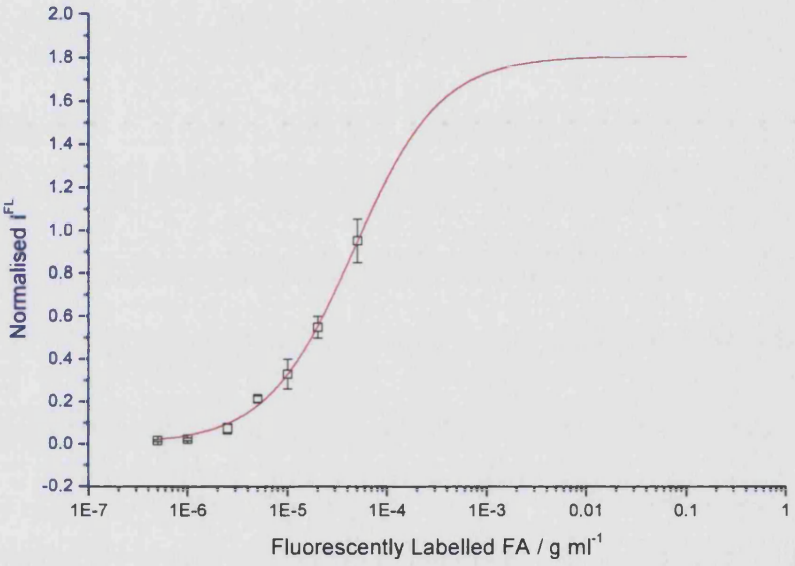

Figure 5.10 Relation between normalised fluorescence signal and the concentration of fluorescently labelled FA binding to the FA-antibody sensing surface.

The fitting of the Langmuir curve determined a dissociation constant (K_D) of 40 μg mL^{-1} ± 5.6 μg mL^{-1}. It is important to notice that the last concentration of fluorescently labelled FA was 50 μg mL^{-1} which is very close to the actual value of K_D. Therefore, the FA antibody sensing surface has the capacity to bind larger quantities of FA but higher concentrations of the fluorescently probe were not available.

In order to determine the dissociation rate constant (k_{off}) and the association rate constant (k_{on}), after the highest concentration fluorescently labelled FA solution had bound, the surface was rinsed with 50 mL of fresh running buffer, in this case HEPES-PF68, followed by recirculation. The decrease in fluorescence signal as a result of this rinsing step was monitored until a new equilibrium was reached. Figure 5.11 presents

an example of the desorption curve obtained, which was determined for two different experiments.

The desorption rate constant was determined using the desorption rate constant equation model presented in the chapter 2 ($R_t = R_0 e^{-k_{off} t}$). The average of the two desorption rate constants determined for two experiments was considered and the associated error was determined using the theory of errors.

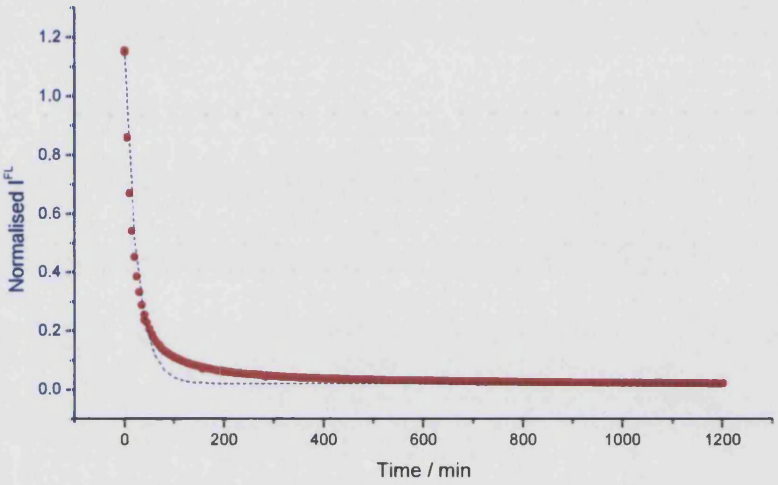

Figure 5.11 Desorption of fluorescently labelled FA from the FA-antibody sensing surface. The curve was fitted using the nonlinear least square fitting (fitting in blue, data in red).

The fluorescently labelled FA desorption from the FA-antibody sensing surface, desorption rate constant k_{off} was determined to be 3.842 x10^{-2} min^{-1} ± 9.2 x10^{-4} min^{-1}. From equation (2.42) it was possible to calculate the value of the association rate constant k_{on}, which was determined to be 9.6 x10^{-4} mL μg^{-1} min^{-1} ± 1.5 mL x10^{-4} mL μg^{-1} min^{-1}.

From the values determined it can be observed that the fluorescently labelled FA has high equilibrium desorption constant K_D. It is important to notice that the FA-antibody was raised against stearic acid which is a long chain fatty acid. The fluorescently labelled FA has a C:11 carbon chain which is considerably smaller when compared to the C:18 used. Therefore, the specificity of the antibody is lower for the fluorescently labelled FA. Again, the fluorescently labelled FA has a large fluorescent label attached

which considerably modifies the similarity between the fluorescent probe and the stearic acid against which the antibody was raised.

The FA-antibody employed had not been tested for determination of epitotes (binding pockets). It is possible that FA would bind to various regions of the antibody, eg, the antigen binding site and the Fc region. FA are hydrophobic small molecules that can interact via Van der Walls forces with various hydrophobic amino acid side chains from the protein, producing other non-desirable binding sites. Therefore, competition between the different binding sites for FA is possible.

However, it is expected that FA with more structural similarities with the stearic acid would present smaller desorption constants than the fluorescently labelled FA.

5.5 Small Chain Fatty Acid Competition Assay and Bilirubin Competition Assay

5.5.1 Non-labelled FA Binding to FA-Antibody

An interesting approach to determine the quantities of FA in an immunoassay is to utilise a competition assay. In this work, the supramolecular structure developed to build the sensor surface to study interactions between FA-antibody and the fluorescently labelled FA was employed in order to perform a competition assay between a non-labelled FA and the fluorescently labelled FA.

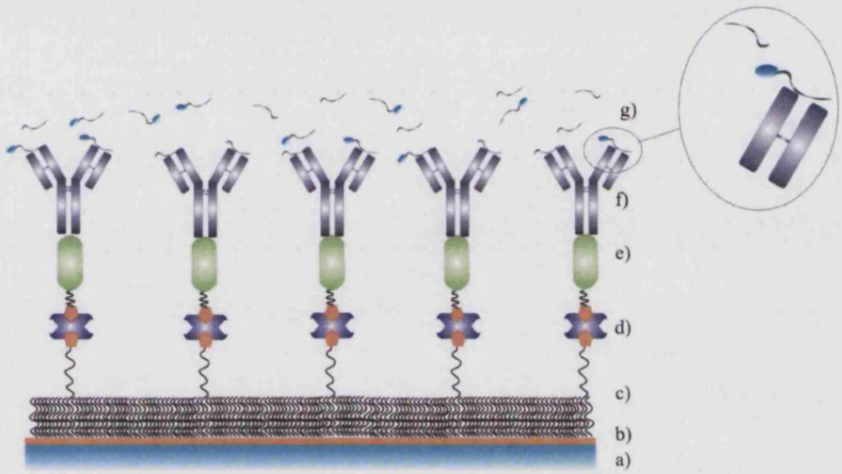

Figure 5.12 Schematic representation of the sensor surface supramolecular structure used in the competition assay. The different layers (a – f) are described in Figure 5.5. Layer g represents the solution mixture containing both the fluorescently labelled FA and the non-labelled FA. Both FA are competing for the same binding site of the FA-antibody.

For the first competition assay the undecanoic acid FA was chosen. Although a small chain FA was employed, the same used in the synthesis of the fluorescently labelled FA, both FA compete directly to the same binding site on the FA-antibody.

In order to perform the competition assay the concentration of the fluorescently labelled FA was kept constant throughout all the experiments, with a concentration of 5 μg mL^{-1}. For all the experiments, the first solution injected on the sensor surface was a solution containing only the fluorescently labelled FA. Subsequently, a mixture of solutions including 5 μg mL^{-1} of fluorescently labelled FA and a non-labelled FA with a range of concentrations from 320 ng mL^{-1} to 1 mg mL^{-1} in a 500 μL HEPES-PF68 buffer solution were injected followed by regeneration of the surface with Ethylene Glycol 50% (v/v).

The change in fluorescence from the competition assays are presented in Figure 5.13. The mixed solutions were recirculated for 5 minutes followed by rinsing for 5 minutes. A scan was performed after rinsing for all mixed solutions.

The regeneration of the surface was carried out for 3 minutes followed by rinsing of the surface for 5 minutes and SPFS scan was recorded. In the same way as the experiments carried out previously, the FA mixed solution was injected at a flow rate of ~ 4000 μL min^{-1} followed by a reduction of the flow rate to 42 μLmin^{-1}.

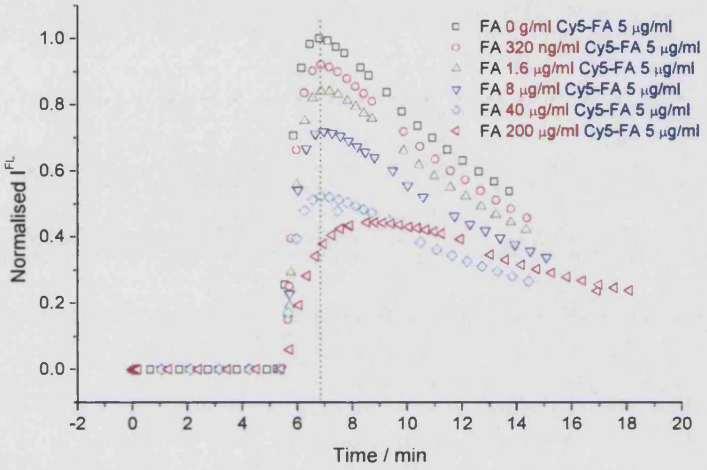

Figure 5.13 The normalised fluorescence kinetics measurements obtained for the different mixed solutions. A constant concentration of the fluorescently labelled (Cy5-FA) of 5 μg mL^{-1} was used mixed with a concentration range of small chain FA from 0 to 200 μg mL^{-1}.

The competition experiments were repeated three times and the same reproducible response was obtained. In order to determine the binding constant of the non-labelled FA the fluorescent signal after 55 seconds following addition of the FA mixture was recorded. The values obtained were treated statistically and the associated error determined. A plot of the concentration of the non-labelled FA versus the normalised fluorescence is presented in Figure 5.14.

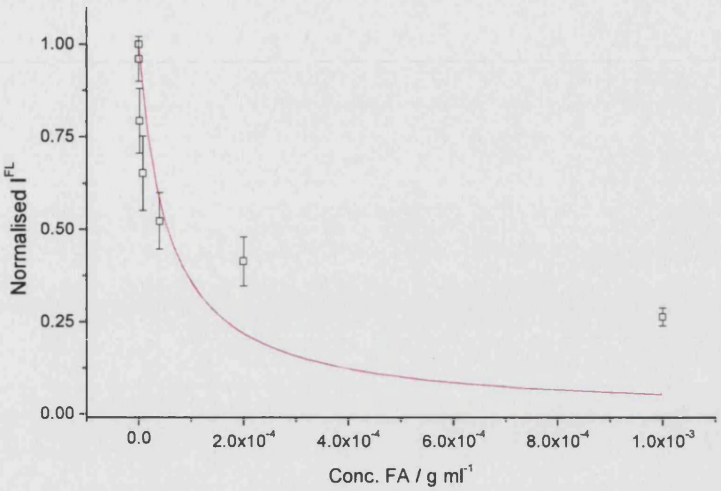

Figure 5.14 Normalised fluorescence intensity versus non-labelled FA concentrations. An estimation of the equilibrium desorption constant of undecoinc acid from FA-antibody was determined by fitting the data to the competition assay model presented in equation (5.12).

Using the theoretical model described by Motulsky and Aranyi [203, 204] assuming a free competition for the same binding site it is possible to determine the equilibrium dissociation constant of the non-labelled FA. The value obtained was 50 μg mL^{-1}± 30 μg mL^{-1}. Although the value of the equilibrium dissociation constant of the non-labelled FA is of the same order of magnitude of the fluorescently labelled FA, which was expected as the carbon chain has the same length, there are three important points to take into consideration when analysing the results obtained.

First, when binding the fluorescent labelled FA to the sensor surface there is an overshoot of the adsorption curve followed by a decreased of the intensity of the signal until the equilibrium is reached (*vide supra Figure 5.4*). This result suggests that the fluorescently labelled FA compete for the same binding site on the FA-antibody or that the molecule has more than one binding site for the FA .

Secondly, the same behaviour is observed when the mixed solutions are injected on the surface. In this case, it suggests that the carbon chain of the fluorescent labelled FA is competing with the undecanoic acid for different binding sites on the antibody as well fluorophore label on the FA itself.

Thirdly, it is important to notice that following the adsorption of a certain quantity of FA the binding appears to take longer to reach its maximum value of equilibrium, therefore there is a change in the association rate constant as well in the dissociation rate

constant. This result suggest that as the quantity of FA bound to the antibody increases, there is an increase in the hydrophobicity of the antibody surface, suggesting that the antibody refolds presenting new binding sites.

Consequently, when plotting the increase of concentration of the non-labelled FA versus the normalised fluorescent signal, it was expected for a standard behaviour that the fluorescence signal would approach zero, as the concentration of the non-labelled FA increased (from equation 5.12). However, as can be observed in Figure 5.14, the values first show a steep decrease with FA concentration followed by a levelling off. When the new binding sites come forward to the surface of the antibody, new rates of association and dissociation are found, contributing for the overall reaction. This phenomenon has been previously described for the binding of FA to all types of albumin [198].

5.5.2 Bilirubin Binding to FA-Antibody

Bilirubin is essentially a waste product, formed when red blood cells die and haemoglobin is broken down. Haemoglobin is broken down within the macrophages to haem and globins; the haem is further degraded to Fe^{2+}, carbon monoxide and bilirubin via the intermediate compound biliverdin.

Since bilirubin is poorly soluble in water, it is carried to the liver bound to albumin. Bilirubin is made water-soluble in the liver by conjugation with uridine diphosphoglucuronic acid or UDPGA. As part of bile, the soluble or "conjugated" bilirubin then passes through the common bile duct and is temporarily stored either in the gallbladder or passes right away into the gut. Some of the excreted bilirubin may be reabsorbed from the gut. Bacteria in the intestines modify bilirubin to form stercobilinogen, causing the brown colour of faeces. The yellow colour of urine is a result of urobilin, another breakdown product of bilirubin [209].

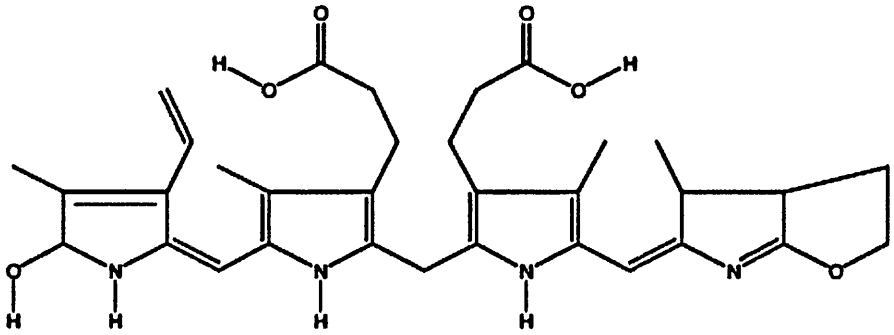

Figure 5.15 Molecular structure of bilirubin. Bilirubin is poorly soluble in water and therefore in the plasma is transported via albumin, competing in this way with the unbound FA present in the blood as well.

Bilirubin (FisherSci, UK) was dissolved in NaOH 0.1N and then HEPES-PF68 buffer was added to a final concentration of 200 μg mL^{-1}.

The procedure used to perform the competition assay of non-labelled FA and fluorescently labelled FA was adopted for the bilirubin competition assay. Therefore, solutions consisting of fluorescently labelled FA mixed with a range of bilirubin concentrations from 0 till 1 μg mL^{-1} were prepared and injected on the surface at a flow rate of ~4000 μl min^{-1} followed by recirculation at 42 μl min^{-1}.

In order to determine the equilibrium dissociation constant of bilirubin the maximum values of fluorescence were considered and the dissociation constant was estimated using the model previously described. Figure 5.16 shows the relation between the bilirubin concentration increase in the injected solutions versus the normalised fluorescence signal.

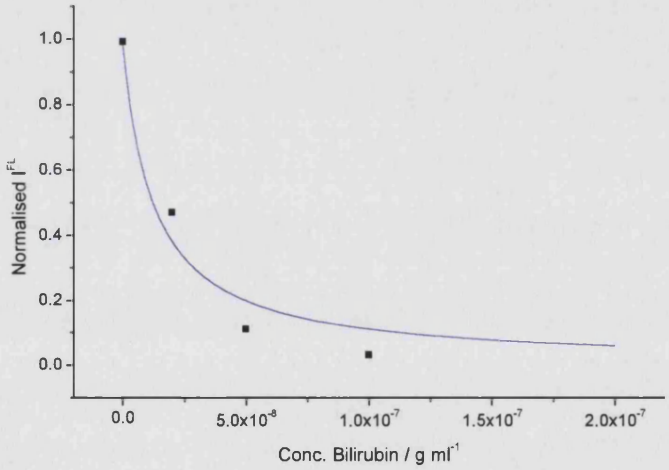

Figure 5.16 Plot of the normalised fluorescence intensity versus bilirubin increasing concentrations in injected solutions.

In this experiment a dissociation constant of 5.4 ng mL^{-1} ± 1.5 ng mL^{-1} was obtained, but while these results demonstrate the generic feasibility of the assay care should be taken in not over interpreting the numerical values as reproducibility of this specific experiment was a problem.

The FA-antibody used in these experiments is completely new, no more studies were produced from it, and no information about epitopes location, specificity, and activity was available. Moreover, the experiments produced for the competition of bilirubin

were carried out a long time after the FA-antibody had been produced. Consequently, the antibody might have lost some of its activity during the long storage period.

5.6 Development of a Sensor Surface Using Human Serum Albumin

5.6.1 Assembly of Sensor Surface

FA are transported in blood in a form of albumin complex and few proteins can bind FA as tightly or in such large amounts as albumin does. Therefore, understanding the binding of FA to albumin and apply it to detect the FA is an advantage in the world of science. Kleinfeld et al and Spector have studied these interactions extensively and they have used ADIFAB to detect the partition coefficients of FA in solution to albumin [188, 198, 199, 202].

In this work a sensor surface using albumin was developed in order to detect FA in solution following the same generic approach as for the FA antibody. The first approach for making the sensor surface was based on all the knowledge acquired during the first one and a half years work. Therefore, as mentioned previously, an organised surface with the antigen binding sites turned away from the surface and by locating the fluorophore more than 10 nm from the gold surface, in order to prevent from quenching and from non radiant energy transfer from the fluorophore with the metal layer.

To produce the sensor surface, the same strategy described previously in this chapter was used to build the supramolecular structure consisting of SAM-streptavidin followed by adsorption of biotinylated Protein A. As previously mentioned, Protein A binds favourably to the Fc region of the antibody orienting the antigens binding sites away from the surface.

A 50 μg mL^{-1}solution of Human Serum Albumin Antibody (anti-HSA) in Borax buffer, was injected onto the b-Protein A surface and the binding was followed using SPR. A comparison between the binding of anti-HSA to b-Protein A and the binding of FA-antibody to b-Protein A is presented in Figure 5.17.

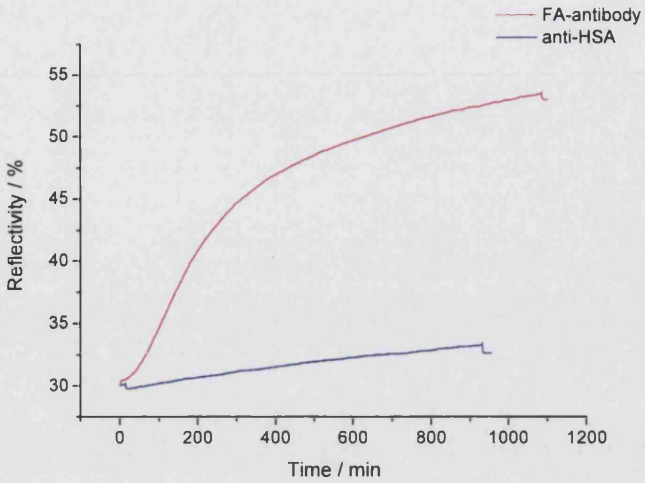

Figure 5.17 Comparison between adsorption of FA-antibody and anti-HSA onto b-Protein A surface followed by SPR.

It can be observed, in Figure 5.17, from the SPR signal that anti-HSA takes longer to reach equilibrium with b-Protein A on the surface than FA-antibody because of its lower binding affinity to protein A. The reason for this is not completely clear at this time.

Because of this low binding rate, a different strategy for anti-HSA immobilisation was employed. Anti-HSA was randomly biotinylated following the procedure used for biotinylation of anti-hCG antibodies in chapter 3. Figure 5.18 schemes the strategy used in this sensing surface for detection of FA.

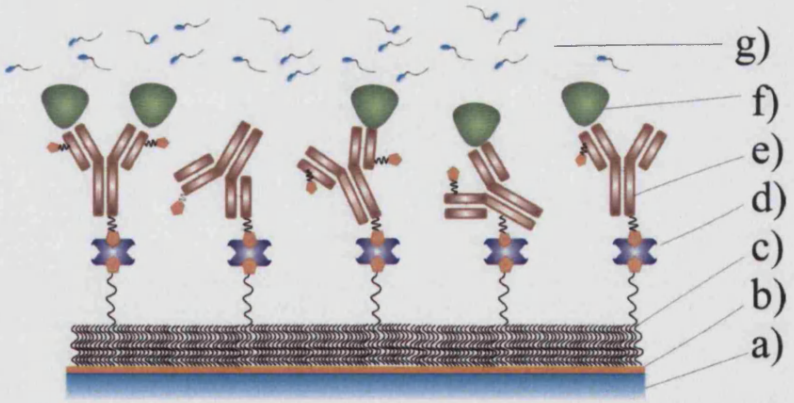

Figure 5.18 Schematic representation of the sensor surface developed using anti-HSA and HSA for detection of FA in solution. a) LaFSN9 glass; b) 50 nm gold; c) binary mixed thiol SAM 1:9; d) Streptavidin; e) Randomly biotinylated Anti-HSA; f)HSA; g) Cy5-FA

The first experiments were designed to verify whether the biotinylated anti-HSA (b-anti-HSA) was still active and to verify the adsorption of albumin on the surface. From the hCG chapter it was concluded that to obtain the maximum loading capacity of the randomly biotinylated antibody surface the optimum ratio of mixed thiols was 1:99.

Therefore, the 1:99 a slide of biotinylated thiols mixture was incubated for 16h and streptavidin was added onto the incubated thiol surface.

A 50 x 10^{-9} M solution of b-anti-HSA in PBS-TA buffer was added onto the thiol-streptavidin matrix. The increase of the reflectivity signal was followed for binding of streptavidin, b-anti-HSA and HSA. After building the antibody monolayer, a 100 μg mL^{-1} solution of HSA in PBS-TA was added onto the surface. All solutions were injected at a constant rate of ~4 mL min^{-1}. Figure 5.19presents the changes in reflectivity due to adsorption of the different proteins onto each produced surface. The binding curves are shown in Figure 5.19.

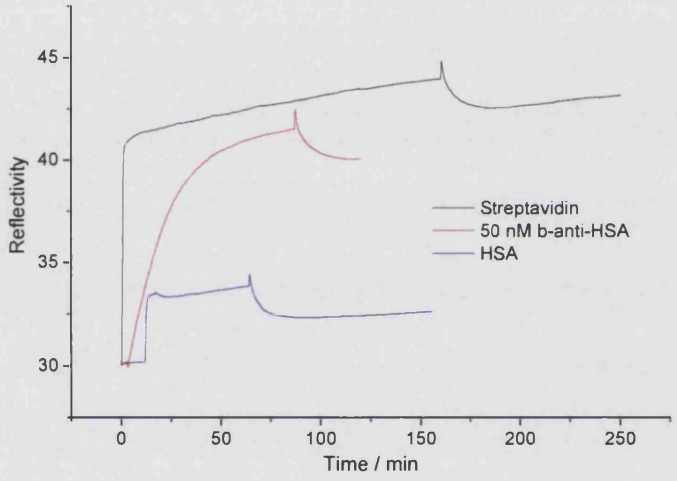

Figure 5.19 Production of the different surface layers: first, adsorption of streptavidin, second adsorption of b-anti-HSA and, finally, adsorption of HSA. The signal follows changes in reflectivity.

In Figure 5.19 a rapid change in the refractive index when HSA adsorbs onto the b-anti-HSA monolayer is observed. This is due to change in the bulk refractive index caused by the use of a highly concentrated solution. Therefore, a smaller concentration of 50 μg mL^{-1} was used in the following experiments.

5.6.2 Binding of Fluorescently Labelled FA to Albumin Immobilised

In order to produce a sensor for FA using albumin adsorbed on the surface, the competition assay of the fluorescently labelled FA against a non-labelled FA towards albumin was adopted. However, the fluorescently labelled FA binding to albumin characteristics were primarily determined. Therefore, following the building of the supramolecular protein layers, the surface was tested for adsorption of fluorescently labelled FA.

Following the adsorption of HSA to the b-anti-HSA surface the buffer was changed to HEPES-PF68 used for FA solutions. A range of solutions from 0 to 200 μg mL^{-1} of fluorescently labelled FA were prepared and injected on the surface. The injection of each fluorescently labelled FA solution was carried out at ~4000 μl mL^{-1} followed by recirculation of the solution at 42 μl mL^{-1}. The intensity of fluorescence produced was followed using SPFS and the results are presented in Figure 5.20. A neutral density filter of 30% was used in order to prevent saturation of the photomultiplier tube.

The fluorescently labelled FA solutions of 200 ng mL^{-1}, 2 μg mL^{-1}, 20 μg mL^{-1}and 200 μg mL^{-1}were subsequently injected onto the HSA monolayer without rinsing or regeneration of the surface. After injection of each concentration, equilibrium was allowed to be established and it was followed by injection of fluorescently labelled FA solution with higher concentration. In Figure 5.20 shows the increase of fluorescence intensity as the difference solutions, from smaller to higher concentrations, are added onto the albumin monolayer.

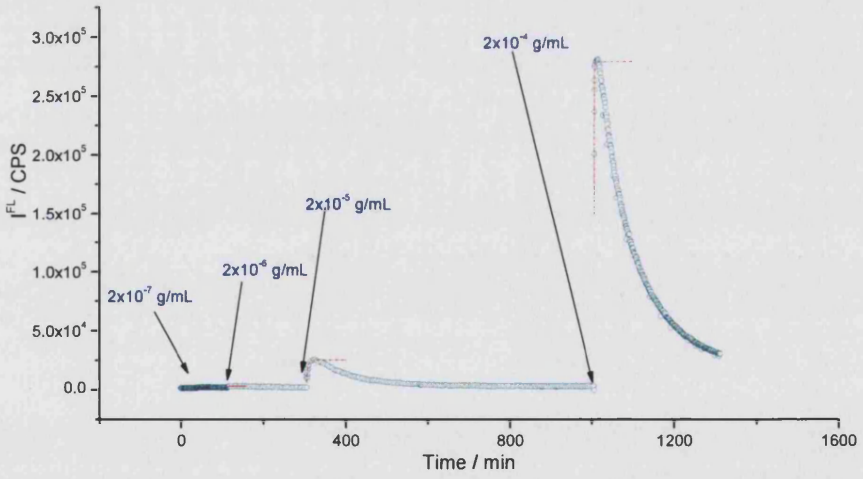

Figure 5.20 Fluorescent intensity change as the different solutions of fluorescently labelled FA are consequently injected on the surface.

It can be observed in Figure 5.20 that after each injection there is an overshoot of the fluorescence signal followed by a decrease until an equilibrium situation is achieved. These results are in accordance with what is described by Spector and Kleinfeld [188, 198] who stated that albumin has more than one binding site and each mole of mole of

FA influences the binding of the next through cooperative effects, producing a configuration adaptation of albumin.

Therefore, there is a competitive effect of the fluorescently labelled fatty acid to the different binding sites and no reproducibility of measurement was achieved. So SPFS is not the best technique to determine the different dissociations constants for each binding site present in albumin.

5.7 Conclusions

In this thesis, a methodology for detection of FA on sensor surfaces has been investigated. FA are low molecular weight molecules present in the majority of biological systems and are extremely important to mammalian health. The level of FA in the blood is a marker for the state of cardiac function.

Two strategies have been studied in order to determine the concentrations of FA: i) Using FA-antibody; ii) Using a sensor surface with albumin the principal carrier of FA in the plasma. A fluorescently labelled FA was synthesised to produce a competition assay with non-labelled FA.

In order to produce the first sensor surface the FA-antibody was orientated on the surface by binding the Fc to the already bound to b-Protein A. Non-specific binding of fluorescently labelled FA was tested on different constituent surfaces and it was found to be negligible.

Therefore, it was possible to determine the equilibrium dissociation constant of 40 μg mL^{-1} ± 5.6 μg mL^{-1} of the fluorescently labelled FA to FA-antibody by determining a dose response curve. A competition assay for unlabelled FA (undecanoic acid) was carried out and the dissociation constant was determined to be 50 μg mL^{-1} ± 30 μg mL^{-1}.

There is a large error associated with this result because when observing with more detail the kinetic binding curve for absorption of the solution containing no competitor (no non-labelled FA) it can be observed as an overshoot of the curve which corresponds to a typical behaviour of a protein capable to bind more than one ligand. This result suggests that the FA-antibody has more than one binding site for the fluorescently labelled FA or that both molecular regions (chromophore and carbon chain) compete for the binding site.

Looking into the results with more detail, we believe that the quantity of FA bound to the antibody influences the binding of more FA because there is an increase in the hydrophobicity of the antibody surface. This suggests that the antibody refolds presenting new binding sites, therefore showing a capacity to adapt to excessive hydrophobicity on the surface. Consequently, the binding of the fluorescently labelled

antibody does not decrease till zero but becomes stable, as there are more binding sites contributing for the overall dissociation constant.

The competition of bilirubin and fluorescently labelled FA binding to FA-antibody was also tested and it was possible to follow the decrease of the fluorescent signal with the increase of bilirubin concentration. However, due to practical problems related with the activity of the FA-antibody it was not possible to reproduce these results. FA-antibody is totally new and not much information about its activity and binding capacity is known until now.

Another strategy was investigated in order to develop a FA sensor. In this last approach HSA, the main FA carrier in the plasma, was immobilised on the surface via a surface bound, randomly biotinylated anti-HSA. However, albumin binds in a very complex way to FA and various binding sites are present, therefore, for the simplicity that is required to produce a sensor surface, albumin is not the suitable option.

Unfortunately, the work with the fluorescently labelled FA had to be finished because there was no more product available for more detailed study and reproducibility of the results. But more studies about the stability of the FA-antibody and the competition of the fluorescently labelled FA and stearic acid should be carried out. The competition assay for FA-antibody was proven to be of potential application for the development of a FA sensor.

6 Plasmonic Enhancement of Fluorescence by Gold Nanoparticles

In this chapter, a description of DNA molecules, colloidal particles and colloidal theory is given. Preliminary results were promising, showing the enhancement of fluorescence intensity due to the presence of GNP in solution.

6.1 DNA

6.1.1 Chemical Structure and Composition

DNA, deoxyribonucleic acid, is a biopolymer made of a large number of deoxyribonucleotides, each nucleotide is structured by a base, a sugar (deoxyribose) and a phosphate group [210, 211]. The bases of DNA carry genetic information, whereas their sugar and phosphate groups perform a structural role.

DNA is the hereditary molecule in all cellular life forms and it has two major functions:

i) To direct its own replication during cell division

ii) To direct the transcription of complementary molecules of RNA for protein synthesis.

Replication of DNA occurs in the presence of DNA polymerases, which are the enzymes responsible for the DNA replication by taking instructions from DNA templates. These extremely specific enzymes replicate DNA with an error frequency of less than one in a million nucleotides [211].

DNA bases are derivatives of purines or pyridines. The purines are adenine and guanine, and the pyrimidines are thymine and cytosine. The bases usually are represented by A, G, T, and C, respectively. In a deoxyribonucleotide, the C-1 carbon atom of deoxyribose is bonded to N-1 of pyrimidine or N-9 of a purine, and with a phosphate ester bound through esterefication of the hydroxyl group attached to C-5 of the sugar. A representation of all four bases and a representation of the bound nucleotide are shown in Figure 6.1.

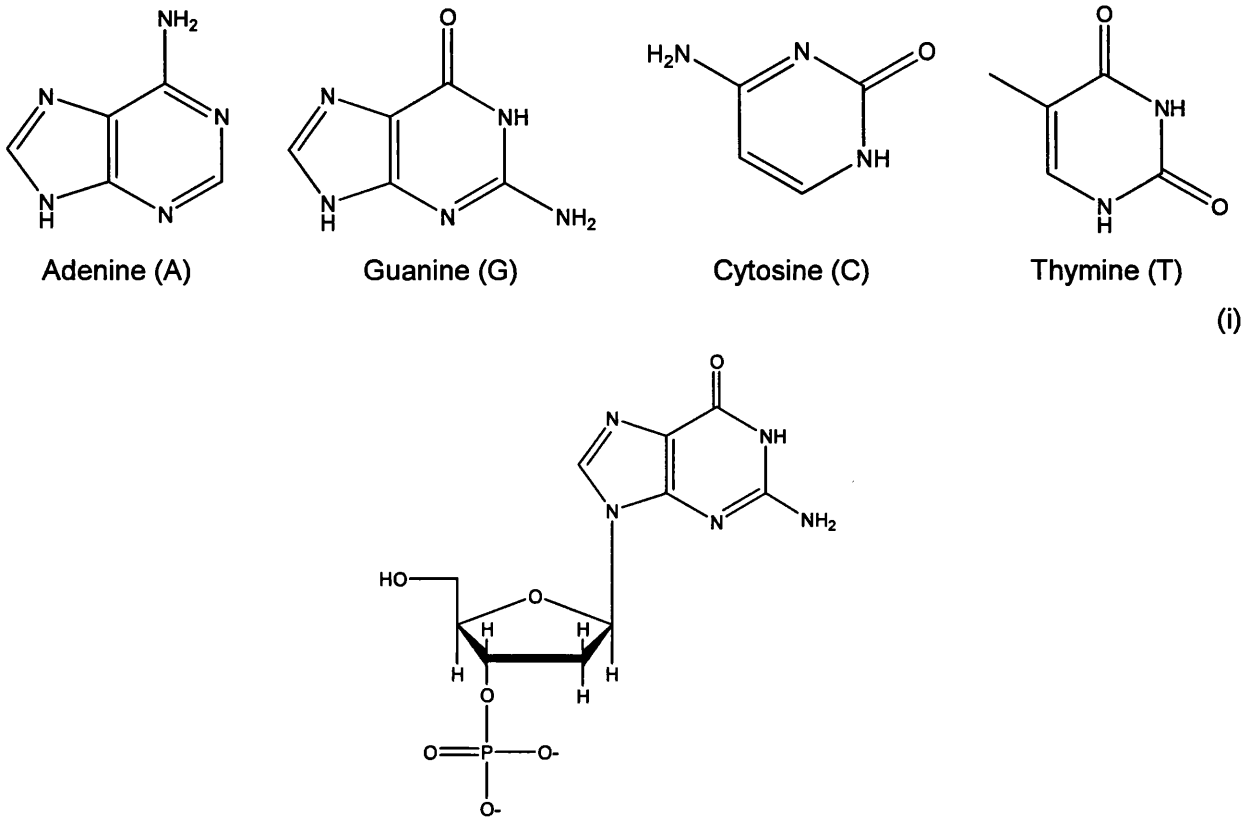

Figure 6.1 (i) DNA bases structures. Adenine and Guanine are derived from purine and Cytosine and Guanine are derived from pyrimidine. (ii) Structure of a nucleotide with a guanine base.

The backbone of DNA, which is invariant through out the molecule, consists of deoxyriboses bound to phosphate groups. More specifically, the 3'-hydroxyl group of the sugar moiety of one deoxyribonucleotide is bound to the 5'-hydroxyl of the adjacent sugar by a phosphodiester bridge. The variable part of the DNA is the sequence of four kinds of bases (A, T, G and C).

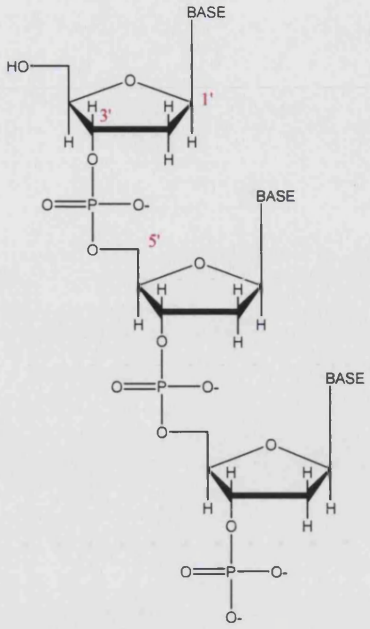

Figure 6.2 Structure of a part of a single strand DNA. In the sugar, carbon 1' is bound to the base and 5' is bound to a hydroxyl group.

One of the properties of the DNA chain it is its polarity and water solubility. One end of the chain has a 5'-OH group attached to the deoxyribose and the other a 3'-OH attached to the phosphate that it is not bound to a further nucleotide. By convention, a single strand DNA (ssDNA) follows from 5'-OH to a 3'-OH. Thus, when a sequence of nucleotides is presented, e.g., ACT, it is known that the 5'-OH end belongs to the deoxyadenosine group and the 3'-OH to the deoxythyminosine group.

6.1.2 DNA double helix

Two DNA single strands can bind to each other in an orderly manner and form a double stranded DNA molecule. Its structure was determined in 1953 by Watson and Crick. They determined the three dimensional structure of DNA by analysing pictures of X-ray diffraction and immediately deduced DNA's mechanism of replication.

The most important features of their model are:

1. It consists of two polynucleotide strands that wind about a common axis with a right handed twist to form an approximately 20 Å diameter double helix. The two strands run in opposite directions and so are said to be antiparallel.
2. The purine and pyrimidine bases are on the inside of the double helix whereas the phosphate and deoxyribose units are on the outside. The planes of the bases are perpendicular to the helix axis.

3. The diameter of the helix is approximately 20 Å. Each base on one strand is separated from the other by 3.4 Å and related by a rotation of 36 degrees. Hence, the helical structure repeats after 10 residues on each single strand, that is, intervals of 34 Å.
4. The two chains are held together through hydrogen bonds between pairs of bases. Adenine binds always to thymine and guanine is always paired with cytosine.
5. The sequence of bases along the polynucleotide chain is not restricted in any way. Thus, the precise sequence of bases carries the genetic information.

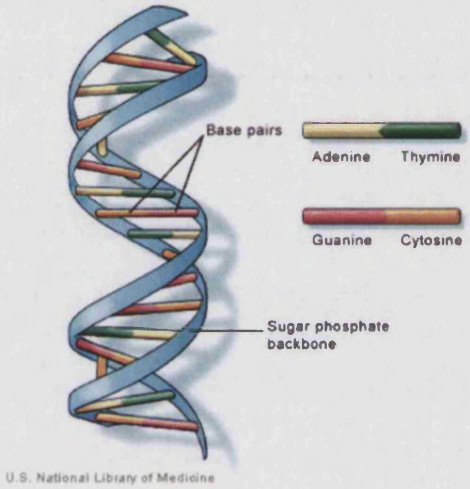

Figure 6.3 Diagram of the double helix DNA with the different sequence of bases, which transport the genetic information.

The most important aspect of the DNA double helix is the specificity of the pairing of bases. It was previously discovered by Chafgaff that the ratios of adenine to thymine and of guanine to cytosine were nearly 1.0 in all the species that he studied, although why was not understood.

With this model, it was determined that adenine must bind to thymine and guanine to cytosine due to steric hindrance factors and hydrogen bonds. The glycosidic bonds that are attached to a pair of bonded bases are always 10.85 Å apart, which is the optimised space for a purine-pyrimide base pair. In contrast, there is insufficient space for two pyrimidines and more than sufficient for two purines. On the other hand, Adenine cannot pair with cytosine because there would be two hydrogens near one of the bonding positions and none at the other. In addition, likewise, guanine cannot pair with thymine. In contrast, adenine forms two hydrogen bonds with thymine and guanine

forms three hydrogen bonds with cytosine. The orientations and distances of these hydrogen bonds are optimal for achieving strong attraction between the bases.

6.1.3 Applications

The specific sequence of bases along a strand of DNA and the unique complementary nature of the pairing between the base pairs (adenine and thymine or cytosine and guanine) of adjacent strands in the double helix is the basis of biodiversity.

The ability of a single-stranded nucleic acid molecule to recognise and bind (hybridise) to its complementary partner in a sample has been used in genetic analyses in order to obtain sequence information. In the biomedical and pharmaceutical industry, this characteristic is widely used to determine mutations in DNA, many of which are responsible for diseases. Therefore, analysis of genes can be used for diagnosis of diseases and moreover can be used for the detection of bacterial pathogens [30, 39, 55, 152, 212-217].

A number of strategies for the detection of DNA strands have been developed including surface hybridisation on sensor chips [Afymetrix] and electrochemical methods. The research developed in the last decade, with more relevance to the work presented to this chapter, is on gold nanoparticles conjugated to oligonucleotides. These materials have been of great interest due to the potential of DNA to pair bases in a programmable way. Therefore, gold nanoparticles coupled to DNA have been used to organise and functionalise gold nanoparticles.

Alivisatos et al. were able to pattern DNA – nanoparticles conjugates on the nanometre scale using DNA base pairing interactions. Employing single stranded DNA oligonucleotides of a defined length and sequence, they were able to synthesise what they have defined as "nanocrystal molecules", in which discrete numbers of gold nanocrystals were organised into spatially defined structures [218].

Mirkin and Letsinger measured the formation of nanoparticles networks, formed by the specific hybridisation of tethered oligo's attached the gold nanoparticles. This produced a colorimetric sensor, due to changes in the surface plasmon band (SPB) (described in section 6.2.2) on aggregation of nanoparticles into the network [219-223]. The aggregation of gold nanoparticles linked through oligonucleotides gives a red-to-blue colour change (red shift from 520 nm to 600 nm) that can be used in DNA-sensing. It was shown that various macroscopic nanoparticles assemblies have plasmon

frequency changes that are inversely dependent on the oligonucleotide linker length. By controlling the gold nanoparticles composition, periodicity and the aggregate thermal stability, Mirkin and Letsinger were able to demonstrate the influence on optical, mechanical and electrical properties of gold nanoparticles [224].

The optical properties of gold nanoparticles with a diameter range from 13 to 17 nm, due to the SPB, led to the development of a highly selective diagnostic method for DNA detection, based on the distance-related SPB of the particles. It was found that the SPB changes are inversely dependent on the oligonucleotide linker length, controlling the interparticle distance (section 6.2.2) [225]. Another parameter that controls the shift of the SPB was found to be the aggregate size [222]. An understanding of the interdistance dependence and aggregates size and their relationship to materials architecture is essential for nanoparticle network materials production, especially in the biodetection area.

In 2003 Storfoff et al, presented a paper on gold nanoparticle-based detection system for a DNA-based diagnostic application. In this system, oligonucleotides were immobilised on a surface that captures oligonucleotide targets, which were then detected via hybridisation to gold nanoparticles-attached probes. The gold nanoparticles were then amplified with silver, which allowed measurements using evanescent wave induced light scatter and a comparison with Cy3-based fluorescence probes was provided demonstrating that silver amplification was ~1000 times more sensitive [226].

In this work, the SPB produced by gold nanoparticles through light absorption and the ability to excite fluorophore-DNA linked to gold nanoparticles was measured. First, a description of the synthesis and properties of gold nanoparticles is provided.

6.2 Gold Nanoparticles

6.2.1 Synthesis and Characterisation

Nanoparticles are of great scientific interest as they are effectively a bridge between bulk materials and atomic or molecular structures. A bulk material should have constant physical properties regardless of its size, but at the nano-scale this is often not the case. Size-dependent properties are observed such as quantum confinement in semiconductor particles, surface plasmon resonance in some metal particles and superparamagnetism in magnetic materials.

Metal, dielectric, and semiconductor nanoparticles have been formed, as well as hybrid structures (e.g., core-shell nanoparticles). Nanospheres, nanorods, and nanocups are just a few of the shapes that have been grown. Semiconductor quantum dots and nanocrystals are types of nanoparticles. Such nanoscale particles are used in biomedical applications as drug carriers or imaging agents [227].

Gold nanoparticles are some of the most stable metal nanoparticles [227]. The most common method to synthesise gold nanoparticles is by reduction of gold (III) derivatives, usually using citrate reduction of HAuCl4 in water, which was introduced by Turkevitch in 1951 [227].

There are different techniques to characterise nanoparticles. The most common techniques are electron microscopy (TEM, SEM), atomic force microscopy (AFM), x-ray photoelectron spectroscopy (XPS), powder x-ray diffractometry (XRD), and Fourier transform infrared spectroscopy (FTIR). Studies of electron transport, kinetics of electron-transfer, size effect on the kinetics and the chemical states of gold nanoparticles employing electrochemistry, scanning electrochemical spectroscopy, X-ray absorption near-edge structure (XANES) and angle resolved X-ray photoelectron spectroscopy have been carried out in different systems. These systems are extensively reviewed by Daniel et al [227].

The most interesting characteristic with relevance for the work presented in this chapter is the optoelectronic property of gold nanoparticles, which is related to the surface plasmon adsorption band (SPB) due to the collective oscillation of the conducting electrons of the gold core. The combination of photonics with biology and medicine is very promising for biomolecular manipulations and applications, such as labelling, detection, and transfer of drugs, including genetic materials [227]

6.2.2 The Surface Plasmon Absorption Band (SPB)

Nanoparticles follow the quantum mechanical rules when the de Broglie wavelength of the valence electrons is of the same order as the size of the particle itself [227]. When this occurs, the particles behave electronically as one-dimensional quantum boxes. The free electrons are trapped in such metal boxes and present a characteristic oscillation frequency of the plasmon resonance band (PRB) observed near 530 nm in the 5-20 nm diameter particle size range. Thus, the deep red colour of gold nanoparticles solutions in water reflects the surface plasmon absorption band (SPB). At the surface of nanoparticles there are collective oscillations of electrons, due to the 6s electrons of the conducting band, which, by light excitation, produce the SPB.

The nature of the SPB was determined by Mie in 1908 [228]. According to Mie's theory, the total cross section composed of the SP absorption and scattering is given as a summation overall of the electric and the magnetic oscillations. By solving, Maxwell's equations for spherical particles with the appropriate boundary conditions the surface plasmons were theoretically described. Mie's theory assigns the plasmon band of spherical particles to the dipole oscillations of the free electrons in the conduction band occupying the energy states immediately above the Fermi energy level [229].

The characteristics of the SPB are:

i) its position around 520 nm;

ii) Its sharp decrease with the decreasing core size for gold nanoparticles (with a core diameter range between 1.4 – 3.2 nm) due to the quantum size that becomes important for particles with core size < 3 nm and also cause a slight blue shift. The decrease of intensity of the SPB as particle size decreases is accompanied by broadening of the plasmon bandwidth.

iii) Step like spectral structures indicating transition to the discrete unoccupied levels of the conducting band on gold nanoparticles with core diameters between 1.1 and 1.9 nm.

Thus, the SPB is absent for gold nanoparticles with diameters < 2 nm, as well as for bulk gold (except via specific coupling of light via prisms).

The SPB is influenced by particle shape, medium dielectric constant, temperature and pressure. Coffer et al. reported the effect of pressure on the peak position and the line width of the surface plasmon absorption spectra in colloidal gold and silver particles. In

their work, it was observed that for large particles a red-shift was produced in the spectra when the pressure was increased [230].

As predicted by Mie's theory, the refractive index of the solvent induces a shift on the SPB. Englebienne determined affinity constants of different interactions between protein antigens and their specific antibodies, using the shift in the SPB wavelength of colloidal gold particles due to changes in the refractive index of the interface [231].

6.2.3 Fluorescence Using Gold Nanoparticles

Fluorescence studies of gold nanoparticles have been carried out under various conditions [58, 232-241], including femtosecond emission [232] and steady-state investigation of the interaction between thiolate ligands and the gold core [233]. It has been observed that resonant energy transfer in fluorescent ligand-capped gold nanoparticles is a phenomenon of high relevance for biophotonics [240, 242] and material sciences [130, 242, 243] but is not yet well understood.

The radiative and non-radiative rates critically depend on the size and shape of the gold nanoparticles, the distance between the dye molecules, the orientation of the dipole with respect to the dye-nanoparticle axis, and the overlap of the molecule's emission with the nanoparticles absorption spectrum [241].

A study of the radiative and non-radiative decay rates were in a lissamine dye molecule spaced 1 nm from the surface of variously size gold nanoparticles ranging from 1 nm to 30 nm, using time-resolved fluorescence was performed by Dulkeith [239]. It was concluded that fluorescence quenching was caused not only by an increase of the nonradiative rate (assumed to be resonant energy transfer only), but as well, by a decrease in the dye's radiative rate. The most pronounced quenching effect was found in the smallest gold nanoparticles of 1 nm radius.

The increase in fluorescence yield was observed when nonradiative decay channels were suppressed, e.g., via formation of thin films of a hybrid system comprising thiophene based polymer mixed with gold nanoparticles [236].

Different research groups have looked into application of the optical properties of the gold nanoparticles and organic fluorescence dyes. Hybrid molecules composed of biomolecules, such as proteins or polynucleotides, and nonbiological inorganic objects (for example, tiny particles of insulators, semiconductors, and metals) have been

assembled, recently. Duberetret et al., for example, have introduced a hybrid material composed of 1.4 nm diameter gold nanoparticles, an organic dye and a 25-nucleotide long ssDNA molecule, which forms a hairpin-shaped structure when dissociated with the complementary strand, bringing the dye close to the metal surface [240]. In this case, as mentioned previously, the fluorescence quenching is only due primarily to the gold, as the surface plasmon resonance is not present for particles with a diameter lower than 2 nm. When the complementary strand is present, the fluorescence signal increases as the dye becomes captured further away from the surface due to hybridization with the complementary strand.

On the other hand, Li et al. have developed a novel fluorescence quenching based assay by exploiting the ability to create conditions where ssDNA adsorbs on negatively charge gold nanoparticles while dsDNA does not. The probe is tagged with a dye that is quenched when it is not hybridised with the components of the analyte. They were able to measure sub-femtomole amounts of the untagged target [244].

Dulkeith et al. produced a study to show the influence of gold nanoparticles on the quantum yield of fluorophores, more specifically, of Cy5 fluorophores, conjugated to an oligonucleotide, tuning the space between the chromophore and the gold nanoparticles by varying the ssDNA surface coverage. They have observed decreased quantum efficiencies for all examined distances between 2.2 and 16.2 nm [245].

Others have observed enhancement of fluorescence due to the presence of gold nanoparticles. Thomas et al. used Py-CH_2-NH_2 bound to gold nanoparticles in organic solvents, which exhibit strong emission bands at 383 and 403 nm. However, the new electronic transitions of the pyrene chromophore became allowed when the amine group bound strongly to the gold nanoparticle and are not due to the presence of the surface plasmon band [58].

In this work, we try to prove the enhancement of the fluorescence signal due to excitation of the chromophore via the surface plasmon band produced by the gold nanoparticles. In order to achieve this, gold nanoparticles with a 10 nm diameter were employed. The gold nanoparticles had adsorbed on the surface a layer of streptavidin. Biotinylated ssDNA was coupled to the gold nanoparticles and fluorescently labelled ssDNA target was used. An important aspect taken into to account was that the chromophore would have to be excited by the wavelength of the surface plasmon

resonance produced. Therefore, Alexa Fluor 555 was chosen and coupled to the target ssDNA.

6.3 Colloids Stability

Colloids can be stable for a number of years, as for example, the gold colloidal solutions prepared by Michael Faraday that are still stable for over 150 years (prepared 1850), although this is the most thermodynamically unfavoured state. In order to change into the most favoured state colloids solution need to absorb energy or to have the energy barrier to produce coagulation reduced before they are able to aggregate and form a large deposit of gold on the bottom of the solution container.

6.3.1 Interactions between atoms/molecules

In order to understand colloid stability is it necessary to consider the interactions between particles. These interactions are attractive forces, which arise from fluctuation of dipoles due to the motion of the outer electrons of the molecules or atoms. The free energy of attraction (ΔG^{att}) depends on the distance between the particles (H).

$$\Delta G^{att} = -\Delta W = -\frac{A'}{H^6} \tag{6.1}$$

Where ΔW is the work done in reversibly separating a pair of atoms or molecules, positioned initially at distance d to infinite. The constant A' is related to molecular properties. These attractive forces lead to a decrease in the potential energy.

The other interactions are repulsive forces, which occur when the molecules are sufficiently close that the electron clouds interpenetrate. The free energy of repulsion (ΔG^{rep}) falls of much quicker with the distance between the molecules or atoms and is often approximated as

$$\Delta G^{rep} = \frac{B'}{H^{12}} \tag{6.2}$$

The repulsive forces increase the free energy of the system.

The total molecular interaction potential then may be written as:

$$\Delta G = \Delta G^{rep} + \Delta G^{att} = \left(\frac{B'}{H^{12}}\right) - \left(\frac{A'}{H^6}\right) \tag{6.3}$$

This equation may be simplified in order to obtain the Leonard-Jones equation where the depth of the potential well is defined as $\varepsilon_{\min}$ and where the potential is zero is defined as r_0.

$$\Delta G = 4\varepsilon_{\min}\left[\left(\frac{r_0}{H}\right)^{12} - \left(\frac{r_0}{H}\right)^{6}\right] \tag{6.4}$$

6.3.2 Colloidal particles

A single particle of colloids contains typically 10^3 to 10^{10} molecules (atoms) but never as much as a mole of them. Therefore, interest is focused on the interactions between what are considered large "lumps" consisting of many atoms. Once again, it is the balance of attractive and repulsive forces dictate the physical properties and stability of these colloid systems. Colloidal particles in liquid media are in a constant state of random Brownian motion, and so particle collisions may lead to coagulation unless there is something in solution to stabilise the system.

In order to understand the interactions between colloidal particles it is necessary to keep in mind the three main differences between metallic colloids and metal atoms:

i) Colloids are much larger then their constituent atoms. As a consequence the Van der Waals attraction forces are as well much larger $\left(\Delta G^{att}_{colloid} >> \Delta G^{att}_{atom\ metal}\right)$;

Since each colloidal particle consists of many atoms (or molecules) one approach is to calculate the interparticle pair potential by assuming that each molecule in one particle interacts via a Leonard-Jones potential with another molecule in another particle, and so it is a assumed all the intermolecular potentials. The summation of Van der Waals forces of attraction leads to a first approximation for ΔG^{att} for spherical particles of radius a and a separation between their surfaces H.

$$\Delta G^{att} = -\frac{A_H a}{12H} \tag{6.5}$$

A_H is the Hamaker constant and has units of energy. For particles ΔG^{att} decreases much more slowly than for molecules. Therefore, the interaction between colloidal particles is of much longer range than for molecules (atoms).

ii) Most metal colloids have surface charge.

iii) As a consequence, of this surface charge, hydrated ions with opposite charge present in the surrounding electrolyte are electrostatically attracted to the surface where they form a double layer. This double layer consists of ions with a hydration shell that exist in a space close to the surface, in a diffused way, as they are not adsorbed onto the surface (Figure 6.4).

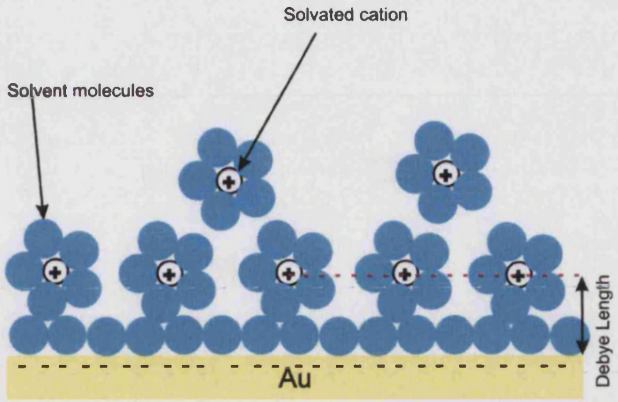

Figure 6.4 Double layer formed by hydrated ions at the surface of colloidal particles in solution

An important consequence of the existence of the double layer is that the surface of the colloidal particles becomes highly charged, with charge extending out a long distance into solution, therefore two colloidal particles will have a tendency to repel each other. Considering the free energy of electrostatic repulsion defined by:

$$\Delta G = 2\pi\varepsilon a\zeta^2 \exp-(\kappa H) \tag{6.6}$$

Where a is the particles radius, ε is the dielectric permittivity of the medium and $\kappa = 3.25x10^9 z\sqrt{c}$ is the inverse Debye length with units of m^{-1} where c is the concentration of the electrolyte and z is the valence of the counter-ions. The inverse Debye length is related to the degree to which two colloids will repel each other. ζ is the zeta potential, which may be thought of as the electrical potential at the surface of the particles associated with the net charge. The degree of charge is related to the bulk and surface properties of the colloids and to the surface modifications on the colloid surface. It can be observed that the free energy of electrostatic repulsion is proportional to $\exp(1/\kappa)$.

The inverse Debye length is proportional to the valence and concentrations of ions of opposite charge of the colloids charge that from the double layer. Thus, increasing the valence and /or the concentration of oppositely charged ions in solution there is an increase in κ therefore there is a decrease in the electrostatic repulsion between two colloidal particles.

From observations of these effects, the Schulze-Hardy rule has been empirically established which shows that the concentration of oppositely charged ions required to coagulate a colloid solution is proportional to $1/z^6$. The addition of higher concentration and/or valence counter-ions reduces the Debye length and the electrical double layer,

reducing the range of the repulsive interaction, and the attraction interactions will start to dominate.

The critical coagulation concentration for a colloid solution is the one where the energy barrier to coagulation at a certain electrolyte concentration is reduced to less than the kinetic, vibrational and rotational energy of the colloid solution.

An overall representation of the different forces interacting in a colloidal solution is presented in.

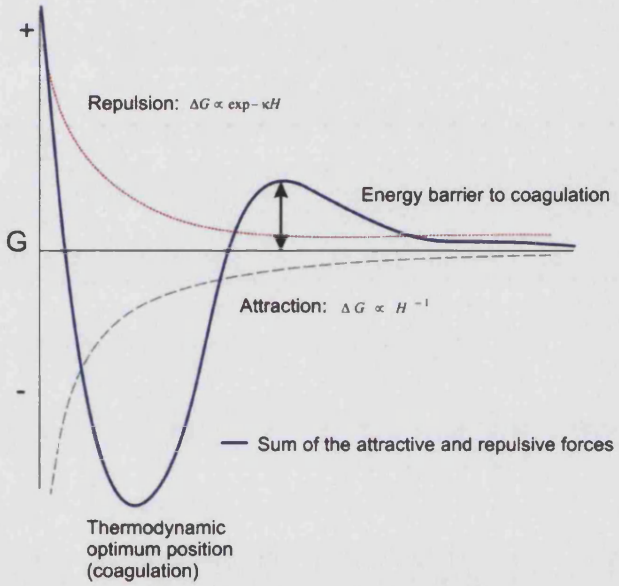

Figure 6.5 Attractive and repulsive forces between two colloidal particles and the sum of these two forces.

Another way to stabilise colloids is to use steric stabilisation. The stericly stabilised system consists of coating the surfaces of colloidal particles with a protective layer that will prevent particles to come in to intimate contact with each other. Some different systems have been applied and by far the best way is to use either synthetic or naturally occurring polymers.

The adsorbed polymer layers on two different colliding particles will produce steric repulsion, therefore preventing form coagulation. If the thickness of each layer is δ, this repulsion occurs at an inter-particle separation $H = 2\delta$ as represented in Figure 6.6. Substituting this into equation 2.5 it is possible to calculate the $\Delta G^{\min}$:

$$\Delta G^{\min} = -\frac{Aa}{24\delta} \tag{6.7}$$

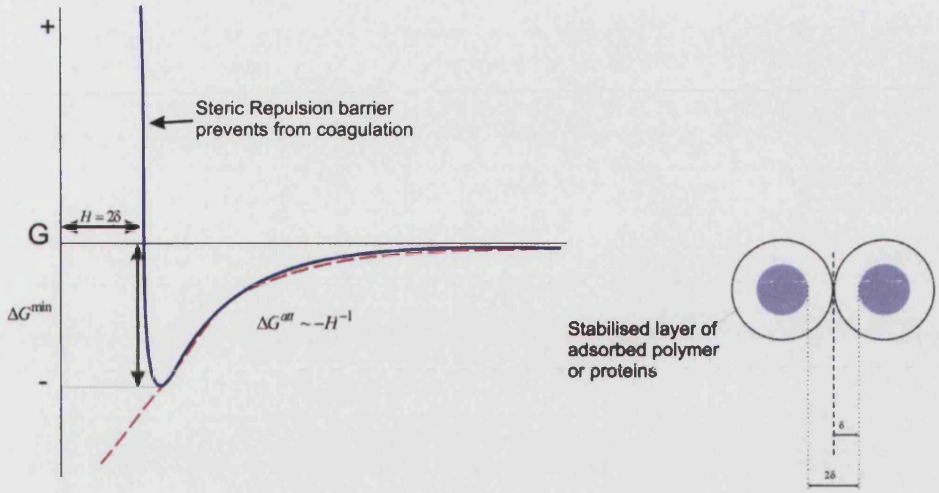

Figure 6.6 Attractive and repulsive result forces for particles stabilised with a polymer absorbed layer.

Cleary, for stabilisation to be effective, $\Delta G^{\min}$ must be less than the average mutual kinetic the shallow minimum on the graph. Therefore, if $\Delta G^{\min} > 1k_BT$ the particles become unstable and coagulate.

In this work, a layer of streptavidin is adsorbed onto the surface of the colloidal particles, hence the colloidal solutions are very stable, and surface chemistry can be employed.

6.4 Materials and Methods

Gold nanoparticles with a layer of streptavidin adsorbed on the surface (Sigma-Aldrich, UK) in a monodispersed solution of 0.01 M phosphate buffer, 20% glycerol, 1% BSA were employed. The average size of the gold nanoparticles was 10 nm with a concentration of 1.63 x 10^{13} particles ml^{-1} and the absorbance measured at 520 nm was 2.6. Considering the area of each particle and the size of streptavidin molecule (5.4 x 5.8 x 4.8 Å) [123] the concentration of streptavidin in this starting solution is 27.4 μM (assuming close packing of streptavidin on the particles surface).

Oligonucleotides were supplied by MWG Biotech. Probe 1 is a 24 base single strand DNA (ssDNA) designed to be free of hairpin and other secondary structures formation previously used and studied by Neumann et al [133]. Probe 1 is biotinylated at the 5' end. Target ssDNA with no mismatch present was labelled at the 5' end with an AlexaFluor® 555 chromophore. The sequences of the oligonucleotides are: Probe 1 5'-biotin-TTT TTT TTT TGT ATC TCA GTT CTA-3' and Target 5'-AlexaFluor 555-TTT TAG AAC TGA GAT ACA-3'.

The ssDNA probe 1 starting solution with a concentration of 100 μM was aliquoted in volumes of 20 μL in PB 10mM, NaCl 0.1 M pH 7, snap frozen using liquid N_2 and stored at -80° C for future application. The ssDNA target with a concentration of 26 μM was aliquoted in volumes of 20 μL in PB 10mM, NaCl 0.1 M pH 7, snap frozen using liquid N_2 and stored as well at -80° C for future application.

6.4.1 Hybrid Gold nanoparticles-Streptavidin-Biotin-DNA (GN-SA-Biot-DNA) Solution Preparation

In order to prepare the hybrid material consisting of gold nanoparticles bound to DNA, 100 μL solution of $50x10^{-9}$ mol L^{-1} ssDNA probe was incubated with 100 μL of 2.6 absorbance solution of gold nanoparticles-streptavidin in an excess, for 2h30 min. The final solution was spun down using a YM 100 Microcon® centrifugal filter device and an Eppendorf centrifuge at 14000 g for 5 min, to remove glycerol and BSA from starting solution. After resuspending three times with phosphate buffer 10 mM (PB) 0.1 M NaCl pH 7 an A^{520nm} of 1.2 was measured with an UV-Vis equipment (Thermal, UK). Therefore, the final concentration of the hybrid material was $12.6x10^{-6}$ mol L^{-1}.

6.4.2 Fluorescence Measurements

The fluorescence measurements were made in a Perkin-Elmer LS 50B luminescence spectrometer. The fluorimeter consists of a light source, two monochromators (excitation and emission, respectively), two polarizers position between the monochromators and the sample holder.

With this equipment, it was possible to scan the excitation wavelength for a determined emission wavelength, as well as to excite the sample at a fixed wavelength, in this case 520 nm, and determine the emission spectra Figure 6.7 depicts the fluormeter set-up used for the following measurements.

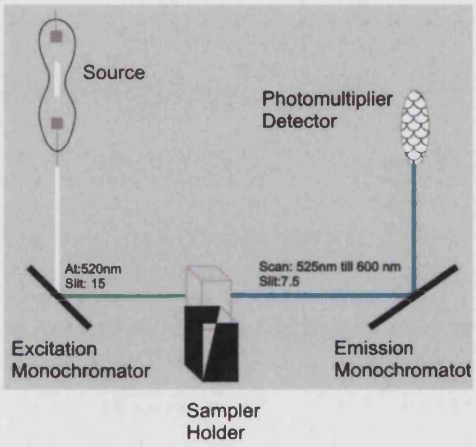

Figure 6.7 Diagram of the fluorimeter used to produce the fluorescence measurements. Note that the excitation monochromator was set at 520 nm in order to excite the gold nanoparticles that will generate the surface plasmon resonance field. This field will excite AlexaFluor 555-ssDNA target, which will emit fluorescence signal with a maximum wavelength of 565 nm.

In order to understand how to use the equipment preliminary measurements with a solution of AlexaFluor 555 were produced. Excitation and emission scans of $1x10^{-6}$ mol L^{-1} AlexaFluor DNA 555 solution are shown in Figure 6.8.

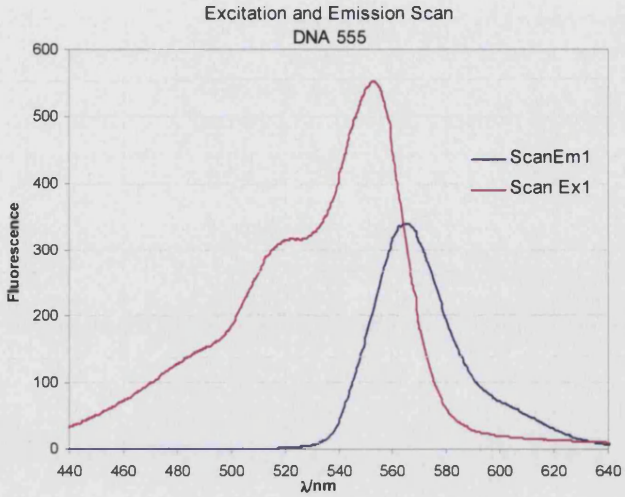

Figure 6.8 Excitation and emission scan using optimised slit positions of Alexa Fluor 555 ssDNA target.

The fluormeter has two slits attached to the monochromators that control the intensity and the density of light that reaches the sampler holder and the detector. In order to obtain the best fluorescence emission scan the excitation slit has to have a larger opening that the emission slit. Different slit conditions were tested with the intention to optimise the emission spectra and it was determined that the excitation slit would have 15 overture and the emission slit a 7.5 overture.

6.4.3 Measurement procedures

A volume of 100 μL of a $1x10^{-6}$ mol L^{-1} Alexa Fluor 555 ssDNA solution was pipetted to a fluorescence cuvette with a total volume of 100 μL. An emission scan using the optimised conditions was determined. Small amounts of GN-SA-biot-ssDNA hybrid were introduced, stirred and left to stabilise. An average of ten emission scans produced one emission scan at each interval of time.

6.5 Quenching and Scattering Effect Observation

A large quenching of fluorescence effect is observed when fluorophores are located close to metallic surfaces and the distance separation between both is smaller than 5 nm. Nonradiative decay channels are the major causes of this effect and resonant energy transfer is considerer to be the dominant decay mode [239, 246]. The fluorescence emissions intensities measurements in solution are affected by scattering/absorption of the gold nanoparticles and by dilution, as small volumes as consecutively introduced in the cuvette for measurements.

Measurements were carried out introducing 100 μL of a non-biotinylated $1x10^{-6}$ mol L^{-1} Alexa Fluor 555 ssDNA in the fluorescence cuvette and recording an emission scan without the presence of gold nanoparticles. A stock solution of GN-SA with a concentration of $10x10^{-6}$ mol L^{-1} was prepared and volumes presented in Table 6-1 were pipetted and left to stabilise in the fluorescence cuvette followed by scanning of the emission fluorescence.

Table 6-1 Volumes of GN-SA stock solution injected into the fluorescence cuvette for measurements and final concentrations of GN-SA in solution.

Volume injected (L)	Total volume (L)	Final conc. of GN-SA (M)
1.63E-06	1.02E-04	2.38E-07
2.5E-06	1.05E-04	4.70E-07
3.44E-06	1.08E-04	7.73E-07
4.48E-06	1.13E-04	1.14E-06
5.65E-06	1.19E-04	1.56E-06

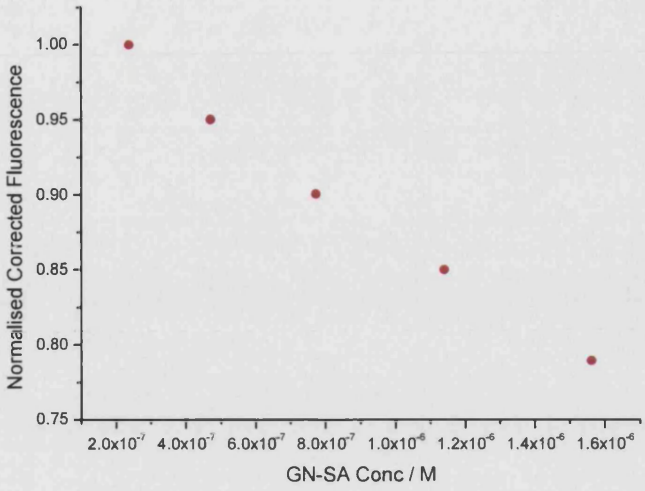

Figure 6.9 Emission intensity of AlexaFluor 555 ssDNA in presence of varying concentrations of gold nanoparticles with a streptavidin layer.

Figure 6.9 shows that there is a decrease in fluorescence due to the presence of gold nanoparticles in the vicinity of the fluorophore as the concentration of GN-SA increases due to quenching and light scattering effects.

The fluorescence data was corrected for dilution effects, by multiplying the measured intensities by the appropriate calculated dilution factors. The corrected intensities were followed by normalisation.

6.6 Fluorescence Enhancement Measurements

The main goal of this project was to try to detect the enhancement of fluorescence emission produced by the surface plasmon resonance field generated after absorption of light. The effect of fluorescence emission excited by the surface plasmon resonance field produced in a gold film has been well described elsewhere [101, 247], however the general mode of excitation of surface plasmons in thin metal layers is by coupling in laser light with a prism.

This surface plasmon field becomes of importance if its energy is of the same order as the energy necessary to excite chromophores located within the field. However, it is important to bear in mind that the chromophores should be located sufficiently away from the metal surface to prevent from metal quenching effects.

In order to detect the excitation of fluorescence due to the surface plasmon resonance field, a hybrid material consisting of a gold nanoparticle and DNA, as previously mentioned, was produced. This GN-SA-biot-ssDNA in the presence of the labelled AlexaFluor 555 ssDNA target hybridises forming the structure presented in Figure 6.10.

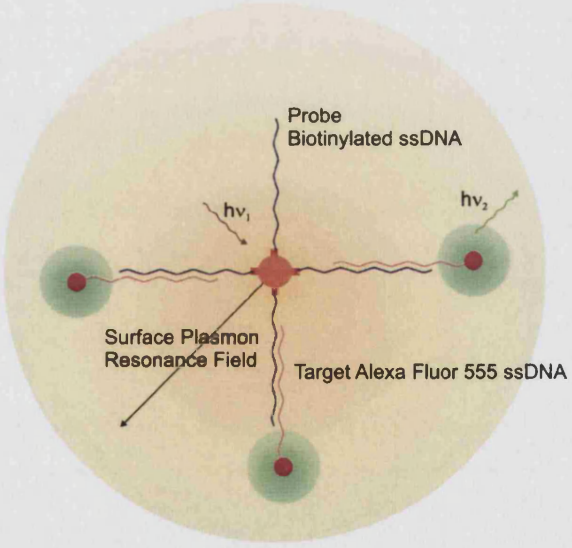

Figure 6.10 Schematic representation of experimental approach. Hybridisation of probe – target oligos' causes increase of fluorescence emission signal, which prevails over quenching effects.

The chromophores attached to the end of the target ssDNA become embedded in the surface plasmon field and are thus excited both by the SPB and directly by the excitation light. The measurements proceeded as previously described but instead of

GN-SA, GN-SA-biot-ssDNA was consecutively added on to the cuvette. The volumes introduced and the final concentrations are presented in Table 6-2.

Table 6-2 Volumes of GN-SA-biot-ssDNA stock solution injected into the fluorescence cuvette for measurements and final concentrations of GN-SA-biot-ssDNA in solution

Volume (L)	Total Volume (L)	Final Conc.of GN-SA-biot-ssDNA (M)
0	1.00E-04	0
6.30E-07	1.01E-04	7.89E-09
1.29E-06	1.02E-04	2.37E-08
1.97E-06	1.04E-04	4.72E-08
2.70E-06	1.07E-04	7.79E-08
3.48E-06	1.10E-04	1.15E-07
4.34E-06	1.14E-04	1.59E-07

Fluorescence scans were taken at different times for each concentration. After each injection, the solution was left to stabilise. When no change in fluorescence intensity was observed, a new concentration of GN-SA-biot-ssDNA was injected. In Figure 6.11 is shown the raw data collected each concentration.

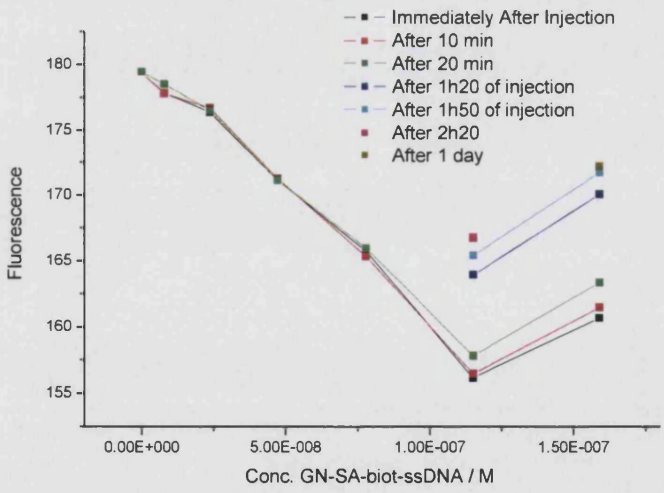

Figure 6.11 Representation of the raw data obtained for each concentration of GN-SA-biot-ssDNA obtained after injection of a determined volume presented in Table 6-2.

It can be observed from Figure 6.11 that the values of raw fluorescence decrease when a new volume of GN-SA-biot-ssDNA is injected. This influence is due to three combined effects: i) a dilution effect after adding the volume; ii) strong absorption/scattering caused by the presence of GN-SA-biot-ssDNA; iii) actual

quenching of the fluorescence emission intensity by the gold nanoparticles hybridizing with the target DNA present in solution. It is important to note that there is always an excess of AlexaFluor 555-ssDNA in solution.

Considering the points when no change in the intensity of fluorescence is observed and correcting for dilution and normalising the fluorescence, the results presented in Figure 6.12 are obtained.

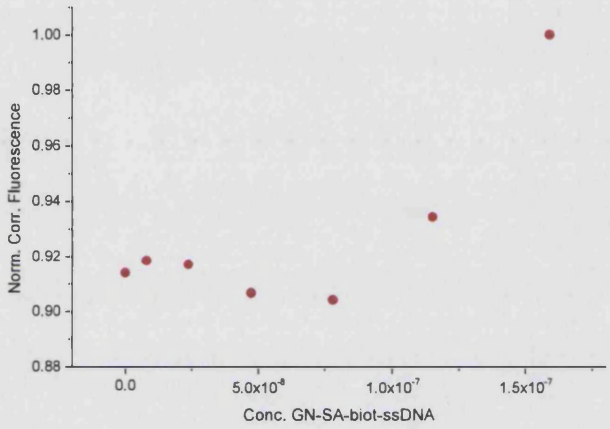

Figure 6.12 Fluorescence intensity emission (normalised to max response) of Alexa Fluor 555–ssDNA in the presence of increasing concentrations of GN-SA-biot-ssDNA.

It can be observed that for large ratios of Alexa Fluor ss-DNA/GN-SA-biot-ssDNA the number of hybridised labelled DNA excited by the gold nanoparticles SPB excitation enhancement is not sufficient to overcome the effects of absorption, quenching and scattering of light.

In contrast, when the number of biot-DNA coupled to gold nanoparticles corresponds to approximately to 200 nM (or greater) the fluorescence signal is increased. It is reasonable to hypothesise that the enhancement of the fluorescence signal is due to the higher contribution of the surface plasmon band to excite the chromophore, when compared with all the quenching effects present in the system.

6.7 Determination of the Maximum Enhancement Possible

In order to determine the conditions of higher enhancement, very preliminary experiments were carried out.

In the previous experiment, a higher concentration of Alexa Fluor 555-ssDNA target was used in solution, and only at a concentration higher than $200x10^{-9}$ mol L^{-1} it was possible to observe the larger contribution of the enhancement of fluorescence signal due to the excitation via the surface plasmon resonance produced by the gold nanoparticles.

For each experiment a concentration of $100x10^{-9}$ mol L^{-1} Alexa Fluor 555-ssDNA was used, keeping the starting volume of the sample at 100 μM. Solutions of $160x10^{-9}$ mol L^{-1}, $800x10^{-9}$ mol L^{-1}, $2x10^{-6}$ mol L^{-1} and $4x10^{-6}$ mol L^{-1} of GN-SA-biot-ssDNA probe were prepared and added to the starting conditions. In this experiment, the dilution factor was taken into account and the results are presented in Figure 6.13.

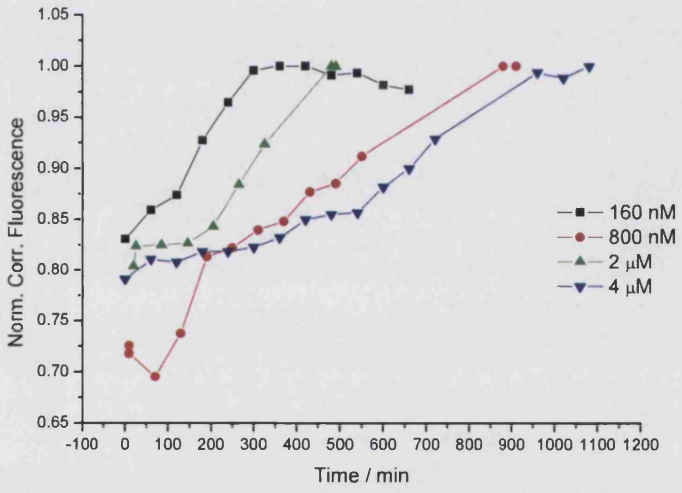

Figure 6.13 Increase of fluorescence signal in time when different concentrations of GN-SA-biot-ssDNA are used for $100x10^{-9}$ mol L^{-1} of Alexa Fluor 555-ssDNA starting solution.

It can be observed that the there is a larger increase of the starting fluorescence signal for a concentration of $800x10^{-9}$ mol L^{-1}. Nevertheless, these are very preliminary experiments and a number of factors influence the results obtained. It can only be concluded that one can observe hybridisation of the ssDNA strands by following the increase of fluorescence signal, which we assumed, is due to the excitation of the chromophore via the surface plasmon band present in the gold nanoparticles.

In order to determine the optimised enhancement there are a number of factors that should be controlled for different experiments, as for example:

1) The number of biot-ssDNA bound to the gold nanoparticles; Measurements using a controlled number of the biot-ssDNA bound to the gold nanoparticle would give a better understanding of the influence of quenching effects and absorption of light from the gold nanoparticles.
2) The influence of different concentrations of gold nanoparticles in the presence of Alexa Fluor 555-ssDNA;
3) From the literature [248] it is observed that DNA hybridises with higher rates when a flow system is used; The hybridisation of DNA could be optimised by of the using a stirring equipment and control of temperature. Another method is to use of $MgCl_2$, which decreases the repulsive interactions between the charged complementary DNA strands. However, by decreasing the repulsive charges in presence of gold nanoparticles is disadvantageous, as it might cause colloidal solution coagulation.
4) Use of a fluormeter that allowed the user to control, with more precision, the filters and the monochromators used as well as other parameters, e.g., wavelength, slits, PMT, etc. could be controlled.
5) A better-structured GNP employing polymers (polyalinine, poly-L-lysine) to increase the distance between the fluorophore and the SPB vicinity decreasing the nonradiative channels

6.8 Conclusion

This work explores the possibility of using the surface plasmon band produced by gold nanoparticles when exposed to light, to excite chromophores present in vicinity of the field. A number of publications have observed the quenching effect via resonant energy transfer from the chromophore to the metal, though the chromophore was not excitable by the plasmonic field in the gold nanoparticles.

In this preliminary work we have also observed the influence of the presence of the nanoparticles in a solution with Alexa Fluor 555-ssDNA. A decrease in the fluorescence signal was observed due to dilution effects, strong absorption of light from the gold nanoparticles and quenching effects.

However, when a hybrid material consisting of GN-SA-biot-DNA was introduced in a solution with Alexa Fluor 555-ssDNA an increase in fluorescence was observed. We attribute this effect to the excitation of the chromophore via the surface plasmon field when hybridisation of the complementary DNA strands has taken place.

If this hypothesis is confirmed than the effect can be explored to produce a "super dye" comprising a very high fluorescence quantum efficiency as the fluorescence emission would be the overall product of a number of dyes located within the vicinity of the plasmon field excited at the same time.

7 Appendix

7.1 APPENDIX I

7.1.1 Electromagnetic Waves [249, 250]

Maxwell's equations are the set of four equations that describe the behaviour of both electric and magnetic fields, as well as their interactions with matter. They express, respectively, how electric charges produce electric fields (Guass' law), the experimental absence of magnetic charges, how currents produce magnetic fields (Ampere's law), and how changing magnetic fields produce electric fields (Faraday's law of induction).

The Maxwell's equations in Gaussian units (CGS) are presented below.

$$\nabla \times \vec{H} = \frac{1}{c}\frac{\partial}{\partial t}\vec{D} + \frac{4\pi}{c}\vec{J} \tag{7.1}$$

$$\nabla \times \vec{E} = -\frac{1}{c}\frac{\partial}{\partial t}\vec{B} \tag{7.2}$$

$$\nabla \cdot \vec{D} = 4\pi\rho \tag{7.3}$$

$$\nabla \cdot \vec{B} = 0 \tag{7.4}$$

Where $\vec{H}$ is the magnetic field intensity, $\vec{D}$ is the electric displacement field, $\vec{J}$ is the current density, $\vec{E}$ is the electric field and $\vec{B}$ is the magnetic flux density.

Maxwell's equations in Gaussian units are based on the CGS system of mechanical units, and were long dominant for theoretical investigation but, are no longer accepted by styles of most scientific journals, textbook publishers and standards bodies. The main reason for such situation is due perhaps to the fact that mechanical units were defined when the idea of "absolute" standards was a novel concept (just before 1800). By the time the problem of the electromagnetic units arose, there were (and still are) many experts and different systems were already in use [250].

This appendix shows how to convert from Gaussian to MKSA system, which was adopted in 1948 and has been well accepted since than and more wildly used by Physics and Electric Engineers.

To convert any equation in Gaussian variables to the corresponding equation in rationalised MKSA quantities (meter, kilogram, second and current (I) as a fourth dimension with ampere as unit) it is only necessary to replace the symbols listed under Gaussian by the corresponding MSKA symbols listed on the right [250]

Quantity	Gaussian	MKSA
Velocity of Light	c	$(\mu_0\varepsilon_0)^{-1/2}$
Electric Field	E	$\sqrt{4\pi\varepsilon_0}E$
Displacement	D	$\sqrt{\frac{4\pi}{\varepsilon_0}}D$
Charge Density (Charge, Current Density, Current, Polarisation)	$\rho(q,J,I,P)$	$\frac{1}{\sqrt{4\pi\varepsilon_0}}\rho(q,J,I,P)$
Magnetic Induction	B	$\sqrt{\frac{4\pi}{\mu_0}}B$
Magnetic Field	H	$\sqrt{4\pi\mu_0}H$
Magnetisation	M	$\sqrt{\frac{\mu_0}{4\pi}}M$
Conductivity	σ	$\frac{\sigma}{4\pi\varepsilon_0}$
Dielectric constant	ε	$\frac{\varepsilon}{\varepsilon_0}$
Permeability	μ	$\frac{\mu}{\mu_0}$

To demonstrate how to obtain the conversion equation will be used as an example:

$$\nabla\times\vec{H}=\frac{1}{c}\frac{\partial}{\partial t}\vec{D}+\frac{4\pi}{c}\vec{J}$$

$$\sqrt{4\pi\mu_0}\nabla\times\vec{H}=\sqrt{\frac{4\pi\mu_0\varepsilon_0}{\varepsilon_0}}\frac{\partial}{\partial t}\vec{D}+\frac{4\pi\sqrt{\mu_0\varepsilon_0}}{\sqrt{4\pi\varepsilon_0}}\vec{J}$$

$$\sqrt{4\pi\mu_0}\nabla\times\vec{H}=\sqrt{4\pi\mu_0}\sqrt{\frac{\varepsilon_0}{\varepsilon_0}}\frac{\partial}{\partial t}\vec{D}+\frac{\sqrt{4\pi\mu_0}\sqrt{4\pi\varepsilon_0}}{\sqrt{4\pi\varepsilon_0}}\vec{J}$$

$$\nabla\times\vec{H}=\frac{\partial}{\partial t}\vec{D}+\vec{J}$$

This follows that the Maxwell's equations are written in MKSA units in a simpler way:

$$\nabla\times\vec{H}=\frac{\partial}{\partial t}\vec{D}+\vec{J} \qquad (2.5)$$

$$\nabla \times \vec{E} = -\frac{\partial}{\partial t}\vec{B} \tag{2.7}$$

$$\nabla \cdot \vec{D} = \rho \tag{2.9}$$

$$\nabla \cdot \vec{B} = 0 \tag{2.11}$$

Maxwell's Theory treats substantial matters as continuous representing its electric and magnetic responses to applied $\vec{E}$- and $\vec{B}$- fields in terms of constants, ε and μ. Consequently, both relative permittivity ε_r and permeability μ_r of the medium are also constant and the refractive index, n, is therefore unrealistically independent of the light frequency. All material media are dispersive thus the media refractive index is frequency dependent; only the vacuum is non-dispersive.

When a dielectric is subjected to an applied electric field, the internal charge distribution is distorted generating electric dipole moments, which contributes to the total internal field. The resultant dipole moment per unit volume is called the electric polarization, $\vec{P}$. For most materials $\vec{E}$ and $\vec{P}$ are related by:

$$(\varepsilon - \varepsilon_0)\vec{E} = \vec{P} \tag{7.5}$$

Since, the field within the material has change we can define a new field quantity, the displacement field $\vec{D}$:

$$\vec{D} = \varepsilon_0 \vec{E} + \vec{P} \text{ or } \vec{E} = \frac{\vec{D}}{\varepsilon_0} - \frac{\vec{P}}{\varepsilon_0} \tag{7.6}$$

The internal field $\vec{E}$ is the different between the field which would exist in the absence of polarisation and the field arising from polarisation.

For a homogeneous, linear and isotropic dielectric $\vec{P}$ and $\vec{E}$ are in the same direction and are mutually proportional. Thus, the displacement $\vec{D}$ is parallel and proportional to the electric field $\vec{E}$ and it follows that one of the constitutive equation is:

$$\vec{D} = \varepsilon_r \varepsilon_0 \vec{E} \tag{7.7}$$

For a homogeneous, linear (nonferromagnetic), isotropic medium, the magnetic flux $\vec{B}$ and the magnetic field $\vec{H}$ are parallel and proportional and are related by another constitutive equation:

$$\vec{B} = \mu_r \mu_0 \vec{H} \tag{7.8}$$

Since the general response of optical media to $\vec{B}$ is only slightly different from that of a vacuum it is sufficient to say that the material becomes polarised. The magnetic polarisation $\vec{M}$ is the magnetic dipole moment per unit volume. The influence of the magnetically polarised medium is determined by:

$$\vec{H} = \mu_0^{-1}\vec{B} - \vec{M} \tag{7.9}$$

Along with equations (7.7), (7.8) and (7.9) there is one more constitutive equation. Known as Ohm's law, states that the electric field, and therefore the force acting on each electron in a conductor, determines the flow of charge.

$$\vec{J} = \sigma\vec{E} \tag{7.10}$$

Where, the constant of proportionality σ is the conductivity of a particular medium.
Considering a general environment of a linear (nonferroelectric and nonferromagnetic), homogeneous, isotropic medium which is physically at rest as a surface of a semi-infinite solid with the dielectric function ($\varepsilon_1 = \varepsilon_1' + i\varepsilon_1''$) adjacent to a medium ε_2 as air or vacuum from expansion of equation (2.5):

$$\left(\nabla \times \vec{H}\right) = \begin{vmatrix} e_x & e_y & e_z \\ \frac{\partial}{\partial x} & \frac{\partial}{\partial y} & \frac{\partial}{\partial z} \\ H_x & H_y & H_z \end{vmatrix} \tag{7.11}$$

$$\left(\nabla \times \vec{H}\right) = \left(\frac{\partial H_z}{\partial y} - \frac{\partial H_y}{\partial z}\right)e_x + \left(\frac{\partial H_z}{\partial x} - \frac{\partial H_x}{\partial z}\right)e_y + \left(\frac{\partial H_y}{\partial x} - \frac{\partial H_x}{\partial y}\right)e_z \tag{7.12}$$

Knowing, $H_x = H_z = 0$, then;

$$\left(\nabla \times \vec{H}\right) = \frac{\partial H_y}{\partial x}e_z - \frac{\partial H_y}{\partial z}e_x \tag{7.13}$$

Therefore for $z > 0$

$$\frac{\partial H_y}{\partial x} = iH_{y2}k_{x2}\exp i\left(k_{x2}x + k_{z2}z - \omega t\right) = ik_{x2}\overrightarrow{H_2} \tag{7.14}$$

$$-\frac{\partial H_y}{\partial z} = -iH_{y2}k_{z2}\exp i\left(k_{x2}x + k_{z2}z - \omega t\right) = -ik_{z2}\overrightarrow{H_2} \tag{7.15}$$

For $z < 0$

$$\frac{\partial H_y}{\partial x} = iH_{y1}k_{x1}\exp i\left(k_{x1}x - k_{z1}z - \omega t\right) = ik_{x1}\overrightarrow{H_1} \tag{7.16}$$

$$-\frac{\partial H_y}{\partial z} = iH_{y1}k_{z1}\exp i\left(k_{x1}x - k_{z1}z - \omega t\right) = ik_{z1}\overrightarrow{H_1} \tag{7.17}$$

And considering a nonconducting medium $\sigma = 0$

$$\nabla \times \vec{H} = \frac{\partial}{\partial t}\vec{D} + \vec{J} = \frac{\partial}{\partial t}\vec{D} = \varepsilon_r \varepsilon_0 \frac{\partial}{\partial t}\vec{E} \tag{7.18}$$

For $z > 0$

$$\frac{\partial E_{x2}}{\partial t} = -i\omega E_{x2} \exp i(k_{x1}x - k_{z1}z - \omega t) = -i\omega \overrightarrow{E_{x2}} \tag{7.19}$$

$$\frac{\partial E_{z2}}{\partial t} = -i\omega E_{z2} \exp i(k_{x1}x - k_{z1}z - \omega t) = -i\omega \overrightarrow{E_{z2}} \tag{7.20}$$

And for $z < 0$

$$\frac{\partial E_{x1}}{\partial t} = -i\omega E_{x1} \exp i(k_{x1}x - k_{z1}z - \omega t) = -i\omega \overrightarrow{E_{x1}} \tag{7.21}$$

$$\frac{\partial E_{z1}}{\partial t} = -i\omega E_{z1} \exp i(k_{x1}x - k_{z1}z - \omega t) = -i\omega \overrightarrow{E_{z1}} \tag{7.22}$$

Than

$$\begin{cases} -ik_{z2}\overrightarrow{H_2} = -i\varepsilon_r \varepsilon_0 \omega \overrightarrow{E_{x1}} \\ ik_{z1}\overrightarrow{H_1} = -i\varepsilon_r \varepsilon_0 \omega \overrightarrow{E_{x2}} \end{cases} \Leftrightarrow \begin{cases} -k_{z2}\overrightarrow{H_2} = -\varepsilon_r \varepsilon_0 \omega \overrightarrow{E_{x1}} \\ k_{z1}\overrightarrow{H_1} = -\varepsilon_r \varepsilon_0 \omega \overrightarrow{E_{x2}} \end{cases} \tag{7.23}$$

Considering the continuity equations (2.6) and eliminating $\overrightarrow{E_x}$ together with the continuity equation (2.19)

$$\begin{cases} \frac{k_{z1}}{\varepsilon_1}\overrightarrow{H_1} + \frac{k_{z2}}{\varepsilon_2}\overrightarrow{H_2} = 0 \\ \overrightarrow{H_1} - \overrightarrow{H_2} = 0 \end{cases} \tag{7.24}$$

Gives the surface plasmon dispersion relation on a semi-infinite solid surface:

$$\frac{k_{z1}}{\varepsilon_1} + \frac{k_{z2}}{\varepsilon_2} = 0 \tag{2.21}$$

or

$$\frac{k_{z1}}{k_{z2}} = -\frac{\varepsilon_1}{\varepsilon_2} \tag{2.22}$$

Considering the Maxwell equation (2.5) and the material equations (2.15) for a nonconducting medium $\sigma = 0$,

$$\nabla \times \vec{H} = \varepsilon_0 \varepsilon_r \frac{\partial \vec{E}}{\partial t} \tag{7.25}$$

Since $\vec{E}$ is assumed to be a well-behaved function, the space and time derivatives can be interchanged. Therefore when taking the curl of (7.25) and considering equation (2.11) and (2.16)

$$\nabla\times\left(\nabla\times\vec{H}\right)=\varepsilon_0\varepsilon_r\frac{\partial}{\partial t}\left(\nabla\times\vec{E}\right) \tag{7.26}$$

$$\nabla\times\left(\nabla\times\vec{H}\right)=-\varepsilon_0\varepsilon_r\mu_0\mu_r\frac{\partial^2\vec{H}}{\partial t^2} \tag{7.27}$$

The vector triple product can be simplified by making use of the operator identity:

$$\nabla\times(\nabla\times)=\nabla(\nabla\cdot)-\nabla^2 \tag{7.28}$$

So that

$$\nabla\times\left(\nabla\times\vec{H}\right)=\nabla\left(\nabla\cdot\vec{H}\right)-\nabla^2\vec{H} \tag{7.29}$$

$$\nabla\times\left(\nabla\times\vec{H}\right)+\nabla^2\vec{H}=\nabla\left(\nabla\cdot\vec{H}\right) \tag{7.30}$$

Since $\nabla\cdot\vec{H}=0$ than

$$\nabla\times\left(\nabla\times\vec{H}\right)+\nabla^2\vec{H}=0 \tag{7.31}$$

Substituting $\nabla\times\left(\nabla\times\vec{H}\right)$from equation (7.27) in (7.31) than:

$$\nabla^2\vec{H}-\varepsilon_0\varepsilon_r\mu_0\mu_r\frac{\partial^2\vec{H}}{\partial t^2}=0 \tag{7.32}$$

So

$$\frac{\partial^2\overrightarrow{H_y}}{\partial x^2}+\frac{\partial^2\overrightarrow{H_y}}{\partial y^2}\frac{\partial^2\overrightarrow{H_y}}{\partial z^2}-\varepsilon_0\varepsilon_r\mu_0\mu_r\frac{\partial^2\overrightarrow{H_y}}{\partial t^2} \tag{7.33}$$

$$k_x^2+k_{zi}^2=\varepsilon_0\varepsilon_r\mu_0\mu_r\omega^2 \tag{7.34}$$

$$k_x^2+k_{zi}^2=\frac{\varepsilon_r\mu_r\omega^2}{c^2}\ ^4 \tag{7.35}$$

$$k_x^2+k_{zi}^2=\frac{\varepsilon_r\omega^2}{c^2}\qquad i=1,2 \tag{2.23}$$

or

$$k_{zi}=\sqrt{\varepsilon_r\frac{\omega^2}{c^2}-k_x^2} \tag{2.24}$$

Thus, for each media it can be written

$$k_{z1}=\sqrt{\varepsilon_1\frac{\omega^2}{c^2}-k_x^2}\qquad\qquad k_{z2}=\sqrt{\varepsilon_2\frac{\omega^2}{c^2}-k_x^2}$$

[4] From Maxwell's relation it is assumed that relative permeability μ_r of the medium is constant and equal to 1 as most optical materials are transparent in the visible and are all essentially "nonmagnetic"

(7.36) (7.37)

Substituting these equations in (2.23) and rearranging

$$\frac{\sqrt{\varepsilon_1 \omega^2/c^2 - k_x^2}}{\varepsilon_1} + \frac{\sqrt{\varepsilon_2 \omega^2/c^2 - k_x^2}}{\varepsilon_2} = 0$$

$$\varepsilon_2 \sqrt{\varepsilon_1 \omega^2/c^2 - k_x^2} = -\varepsilon_1 \sqrt{\varepsilon_2 \omega^2/c^2 - k_x^2}$$

$$\frac{\varepsilon_2^2 \varepsilon_1 \omega^2}{c^2} - \varepsilon_2^2 k_x^2 = \frac{\varepsilon_1^2 \varepsilon_2 \omega^2}{c^2} - \varepsilon_1^2 k_x^2$$

$$\frac{\varepsilon_2 \varepsilon_1 \omega^2}{c^2}(\varepsilon_2 - \varepsilon_1) = k_x^2(\varepsilon_2^2 - \varepsilon_1^2)$$

$$\frac{\varepsilon_2 \varepsilon_1 \omega^2}{c^2}(\varepsilon_2 - \varepsilon_1) = k_x^2(\varepsilon_2 - \varepsilon_1)(\varepsilon_2 + \varepsilon_1) \tag{7.38}$$

Is obtain the dispersion relation (2.25)

$$k_x = \frac{\omega}{c}\sqrt{\frac{\varepsilon_1 \varepsilon_2}{\varepsilon_1 + \varepsilon_2}} \tag{2.25}$$

7.2 APPENDIX II

7.2.1 Total Internal Reflection and Evanescent Wave [249]

Considering a incident monochromatic light wave plane polarized described by

$$\vec{E}_i = \vec{E}_{0i} \exp\left[i\left(\vec{k}_i \cdot \vec{r} - \omega_i t\right)\right] \tag{7.39}$$

passing through two media of different refractive indices n_i and n_t, such as an air-glass interface, part of the light energy is reflected, and part enters the second medium. If the incident light is not perpendicular to the surface then the transmitted light is not parallel to the incident light. The change in direction of the transmitted light is called refraction. Figure 7.1 shows an incident light on a smooth air-glass interface. The angle θ_i between the incident light and the normal to the surface is called angle of incidence.

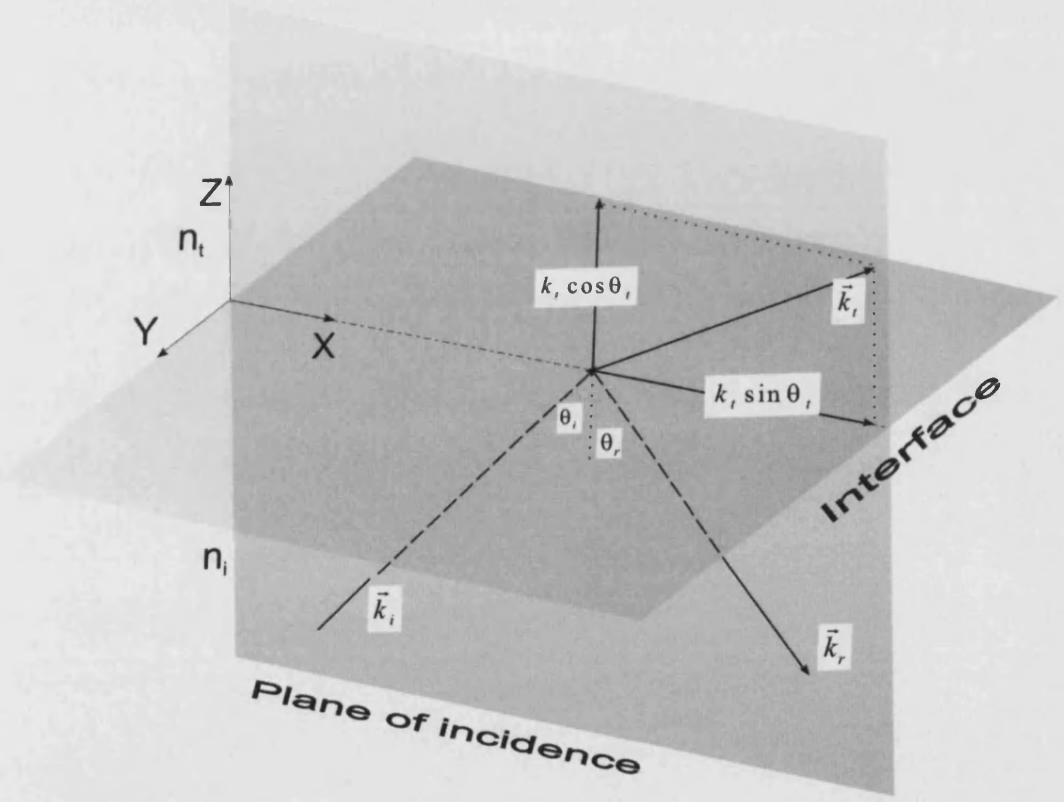

Figure 7.1 Schematic representation of the incident plane wave at the interface between two optical media of different refractive index. The plane of incidence is the x-z and note that reflection angle equals the incident angle, while the transmittance angle is determined by Snell's law.

The reflected light lies in the same plane of incidence and makes an angle of θ_r with the normal to the surface as shown Figure 7.1in which is equal to

$$\theta_i = \theta_r \tag{7.40}$$

This is called Law of reflection.

The light that enters the glass is called the refracted light and produces a refracted angle with the normal to the interface. The light wave travelling in air travels at a certain speed, when it crosses the boundary the velocity of incoming light decreases because there is a change in the refractive index. The refracted angle depends on the incident angle and on the relative speed of light waves in the two media.

$$\frac{1}{v_i}\sin\theta_i = \frac{1}{v_t}\sin\theta_t \tag{7.41}$$

Knowing that the refractive index is related with the velocity of medium by

$$n = \frac{c}{v} \tag{7.42}$$

Than, equation (A.2.3) can be written

$$n_i \sin\theta_i = n_t \sin\theta_t \tag{7.43}$$

When $n_i > n_t$, than $\theta_t > \theta_i$, if θ_i is increased gradually the transmitted light gradually approaches the tangency with the interface, and as it does more the available energy appears in the reflected beam. Finally, when $\theta_t = 90^\circ$, then $\sin\theta_t = 1$ and at that moment the light is totally reflected and the angle is designated the critical angle and is equal to

$$\sin\theta_c = \frac{n_t}{n_i} \tag{7.44}$$

For incident angles greater than or equal to θ_c, all the incoming energy is reflected back into the incident medium in the process known as total internal reflection. As the transmitted angle can not increase higher than 90° and light can not enter back into the optical dense medium then the transmitted light becomes a plane wave travelling along the interface between the two media. This plane wave is the so called evanescent wave.

Considering the transmitted wave function of the electric field is described by:

$$\vec{E}_t = \vec{E}_{0t} \exp i(\vec{k}_t \cdot \vec{r} - \omega t) \tag{7.45}$$

Where

$$\vec{k}_t \cdot \vec{r} = k_{tx} x + k_{tz} z \tag{7.46}$$

There being no y-component of $\vec{k}$. But

$$k_{tx} = k_t \sin\theta_t \tag{7.47}$$

And

$$k_{tz} = k_t \cos\theta_t \tag{7.48}$$

Which is equivalent to write using as well Snell's law:

$$k_{tz} = \pm k_t \sqrt{1 - \frac{n_i^2}{n_t^2} \sin\theta_i} \tag{7.49}$$

Or since in this case $\sin\theta_i > \frac{n_t}{n_i}$, then

$$k_{tz} = \pm i k_t \sqrt{\frac{n_i^2}{n_t^2} \sin\theta_i - 1} = \pm i\beta \tag{7.50}$$

Hence, neglecting the positive exponential, which is physically invalid, the wave amplitude drops off exponentially as it penetrates the less dense medium.

$$\vec{E}_t = \vec{E}_{0t} e^{-\beta z} e^{i\left(k_t x \frac{n_i}{n_t} \sin\theta_i - \omega t\right)}$$

i.e. resulting evanescent field decays exponentially perpendicular to the interface (in the z direction). The decay length, at which the amplitude of the evanescent field is decreased to $1/e$ is the penetration depth d, which is equivalent to write:

$$e^{-\beta d} = e^{-1}$$

$$d = \frac{\lambda}{2\pi\sqrt{\frac{\sin^2\theta_i}{\left(\frac{n_t}{n_i}\right)^2} - 1}} \tag{7.51}$$

The penetration depth is the range of the wavelength used.

7.2.2 *Fresnel Equations*

When the light travels from a medium of a given refractive index n_i into a second medium with refractive index n_t both reflection and refraction of the light occur for certain incident angles. The fraction of the incident light that is reflected from the interface is given by the reflection coefficient r and the fraction refracted by the transmission coefficient t.

When both media forming the interface are dielectrics that are essentially nonmagnetic the amplitude coefficients become:

$$r_{\parallel} \equiv \left(\frac{E_{0r}}{E_{oi}}\right)_{\parallel} \frac{n_t\cos\theta_i - n_i\cos\theta_t}{n_i\cos\theta_t + n_t\cos\theta_i} \tag{7.52}$$

Where E_{0r} and E_{oi} are the amplitudes of the reflected and the incident light, respectively.

Then, the reflectivity R can be calculated by:

$$R = r^2 - = \frac{|E_{0r}|^2}{|E_{oi}|^2} \tag{7.53}$$

7.3 Appendix IV

This appendix pretends only to demonstrate the mechanism of the reaction occurred on the sensor surface during preparation of the self-assembled monolayers.

7.3.1 EDAC's coupling with PFP Mechanism

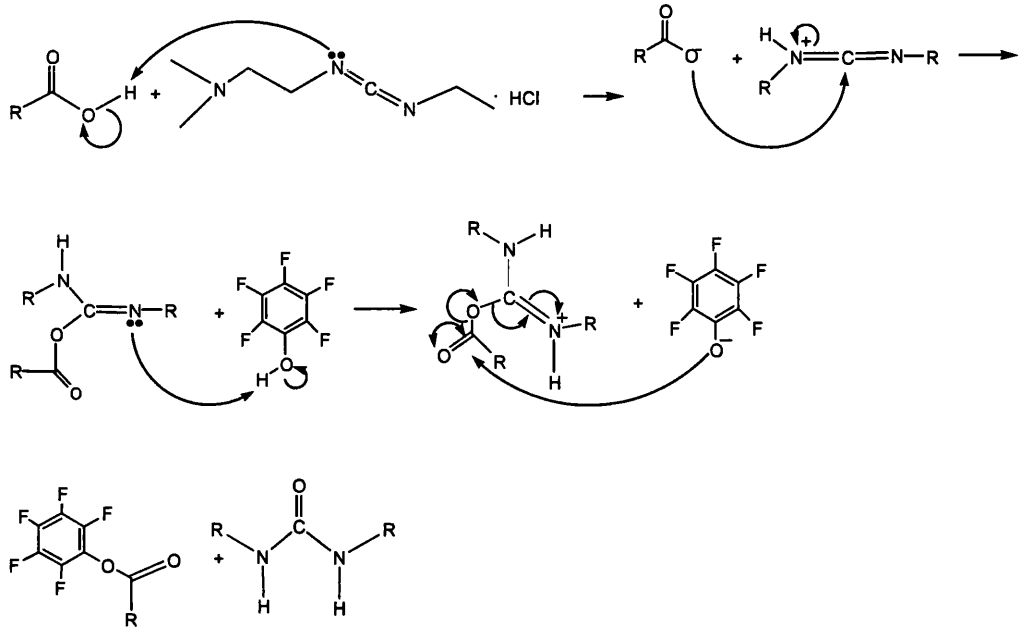

7.3.2 DADOO's coupling Mechanism

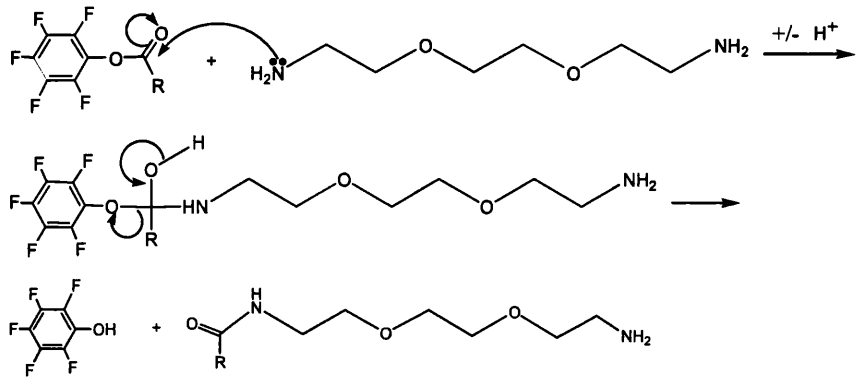

7.3.3 *Biotinylation Mechanism*

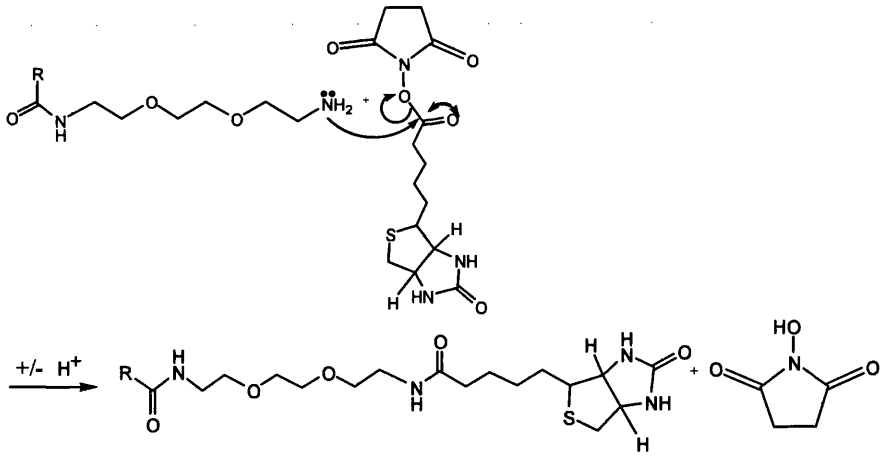

8 Bibliography

1. Horton, H.R., et al., *Principles of Biochemistry.* 2nd edition ed. 1996: Prentice-Hall International, Inc.
2. Oconnor, J.F., et al., *Recent Advances in the Chemistry and Immunochemistry of Human Chorionic-Gonadotropin - Impact on Clinical Measurements.* Endocrine Reviews, 1994. **15**(5): p. 650-683.
3. Hirose, T., *Exogeneous stimulation of corpus luteum formation in the rabbit; influence of extracts of human placenta, decidua fetus, hydatid mole and corpus luteum on the rabbit gonad.* J. Jpn. Gynecol. Soc, 1920. **16**: p. 1055.
4. Ascheim, S. and B. Zondek, *Die Schwangerschaftsdiagnose aus dem Harn durch Nachweis des Hypophysenvorderlappen-hormone. II. Pracktishe und Theoretische Ergebnisse aus den harnuntersuchungen.* Klin Wochenschr, 1928. **7**(1453).
5. Lapthorn, A.J., et al., *Crystal-Structure of Human Chorionic-Gonadotropin.* Nature, 1994. **369**(6480): p. 455-461.
6. Wu, H., et al., *Structure of human chorionic gonadotropin at 2.6 A resolution from MAD analysis of the selenomethionyl protein.* Structure, 1994. **2**: p. 545-58.
7. Tegoni, M., et al., *Crystal structure of a ternary complex between human chorionic gonadotropin (hCG) and two Fv fragments specific for the alpha and beta-subunits.* Journal of Molecular Biology, 1999. **289**(5): p. 1375-1385.
8. Berger, P., et al., *The ISOBM TD-7 Workshop on hCG and related molecules.* Tumor Biology, 2002. **23**(1): p. 1-38.
9. Brody, S. and G. Carlstrom, *Immunoassay of human chorionic gonadotropin in normal and pathologic pregnancy,.* Journal of Clinical Endocrinology and Metabolism, 1962. **22**: p. 564.
10. Henry, R., et al., *Development of a nanoparticle-based surface-modified fluorescence assay for the detection of prion proteins.* Analytical Biochemistry, 2004. **334**(1): p. 1-8.
11. Wide, L. and C.A. Gemzell, *An immunological pregnancy test.* Acta Endocrinologica, 1960. **35**: p. 261.
12. Dostalek, J., et al., *Surface plasmon resonance biosensor based on integrated optical waveguide.* Sensors and Actuators B-Chemical, 2001. **76**(1-3): p. 8-12.
13. Spinke, J., et al., *Molecular recognition at self-assembled monolayers: The construtrion of multicomponent multilayers.* Langmuir, 1993. **9**: p. 1821-1825.
14. Catty, D., *Antibodies: A practical approach*, ed. D. Rickwood and B.D. Hames. Vol. Volume 1. 1988, Oxford: IRL Press.
15. http://pim.medicine.dal.ca/atb.htm.
16. Goding, J.W., *Monoclonal Antibodies: Principles and practice.* 1996, Academic Press Limited. p. 72-100.
17. Kohler, G. and C. Milstein, *Continuous cultures of fused cells secreting antibody of predefined specificity (Reprinted from Nature, vol 256, 1975).* Journal of Immunology, 2005. **174**(5): p. 2453-2455.
18. Kohler, G., T. Pearson, and C. Milstein, *Fusion of T-Cells and B-Cells.* Somatic Cell Genetics, 1977. **3**(3): p. 303-312.
19. Kohler, G. and C. Milstein, *Derivation of Specific Antibody-Producing Tissue-Culture and Tumor Lines by Cell-Fusion.* European Journal of Immunology, 1976. **6**(7): p. 511-519.
20. Kohler, G., S.C. Howe, and C. Milstein, *Fusion between Immunoglobulin-Secreting and Nonsecreting Myeloma Cell Lines.* European Journal of Immunology, 1976. **6**(4): p. 292-295.
21. Organization, B.I., *What is Biotechnology?* 1989., Washington, D.C.

22. Canziani, G., et al., *Exploring biomolecular recognition using optical biosensors.* Methods, 1999. **19**: p. 253-269.
23. Rogers, K.R., *Principles of Affinity-Based Biosensors.* Molecular Biotechnology, 2000. **14**(2): p. 109-29.
24. Pearson, J.E., A. Gill, and P. Vadgam, *Analytical aspects of biosensors.* Ann. Clin. Biochem., 2000. **37**: p. 119-145.
25. Cooper, M.A., *Optical biosensors in drug discovery.* Nature Reviews Drug Discovery, 2002. **1**(7): p. 515-528.
26. Leatherbarrow, R.J. and P.R. Edwards, *Analysis of molecular recognition using optical biosensors.* Current Opinion in Chemical Biology, 1999. **3**(5): p. 544-547.
27. Homola, J., S.S. Yee, and G. Gauglitz, *Surface plasmon resonance sensors: review.* Sensors and Actuators B: Chemical, 1999. **54**(1-2): p. 3-15.
28. Nice, E.C. and B. Catimel, *Instrumental biosensors: new perspectives for the analysis of biomolecular interactions.* Bioessays, 1999. **21**(4): p. 339-352.
29. Van Regenmortel, M.H.V., *Analysis of structure-activity relationships with biosensors.* Biochemical Society Transactions, 1999. **27**(2): p. 329-331.
30. Hill, H.A.O. and J.J. Davis, *Biosensors: past, present and future.* Biochemical Society Transactions, 1999. **27**(2): p. 331-335.
31. Malmqvist, M., *BIACORE: an affinity biosensor system for characterization of biomolecular interactions.* Biochemical Society Transactions, 1999. **27**(2): p. 335-340.
32. Paddle, B.M., *Biosensors for chemical and biological agents of defence interest.* Biosensors & Bioelectronics, 1996. **11**(11): p. 1079-1113.
33. Frew, J.E. and H.A.O. Hill, *Electrochemical Biosensors.* Analytical Chemistry, 1987. **59**(15): p. A933-&.
34. Turner, A.P.F., I. Karube, and G.S. Wilson, *Biosensors: Fundamentals and Applications.* 1987, New York: Oxford Universtity Press.
35. Clark, L.C. and C. Lyons, http://chem.ch.huji.ac.il/~eugeniik/history/clark_leland.htm. Annals New York Academy of Sciences, 1962. **102**: p. 29-45.
36. Guilbault, G.G. and J. Montalvo, *A urea-specific enzyme electrode.* Journal of American Chemical Society, 1969. **91**: p. 2164-2165.
37. Conney, C.L., et al., *Enzyme Engineering.* Eds. E. K. Pye and L. B. Wingard Jnr. ed. Vol. 2. 1974, New York: Plenum. 411-417.
38. Davis, C., Annals of Microbiology, 1975. **26A**: p. 175-186.
39. Turner, A.P.F. *Biosensors: Past, Present and Future* http://www.cranfield.ac.uk/biotech/chinap.htm. [cited; Available from: http://www.cranfield.ac.uk/biotech/chinap.htm.
40. Cullen, D.C., R.S. Sethi, and C.R. Lowe, *Multi-analyte miniature conductance biosensor.* Analytica Chimica Acta, 1990. **231**: p. 33-40.
41. Grate, J.W., S.J. Martin, and R.M. White, *Accoustic wave microsensors Part 2.* Anal. Chem., 1993a. **65**: p. 987A-996A.
42. Narayanaswamy, R., *Optical Chemical Sensors - Transduction and Signal-Processing.* Analyst, 1993. **118**(4): p. 317-322.
43. Astles, J.R. and W.G. Miller, *Measurement of Free Phenytoin in Blood with a Self-Contained Fiberoptic Immunosensor.* Analytical Chemistry, 1994. **66**(10): p. 1675-1682.
44. Huang, W., et al., *Homogeneous Biochemiluminiescence competitive-binding assay for folate based on a coupled glucose-6-phosphate dehydrogenase-bacterial luci-ferase enzyme-system.* Anal. Chem., 1996. **68**: p. 1646-50.
45. Li, X. and Z. Rosenzweig, *A fiber-optic sensor of rapid analysis of bilirubin in serum.* Anal. Chim. Acta, 1997. **353**: p. 263-73.
46. Rico, C.M., et al., *Development of a Flow Fluoroimmunosensor for Determination of Theophylline.* Analyst, 1995. **120**(10): p. 2589-2591.

47. Zhang, W., H.D. Chang, and G.A. Rechnitz, *Dual-enzyme fiber optic biosensor for pyruvate.* Analytica Chimica Acta, 1997. **350**(1-2): p. 59-65.
48. Mignani, A.G. and F. Baldini, *Fibre-optic sensors in health care.* Physics in Medicine and Biology, 1997. **42**(5): p. 967-979.
49. Marazuela, M.D., et al., *Free cholesterol fibre-optic biosensor for serum samples with simplex optimization.* Biosens Bioelectron, 1997. **12**: p. 233-40.
50. Taitt, C.R., G.P. Anderson, and F.S. Ligler, *Evanescent wave fluorescence biosensors.* Biosensors & Bioelectronics, 2005. **20**(12): p. 2470-2487.
51. Baier, R.E. and R.C. Dutton, *Initial events in interaction of blood with a foreign surface.* J. Biomed. Mater. Res., 1969. **3**: p. 191-206.
52. Harrick, N.J. and G.I. Loeb, *Multiple Internal Reflection Fluorescence Spectrometry.* Analytical Chemistry, 1973. **45**(4): p. 687-691.
53. Kronick, M.N. and W.A. Little, *New Fluorescent Immunoassay.* Bulletin of the American Physical Society, 1973. **18**(5): p. 782-782.
54. Kronick, M.N. and W.A. Little, *New Immunoassay Based on Fluorescence Excitation by Internal- Reflection Spectroscopy.* Journal of Immunological Methods, 1975. **8**(3): p. 235-240.
55. Collings, A.F. and F. Caruso, *Biosensors: recent advances.* Reports on Progress in Physics, 1997. **60**(11): p. 1397-1445.
56. Ockman, N., *Antibody-Antigen Interaction at an Aqueous-Solid Interface - Study by Means of Polarized Infrared Atr Spectroscopy.* Biopolymers, 1978. **17**(5): p. 1273-1284.
57. Sutherland, R.M., et al., *Immunoassays at a Quartz-Liquid Interface - Theory, Instrumentation and Preliminary Application to the Fluorescent Immunoassay of Human Immunoglobulin-G.* Journal of Immunological Methods, 1984. **74**(2): p. 253-265.
58. Badley, R.A., et al., *Optical Biosensors for Immunoassays - the Fluorescence Capillary-Fill Device.* Philosophical Transactions of the Royal Society of London Series B-Biological Sciences, 1987. **316**(1176): p. 143-160.
59. Deacon, J.K., et al., *An Assay for Human Chorionic-Gonadotropin Using the Capillary Fill Immunosensor.* Biosensors & Bioelectronics, 1991. **6**(3): p. 193-199.
60. Parry, R.P., C. Love, and G.A. Robinson, *Detection of Rubella Antibody Using an Optical Immunosensor.* Journal of Virological Methods, 1990. **27**(1): p. 39-48.
61. Robinson, G.A., *Optical Immunosensing Systems - Meeting the Market Needs.* Biosensors & Bioelectronics, 1991. **6**(3): p. 183-191.
62. Choquette, S.J., L. Locasciobrown, and R.A. Durst, *Planar Wave-Guide Immunosensor with Fluorescent Liposome Amplification.* Analytical Chemistry, 1992. **64**(1): p. 55-60.
63. Zhou, Y., et al., *An Evanescent Fluorescence Biosensor Using Ion-Exchanged Buried Wave-Guides and the Enhancement of Peak Fluorescence.* Biosensors & Bioelectronics, 1991. **6**(7): p. 595-607.
64. Carlyon, E.E., et al., *A Single-Mode Fiberoptic Evanescent Wave Biosensor.* Biosensors & Bioelectronics, 1992. **7**(2): p. 141-146.
65. Nylander, C., B. Liedberg, and T. Lind, *Gas detection by means of surface plasmon resonance.* Sensors and Actuators, 1982/83. **3**: p. 79-88.
66. Liedberg, B., C. Nylander, and I. Lundström, *Surface plasmon resonance for gas detection and biosensing.* Sensors and Actuators, 1983. **4**: p. 299-304.
67. Weiss, M.N., R. Srivastava, and H. Groger, *Experimental investigation of a surface plasmon-based integrated-optic humidity sensor.* Electronics Letters, 1996. **32**(9): p. 842-843.
68. Chadwick, B. and M. Gal, *An Optical-Temperature Sensor Using Surface-Plasmons.* Japanese Journal of Applied Physics Part 1-Regular Papers Short Notes & Review Papers, 1993. **32**(6A): p. 2716-2717.

69. Miwa, S. and T. Arakawa, *Selective gas detection by means of surface plasmon resonance sensors.* Thin Solid Films, 1996. **282**(1-2): p. 466-468.
70. Abdelghani, A., et al., *Surface plasmon resonance fibre-optic sensor for gas detection.* Sensors and Actuators B-Chemical, 1997. **39**(1-3): p. 407-410.
71. Niggemann, M., et al., *Remote sensing of tetrachloroethene with a micro-fibre optical gas sensor based on surface plasmon resonance spectroscopy.* Sensors and Actuators B-Chemical, 1996. **34**(1-3): p. 328-333.
72. Podgorsek, R.P., et al., *Optical gas sensing by evaluating ATR leaky mode spectra.* Sensors and Actuators B-Chemical, 1997. **39**(1-3): p. 349-352.
73. Chadwick, B. and M. Gal, *Enhanced Optical-Detection of Hydrogen Using the Excitation of Surface-Plasmons in Palladium.* Applied Surface Science, 1993. **68**(1): p. 135-138.
74. Chadwick, B., et al., *A Hydrogen Sensor-Based on the Optical-Generation of Surface- Plasmons in a Palladium Alloy.* Sensors and Actuators B-Chemical, 1994. **17**(3): p. 215-220.
75. Ashwell, G.J. and M.P.S. Roberts, *Highly selective surface plasmon resonance sensor for NO2.* Electronics Letters, 1996. **32**(22): p. 2089-2091.
76. Granito, C., et al., *Toluene vapour sensing using copper and nickel phthalocyanine Langmuir-Blodgett films.* Thin Solid Films, 1996. **285**: p. 98-101.
77. Zhu, D.G., M.C. Petty, and M. Harris, *An Optical Sensor for Nitrogen-Dioxide Based on a Copper Phthalocyanine Langmuir-Blodgett-Film.* Sensors and Actuators B-Chemical, 1990. **2**(4): p. 265-269.
78. Vukusic, P.S. and J.R. Sambles, *Cobalt Phthalocyanine as a Basis for the Optical Sensing of Nitrogen-Dioxide Using Surface-Plasmon Resonance.* Thin Solid Films, 1992. **221**(1-2): p. 311-317.
79. Agbor, N.E., et al., *An optical gas sensor based on polyaniline Langmuir-Blodgett films.* Sensors and Actuators B-Chemical, 1997. **41**(1-3): p. 137-141.
80. Van Gent, J., et al., *Design and Realization of a Surface-Plasmon Resonance-Based Chemo-Optical Sensor.* Sensors and Actuators a-Physical, 1991. **26**(1-3): p. 449-452.
81. Jung, C.C., et al., *Chemical electrode surface plasmon resonance sensor.* Sensors and Actuators B-Chemical, 1996. **32**(2): p. 143-147.
82. Spinke, J., et al., *Molecular Recognition at Self-Assembled Monolayers - Optimization of Surface Functionalization.* Journal of Chemical Physics, 1993. **99**(9): p. 7012-7019.
83. Flanagan, M.T. and R.H. Pantell, *Surface-Plasmon Resonance and Immunosensors.* Electronics Letters, 1984. **20**(23): p. 968-970.
84. Kooyman, R.P.H., et al., *Surface-Plasmon Resonance Immunosensors - Sensitivity Considerations.* Analytica Chimica Acta, 1988. **213**(1-2): p. 35-45.
85. Mayo, C.S. and R.B. Hallock, *Immunoassay Based on Surface-Plasmon Oscillations.* Journal of Immunological Methods, 1989. **120**(1): p. 105-114.
86. Daniels, P.B., et al., *Surface-Plasmon Resonance Applied to Immunosensing.* Sensors and Actuators, 1988. **15**(1): p. 11-18.
87. Lepesheva, G.I., et al., *Direct-Detection of Antigens in Langmuir-Blodgett-Films of Immunoglobulins-G Formed by the Method of Surface-Plasmon Resonance Using a Piezoelectric System.* Biochemistry-Moscow, 1994. **59**(7): p. 701-705.
88. Cullen, D.C., R.G.W. Brown, and C.R. Lowe, *Detection of Immuno-Complex Formation Via Surface-Plasmon Resonance on Gold-Coated Diffraction Gratings.* Biosensors, 1987. **3**(4): p. 211-225.
89. Geddes, N.J., et al., *Immobilization of Igg onto Gold Surfaces and Its Interaction with Anti-Igg Studied by Surface-Plasmon Resonance.* Journal of Immunological Methods, 1994. **175**(2): p. 149-160.
90. Lawrence, C.R., et al., *Surface plasmon resonance studies of immunoreactions utilizing disposable diffraction gratings.* Biosensors and Bioelectronics, 1996. **11**(4): p. 389-400.

91. Caruso, F., et al., *Investigation of Immune-Reactions in a Flow-Injection System Using Surface-Plasmon Resonance.* Colloids and Surfaces a-Physicochemical and Engineering Aspects, 1995. **103**(3): p. 147-157.
92. Davies, J., et al., *Use of Scanning Probe Microscopy and Surface-Plasmon Resonance as Analytical Tools in the Study of Antibody-Coated Microtiter Wells.* Langmuir, 1994. **10**(8): p. 2654-2661.
93. Leung, P.T., et al., *Modeling of Particle-Enhanced Sensitivity of the Surface-Plasmon-Resonance Biosensor.* Sensors and Actuators B-Chemical, 1994. **22**(3): p. 175-180.
94. Severs, A.H. and R.B.M. Schasfoort, *Enhanced Surface-Plasmon Resonance Inhibition Test (Esprit) Using Latex-Particles.* Biosensors & Bioelectronics, 1993. **8**(7-8): p. 365-370.
95. Brecht, A. and G. Gauglitz, *Label free optical immunoprobes for pesticide detection.* Analytica Chimica Acta, 1997. **347**(1-2): p. 219-233.
96. Severs, A.H., R.B.M. Schasfoort, and M.H.L. Salden, *An Immunosensor for Syphilis Screening Based on Surface-Plasmon Resonance.* Biosensors & Bioelectronics, 1993. **8**(3-4): p. 185-189.
97. Abel, A.P., et al., *Fiber-Optic Evanescent Wave Biosensor for the Detection of Oligonucleotides.* Anal. Chem., 1996. **68**: p. 2905-2912.
98. L. Nencinia, et al., *A fibre-optic immunosensor for 2,4-dichlorophenoxyacetic acid detection.* Sensors and Actuators B: Chemical, 1998. **39**: p. 353-359.
99. Attridge, J.W., et al., *Sensitivity Enhancement of Optical Immunosensors by the Use of a Surface-Plasmon Resonance Fluoroimmunoassay.* Biosensors & Bioelectronics, 1991. **6**(3): p. 201-214.
100. Schmidt, E.K., et al., *Incorporation of the acetylcholine receptor dimer from Torpedo californica in a peptide supported lipid membrane investigated by surface plasmon and fluorescence spectroscopy.* Biosensors & Bioelectronics, 1998. **13**(6): p. 585-591.
101. Neumann, T., et al., *Surface-plasmon fluorescence spectroscopy.* Advanced Functional Materials, 2002. **12**(9): p. 575-586.
102. Liebermann, T. and W. Knoll, *Surface-plasmon field-enhanced fluorescence spectroscopy.* Colloid Surf. A-Physicochem. Eng. Asp., 2000. **171**(1-3): p. 115-130.
103. Liebermann, T., et al., *Complement hybridization from solution to surface-attached probe-oligonucleotides observed by surface-plasmon-field-enhanced fluorescence spectroscopy.* Colloids and Surfaces, 2000. **169**(1-3): p. 337-350.
104. Liebermann, T. and W. Knoll, *Parallel Multispot Detection of Target Hybridization to Surface-Bound Probe Oligonucleotides of Different Base Mismatch by Surface-Plasmon Field-Enhanced Fluorescence Microscopy.* Langmuir, 2003. **19**(5): p. 1567 -1572.
105. Kambhampati, D., P.E. Nielsen, and W. Knoll, *Investigating the kinetics of DNA-DNA and PNA-DNA interactions using surface plasmon resonance-enhanced fluorescence spectroscopy.* Biosensors & Bioelectronics, 2001. **16**(9-12): p. 1109-1118.
106. Yu, F., et al., *Surface plasmon fluorescence immunoassay of free prostate-specific antigen in human plasma at the femtomolar level.* Analytical Chemistry, 2004. **76**(22): p. 6765-6770.
107. Ekgasit, S., G. Stengel, and W. Knoll, *Concentration of dye-labeled nucleotides incorporated into DNA determined by surface plasmon resonance-surface plasmon fluorescence spectroscopy.* Analytical Chemistry, 2004. **76**(16): p. 4747-4755.
108. Ekgasit, S., et al., *Resonance shifts in SPR curves of nonabsorbing, weakly absorbing, and strongly absorbing dielectrics.* Sensors and Actuators B-Chemical, 2005. **105**(2): p. 532-541.

109. Ekgasit, S., C. Thammacharoen, and W. Knoll, *Surface plasmon resonance spectroscopy based on evanescent field treatment.* Analytical Chemistry, 2004. **76**(3): p. 561-568.
110. Ekgasit, S., et al., *Evanescent field in surface plasmon resonance and surface plasmon field-enhanced fluorescence spectroscopies.* Analytical Chemistry, 2004. **76**(8): p. 2210-2219.
111. Ekgasit, S., et al., *Influence of the metal film thickness on the sensitivity of surface plasmon resonance biosensors.* Applied Spectroscopy, 2005. **59**(5): p. 661-667.
112. Ekgasit, S., F. Yu, and W. Knoll, *Fluorescence intensity in surface-plasmon field-enhanced fluorescence spectroscopy.* Sensors and Actuators B: Chemical, 2005. **104**(2): p. 294-301.
113. Ekgasit, S., F. Yu, and W. Knoll, *Displacement of molecules near a metal surface as seen by an SPR-SPFS biosensor.* Langmuir, 2005. **21**(9): p. 4077-4082.
114. Yu, F., et al., *Attomolar sensitivity in bioassays based on surface plasmon fluorescence spectroscopy.* Journal of the American Chemical Society, 2004. **126**(29): p. 8902-8903.
115. Wink, T., et al., *Self-assembled monolayers for biosensors.* Analyst, 1997. **122**(4): p. R43-R50.
116. Ltd, K.I., *Langmuir and Langmuir-Blodgett Films*, KSV Instruments LTD: Helsinki, Finland.
117. Girard-Egrot, A.P., S. Godoy, and L.J. Blum, *Enzyme association with lipidic Langmuir-Blodgett films: Interests and applications in nanobioscience.* Advances in Colloid and Interface Science, 2005. **116**(1-3): p. 205-225.
118. Ulman, A., *Formation and structure of self-assembled monolayers.* Chemical Reviews, 1996. **96**(4): p. 1533-1554.
119. Ulman, A., et al., *Concentration-Driven Surface Transition in the Wetting of Mixed Alkanethiol Monolayers on Gold.* Journal of the American Chemical Society, 1991. **113**(5): p. 1499-1506.
120. Bain, C.D., et al., *Formation of Monolayer Films by the Spontaneous Assembly of Organic Thiols from Solution onto Gold.* Journal of the American Chemical Society, 1989. **111**(1): p. 321-335.
121. Evans, S.D., et al., *Self-Assembled Monolayers of Alkanethiols Containing a Polar Aromatic Group - Effects of the Dipole Position on Molecular Packing, Orientation, and Surface Wetting Properties.* Journal of the American Chemical Society, 1991. **113**(11): p. 4121-4131.
122. Schonherr, H., Ph.D. Thesis, Twente University, 2000.
123. Hendrickson, W.A., et al., *Crystal-Structure of Core Streptavidin Determined from Multiwavelength Anomalous Diffraction of Synchrotron Radiation.* Proceedings of the National Academy of Sciences of the United States of America, 1989. **86**(7): p. 2190-2194.
124. Haussling, L., et al., *Biotin-Functionalized Self-Assembled Monolayers on Gold - Surface-Plasmon Optical Studies of Specific Recognition Reactions.* Langmuir, 1991. **7**(9): p. 1837-1840.
125. Knoll, W., et al., *Streptavidin arrays as supramolecular architectures in surface-plasmon optical sensor formats.* Colloids and Surfaces, 2000. **161**(1): p. 115-137.
126. Darst, S.A., et al., *2-Dimensional Crystals of Streptavidin on Biotinylated Lipid Layers and Their Interactions with Biotinylated Macromolecules.* Biophysical Journal, 1991. **59**(2): p. 387-396.
127. Raether, H., *Spinger Tracks in Morden Physics.* Surface Plasmons on Smooth and Rough Surfaces and on Gratings. Vol. 111. 1988: Springer-Verlag.
128. Knoll, W., *Interfaces and thin films as seen by bound electromagnetic waves.* Annual Review of Physical Chemistry, 1998. **49**: p. 569-638.

129. Chen, W., A. Harstein, and E. Burstein, *Surface Polaritons at Atr Configurations.* Bulletin of the American Physical Society, 1974. **19**(3): p. 324-324.
130. Lakowicz, J.R., *Principles of Fluorescence Spectroscopy.* Second Edition ed. 1999, New York: Kluwer Academic/Plenum Plublishers.
131. Ha, T., *Single-molecule fluorescence resonance energy transfer.* Methods, 2001. **25**(1): p. 78-86.
132. Knoll, W., et al., *Supramolecular functional interfacial architectures for biosensor applications.* Physical Chemistry Chemical Physics, 2003. **5**(23): p. 5169-5175.
133. Neumann, T., *Strategies for Detecting DNA Hybridisation Using Surface Plasmon Fluorescence Spectroscopy*, in *Dep. of Chemistry and Pharmacy.* 2001, University of Mainz: Mainz.
134. Liebermann, T. and W. Knoll, *Surface-plasmon field-enhanced fluorescence spectroscopy.* Colloids and Surfaces A: Physicochemical and Engineering Aspects, 2000. **171**(1-3): p. 115-130.
135. Ulman, A., *An Introduction to Ultrathin Organic Films.* 1991, London: Academic Press.
136. Atkins, P.W., *Physical Chemistry*, ed. ed. 2001, New York: W.H. Freeman & Company.
137. Myszka, D.G., *Kinetic analysis of macromolecular interactions using surface plasmon resonance biosensors.* Current Opinion in Biotechnology, 1997. **8**(1): p. 50-57.
138. Scheller, A., *Wasplas.* 2003, Max-Planck-Institut fur Polymerforshung: Mainz.
139. Haussling, L., et al., *Direct Observation of Streptavidin Specifically Adsorbed on Biotin-Functionalized Self-Assembled Monolayers with the Scanning Tunneling Microscope.* Angewandte Chemie-International Edition in English, 1991. **30**(5): p. 569-572.
140. Cox, R.M.Z.E.C., *DNA Stretching on functionalized gold surfaces.* Nucleic Acids Research, 1994. **22**(3): p. 492-497.
141. Zhongping Yang, W.F., Tom Oliver, Ashutosh Chilkoti, *Light-Activated Affinity Micropatterning of Proteins on Self-Assembled Monolayers on Gold.* Langmuir, 2000. **16**: p. 1751-1758.
142. Lahiri, J., et al., *A strategy for the generation of surfaces presenting ligands for studies of binding based on an active ester as a common reactive intermediate: A surface plasmon resonance study.* Anal. Chem., 1999. **71**(4): p. 777-790.
143. Bain, C.D. and G.M. Whitesides, *Formation of Monolayers by the Coadsorption of Thiols on Gold - Variation in the Length of the Alkyl Chain.* Journal of the American Chemical Society, 1989. **111**(18): p. 7164-7175.
144. Invitrogen. *Amine-Reactive Probes.* 2005 [cited.
145. Yu, F., *Surface Plasmon Fluorescence Spectroscopy and Surface Plasmon Diffraction in Biomolecular Interaction Studies.* 2004, Max-Planck-Institut fur Polymerforschung.
146. Knoll, W., et al., *Streptavidin arrays as supramolecular architectures in surface-plasmon optical sensor formats.* Colloids and Surfaces a-Physicochemical and Engineering Aspects, 2000. **161**(1): p. 115-137.
147. Schneider, B.H., et al., *Highly sensitive optical chip immunoassays in human serum.* Biosensors and Bioelectronics, 2000. **15**(1-2): p. 13-22.
148. Bass, S., R. Greene, and J.A. Wells, *Hormone phage: An enrichment method for variant proteins with altered binding properties.* Proteins: Structure, Functions, and Genetics, 2004. **8**(4): p. 308-314.
149. Mittlerneher, S., et al., *Spectroscopic and Surface-Analytical Characterization of Self-Assembled Layers on Au.* Biosensors & Bioelectronics, 1995. **10**(9-10): p. 903-916.

150. Yu, F., D.F. Yao, and W. Knoll, *Surface plasmon field-enhanced fluorescence spectroscopy studies of the interaction between an antibody and its surface-coupled antigen.* Analytical Chemistry, 2003. **75**(11): p. 2610-2617.
151. Mullett, W.M., E.P.C. Lai, and J.M. Yeung, *Surface plasmon resonance-based immunoassays.* Methods, 2000. **22**(1): p. 77-91.
152. Rich, R.L. and D.G. Myszka, *Survey of the year 2000 commercial optical biosensor literature.* Journal of Molecular Recognition, 2001. **14**(5): p. 273-294.
153. Karlsson R., *Real-Time Competitive Kinetic Analysis of Interactions between Low-Molecular-Weight Ligands in Solution and Surface-Immobilized Receptors.* Analytical Biochemistry, 1994. **221**(1): p. 142-151.
154. Gestwicki, J.E., H.V. Hsieh, and J.B. Pitner, *Using receptor conformational change to detect low molecular weight analytes by surface plasmon resonance.* Analytical Chemistry, 2001. **73**(23): p. 5732-5737.
155. Adamczyk, M., J.A. Moore, and Z. Yu, *Application of Surface Plasmon Resonance toward Studies of Low-Molecular-Weight Antigen-Antibody Binding Interactions.* Methods, 2000. **20**(3): p. 319-328.
156. Malicka, J., et al., *Surface plasmon-coupled ultraviolet emission of 2,5-diphenyl-1,3,4-oxadiazole.* Journal of Physical Chemistry B, 2004. **108**(50): p. 19114-19118.
157. Matveeva, E., et al., *Myoglobin immunoassay utilizing directional surface plasmon- coupled emission.* Analytical Chemistry, 2004. **76**(21): p. 6287-6292.
158. Attridge, J.W., et al., *Sensitivity enhancement of optical immunosensors by the use of a surface plamon resonance fluoroimmunoassay.* Biosensors & Bioelectronics, 1991. **6**: p. 201-214.
159. Green, R.J., et al., *Surface plasmon resonance for real time in situ analysis of protein adsorption to polymer surfaces.* Biomaterials, 1997. **18**(5): p. 405-413.
160. Ekins, R. and P. Edwards, *On the meaning of "sensitivity": A rejoinder.* Clinical Chemistry, 1998. **44**(8): p. 1773-1776.
161. Chetcuti, A.F., D.K.Y. Wong, and M.C. Stuart, *An indirect perfluorosulfonated ionomer-coated electrochemical immunosensor for the detection of the protein human chorionic gonadotrophin.* Analytical Chemistry, 1999. **71**(18): p. 4088-4094.
162. Schneider, B.H., et al., *Optical chip immunoassay for hCG in human whole blood.* Biosensors and Bioelectronics, 2000. **15**(11-12): p. 597-604.
163. Zhang, B., et al., *A novel piezoelectric quartz micro-array immunosensor based on self-assembled monolayer for determination of human chorionic gonadotropin.* Biosensors & Bioelectronics, 2004. **19**(7): p. 711-720.
164. Valagussa, F., et al., *Dietary supplementation with n-3 polyunsaturated fatty acids and vitamin E after myocardial infarction: results of the GISSI-Prevenzione trial.* Lancet, 1999. **354**(9177): p. 447-455.
165. Albert, C.M., et al., *Fish consumption and risk of sudden cardiac death.* Jama-Journal of the American Medical Association, 1998. **279**(1): p. 23-28.
166. Singh, R.B., et al., *Randomized, double-blind, placebo-controlled trial of fish oil and mustard oil in patients with suspected acute myocardial infarction: The Indian experiment of infarct survival .4.* Cardiovascular Drugs and Therapy, 1997. **11**(3): p. 485-491.
167. Siscovick, D.S., et al., *Dietary-Intake and Cell-Membrane Levels of Long-Chain N-3 Polyunsaturated Fatty-Acids and the Risk of Primary Cardiac-Arrest.* Jama-Journal of the American Medical Association, 1995. **274**(17): p. 1363-1367.
168. Delorgeril, M., et al., *Mediterranean Alpha-Linolenic Acid-Rich Diet in Secondary Prevention of Coronary Heart-Disease.* Lancet, 1994. **343**(8911): p. 1454-1459.
169. Katz, A.M., *Trans-fatty acids and sudden cardiac death.* Circulation, 2002. **105**(6): p. 669-671.

170. Jones, R.L., et al., *Association between Inhibition of Arachidonic-Acid Release and Prevention of Calcium Loading During Atp Depletion in Cultured Rat Cardiac Myocytes.* American Journal of Pathology, 1989. **135**(3): p. 541-556.
171. Paolisso, G., et al., *Association of fasting plasma free fatty acid concentration and frequency of ventricular premature complexes in nonischemic non-insulin-dependent diabetic patients.* American Journal of Cardiology, 1997. **80**(7): p. 932-937.
172. Jouven, X., et al., *Circulating nonesterified fatty acid level as a predictive risk factor for sudden death in the population.* Circulation, 2001. **104**(7): p. 756-761.
173. Lemaitre, R.N., et al., *Cell membrane trans-fatty acids and the risk of primary cardiac arrest.* Circulation, 2002. **105**(6): p. 697-701.
174. Oomen, C.M., et al., *Association between trans fatty acid intake and 10-year risk of coronary heart disease in the Zutphen Elderly Study: a prospective population-based study.* Lancet, 2001. **357**(9258): p. 746-751.
175. Richieri, G.V. and A.M. Kleinfeld, *Free Fatty-Acids Are Produced in and Secreted from Target-Cells Very Early in Cytotoxic Lymphocyte-T-Mediated Killing.* Journal of Immunology, 1991. **147**(8): p. 2809-2815.
176. Richieri, G.V. and A.M. Kleinfeld, *Free Fatty-Acids Inhibit Cytotoxic Lymphocyte-T-Mediated Lysis of Allogeneic Target-Cells.* Journal of Immunology, 1990. **145**(4): p. 1074-1077.
177. Richieri, G.V., M.F. Mescher, and A.M. Kleinfeld, *Short-Term Exposure to Cis-Unsaturated Free Fatty-Acids Inhibits Degranulation of Cytotoxic Lymphocytes-T.* Journal of Immunology, 1990. **144**(2): p. 671-677.
178. Richieri, G.V. and A.M. Kleinfeld, *Free Fatty-Acid Perturbation of Transmembrane Signaling in Cyto-Toxic Lymphocytes-T.* Journal of Immunology, 1989. **143**(7): p. 2302-2310.
179. Scapin, G., J.I. Gordon, and J.C. Sacchettini, *Refinement of the Structure of Recombinant Rat Intestinal Fatty Acid-Binding Apoprotein at 1.2-a Resolution.* Journal of Biological Chemistry, 1992. **267**(6): p. 4253-4269.
180. Sacchettini, J.C., J.I. Gordon, and L.J. Banaszak, *Crystal-Structure of Rat Intestinal Fatty-Acid-Binding Protein - Refinement and Analysis of the Escherichia-Coli-Derived Protein with Bound Palmitate.* Journal of Molecular Biology, 1989. **208**(2): p. 327-339.
181. Richieri, G.V., R.T. Ogata, and A.M. Kleinfeld, *A Fluorescently Labeled Intestinal Fatty-Acid Binding-Protein - Interactions with Fatty-Acids and Its Use in Monitoring Free Fatty-Acids.* Journal of Biological Chemistry, 1992. **267**(33): p. 23495-23501.
182. Vincent, S.H. and U. Mullereberhard, *A Protein of the Z-Class of Liver Cytosolic Proteins in the Rat That Preferentially Binds Heme.* Journal of Biological Chemistry, 1985. **260**(27): p. 4521-4528.
183. Storch, J., N.M. Bass, and A.M. Kleinfeld, *Studies of the Fatty Acid-Binding Site of Rat-Liver Fatty Acid-Binding Protein Using Fluorescent Fatty-Acids.* Journal of Biological Chemistry, 1989. **264**(15): p. 8708-8713.
184. Nemecz, G., et al., *Interaction of Fatty-Acids with Recombinant Rat Intestinal and Liver Fatty Acid-Binding Proteins.* Archives of Biochemistry and Biophysics, 1991. **286**(1): p. 300-309.
185. Richieri, G.V., R.T. Ogata, and A.M. Kleinfeld, *Equilibrium-Constants for the Binding of Fatty-Acids with Fatty-Acid-Binding Proteins from Adipocyte, Intestine, Heart, and Liver Measured with the Fluorescent-Probe Adifab.* Journal of Biological Chemistry, 1994. **269**(39): p. 23918-23930.
186. Richieri, G.V., R.T. Ogata, and A.M. Kleinfeld, *Thermodynamics of Fatty-Acid-Binding to Fatty-Acid-Binding Proteins and Fatty-Acid Partition between Water and Membranes Measured Using the Fluorescent-Probe Adifab.* Journal of Biological Chemistry, 1995. **270**(25): p. 15076-15084.
187. Ballou, G.A., et al., *THE HEAT COAGULATION OF HUMAN SERUM ALBUMIN*

J. Biol. Chem., 1944. **153**(2): p. 589-605.
188. Spector, A., *Fatty acid binding to plasma albumin.* J. Lipid Res., 1975. **16**(3): p. 165-179.
189. http://www2.hawaii.edu/~chungeun/. *Human Albumin Ribbon Structure.* [cited.
190. Lovrien, R., *Interactions of dodecyl sulfate anions of low concentration with alkaline bovine serum albumin.* J. Amer. Chem. Soc, 1963. **85**: p. 3677-3682.
191. Karush, R., *Heterogeneity of the binding sites of bovine serum albumin.* J. Amer. Chem. Soc, 1950. **72**: p. 2705-2713.
192. Karush, R., *The interaction of optically isomeric dyes with human serum albumin.* J. Amer. Chem. Soc, 1954. **76**: p. 5536-5542.
193. Burton, K.P., et al., *Accumulation of Arachidonate in Triacylglycerols and Unesterified Fatty-Acids During Ischemia and Reflow in the Isolated Rat-Heart - Correlation with the Loss of Contractile Function and the Development of Calcium Overload.* American Journal of Pathology, 1986. **124**(2): p. 238-245.
194. Ford, D.A., et al., *The Rapid and Reversible Activation of a Calcium-Independent Plasmalogen-Selective Phospholipase-A2 During Myocardial-Ischemia.* Journal of Clinical Investigation, 1991. **88**(1): p. 331-335.
195. Reaven, G.M., et al., *Measurement of Plasma-Glucose, Free Fatty-Acid, Lactate, and Insulin for 24-H in Patients with Niddm.* Diabetes, 1988. **37**(8): p. 1020-1024.
196. Legaspi, A., et al., *Whole-Body Lipid and Energy-Metabolism in the Cancer-Patient.* Metabolism-Clinical and Experimental, 1987. **36**(10): p. 958-963.
197. Brown, R.E., et al., *Fatty-Acids and the Inhibition of Mitogen-Induced Lymphocyte-Transformation by Leukemic Serum.* Journal of Immunology, 1983. **131**(2): p. 1011-1016.
198. Richieri, G.V., A. Anel, and A.M. Kleinfeld, *Interactions of Long-Chain Fatty-Acids and Albumin - Determination of Free Fatty-Acid Levels Using the Fluorescent- Probe Adifab.* Biochemistry, 1993. **32**(29): p. 7574-7580.
199. Richieri, G.V. and A.M. Kleinfeld, *Unbound Free Fatty-Acid Levels in Human Serum.* Journal of Lipid Research, 1995. **36**(2): p. 229-240.
200. Kleinfeld, A.M., et al., *Increases in serum unbound free fatty acid levels following coronary angioplasty.* American Journal of Cardiology, 1996. **78**(12): p. 1350-1354.
201. Ashbrook, J.D., et al., *Long-Chain Fatty-Acid Binding to Human Plasma Albumin.* Journal of Biological Chemistry, 1975. **250**(6): p. 2333-2338.
202. Spector, A.A., J.E. Fletcher, and J.D. Ashbrook, *Analysis of Long-Chain Free Fatty Acid Binding to Bovine Serum Albumin by Determination of Stepwise Equilibrium Constants.* Biochemistry, 1971. **10**(17): p. 3229-&.
203. Aranyi, P., *Kinetics of the Hormone-Receptor Interaction - Competition Experiments with Slowly Equilibrating Ligands.* Biochimica Et Biophysica Acta, 1980. **628**(2): p. 220-227.
204. Motulsky, H.J. and L.C. Mahan, *The Kinetics of Competitive Radioligand Binding Predicted by the Law of Mass-Action.* Molecular Pharmacology, 1984. **25**(1): p. 1-9.
205. http://www.piercenet.com/Objects/View.cfm?type=Page&ID=75D6C066-AB3E-4B74-87F2-C38A85F0DBC4. (2002) *Comparison of Protein A, A/G, G and L. .* **Volume**,
206. Pierce, *b-Protein A.*
207. Unlu, M., M.E. Morgan, and J.S. Minden, *Difference gel electrophoresis: A single gel method for detecting changes in protein extracts.* Electrophoresis, 1997. **18**(11): p. 2071-2077.
208. Chan, H.L., et al., *Proteomic analysis of redox- and ErbB2-dependent changes in mammary luminal epithelial cells using cysteine- and lysine-labelling two-dimensional difference gel electrophoresis.* Proteomics, 2005. **5**(11): p. 2908-2926.

209. Wikipedia. http://en.wikipedia.org/wiki/Bilirubin. 2006 [cited.
210. Voet and Voet, *Biochemistry*. 2ND edition ed. 2000: Wiley.
211. Stryer, L., *DNA and RNA: Molecules of Heredity*, in *Biochemistry*. 1988, W. H. Freeman and Company: New York. p. 71-90.
212. Mohanty, S.P., *Biosensors: A Survey Report*. 2001. p. 1-15.
213. Tawa, K. and W. Knoll, *Hybridization process of immobilized DNA observed by surface plasmon fluorescence spectroscopy*. Abstracts of Papers of the American Chemical Society, 2002. **223**: p. 475-coll.
214. Myszka, D.G., *Survey of the 1998 optical biosensor literature*. Journal of Molecular Recognition, 1999. **12**(6): p. 390-408.
215. Rich, R.L. and D.G. Myszka, *Survey of the 1999 surface plasmon resonance biosensor literature*. Journal of Molecular Recognition, 2000. **13**(6): p. 388-407.
216. Rich, R.L. and D.G. Myszka, *Survey of the year 2001 commercial optical biosensor literature*. Journal of Molecular Recognition, 2002. **15**(6): p. 352-376.
217. Hall, E.A.H., *Recent Progress in Biosensor Development*. International Journal of Biochemistry, 1988. **20**(4): p. 357-362.
218. Alivisatos, A.P., et al., *Organization of 'nanocrystal molecules' using DNA*. Nature, 1996. **382**(6592): p. 609-611.
219. Mucic, R.C., et al., *DNA-directed synthesis of binary nanoparticle network materials*. Journal of the American Chemical Society, 1998. **120**(48): p. 12674-12675.
220. Mitchell, G.P., C.A. Mirkin, and R.L. Letsinger, *Programmed assembly of DNA functionalized quantum dots*. Journal of the American Chemical Society, 1999. **121**(35): p. 8122-8123.
221. Reynolds, R.A., C.A. Mirkin, and R.L. Letsinger, *Homogeneous, nanoparticle-based quantitative colorimetric detection of oligonucleotides*. Journal of the American Chemical Society, 2000. **122**(15): p. 3795-3796.
222. Taton, T.A., et al., *The DNA-mediated formation of supramolecular mono- and multilayered nanoparticle structures*. Journal of the American Chemical Society, 2000. **122**(26): p. 6305-6306.
223. Storhoff, J.J., et al., *One-pot colorimetric differentiation of polynucleotides with single base imperfections using gold nanoparticle probes*. Journal of the American Chemical Society, 1998. **120**(9): p. 1959-1964.
224. Storhoff, J.J., et al., *What controls the optical properties of DNA-linked gold nanoparticle assemblies?* Journal of the American Chemical Society, 2000. **122**(19): p. 4640-4650.
225. Elghanian, R., et al., *Selective colorimetric detection of polynucleotides based on the distance-dependent optical properties of gold nanoparticles*. Science, 1997. **277**(5329): p. 1078-1081.
226. Storhoff, J.J., et al., *Gold nanoparticle-based detection of genomic DNA targets on microarrays using a novel optical detection system*. Biosensors & Bioelectronics, 2004. **19**(8): p. 875-883.
227. Daniel, M.C. and D. Astruc, *Gold nanoparticles: Assembly, supramolecular chemistry, quantum-size-related properties, and applications toward biology, catalysis, and nanotechnology*. Chemical Reviews, 2004. **104**(1): p. 293-346.
228. Mie, G., *Beitrage zur Optik Truber Medien, Speziell Kolloidaler Metallosungen*. Ann. Phys., 1908. **25**: p. 377-445.
229. Alvarez, M.M., et al., *Optical absorption spectra of nanocrystal gold molecules*. Journal of Physical Chemistry B, 1997. **101**(19): p. 3706-3712.
230. Coffer, J.L., J.R. Shapley, and H.G. Drickamer, *The Effect of Pressure on the Surface-Plasmon Absorption-Spectra of Colloidal Gold and Silver Particles*. Journal of the American Chemical Society, 1990. **112**(10): p. 3736-3742.
231. Englebienne, P., *Use of colloidal gold surface plasmon resonance peak shift to infer affinity constants from the interactions between protein antigens and*

antibodies specific for single or multiple epitopes. Analyst, 1998. **123**(7): p. 1599-1603.
232. Hwang, Y.N., et al., *Femtosecond emission studies on gold nanoparticles.* Journal of Physical Chemistry B, 2002. **106**(31): p. 7581-7584.
233. Ming, M., Y. Chen, and A. Katz, *Steady-state fluorescence-based investigation of the interaction between protected thiols and gold nanoparticles.* Langmuir, 2002. **18**(6): p. 2413-2420.
234. Sleytr, U.B., et al., *Characterization and use of crystalline bacterial cell surface layers.* Progress in Surface Science, 2001. **68**: p. 231-278.
235. Wang, T.X., et al., *Preparation, characterization, and photophysical properties of alkanethiols with pyrene units-capped gold nanoparticles: Unusual fluorescence enhancement for the aged solutions of these gold nanoparticles.* Langmuir, 2002. **18**(5): p. 1840-1848.
236. Sarathy, K.V., et al., *Novel fluorescence and morphological structures in gold nanoparticle-polyoctylthiophene based thin films.* Chemical Physics Letters, 2000. **318**(6): p. 543-548.
237. Qian, W., et al., *Atomic force microscopic studies of site-directed immobilization of antibodies using their carbohydrate residues.* Chemistry of Materials, 1999. **11**(6): p. 1399-+.
238. Makarova, O.V., et al., *Adsorption and encapsulation of fluorescent probes in nanoparticles.* Journal of Physical Chemistry B, 1999. **103**(43): p. 9080-9084.
239. Dulkeith, E., et al., *Fluorescence quenching of dye molecules near gold nanoparticles: Radiative and nonradiative effects.* Physical Review Letters, 2002. **89**(20).
240. Dubertret, B., M. Calame, and A.J. Libchaber, *Single-mismatch detection using gold-quenched fluorescent oligonucleotides.* Nature Biotechnology, 2001. **19**(4): p. 365-370.
241. Gu, T., J.K. Whitesell, and M.A. Fox, *Energy transfer from a surface-bound arene to the gold core in omega-fluorenyl-alkane-1-thiolate monolayer-protected gold clusters.* Chemistry of Materials, 2003. **15**(6): p. 1358-1366.
242. Imahori, H. and S. Fukuzumi, *Porphyrin monolayer-modified gold clusters as photoactive materials.* Advanced Materials, 2001. **13**(15): p. 1197-+.
243. Wilcoxon, J.P., et al., *Photoluminescence from nanosize gold clusters.* Journal of Chemical Physics, 1998. **108**(21): p. 9137-9143.
244. Li, H.X. and L.J. Rothberg, *DNA sequence detection using selective fluorescence quenching of tagged oligonucleotide probes by gold nanoparticles.* Analytical Chemistry, 2004. **76**(18): p. 5414-5417.
245. Dulkeith, E., et al., *Gold nanoparticles quench fluorescence by phase induced radiative rate suppression.* Nano Letters, 2005. **5**(4): p. 585-589.
246. Aslan, K., et al., *Metal-enhanced fluorescence solution-based sensing platform.* Journal of Fluorescence, 2004. **14**(6): p. 677-679.
247. Vareiro, M.M.L.M., et al., *Surface Plasmon Fluorescence Measurements of Human Chorionic Gonadotrophin: Role of Antibody Orientation in Obtaining Enhanced Sensitivity and Limit of Detection.* Analytical Chemistry, 2005. **77**(8): p. 2426 - 2431.
248. Neumann, T. and W. Knoll, *Mismatch discrimination in oligonucleotide hybridization reactions using single strand binding protein. A surface plasmon fluorescence study.* Israel Journal of Chemistry, 2001. **41**(1): p. 69-78.
249. Hecht, E., *Optics.* 4th Edition ed. 2002, San Francisco, USA: Addison Wesley.
250. Jackson, J.D., *Classical Electrodynamics.* 2nd Edition ed. 1975: John Wiley & Sons, Inc.